

LEGIBILITY NOTICE

A major purpose of the Technical Information Center is to provide the broadest dissemination possible of information contained in DOE's Research and Development Reports to business, industry, the academic community, and federal, state and local governments.

Although a small portion of this report is not reproducible, it is being made available to expedite the availability of information on the research discussed herein.

DOE/JPL/956766--85/01

DE85 016575

FINAL REPORT
DOE/JPL Contract Co., 956766
Electrical Research on Solar cells and Photovoltaic Materials

This effort is being conducted pursuant to an Interagency Agreement between the Department of Engineering (DOE) and the National Aeronautics and Space Administration (NASA) and in furtherance of work under Prime Contract NAS 7-918 between NASA and the California Institute of Technology.

John Orehotsky
Professor of Engineering
and Physics
Wilkes College
Wilkes-Barre, PA 18766

Project Identification - Silicon Material
March 5, 1985
DRL No. 213

INTRODUCTION

An important objective of the Flat-Plate Solar Cell Array Program is to increase the service lifetime of the photovoltaic modules used for terrestrial energy applications. The current-voltage response characteristics of the solar cells encapsulated in the modules is found to degrade with service time and this degradation places a limitation on the useful lifetime of the modules.

Corrosion appears to be one important physical mechanism that degrades the current-voltage response of the solar cells, and any effort that increases the lifetime by stopping the I-V degradation must address the question of minimizing the corrosion activity associated with the composite metallurgy, anti-reflection coating and p-n semiconductor materials that comprise a typical solar cell.

Minimizing the corrosion activity involves a consideration of both the electrochemical characteristics of the various composite materials in the cells and the ionic conductive properties of the pottant polymer used to encapsulate the cells. Consequently, the most desirable flat-plate array system would involve solar cells consisting of highly polarizable materials with similar electrochemical potentials where the cells would be encapsulated in polymers whose ionic concentrations and mobilities are negligibly small. Specifying a suitable polymer for pottant use is not an easy task since cross-linking agents, plasticizers, absorbed water and other ingredients can contribute significantly to the concentration of ions in the polymer.

Another possible mechanism limiting the service lifetime of the photovoltaic modules is the gradual loss of the electrical insulation characteristics of the polymer pottant due to water absorption or due to polymer degradation from light or heat effects.

A systematic study of the properties of various polymer pottant materials and of the electrochemical corrosion mechanisms in solar cell

materials is required for advancing the technology of terrestrial photovoltaic modules. The items of specific concern in the sponsored research activity at Wilkes College involve:

- I. Kinetics of plasticizer loss in PVB
- II. Kinetics of water absorption and desorption in PVB
- III. Kinetics of water absorption and desorption in EVA
- IV. The electrical properties of PVB as a function of temperature and humidity
- V. The electrical properties of EVA as a function of temperature and humidity.
- VI. Solar cell corrosion characteristics
- VII. Water absorption effects in PVB and EVA
- VIII. Ion implantation and radiation effects in PVB and EVA

1 - Kinetics of Plasticizer Loss in PVB

The kinetics of plasticizer loss in PVB were evaluated gravimetrically at temperatures of 98 °, 83 °, 76 °, and 64 ° C on Monsanto Saflex PVB samples that were previously dried for two weeks at 25 ° C in a desiccator. The isothermal time dependence of the normalized weight loss of the PVB samples in a dry box at the various temperatures is presented in Figure 1.1. Because of limited time, the weight loss kinetics were not monitored to completion but the results at 98 ° C show that at least 23 weight percent of the PVB is plasticizer. This result is in reasonable accord with Monsanto specifications which suggest that 28% of the PVB is plasticizer where the identity of the plasticizer is 90% dihexyl adipate and 10% di(butylbenzyl) phthalate.

The plasticizer weight loss kinetics can be characterized by an initial transient where the isothermal normalized weight loss is a linear function (Figs. 1.2 to 1.4) of time:

$$w_t/w_o = -\alpha t + \beta \quad 1.1$$

where $\beta=1$ and where the rate constant α obeys (Fig. 1.5) an Arrhenius relationship:

$$\alpha = \alpha_o \exp(-Q_I/RT) \quad 1.2$$

involving an activation energy (Q_I) and pre-exponential factor (α_o) of 26 Kcal/mole and $9.9(10^{12})$ hours respectively:

$$Q_I = 26 \text{ Kcal/mole} \quad 1.3$$

$$\alpha_o = 9.9(10^{12}) \text{ hrs}^{-1} \quad 1.4$$

This initial transient is followed by a kinetic stage where the normalized weight loss is dependent (Figs. 1.2 to 1.3) on the square root of time:

$$w_t/w_o = -\gamma t^{1/2} + \delta \quad 1.5$$

where $\delta \approx 1.05$ and where the rate constant γ was found (Fig. 1.6) to

have an Arrhenius temperature dependency:

$$\gamma = \gamma_0 \exp(-Q_{II}/RT) \quad 1.6$$

characterized by an activation energy Q_{II} and a pre-exponential γ_0 factor of:

$$Q_{II} = 16 \text{ Kcal/mole} \quad 1.7$$

$$\gamma_0 = 3.4(10^7) \text{ hrs}^{-1} \quad 1.8$$

A dependence on the square root of time is expected from simple volume diffusion considerations for the semi-infinite plate geometry of the PVB samples.

A complete summary of the characterizing parameters for the plasticizer loss kinetics on PVB for both stages is presented in Table 1.1. From this information, the weight loss is found to obey the kinetic equations for Stage I:

$$w_t/w_0 = 9.9(10^{12})[\exp(-1300/T)]t + 1 \quad 1.9$$

and the kinetic equation for Stage II:

$$w_t/w_0 = 3.4(10^7)[\exp(-800/T)]t^{1/2} + 1.05 \quad 1.10$$

These equations can be used to predict the plasticizer loss rate per gram of PVB at various temperatures, and these results are presented in Table 1.2.

Table 1.1

Response characteristics and kinetic parameters for both stages of plasticizer loss in PVB as determined by normalized weight loss (W_t/W_0) measurements.

	Stage I	Stage II
Rate Equation	$w_t/w_0 = -\alpha t + \beta$	$w_t/w_0 = -\gamma t^{1/2} + \delta$
Rate constant	$\alpha = \alpha_0 \exp(-Q_I/RT)$	$\gamma = \gamma_0 \exp(-Q_{II}/RT)$
Pre-exponential	$\alpha_0 = 9.9(10^{12})$	$\gamma_0 = 3.4(10^7)$
Activation Energy	$Q_I = 26 \text{ Kcal/mole}$	$Q_{II} = 16 \text{ Kcal/mole}$
Intercept	$\beta = 1$	$\delta \approx 1.05$

Table 1.2

First stage plasticizer loss rates at various temperatures.

<u>Temperature</u> <u>(° C)</u>	<u>Grams plasticizer lost per gram PVB per hour</u>
25	$1.1 (10^{-6})$
50	$3.1 (10^{-5})$
85	$1.3 (10^{-3})$

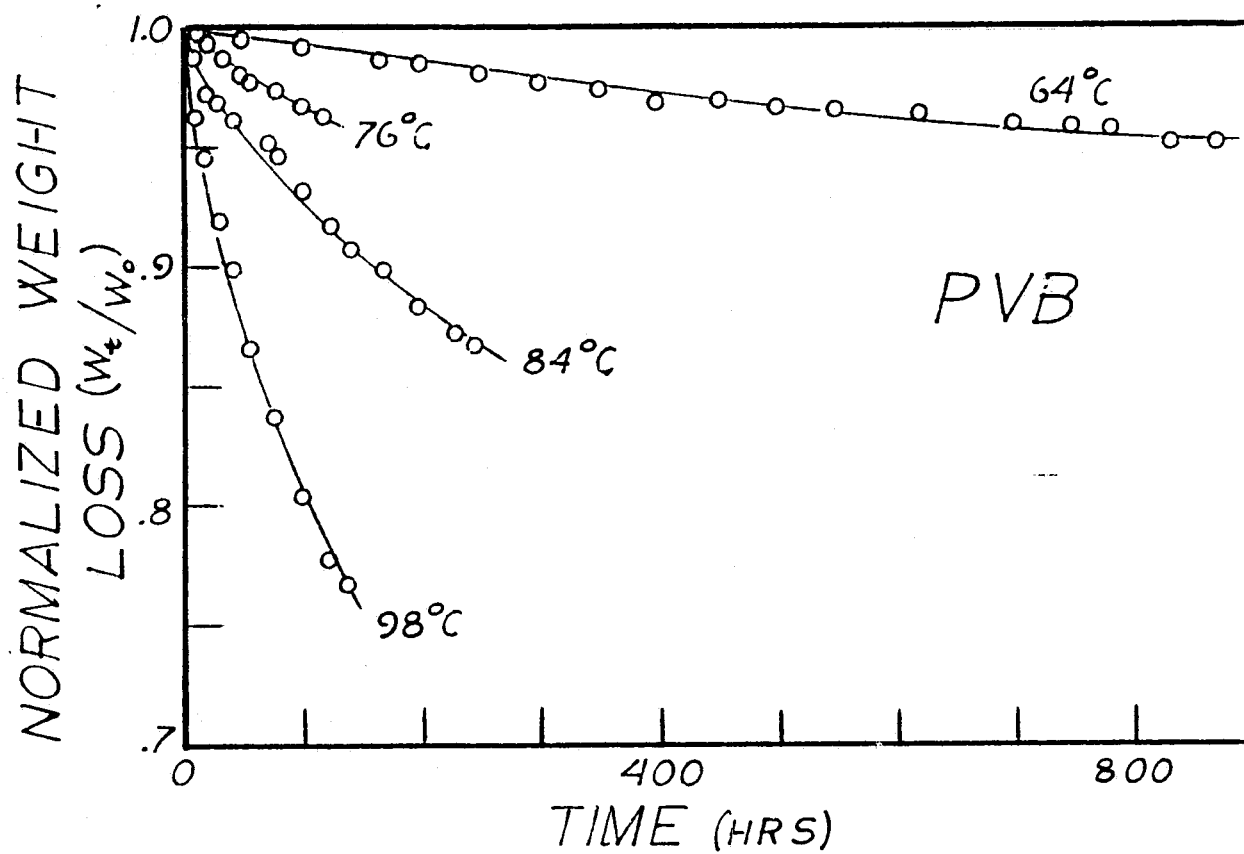


Fig 1.1-Normalized weight loss of plasticizer in PVB as a function of time at selected temperatures.

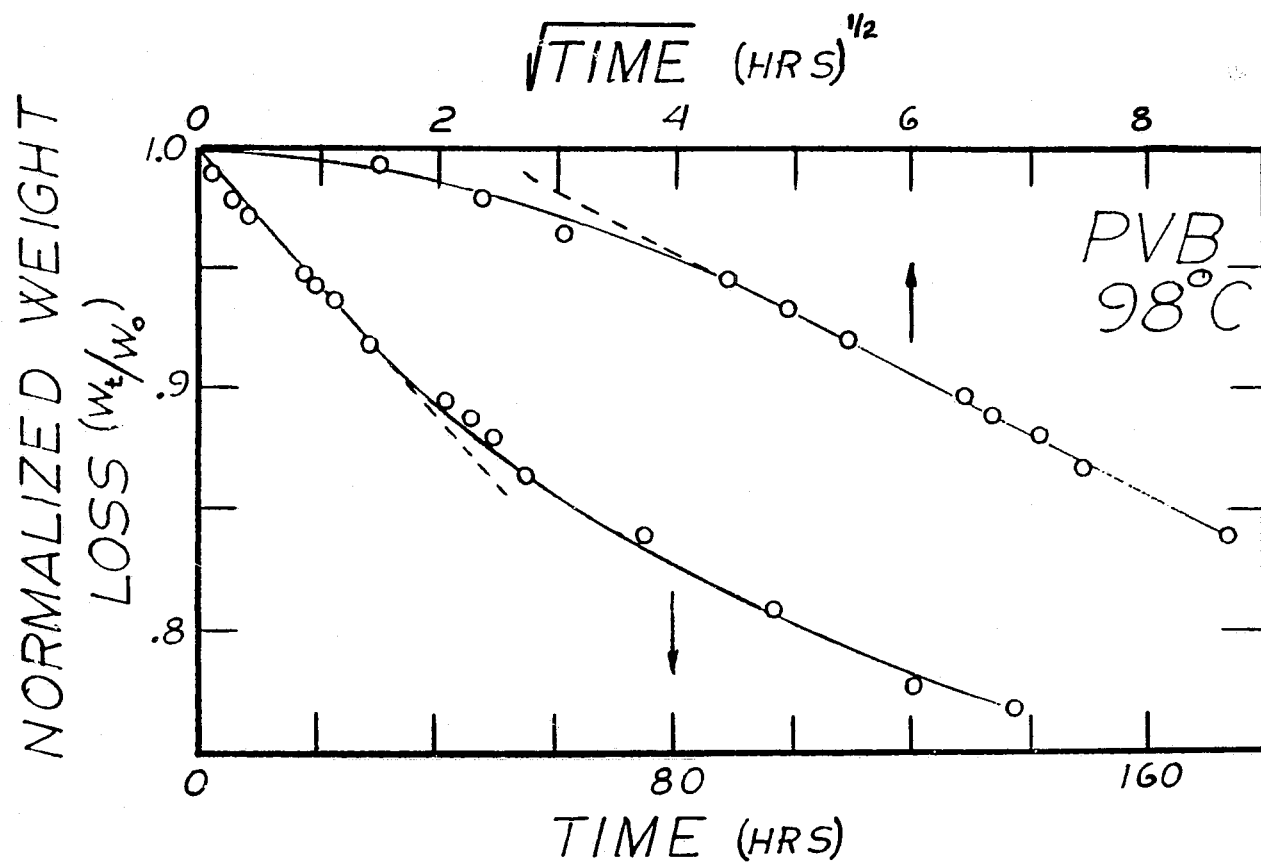


Fig. 1.2-Normalized weight loss of plasticizer in PVB at 98°C as a function of time and square root of time.

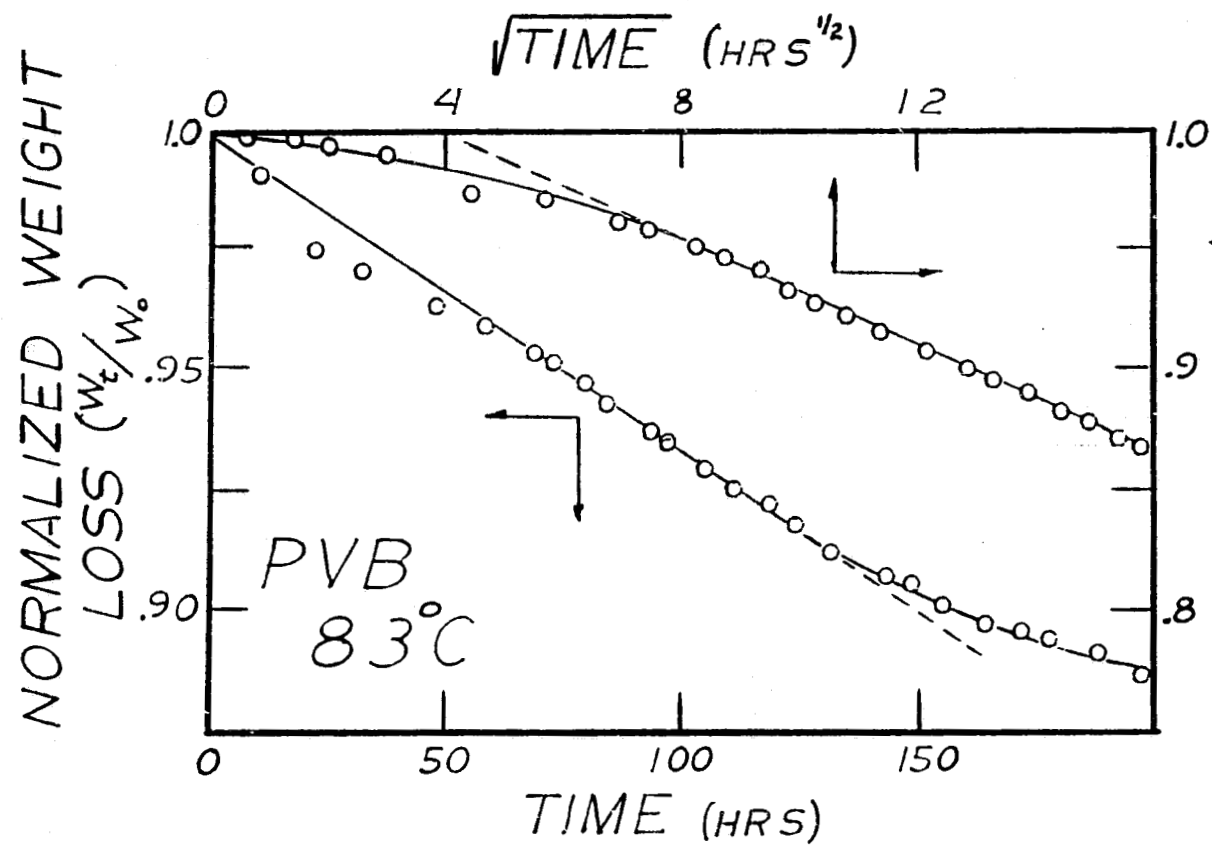


Fig. 1.3-Normalized weight loss of plasticizer in PVB at 83°C as a function of time and square root of time.

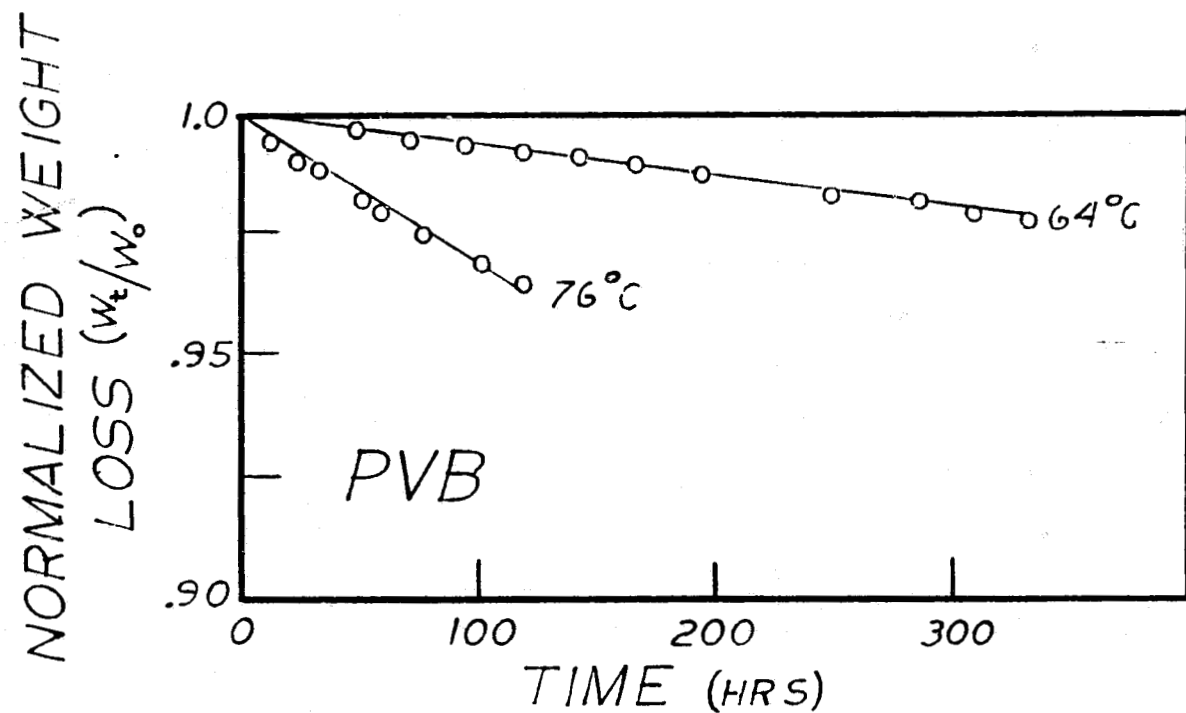


Fig. 1.4 -Time dependence of the normalized weight loss of plasticizer in PVB at 63°C and 76°C (initial transient stage).

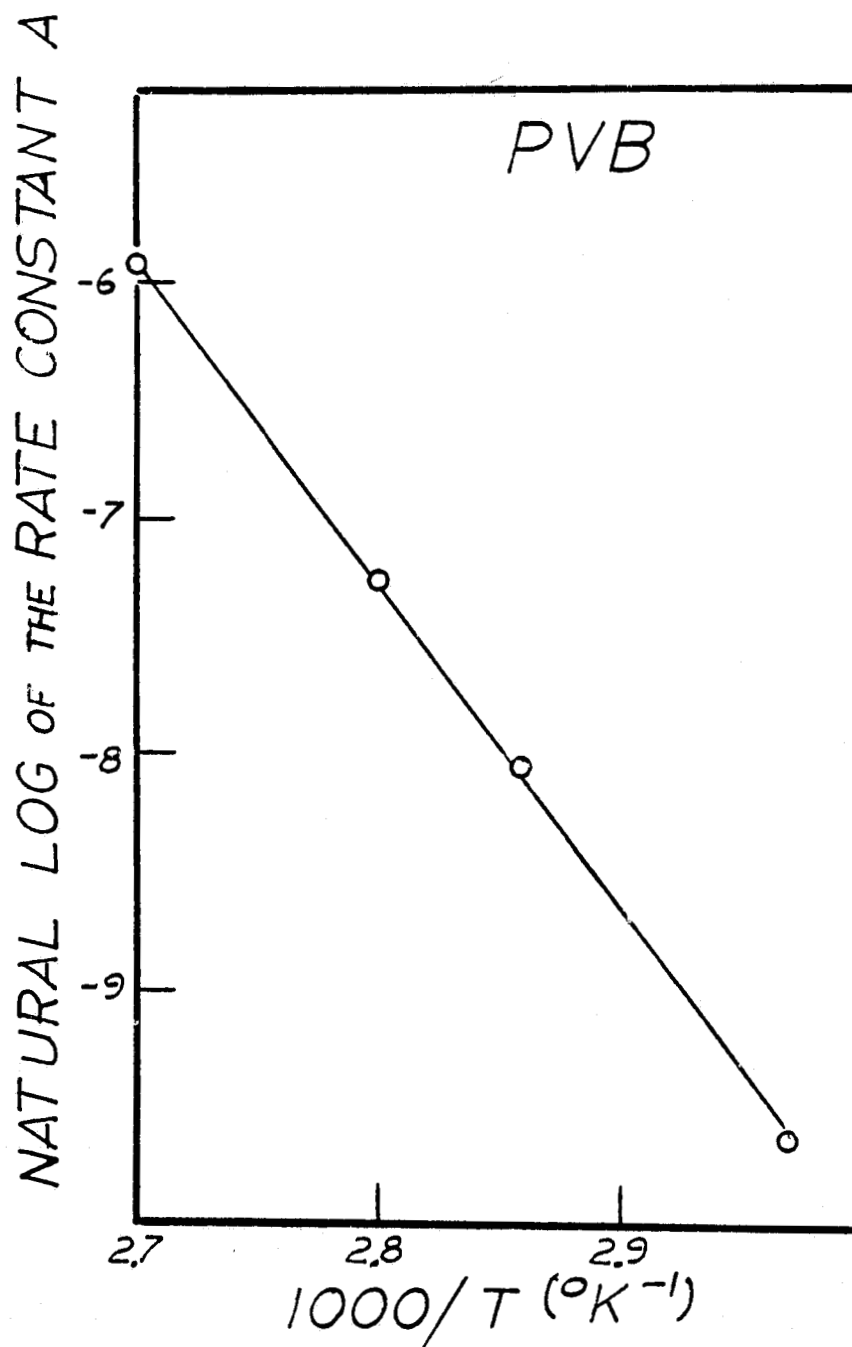


Fig. 1.5-Natural log of the rate constant A for initial stage of plasticizer weight loss in PVB as a function of reciprocal temperature.

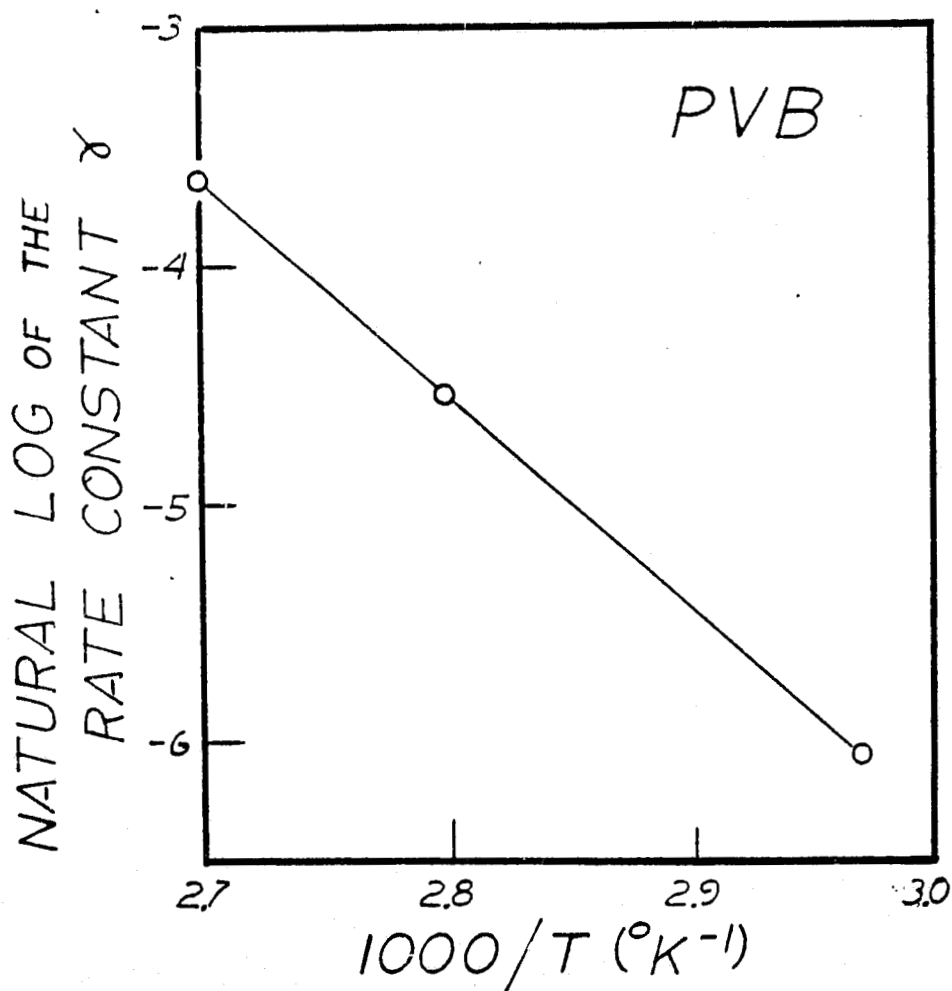


Fig. 1.6-Natural log of the rate constant (k) for second stage plasticizer weight loss kinetics in PVB as a function of reciprocal temperature.

II. Kinetics of Water Absorption and Desorption in PVB

Experimental Procedure

The kinetics of water absorption and the kinetics of water desorption in PVB were evaluated gravimetrically at various temperatures between 53° and 85 ° C. The experimental procedure consisted of weighing PVB samples that had been dried in a desiccator for several weeks. The samples were of constant thickness, and represented a semi-infinite plate geometry. Each dried sample was "quenched" into a temperature/humidity chamber operating at a 100% humidity level and at a selected temperature between 53° and 85 ° C. The weight gain of each sample was monitored continuously as water was absorbed from the surrounding ambient. After the samples were saturated with water, each sample was transferred into a dry box where the desorption characteristics were monitored gravimetrically as a function of time at temperatures corresponding to the values used in the water absorption studies.

Results

The time dependence of the normalized weight gain for absorption and weight loss for desorption are both presented in Figure 2.1 which shows that the isothermal desorption in PVB is a much faster kinetic process than water absorption by several orders of magnitude. Figure 2.1 also shows that water desorption is a temperature dependent phenomena while water absorption is relatively temperature independent.

A more detailed analysis of the time dependence for normalized weight gain data in water absorption (Figs. 2.2 to 2.5) and for the normalized weight loss in water desorption (Figs. 2.6 to 2.8) at the various run temperatures showed a two stage kinetic behavior. The initial

transient stage (Stage I) for weight gain in water absorption and weight loss in desorption showed (Figs. 2.2 to 2.8) a linear time dependence:

Stage I (absorption):

$$w_t/w_o = At + B \quad 2.1$$

Stage I (desorption):

$$w_t/w_o = -Ct + D \quad 2.2$$

The associated rate constants A and C appear to obey (Figs. 2.9 and 2.10) an Arrhenius temperature dependency:

Stage I (absorption):

$$A = A_o \exp(-Q_I^a/RT) \quad 2.3$$

Stage I (desorption):

$$C = C_o \exp(-Q_I^d/RT) \quad 2.4$$

where

$$Q_I^a = 4.2 \text{ Kcal/mole} \quad 2.5$$

$$A_o = 29 \text{ hrs}^{-1} \quad 2.6$$

$$Q_I^d = 16 \text{ Kcal/mole} \quad 2.7$$

$$C_o = 5.5(10^{10}) \text{ hrs}^{-1} \quad 2.8$$

This initial transient stage is followed by a second ^{stage} behavior (Stage II) where the normalized weight gain in water absorption and weight loss in desorption were both dependent (Figs. 2.2 to 2.8) on the square root of time:

Stage II (absorption):

$$w_t/w_o = Et^{1/2} + F \quad 2.9$$

Stage II (desorption):

$$\omega_t/\omega_o = -G t^{1/2} + H \quad 2.10$$

The rate constants E and G for second stage behavior also displayed (Figs. 2.9 and 2.10) an Arrhenius temperature dependency:

Stage II (absorption):

$$E = E_o \exp(-Q_E^a/RT) \quad 2.11$$

Stage II(desorption):

$$G = G_o \exp(-Q_E^d/RT) \quad 2.12$$

where the associated activation energies and pre-exponential factors are:

$$Q_E^a = 6.3 \text{ Kcal/mole} \quad 2.13$$

$$E_o = 3.6 (10^2) \text{ hrs}^{-1/2} \quad 2.14$$

$$Q_E^d = 7.1 \text{ Kcal/mole} \quad 2.15$$

$$G_o = 2.2 (10^4) \text{ hrs}^{-1/2} \quad 2.16$$

Table 2.1 summarizes the kinetic response equations, the rate constant equations, and the associated activation energy and pre-exponential kinetic parameters for first and second stage behavior in both water absorption and desorption. From this information, the rate equations can be expressed as:

Stage I(absorption):

$$\omega_t/\omega_o = 2.9(10^1) [\exp(-2100/T)] t + 1 \quad 2.17$$

Stage II(absorption):

$$\omega_t/\omega_o = 3.6(10^2) [\exp(-3100/T)] t^{1/2} + 1.2 \quad 2.18$$

Stage I(desorption):

$$w_t/w_o = 5.5(10^{10})[\exp(-8000/T)] t + 1 \quad 2.19$$

Stage II(desorption):

$$w_t/w_o = 2.2(10^4)[\exp(-9500/T)] t^{1/2} + 1.06 \quad 2.20$$

From these equations, the rate of water absorbed per gram of PVB per hour for first stage behavior can be evaluated at various temperatures. These results are presented in Table 2.2 where they are compared with the previously determined (Table 1.2) plasticizer loss rate.

Discussion

An understanding of the water absorption and desorption processes in PVB must account for the following observed experimental features:

- (i) Desorption in several orders of magnitude faster than absorption.
- (ii) Both absorption and desorption exhibit a two stage kinetic response.
- (iii) The second kinetic stage in both absorption and desorption obey a square root of time dependency suggestive of a volume diffusion mechanism.
- (iv) The weight loss kinetics in desorption is highly temperature dependent, while the weight gain kinetics in absorption appear to be relatively temperature insensitive.
- (v) The activation energy for second stage desorption is approximately equal to the activation energy for second stage absorption

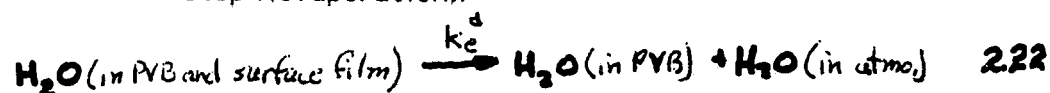
$$(Q_{II}^a \cong Q_{II}^d \cong 7 \text{ Kcal/mole}).$$

To facilitate an understanding of these observed features, an attempt is made to model the absorption and desorption process by a sequence of reaction steps. For a water saturated PVB sample with water inside the PVB and a film of water absorbed on the surface of the PVB, the overall desorption process is:

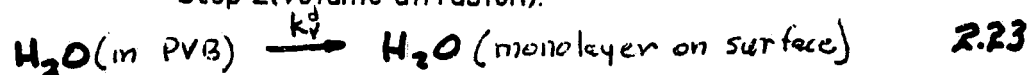


A possible sequence of the desorption reaction steps is illustrated schematically in Figure 2.11. The steps involve: an evaporation of the surface water film into the atmosphere (Step 1), a volume diffusion of water molecules from the interior of the PVB to form a monolayer on the surface (Step 2), and a desorption of this monolayer into the atmosphere (Step 3). These reaction steps in equation form become:

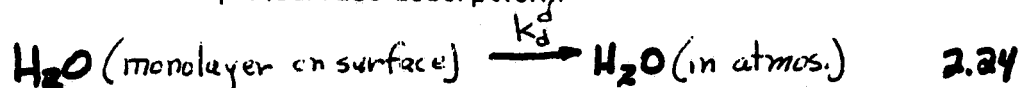
Step 1(evaporation):



Step 2(volume diffusion):



Step 3(surface desorption):



where k_e^d , k_v^d , and k_d^d , are the rate constants for the surface film evaporation, volume diffusion, and surface desorption steps respectively.

This proposed sequence appears to be in reasonable accord with the experimentally observed desorption kinetics if Step 1 is associated with Stage I behavior, and if Steps 2 and 3--where Step 2 is rate limiting--are associated with Stage II behavior.

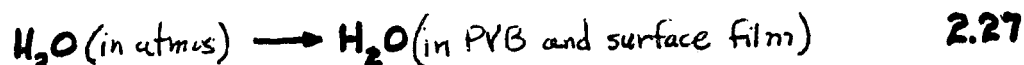
From simple considerations, a linear time dependent weight loss response is expected and observed for Step I -- Stage I behavior where a water film is evaporating from a semi-infinite plate geometrical configuration. This entire film must be evaporated before water molecules in the PVB can diffuse to the surface and desorb into the atmosphere. Stage I must then be followed by a second stage behavior corresponding to Steps 2 and 3 where, if volume diffusion is rate limiting ($k_v^d < k_d^d$), the weight loss kinetics for the second state will be linear with the square root of time as is observed. If the evaporation mechanism is responsible for Stage I behavior, and if the volume diffusion mechanism is responsible for Stage II behavior, the associated rate constants should be given by the equations.

$$k_e^d = C = C_0 \exp(-Q_I^d/RT) = 5(10^{10}) [\exp(-8000/T)] \quad 2.25$$

$$k_v^d = G = G_0 \exp(-Q_{II}^d/RT) = 2.2(10^4) [\exp(-3500/T)] \quad 2.26$$

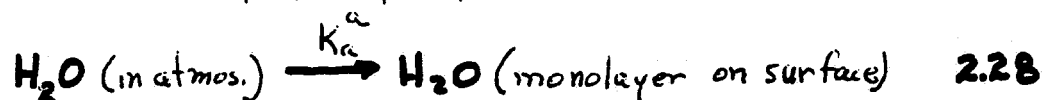
which show that the overall desorption kinetics must be highly temperature sensitive as is apparent in Figure 2.1.

The water absorption process can also be modeled by a sequence of reaction steps. The overall reaction:

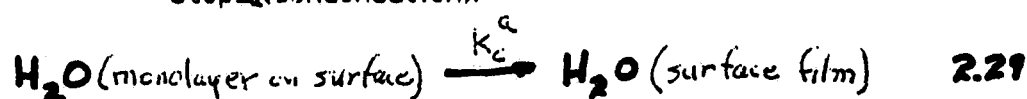


could involve the reaction steps illustrated in Figure 2.12 where these steps are expected to be roughly analogous to the reverse of the equations (Eqs. 2.22 to 2.24) for the desorption reaction steps:

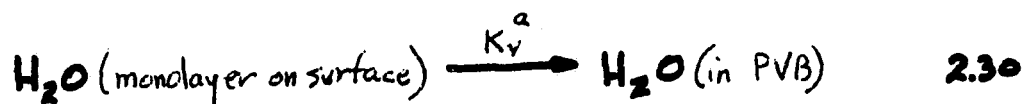
Step 1 (adsorption):



Step 2a(condensation):



Step 2b(volume diffusion):



Step 1 is the adsorption of a monolayer of water on the PVB surface, Step 2a is the condensation of successive monolayers to form a film, and Step 2b, which conceptually occurs simultaneously with Step 2a, is the diffusion of the monolayer into the PVB. The rate constants k_a^a , k_c^a , k_v^a correspond to these adsorption, condensation, and volume diffusion reaction mechanisms respectively. Relative to this proposed reaction sequence, an analysis of the experimental data for the absorption kinetics suggests that:

$$k_a^a > k_c^a > k_v^a \quad 2.31$$

Stage I absorption kinetics would then be associated with Step 2a as the rate limiting step while Stage II would result from the volume diffusion rate limiting mechanism associated with Step 2b as expected from the $t^{1/2}$ response. The rate constants for the water absorption process would then be given by:

$$k_c^a = A = A_0 \exp(-Q_1^a/RT) = 2.9(10^4) \exp(-2100/T) \quad 2.32$$

$$k_v^a = F = F_0 \exp(-Q_2^a/RT) = 3.6(10^2) \exp(-3100/T) \quad 2.33$$

which shows that the absorption process should be temperature sensitive. There are some difficulties with this proposed reaction sequence and the specification of its rate determining steps. The main difficulty is the

relative temperature insensitivity of the absorption kinetics which presumably results from the Step 2a mechanism responsible for the Stage I behavior. The kinetic theory of gases suggests that the arrival rate (η) of water molecules on the PVB surface should be proportional to the water vapor partial pressure (p) and inversely related to the square root of the temperature:

$$\eta \sim p/\sqrt{T}$$

2.35

Knowing the temperature dependence for the vapor pressure of water and making several judicious assumptions, the rate of water absorption weight gain at 85 °C is calculated to be four times faster than at 52°C. Table 2.2 shows that the rate of weight gain for Stage I water absorption at 85°C is only about twice as fast at the rate at 50°C. This kinetic theory of gases approach also suggests that an activation energy of 13 Kcal/mole can be associated with the Step 2a, Stage I absorption behavior, and this value is not consistent with the experimentally observed value of 4.2 Kcal/mole.

Another difficulty results when the rate constants k_v^a and k_v^d for the volume diffusion steps associated in absorption and desorption are compared. At any given temperature, Equations 2.26 and 2.33 ^{show} that the rate constants for the volume diffusion process in absorption and desorption are not equal.

$$k_v^a \ll k_v^d$$

2.36

This unexpected inequality does not result from the activation energies (Q^a_{II} and Q^d_{II}) for volume diffusion in absorption and desorption. The values of these activation energies are, as expected, approximately equal

$$Q^a_{II} \approx Q^d_{II} \approx 6.5 \text{ Kcal/mole}$$

2.37

The large inequality in the rate constants reflect a high and unexpected difference in the pre-exponential factors E and G where

$$E_0 = 3.6(10^3) \ll 2.2(10^4) = G_0$$

2.38

This apparent difference in the pre-exponential factors suggests that Stage II behavior in absorption or desorption may not be governed by the proposed volume diffusion considerations.

The proposal that volume diffusion is the mechanism responsible for Stage II behavior in both absorption and desorption can be evaluated in more detail by performing an additional experiment. The experiment consist of monitoring Stage II absorption and desorption kinetics in PVB samples of different thickness (d) values. If volume diffusion is the governing mechanism, a simple plot of the weight loss kinetics as a function of the square root of time/thickness ratio ($t^{1/2}/d$) should yield a linear superimposed plot for all the data from the samples of various thicknesses:

$$w_t/w_0 = K t^{1/2}/d$$

2.39

Sample thickness of .033, .066, .132, and .152 cm, were used for the experiment. The kinetics^{were} monitored gravimetrically at 53° for water absorption and at 75° C for water desorption. The analysis consisted of correcting^{for} both the weight and time data for the first stage (surface film) effect assuming that both first and second stage behavior occur simultaneously in absorption and occur sequentially in desorption. The corrected data is then expected to represent second stage kinetic behavior alone without any perturbing influence from the first stage response.

For water absorption, a typical plot of the second stage normalized weight gain during water absorption as a function of time after suitably correcting for the first stage surface film effect is shown in Figure 2.13 for a 0.152 cm thick PVB sample. The corrected data display a $t^{1/2}$ time

dependency for the second stage behavior and this dependency was evident in the corrected data for all the absorption and desorption experiments in the PVB samples for the thickness values used in these experiments.

The corrected absorption data for the PVB samples of various thickness were plotted against $t^{1/2}/d$ and the results (Fig. 2.14) superimpose on a linear dependency showing that the volume diffusion mechanism is instrumental in determining the second stage water absorption kinetic response characteristics.

The water desorption data as a function of sample thickness in the PVB samples were also corrected for first stage effects and the second stage results, when plotted against $t^{1/2}/d$ (Fig. 2.15), also displayed the linearity and superposition.

These experiments provide supportive evidence that volume diffusion is the mechanism responsible for Stage II behavior in both water absorption and desorption.

TABLE 21

Response characteristics and kinetic parameters for both stages of water absorption and desorption as determined by weight loss measurements.

	<u>Absorption</u>		<u>Desorption</u>	
	<u>Stage I</u>	<u>Stage II</u>	<u>Stage I</u>	<u>Stage II</u>
Rate Equation	$\frac{Wt}{W_o} = At + B$	$\frac{Wt}{W_o} = Et^{1/2} + F$	$\frac{Wt}{W_o} = -Ct + D$	$\frac{Wt}{W_o} = -Gt^{1/2} + H$
Rate Constant	$A = A_o \exp(-Q^a_1/RT)$	$E = E_o \exp(-Q^a_{II}/RT)$	$C = C_o \exp(-Q^d_1/RT)$	$G = G_o \exp(-Q^d_{II}/RT)$
Pre-exponential	$A_o = 2.9(10^{-1})$	$E_o = 3.6(10^2)$	$C_o = 5.5(10^{10})$	$G_o = 2.2(10^4)$
Activation Energy (Kcal/mole)	$Q^a_1 = 4.2$	$Q^a_{II} = 6.3$	$Q^d_1 = 16$	$Q^d_{II} = 7.1$
Intercept	$B = 1.0$	$F = 1.2$	$D = 1.0$	$H = 1.06$

Table 2.2

Rates of plasticizer loss, water absorbed, and water deabsorbed in PVB
at various temperatures during first stage behavior

<u>temperature</u> <u>(°C)</u>	<u>grams plasticizer</u> <u>lost per gram PVB</u> <u>per hour</u>	<u>grams water</u> <u>absorbed per gram</u> <u>PVB per hour</u>	<u>grams water</u> <u>deabsorbed per</u> <u>gram PVB per hour</u>
25	⁻⁶ 1.1 (10)	⁻² 2.5 (10)	⁻¹ 1.1 (10)
50	⁻⁵ 3.1 (10)	⁻² 4.0 (10)	⁻¹ 9.4 (10)
85	⁻³ 1.3 (10)	⁻² 7.8 (10)	9.2

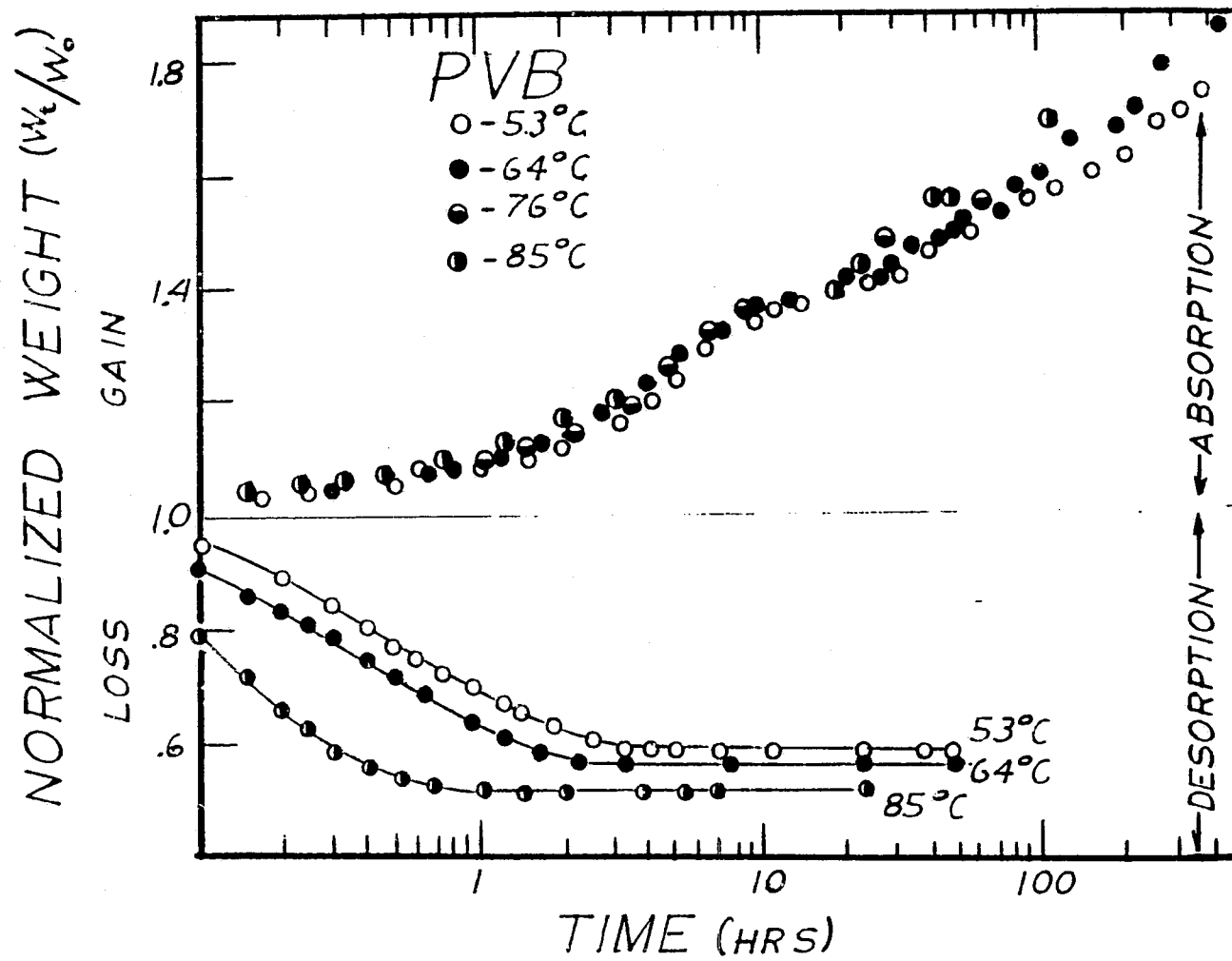


Fig. 2.1-Kinetics of water absorption and desorption in PVB at selected temperatures.

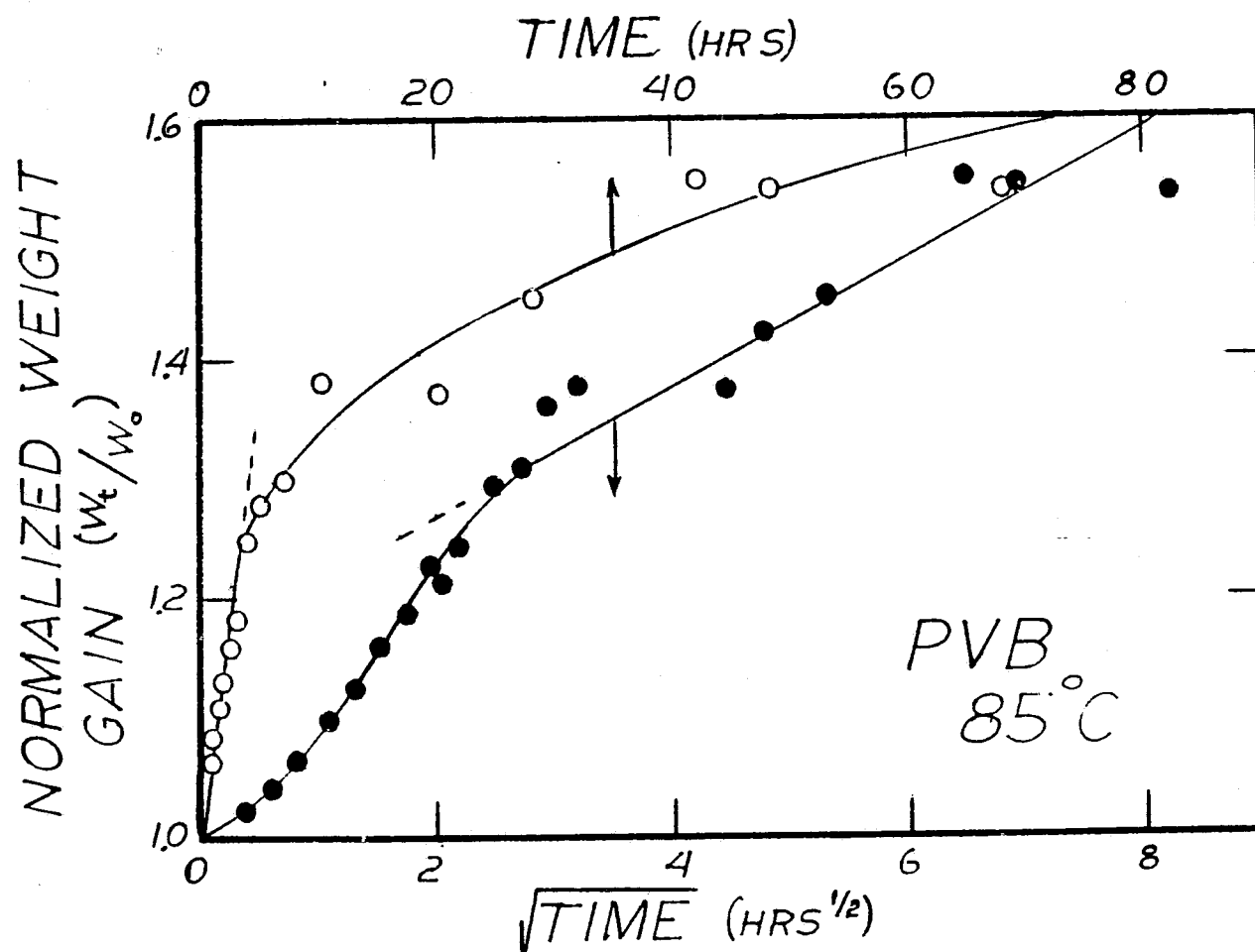


Fig. 2.2-Water absorption kinetics in PVB at 85°C.

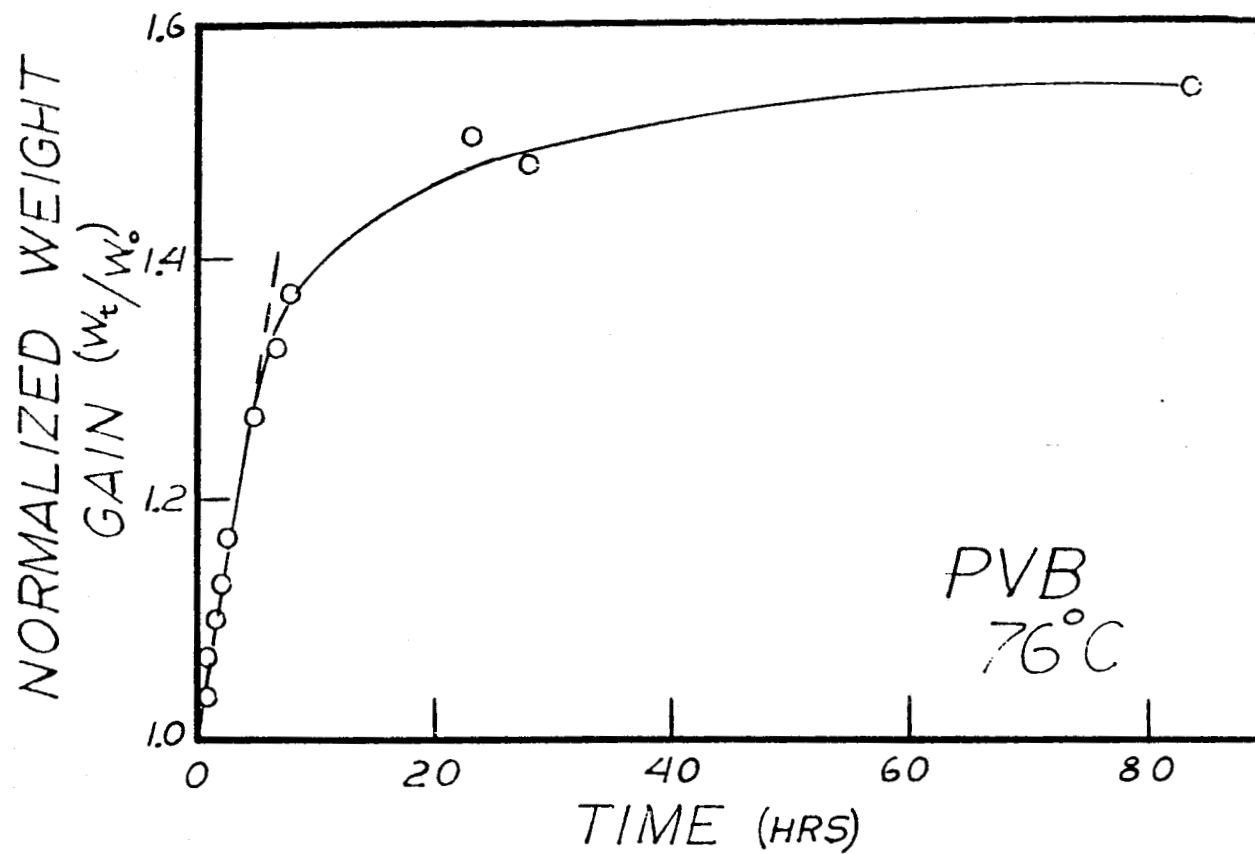


Fig. 2.3 Water absorption kinetics in PVB at 76°C.

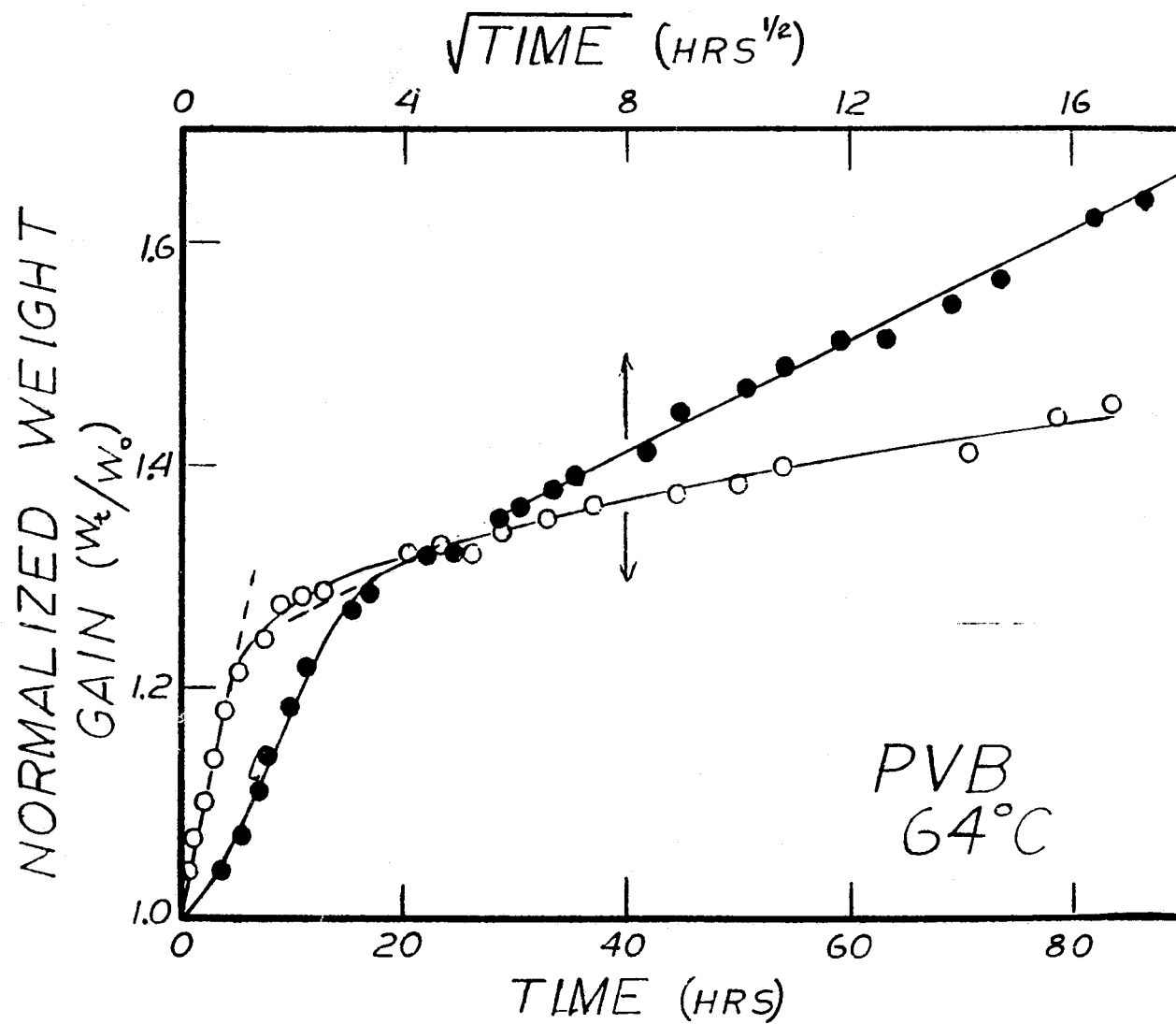


Fig. 2.4-Water absorption kinetics in PVB at 64°C.

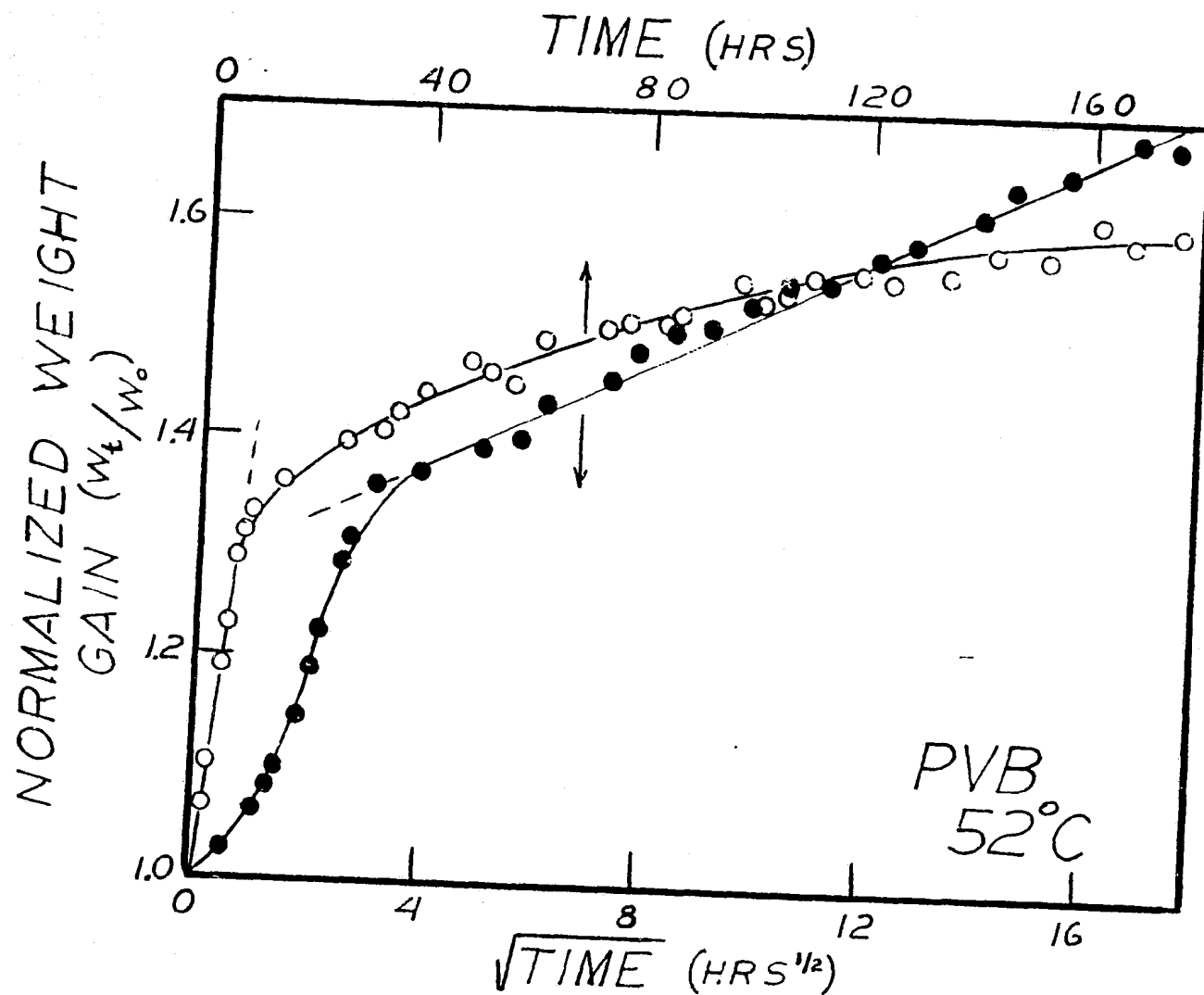


Fig. 2.5-Water absorption kinetics in PVB at 52°C .

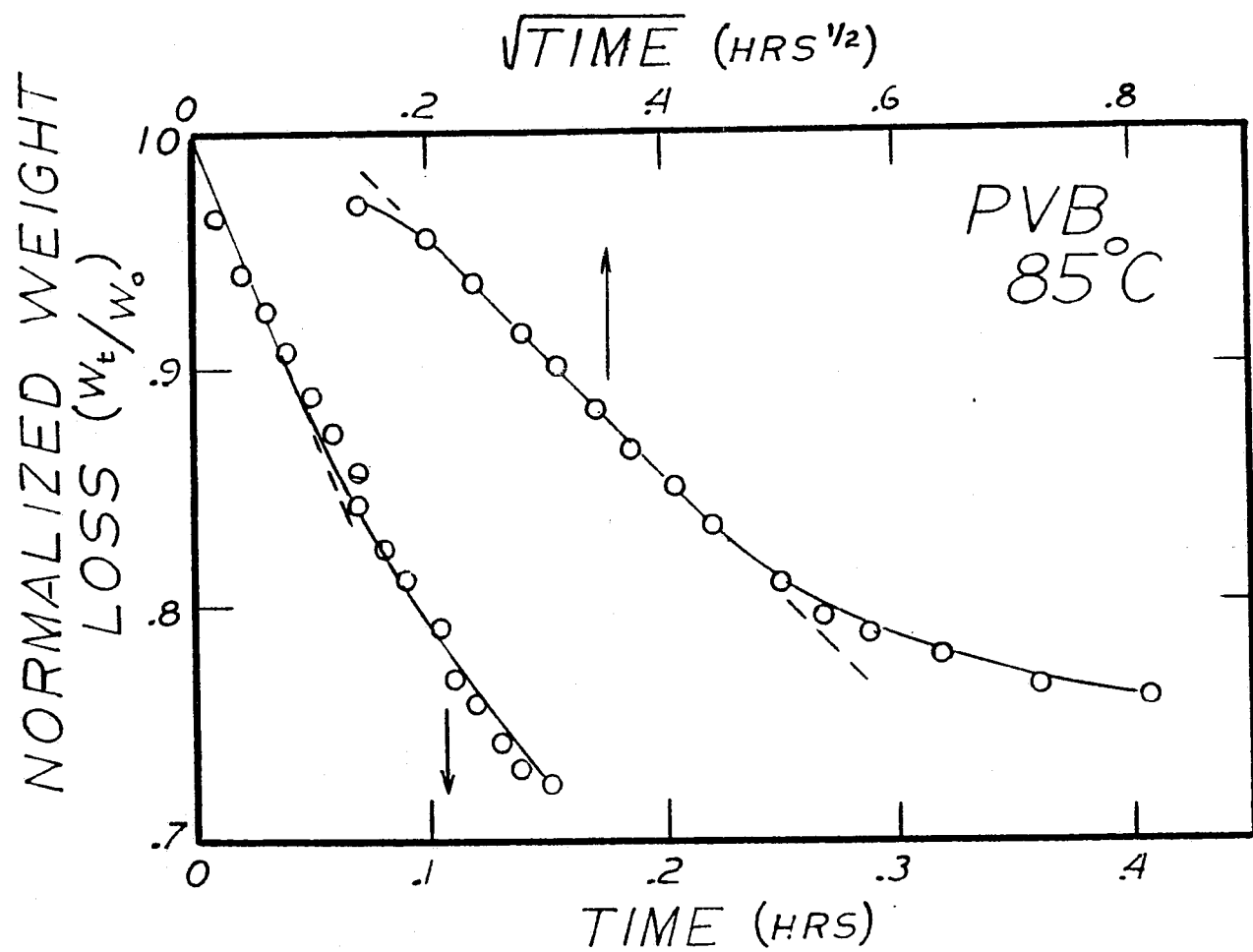


Fig. 2.6-Water desorption kinetics in PVB at 85°C.

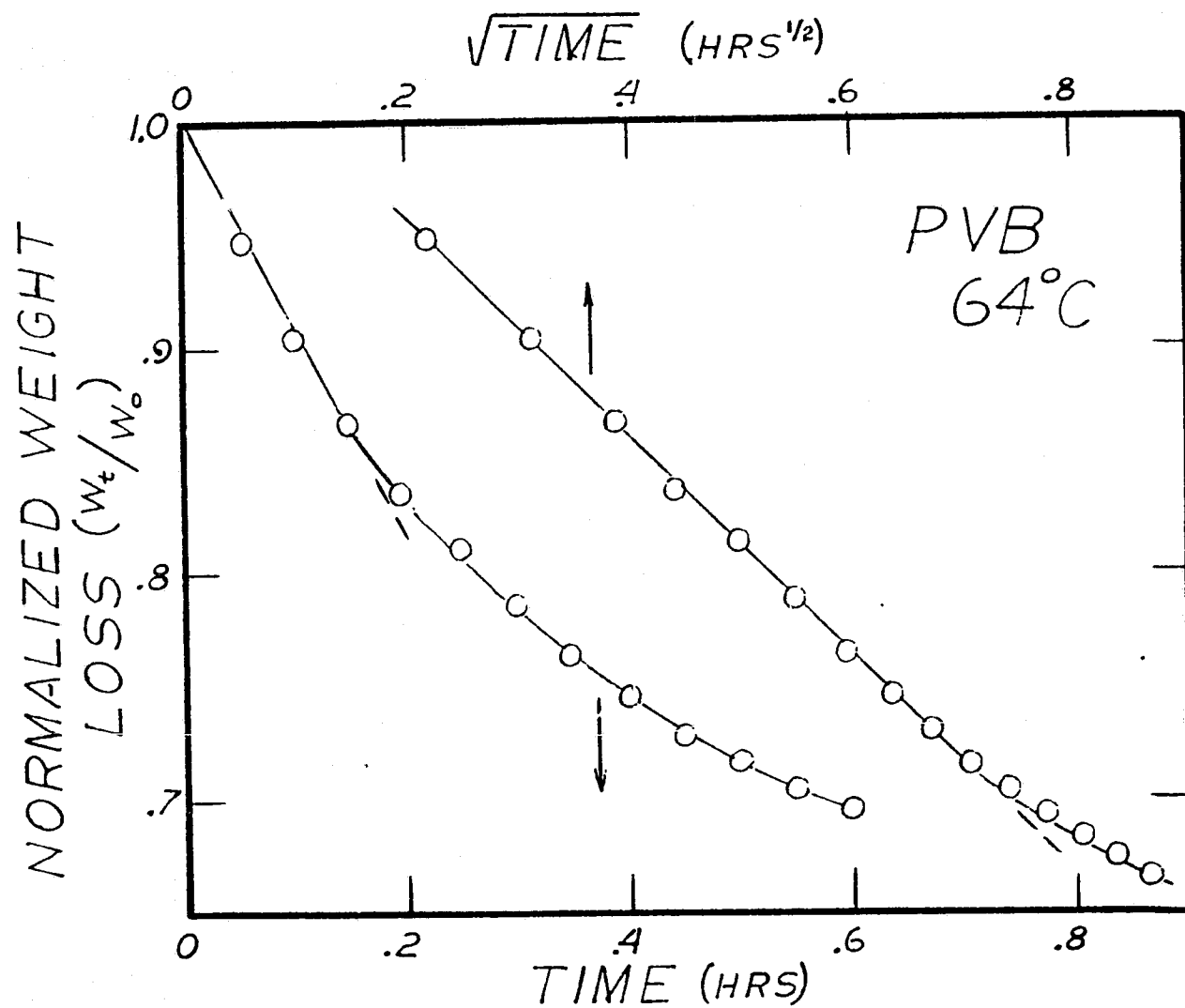


Fig. 2.7-Water desorption kinetics in PVB at 64°C.

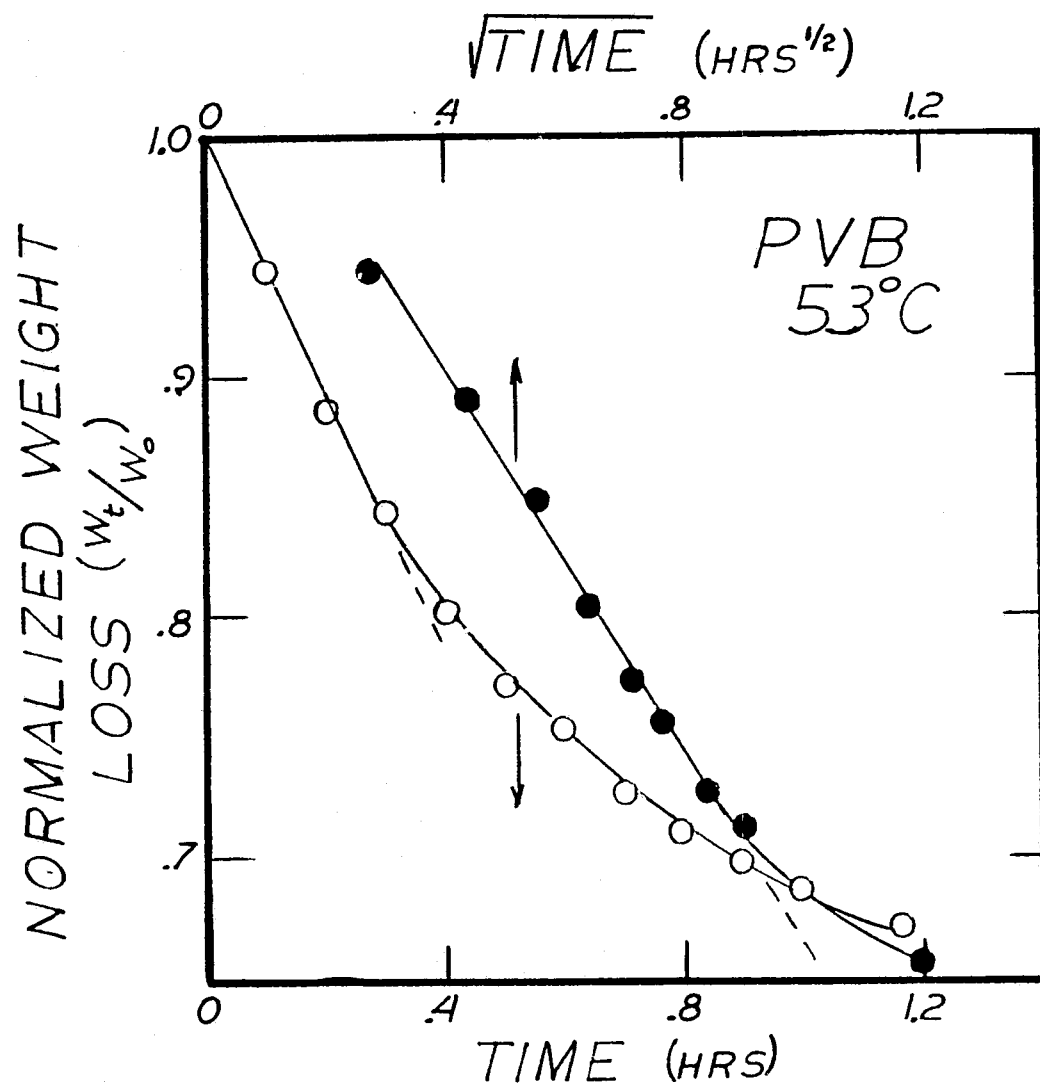


Fig. 2.8-Water desorption kinetics in PVB at 53°C.

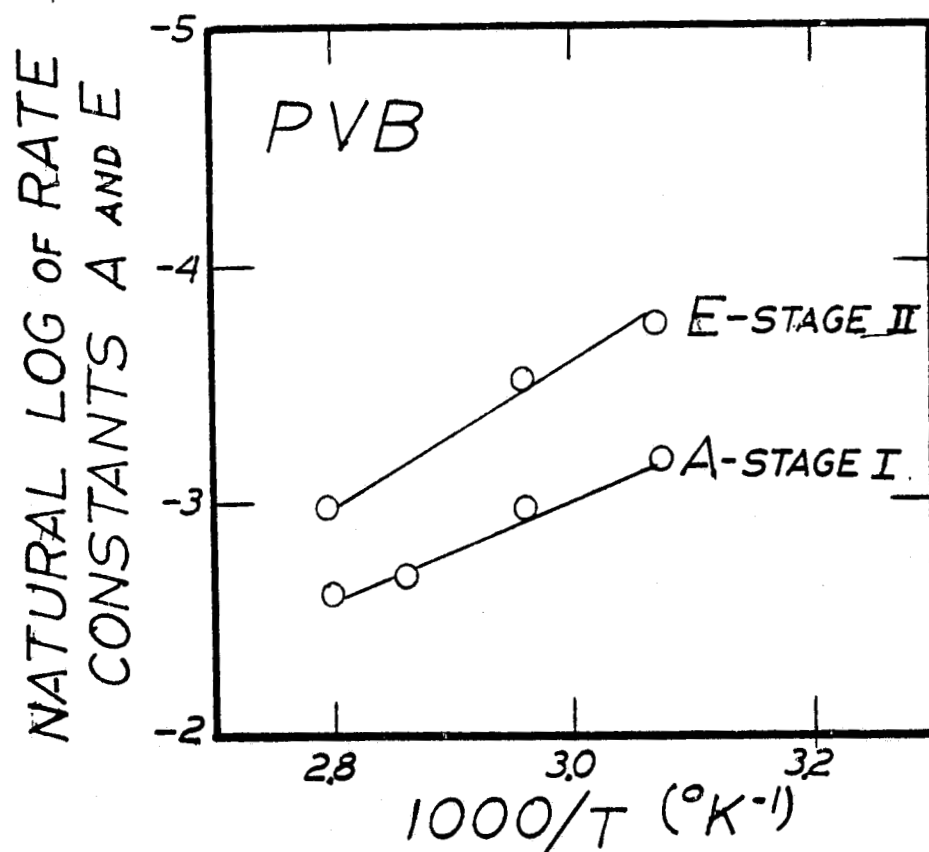


Fig. 2.9 -Temperature dependence of the rate constants A and E for stage I and stage II water absorption in PVB.

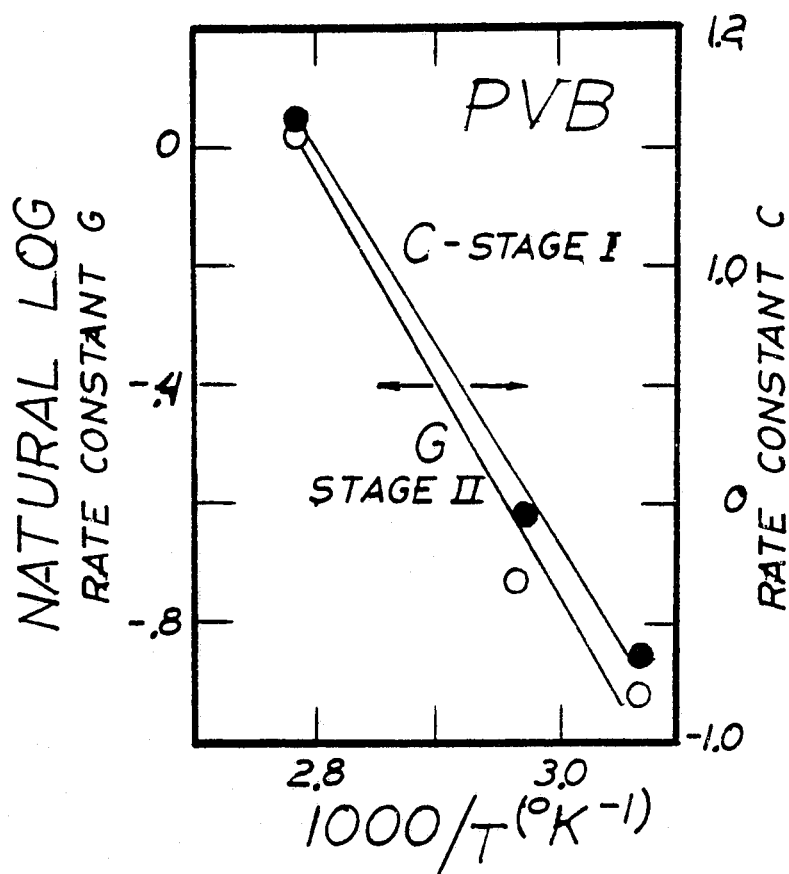
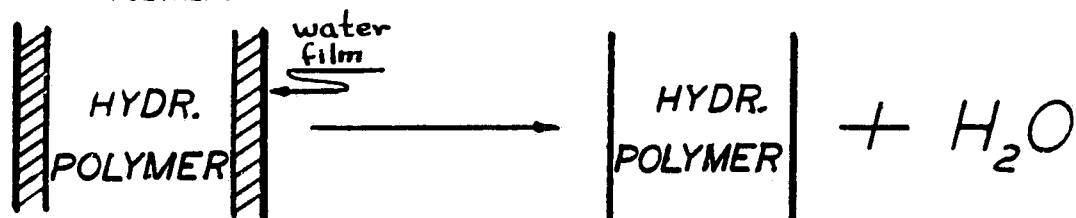


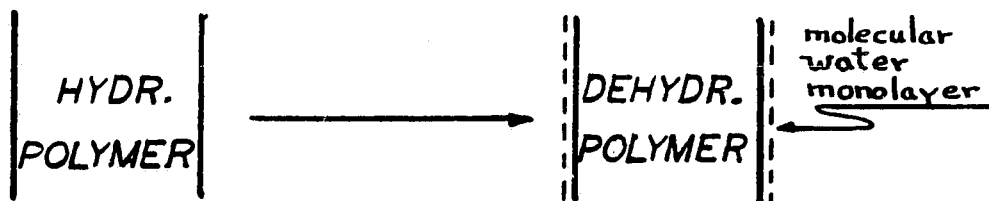
Fig. 2.10-Temperature dependence of rate constants C and G for stage I and stage II water desorption in PVB.

WATER DESORPTION MODEL

STEP 1: EVAPORATION OF THE WATER FILM ON THE SURFACE OF THE HYDRATED POLYMER.



STEP 2: DEHYDRATION OF THE POLYMER BY DIFFUSION OF WATER MOLECULES OUT OF HYDRATED POLYMER TO THE SURFACE OF THE POLYMER.



STEP 3: DESORPTION OF THE WATER MOLECULES ON THE SURFACE OF THE DEHYDRATED POLYMER.

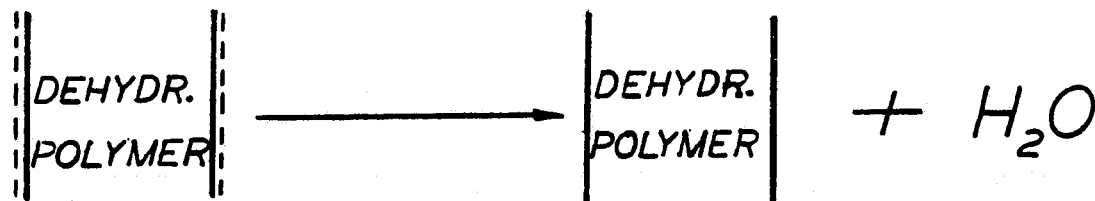
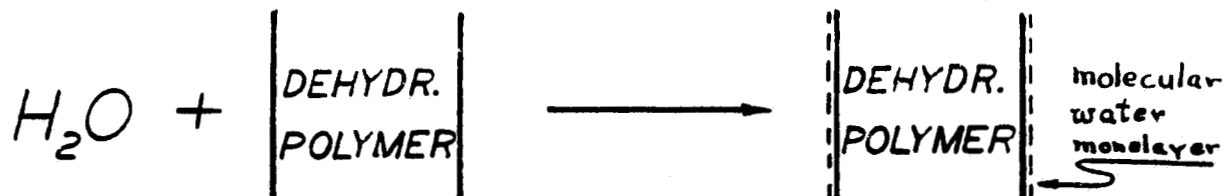


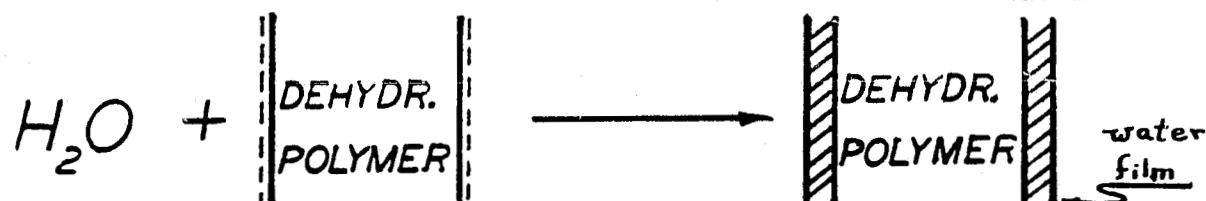
Fig. 2.11 - Schematic illustration of a possible sequence of reaction steps for removing water from both the surface and the bulk of a polymer to form a dehydrated polymer.

WATER ABSORPTION MODEL

STEP 1: ABSORPTION OF ATMOSPHERIC WATER VAPOR ON DEHYDRATED POLYMER TO FORM AN INITIAL MONOLAYER OF WATER ON SURFACE OF POLYMER.



STEP 2a: CONDENSATION OF ATMOSPHERIC WATER VAPOR AS SUCCESSIVE MONOLAYERS TO FORM A FILM OF WATER ON THE SURFACE OF THE DEHYDRATED POLYMER.



STEP 2b: DIFFUSION INTO THE POLYMER OF THE WATER MOLECULES ON THE SURFACE TO FORM A HYDRATED POLYMER



Fig. 2.12 - Schematic illustration of a possible sequence of reaction steps for water absorption to form a hydrated polymer whose surface is covered with a film of water.

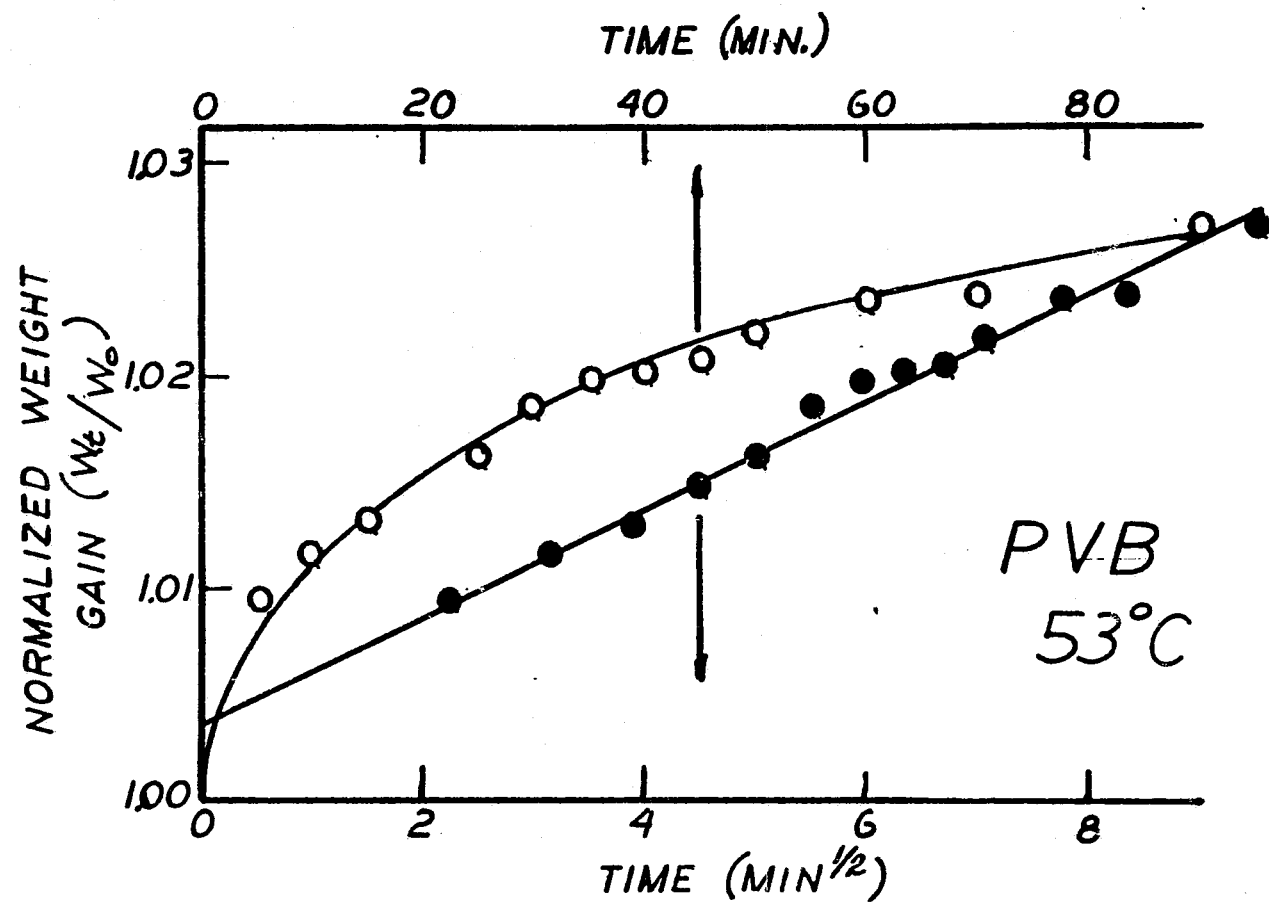


Fig. 2.13 - Water absorption kinetics in 0.152 cm thick PVB at 53°C.

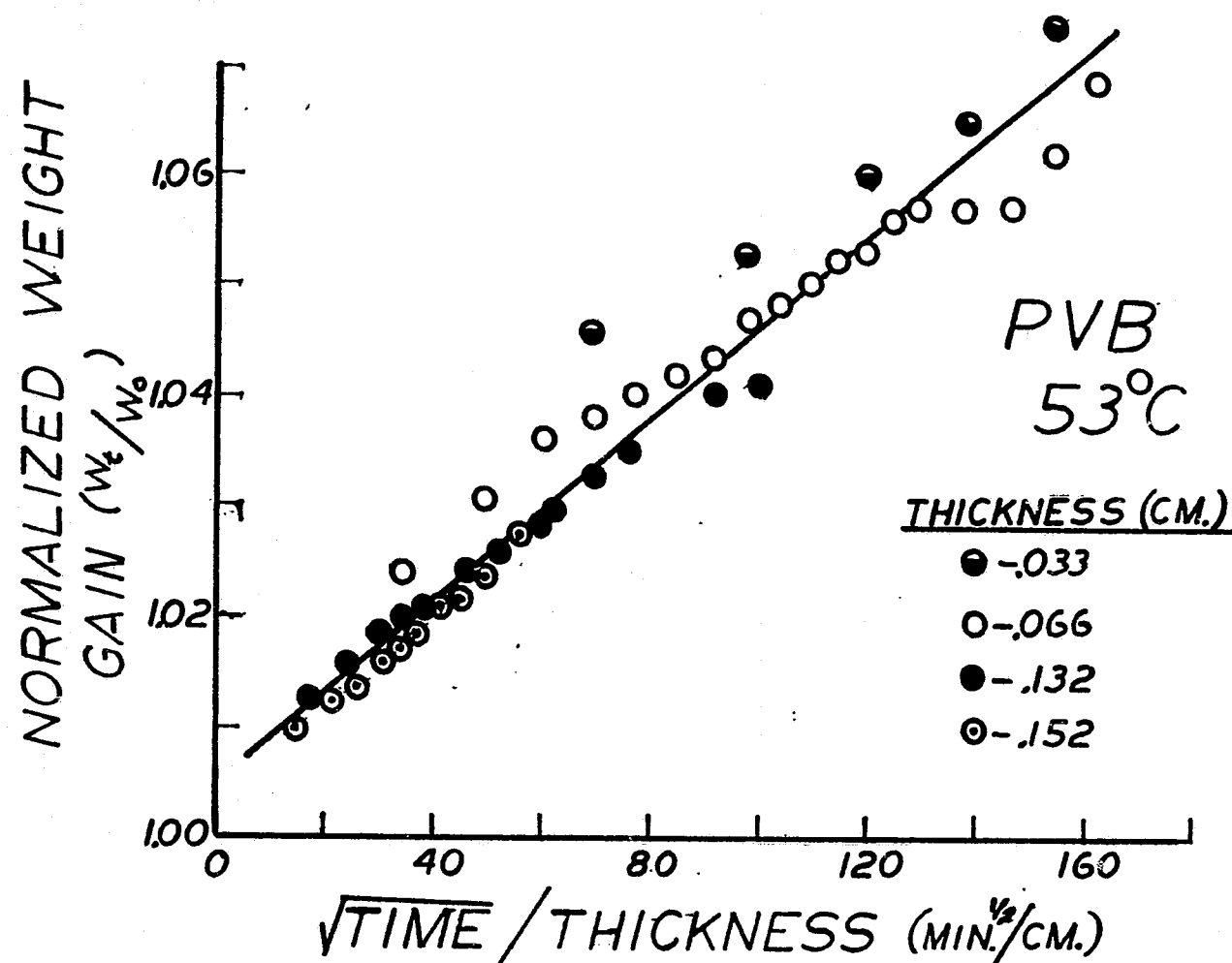


Fig. 2.14 - Thickness dependence of water absorption kinetics in PVB at 53°C.

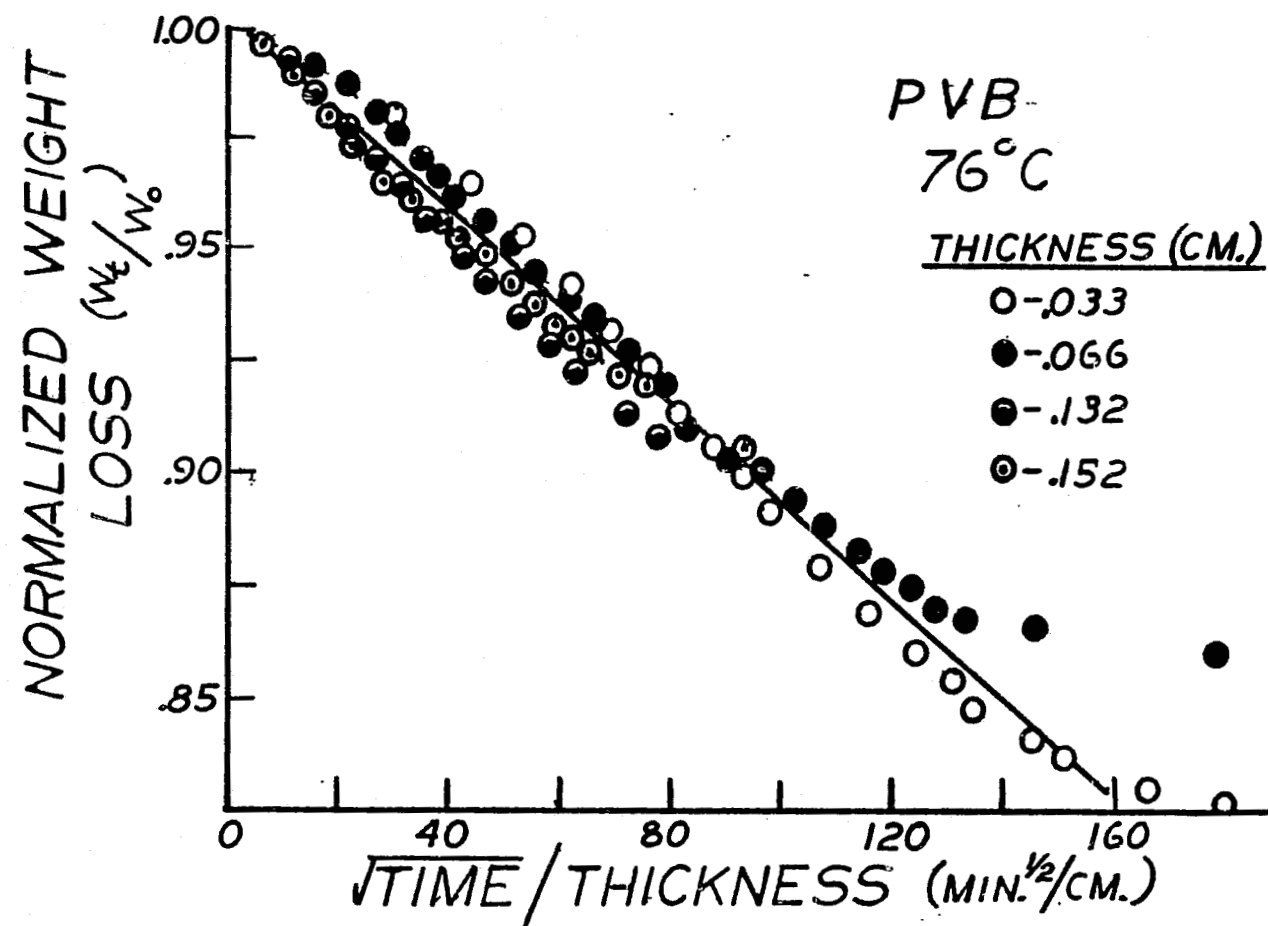


Fig. 2.15 - Thickness dependence of water desorption kinetics in PVB.

III. Kinetics of Water Absorption and Desorption in EVA

Experimental Procedure

The kinetics of water absorption and the kinetics of water desorption in EVA were evaluated gravimetrically at various temperatures between 40^o and 88^oC. The experimental procedure consisted of weighing EVA samples that had been dried in a desiccator for several weeks. The samples were of constant thickness, and represented a semi-infinite plate geometry. Each dried sample was "quenched" into a temperature/humidity chamber operating at a 100% humidity level and at selected temperatures between 40^o and 88^oC. The weight gain of each sample was monitored continuously as water was absorbed from the surrounding ambient. After the samples were saturated with water, the samples were transferred into a dry box and the desorption characteristics were then monitored gravimetrically.

Results

A comparison of the weight w_0^e of the desiccated dried sample and the measured starting weight w_0^a at zero time of the sample in the temperature/humidity chamber is shown in Table 3.1 where it is apparent that the measured starting weight is considerably larger than the desiccated dried weight which is the expected starting weight of the sample. This comparison suggests that EVA surface absorbs a layer of water immediately upon insertion into the temperature/humidity chamber. The weights ($w_0^a - w_0^e$) of these initially formed layers at the various temperatures for water absorption are listed in Table 3.1. To correct for variations in sample size, the weight of this initially formed surface layer is normalized by the w_0^e expected starting weight, and the

resulting normalized $[w_0^a - w_0^e] / w_0^e$ values (Table 3.1) are found to be temperature dependent (Fig. 3.1) according to the relationship:

$$\frac{w_0^a - w_0^e}{w_0^e} = 8(10^{-4})T + 15 \quad 3.1$$

where T is the temperature in degrees centigrade. An attempt is currently being made to justify this linear temperature dependence. The feature that the intercept is 15°C rather than 0°C defies explanation.

The time dependence of the apparent normalized weight gain w_t/w_0^a due to water absorption at 40°, 50°, 60°, 75°, and 88°C in a 100% humid environment is shown in Figure 3.2 while Figures 3.3 to 3.7 present a more detailed analysis of the data at the various temperatures. This detailed analysis shows that water absorption in EVA occurs in two stages. The initial stages (Stage I) displays a linear time dependence for the normalized weight gain:

$$w_t/w_0^a = A^a t + B \quad 3.2$$

where the rate constant A and the intercept B determined at the various run temperatures are presented in Table 3.2. The rate constant A^a is found to be exponentially temperature dependent (Figure 3.8):

$$A^a = 0.2 \exp(-350/T) \quad 3.3$$

which, when expressed in Arrhenius form:

$$A^a = A_0^a \exp(-Q_A^I/RT)$$

gives an activation energy Q_A^I for this Stage I absorption of 0.7 Kcal./mole and a pre-exponential value of 0.2 hrs. as shown in Table 3.3. Using these parameters, the normalized weight gain kinetics for the initial stage can be expressed as

$$w_t/w_0^a = 0.2 [\exp(-350/T)] t + 1 \quad 3.4$$

This initial stage of water absorption is followed by a second kinetic stage (Stage II) where the normalized weight gain appears to obey (Figs. 3.3 to 3.7) a square root of time response:

$$w_t / w_o^a = C^a t^{1/2} + D^a \quad 3.5$$

The rate constant C^a and the intercept D^a determined at the various run temperatures are shown in Table 3.2. The rate constant C^a is exponentially temperature dependent (Figure 3.9):

$$C^a = C_o^a \exp(-Q_A^{\ddagger}/RT) = 23 \exp(-2550/T) \quad 3.6$$

with an activation energy Q_A^{\ddagger} of the 5.1 Kcal/mole and a pre-exponential C_o^a value of 23 hr.^{-1/2} (Table 3.3). With these values, the normalized weight gain kinetics for this second stage water absorption process, is given by:

$$w_t / w_o^a = 23 [\exp(-2550/T)] t^{1/2} + 1.4 \quad 3.7$$

The Stage II kinetic response concludes when the monitored weight becomes time independent and the EVA is saturated with its equilibrium amount of absorbed water. Reaching equilibrium is a time consuming experimental process that could not be completely justified for the amount of useful information that could be obtained. As a result, equilibrium was never unambiguously achieved before the experimental absorption runs at the various temperatures were terminated. However, the runs were terminated when the experimental weight gain results clearly indicated that equilibrium was being approached. The final measured sample weight w_{oo} shown in Table 3.1 for each run temperature is believed to be representative of the equilibrium water saturated EVA sample weight. From these values of the final measured weights, the true weight change $w_{oo} - w_o^e$ of each saturated sample at their respective

absorption run temperatures can be evaluated. The results are presented in Table 3.1. This true weight change is believed to represent the sum of weights of both the water absorbed inside the EVA sample and the water film absorbed on the surface of the EVA sample.

The water desorption kinetic run started with the termination of each absorption kinetic run. The experimental procedure consisted of removing the water saturated sample from the temperature/humidity chamber and "quenching" the sample in a dry box maintained at the same temperature and at a 0% humidity. The weight of the sample was monitored continuously during this quenching-desorption process. The final measured weight during the absorption runs were the expected starting weights for the desorption runs as indicated in Table 3.1. The measured starting weights w_0^a of the desorbing samples were significantly smaller than the expected starting weights as indicated in Table 3.1. The difference between the expected and measured starting weights ($w_0^e - w_0^a$) shown in Table 3.1 is believed to represent some surface film water that is instantaneously evaporated when the quenching is consumated. When normalizing this $w_0^e - w_0^a$ weight difference by the expected starting weight to correct for difference in sample area, the true weight change ratio $[w_0^e - w_0^a]/w_0^e$ of this instantaneously lost surface layer can be evaluated at each run temperature. The results (Table 3.1) when plotted against the run temperature (Figure 3.10) exhibit a considerable amount of scatter from a linear type of dependence that was evident (Figure 3.1) in the absorption data.

The time dependence of the normalized weight loss due to water desorption from water saturated EVA samples at 40°, 50°, 60°, 75°, and 88°C in a zero percent humidity environment is comparatively displayed in Figure 3.2 with the analogous normalized weight gain absorption data. Desorption is clearly a faster kinetic process than absorption.

The details of the time dependence for the water desorption process in EVA at each run temperature are shown in Figures 3.11 to 3.15. Similar to absorption, water desorption in EVA is also a two stage kinetic process where the first stage is linear with time (Eq. 3.2) and the second stage is linear with the square root of time (Eq. 3.5). The characterizing rate constants A^d and C^d and intercepts B^d and D^d for Stage I and Stage II behavior respectively for the desorption process are presented in Table 3.2 for the various run temperatures. The Stage I rate constant A^d is exponentially temperature dependent (Fig. 3.8):

$$A^d = 167 \exp(-3050/T) = A_0^d \exp(-Q_D^I/RT) \quad 3.8$$

which yields a characterizing activation energy Q_D^I for Stage I water desorption of 6.1 Kcal/mole. The Stage II desorption rate constant C^d can be represented by an exponential temperature dependency (Fig. 3.9--dashed line) provided one data point is neglected, and this particular temperature dependency is given by the relationship:

$$C^d = 159 \exp(-2050/T) = C_0^d \exp(-Q_D^{II}/RT) \quad 3.9$$

where the characterizing activation energy Q_D^{II} is 5100 Kcal/mole. Using these equations and the intercept values given in Table 3.2, the normalized weight loss kinetics for water desorption in Stage I and Stage II behavior can be expressed as:

$$\text{Stage I} \\ w_t/w_0^e = -167[\exp(-3050/T)]t + 1 \quad 3.10$$

$$\text{Stage II} \\ w_t/w_0^e = -159[\exp(-2050/T)]t^{1/2} + 1.07 \quad 3.11$$

Table 3.3 presents a comparative summary of the activation energies and the pre-exponential rate constant factors for the Stage I and Stage II absorption and desorption kinetic processes.

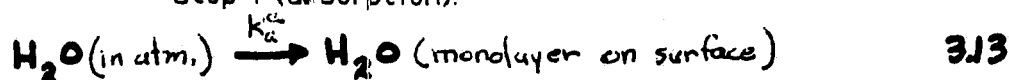
Discussion

The two stage kinetic response evident for both water absorption and desorption in EVA is identical to the kinetic response observed in PVB. The model previously employed (Figs. 2.11 and 2.12) to explain the kinetic behavior in PVB, would also be appropriate for EVA. In the absorption process, this model suggests that water in the atmosphere reacts with a dehydrated polymer by being absorbed into the polymer and by being adsorbed as a layer on the surface of the polymer. The final result is a hydrated polymer covered by a surface water film as shown in Figure 2.12. The overall reaction for water would then be:

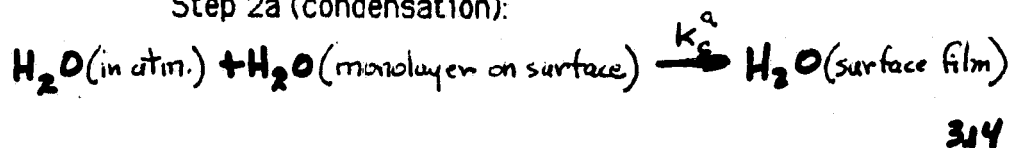


As was suggested previously for water absorption in PVB, this overall reaction can be expressed as the sum of several component sequential reaction steps as is also illustrated schematically in Figure 2.12. These reaction steps with their associated rate constants k_a^a , k_c^a , k_v^a are:

Step 1 (adsorption):



Step 2a (condensation):



Step 2b (volume diffusion):



where Step 1 corresponds to the adsorption of atmospheric water as a monolayer on the surface of the polymer; Step 2a corresponds to the condensation of successive monolayers to form a film of water on the polymer surface; and Step 2b which occurs simultaneously with Step 2a corresponds to the water molecules on the surface diffusing into the

polymer sample. The absorption kinetics of the polymer will then be determined by the rate constant k of the slowest sequential reaction step. When the slowest sequential reaction step involves two simultaneously occurring reactions, the absorption kinetics can exhibit a two-stage kinetic response where the first stage is governed to the faster of the two reactions while the second stage is governed by the slower of the two reactions. Experimentally, the second stage would become apparent only when the first stage reaction has gone to completion. If the rate constants for the component reaction steps lie in the sequence

$$k_a^a > k_c^a > k_v^a$$

3.16

the model would predict a two-stage kinetic response where the first stage corresponds to the building up of successive monolayers (Step 2a--Equation 3.14) to form a surface film. The surface film will continue to grow in thickness until an equilibrium thickness is achieved and then the second simultaneously occurring stage--corresponding to water molecules, diffusing into the polymer from the surface (Step 2b--Equation 3.15) will become apparent. The kinetic theory of gases suggests that the growth of a film of water on the polymer surface during the first kinetic stage of water absorption will result in a weight gain that is linear with time while simple volume diffusion theory with the appropriate boundary conditions predicts that the second kinetic stage for diffusing water into the polymer will result in a weight gain that is linear with the square root of time. The fact that these predictions are consistent with the experimental observations (Figures 3.3 to 3.7) provides credibility to the proposed model for water absorption in EVA.

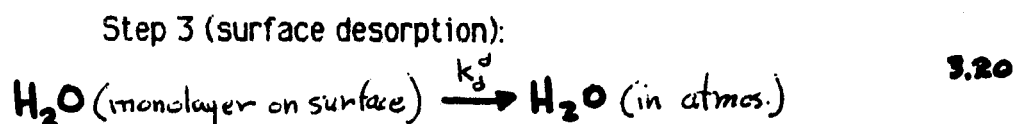
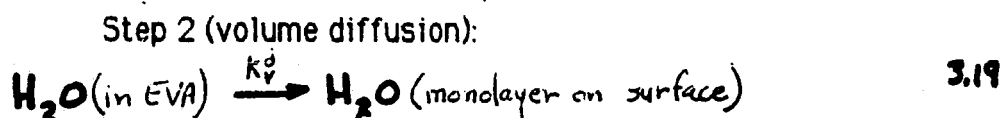
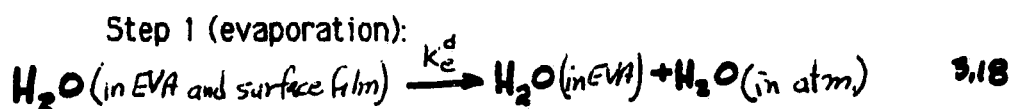
While the kinetic theory of gases predicts the experimentally observed linear time dependence for weight gain during the first stage behavior, the theory also predicts that the weight gain rate should be much more temperature sensitive than is observed experimentally, and that the

activation energy should be significantly larger than the experimentally obtained value of 0.7 Kcal/mole.

The desorption kinetics can also be modeled by a sequence of reactions involving a rate limiting step, as was suggested in the previous PVB work. The overall reaction is given by:



and analogous to the proposed desorption mechanism in PVB, this reaction is proposed to be the sum of the sequential component reactions:



These reactions are presented schematically in Figure 2.11 for the PVB work where the first step in the reaction sequence (Equation 3.18) involves the evaporation of the adsorbed layer of water on the surface of the polymer. This reaction must go to completion before the necessary boundary conditions are established for the second reaction step (Equation 3.19) to be activated. In the second reaction step, water molecules in the interior of the polymer diffuse out to the surface where they form a molecular monolayer which then evaporates (Step 3) into the atmosphere.

This reaction sequence is consistent with experimental weight loss desorption observations if the rate constants for the desorption component reaction steps is smallest for Step 1 and largest for Step 3:

$$k_d^d > k_v^d > k_e^d$$

3.21

Initially the weight loss kinetics would then be determined by Step 1 (Equation 3.18) until this evaporation reaction goes to completion. Upon completion, the weight loss kinetics would then be given by diffusion of water out of the polymer (Step 2--Equation 3.19) until the polymer is completely dehydrated. The weight loss kinetics would then occur in two stages. The first stage is due to evaporation of a surface film and is expected to be linear with time. The second stage results from volume diffusion of water out of the polymer, and is expected to be linear with the square root of time. These expected features for the weight loss kinetics are evident in the experimental desorption data (Figures 3.11 to 3.15). This two stage behavior with its associated time dependencies for desorption kinetics is the reverse equivalent of the absorption kinetic response but an important distinction exists. If the proposed reaction mechanisms correctly model the absorption and desorption processes, the Stage I and Stage II reaction mechanisms (Equations 3.14 and 3.15) occur concurrently in absorption where the Stage I reaction response is assumed to initially mask the Stage II reaction mechanism response. In desorption kinetics, the Stage I reaction and the Stage II reaction mechanisms (Equations 3.18 and 3.19) occur sequentially where the Stage II reaction initiates only after the Stage I reaction terminates. This very important distinction has considerable usefulness in a subsequent discussion of several anomalous features associated with the second stage rate constant data.

The suggestion that Stage I and Stage II behavior occur concurrently in absorption permits a more detailed analysis of the absorption data where this analysis will result in an indication of the solubility limit of water in EVA as a function of temperature. The solubility of water in EVA cannot be extracted from the true weight change given in Table I because this weight change is the sum of the weight of the water film adsorbed on the surface and the weight of the water absorbed into the EVA to its

solubility limit. Since film formation and volume diffusion are occurring concurrently in water absorption, the Stage II -- square root of time absorption kinetic response in Figures 3.3 to 3.7 can be extrapolated to a zero time intercept. The value of this intercept is the normalized weight gains w_s/w_0^a due to forming a film of equilibrium final thickness. Table 3.4 presents these intercepts along with the total normalized weight gain w_{00}/w_0^a as determined from the time independent, saturated normalized weight gain values for each absorption run. From these values, the total weight gain w_{00} , the weight gain w_s due to surface film formation, the weight gain w_v due to volume absorption, and the solubility limit of water in EVA can be evaluated. The results are presented in Table 3.4 and in Figure 3.16 where the temperature dependence for the limit of water solubility in EVA is displayed. The solubility increases with increasing temperature up to approximately 80°C.

The apparent retrograde solubility above 80°C does not necessarily suggest that the EVA water phase diagram is characterized by an invariant reaction at approximately 80°C, but rather may be associated with a hydrolyzing reaction.

The other piece of information that can be extracted from the results in Table 3.4 is the equilibrium thickness of the water film adsorbed to the EVA surface. This thickness can be easily calculated from the surface water weight (w_s) data, and the results as function of temperature are presented in Figure 3.17.

The final aspect of the data that requires some discussion is rate constant data and their associated Q_D^I , Q_A^I , Q_D^{II} , and Q_A^{II} , activation energies for the two-stage kinetics in both water absorption and water desorption. The Q_A^{II} , and Q_D^{II} activation energies are associated with second stage behavior in absorption and desorption respectively. Since

second stage behavior involves the bulk diffusion of water molecules into the polymer and out of the polymer in absorption and desorption respectively, the Q_A^{II} , and Q_D^{II} activation energies should be numerically equal. Numerical equality is suggested in Table 3.3 but an examination of Figure 3.9 reveals a difficulty in unambiguously determining the value of the Q_D^{II} , activation energy for Stage II desorption kinetics. The difficulty resides in the fact that the Stage II desorption rate constant data points do not obey a well-defined Arrhenius temperature dependency as expected for a volume diffusion controlled mechanism.

In contrast, the volume diffusion controlled Stage II absorption behavior rate constant data points do obey the Arrhenius Law (Figure 3.9) which yields a well defined value for the Q_A^{II} activation energy. This experimentally observed noncompliance with Arrhenius for Stage II desorption rate constant data and compliance for Stage II absorption rate constant data can be explained by appealing again to the proposed models where Stage II volume diffusion during absorption was suggested to occur concurrently with Stage I surface film formation while Stage II volume diffusion during desorption was suggested to occur sequentially after the Stage I surface film evaporation reaction goes to completion. The analysis for both absorption and desorption Stage II behavior consisted of analyzing the normalized weight change for a square root of time dependence where the time values were referenced to an origin at the instant of quenching. This origin is correct for the absorption run where volume diffusion occurs concurrently with surface film formation, and starts at the instant of quenching. This origin is not correct for the desorption run where volume diffusion does not start at the instant of quenching, but rather starts at the time when the surface film is completely evaporated, and Stage I behavior terminates. The Stage II absorption analysis should then yield correct information and the resulting

rate constants should obey an Arrhenius relationship as is observed experimentally. The Stage II desorption analysis based on a time origin at the instant of quenching will not yield completely correct information about rate constants, and it is not surprising that an Arrhenius relationship is not strictly obeyed. These Stage II absorption rate constant data points, if not completely correct, are in approximate enough agreement with an Arrhenius slope of the 5.2 Kcal/mole (Fig. 9) activation energy to suggest that $Q_A^{II} \simeq Q_D^{II}$.

The observation of Arrhenius compliance and non-compliance for Stage II, absorption and desorption rate constant data respectively as a result of choosing the time origin at the instant of quenching, provides a measure of indirect confirmation for the validity of the proposed models. Because of the uncertainty in choosing the appropriate time origin for the Stage II desorption data analysis, no attempt has been made to re-examine and correct this data.

While the Q_A^{II} and Q_D^{II} volume diffusion controlled activation energies are expected to be equal from volume diffusion considerations, the Q_A^I and Q_D^I activation energies associated the Stage I absorption condensation and desorption evaporation reactions respectively, are not expected to be equal particularly if the polymer is even slightly hydrophobic. If the polymer has hydrophobic tendencies, evaporation of a surface film will be much faster than condensation. The Stage I kinetics can then be represented by the typical energy barrier diagram shown in Figure 3.18 where the energy to climb over the barrier for the condensation reaction is significantly larger than the barrier clearing energy for the reverse evaporation reaction. The implications of this diagram are that the Stage I desorption kinetics are faster than the absorption kinetics as is observed experimentally (Fig. 3.2).

The preceding discussion does provide a reasonable explanation for the observed experimental results but the one feature associated with the

rate constant that has yet to be resolved is that C_0 pre-exponential factors for the Stage II volume diffusion mechanism in both absorption and desorption were expected to be equal and were found to differ (Table 3.3) by almost two orders of magnitude.

This inconsistency between the C_0 pre-exponential factor for absorption and for desorption was also apparent in the PVB data, and it suggests that the mechanism responsible for the observed second stage kinetic response in both water absorption and desorption may be more complex than a simple volume diffusion process. A sequence of additional experiments to examine the second stage behavior in more detail, were performed to help elucidate the governing mechanism. The experiment consisted of measuring the second stage absorption and desorption normalized weight change kinetics response in EVA samples of different thickness value. If volume diffusion is the rate controlling mechanism for Stage II behavior, the weight change results for the various sample thicknesses should superimpose on a linear square root of time/thickness ($t^{1/2}/d$) dependence:

$$w_t/w_\infty = K t^{1/2}/d$$

3.22

Sample thickness were .045, .094, .191, and .284 cm for EVA. The kinetics were monitored gravimetrically at 53⁰ C for water absorption and at 76⁰C for water desorption. The anlysis consisted of correcting both the weight and time data for the first stage (surface film) effect assuming that both first and second stage behavior occur simultaneously in absorption and occur sequentially in desorption. The corrected data is then expected to represent second stage kinetic behavior alone without any perturbing influence from the first stage response.

The corrected Stage II absorption and desorption weight change results as a function of $t^{1/2}/d$ are shown in Figures 3.19 and 3.20 respectively. While some scatter exists, superposition and linearity are evident in the data suggesting that volume diffusion controls the Stage II behavior for both water absorption and water desorption. The apparent scatter in the data is not unexpected since the weight changes being monitored are rather small and the associated errors when correcting the data can become fairly large.

TABLE 3.1

Weight characteristics of EVA during absorption and desorption.

Temperature Humidity Conditions T(°C)/H (%)	W_o^e : Expected Starting Weight (gms)	W_o^a : Measured Starting Weight (gms)	W_{∞} : Measured Final Weight (gms)	$W_{\infty} - W_o^a$: Apparent Weight Change (gms)	$W_{\infty} - W_o^e$: True Weight Change (gms)	$W_o^a - W_o^e$: Weight of Initially Formed Surface Layer (gms)	$W_o^e - W_o^a$: Weight of Initially Lost Surface Layer (gms)	$\frac{W_o^e - W_o^a}{W_o^e}$: Normalized Initial Layer Weight
88/0 → 88/100+	1.600*	1.691	2.366	.675	.766	.091	----	.057
88/100 → 88/0 ●	2.366	1.750	1.599	.151	.767	----	.616	.260
75/0 → 75/100+	1.821*	1.914	2.804	.890	.983	.093	----	.051
75/100 → 75/0 ●	2.804	2.388	1.824	.564	.980	----	.416	.148
60/0 → 60/100+	1.520*	1.575	2.593	1.018	1.073	.55	----	.036
60/100 → 60/0 ●	2.593	2.092	1.519	.573	1.074	----	.501	.193
50/0 → 50/100+	1.600*	1.647	2.565	.918	.965	.047	----	.029
50/100 → 50/0 ●	2.565	2.198	1.602	.596	.963	----	.367	.143
40/0 → 40/100+	1.608*	1.613	2.295	.682	.695	.013	----	.008
40/100 → 40/0 ●	2.295	2.149	1.603	.546	.692	----	.146	.063

* - Original weight of desiccated dried sample.

+ - Absorption run

● - Desorption run

TABLE 3.2

Characterizing rate constants for Stage I and Stage II kinetic behavior for the normalized weight gain in water absorption and the normalized weight loss in water desorption in EVA.

<u>Temp.</u>	<u>STAGE I</u>		<u>STAGE II</u>	
	$\frac{W_t}{W_a^0} = At + B$		$\frac{W_t}{W_o^a} = Ct^{\frac{1}{2}} + D$	
	<u>A</u>	<u>B</u>	<u>C</u>	<u>D</u>
	<u>Absorption</u>			
	(hrs. ⁻¹)		(hrs. ^{-1/2})	
88°C	.030	1.0	.0190	1.285
75°C	.080	1.0	.0125	1.460
60°C	.068	1.0	.010	1.570
50°C	.071	1.0	.0082	1.490
40°C	.031	1.0	.0062	1.335
	<u>Desorption</u>			
	(min. ⁻¹)		(min. ^{-1/2})	
88°C	.030	1.0	--	--
75°C	.031	1.0	.0723	1.063
60°C	.0175	1.0	.0690	1.070
50°C	.0130	1.0	.0605	1.071
40°C	.0073	1.0	.441	1.066

TABLE 3.3

Activation energies and pre-exponential factors for Stage I and Stage II kinetic response in water absorption and desorption in EVA.

STAGE I -- Surface Film

	<u>Q^I (kcal/mole)</u>	<u>A_0 (min. $^{-1}$)</u>
Absorption	0.7 ($=Q^I_A$)	.0033 (0.2 hrs. $^{-1}$)
Desorption	6.1 ($=Q^I_D$)	167

STAGE II -- Volume Diffusion

	<u>Q^{II} (kcal/mole)</u>	<u>C_0 (min $^{-\frac{1}{2}}$)</u>
Absorption	5.1 ($=Q^{II}_A$)	3 (23 hrs. $^{-\frac{1}{2}}$)
Desorption	5.1 ($=Q^{II}_D$)	159

TABLE 3.4

Weight gain characteristics of EVA in water absorption due to surface film formation and volume absorption.

Temperature	W_{∞}/W_0^a : Total Normalized Weight Gain	W_{∞} : Total Weight Gain per Gram EVA (gms)	W_s/W_0^b : Total Normalized Weight Gain Due to Surface Film Formation (gms)	W_s : Weight Gain per Gram EVA Due to Surface Film Formation (gms)	W_v : Weight Gain per Gram EVA Due to Volume Absorption (gms)	$W\%$: Weight Percent Solubility of Water in EVA (%)
88°C	1.48+	.48	1.285*	.285	.195	16.3
75°C	1.70+	.70	1.460*	.460	.240	19.3
60°C	1.68+	.68	1.570*	.570	.110	9.9
50°C	1.58+	.58	1.490*	.490	.090	8.2
40°C	1.42+	.42	1.335*	.335	.085	7.8

+ Determined from data in Table 3.1

* Taken from extrapolated D intercept values in Table 3.2

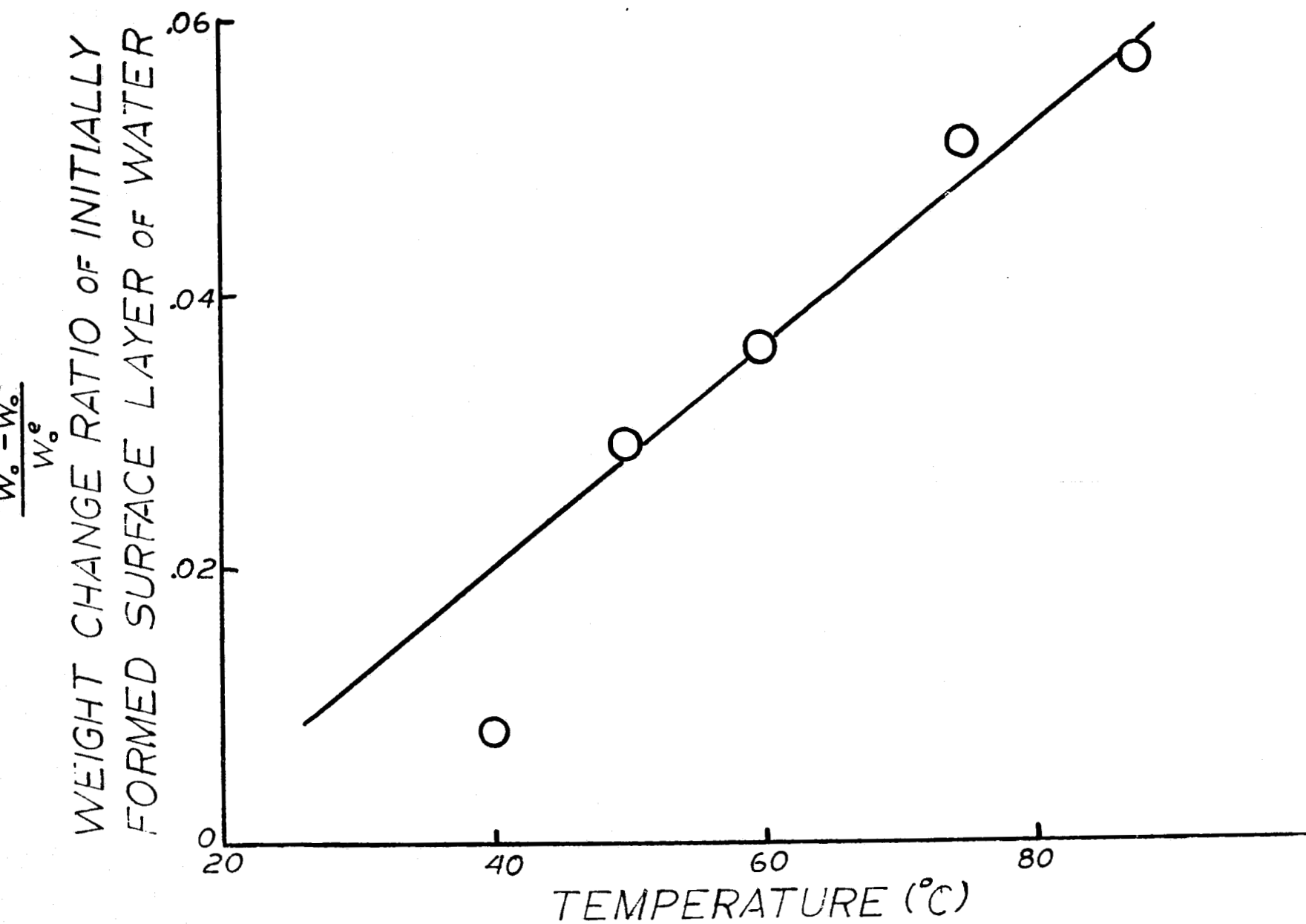


Fig. 3.1-Temperature dependence of the normalized weight for the initially formed surface layer of water during water absorption in EVA.

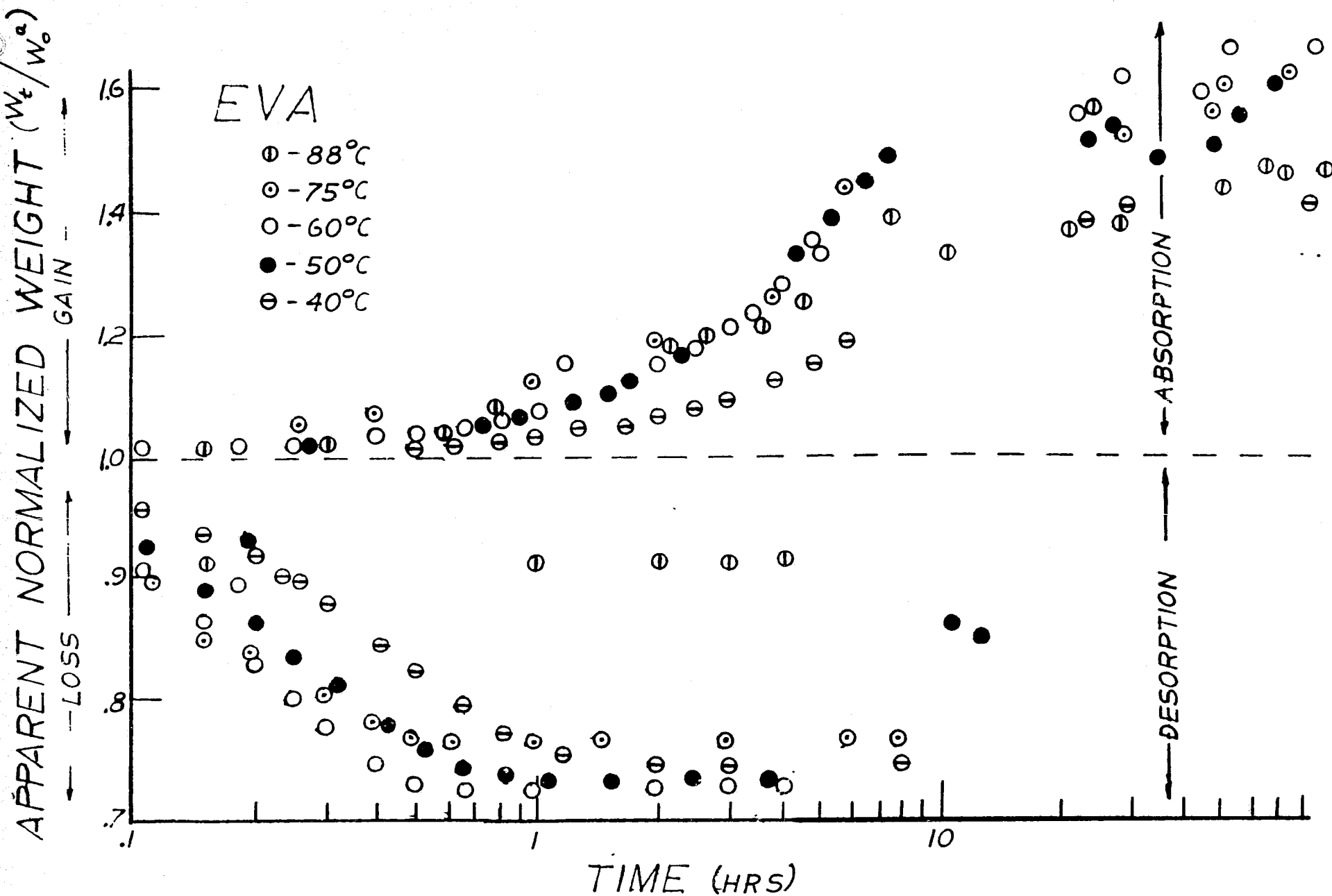


Fig. 3.2-Time dependence of normalized weight change during absorption and desorption of water in EVA at selected temperatures.

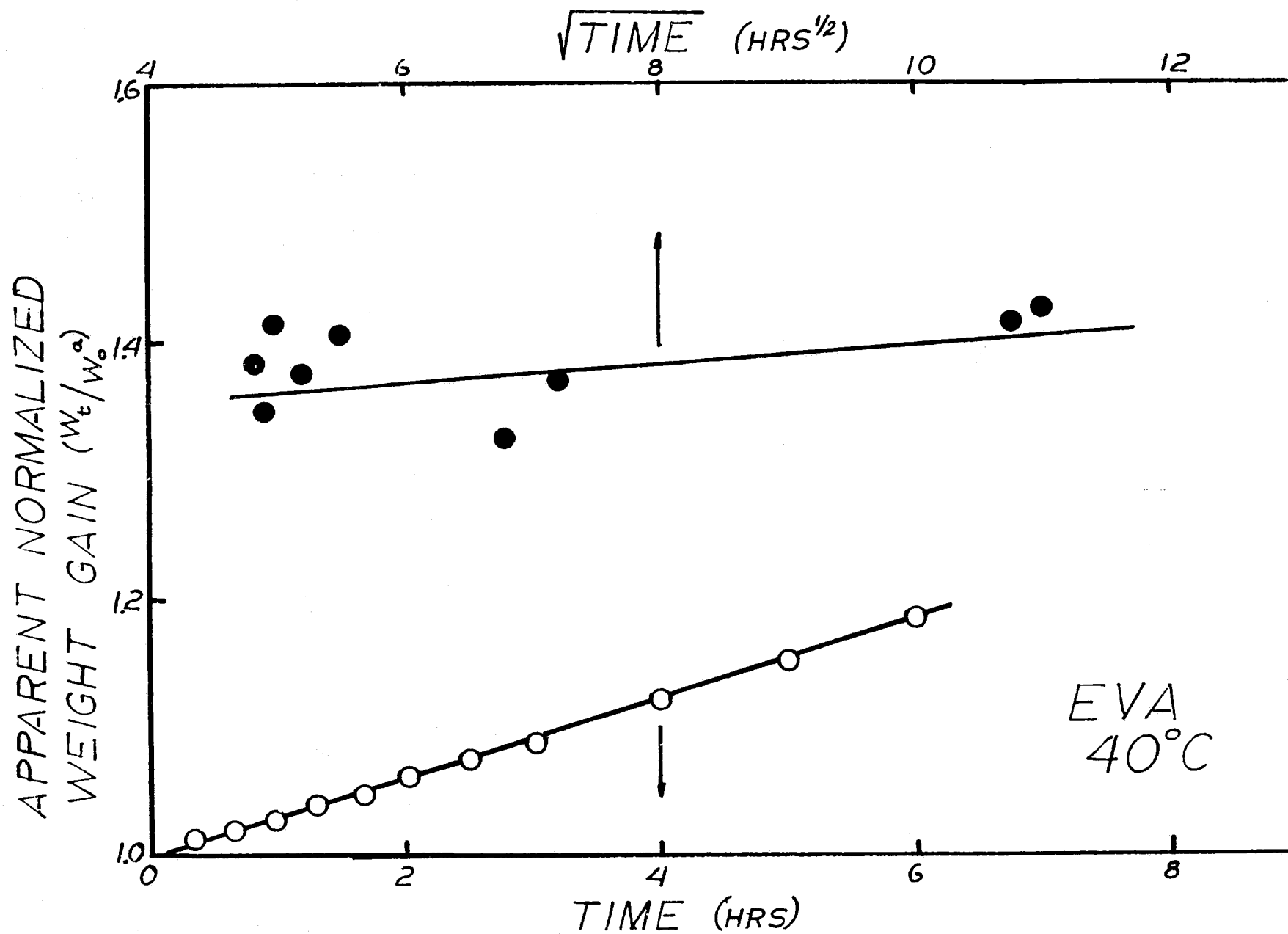


Fig. 3.3-Time and square root of time dependence of normalized weight gain in EVA due to water absorption.

APPARENT NORMALIZED
WEIGHT GAIN (w_t/w_a)

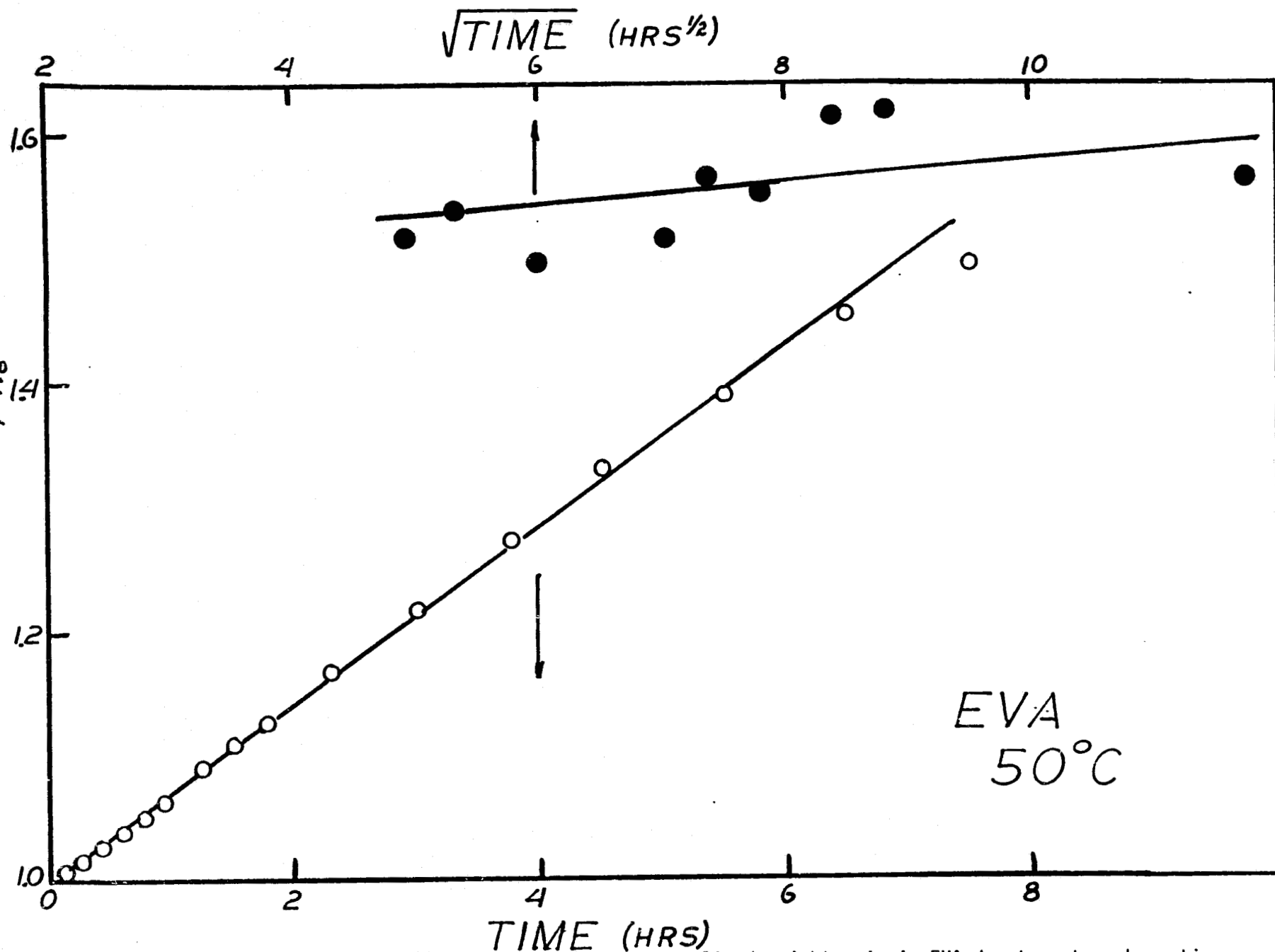


Fig. 3.4-Time and square root of time dependencies of normalized weight gain in EVA due to water absorption at 50°C.

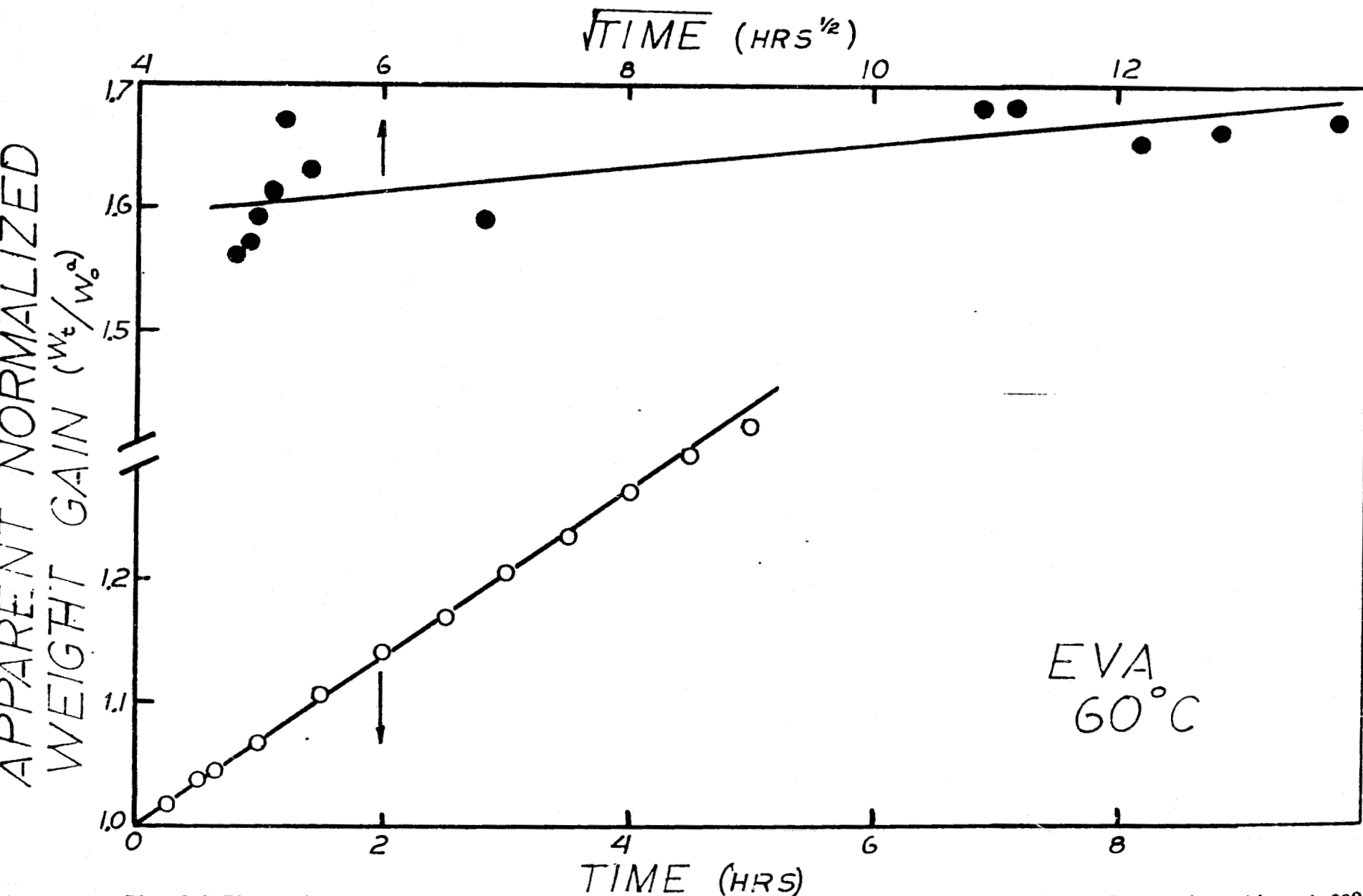


Fig. 3.5-Time and square root of time dependencies of normalized weight gain in EVA due to water absorption at 60°C.

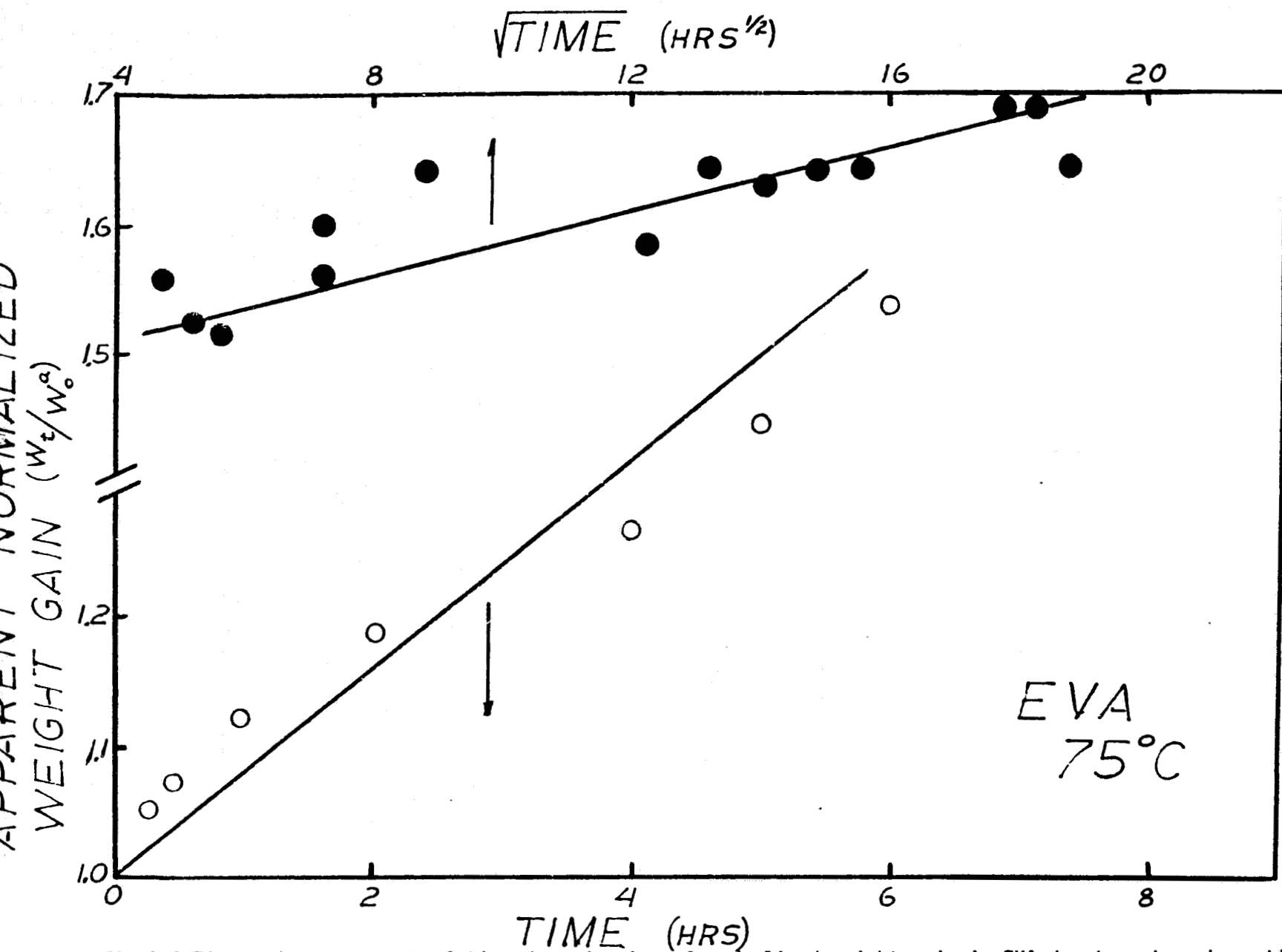


Fig 3.6-Time and square root of time dependencies of normalized weight gain in EVA due to water absorption at 75°C.

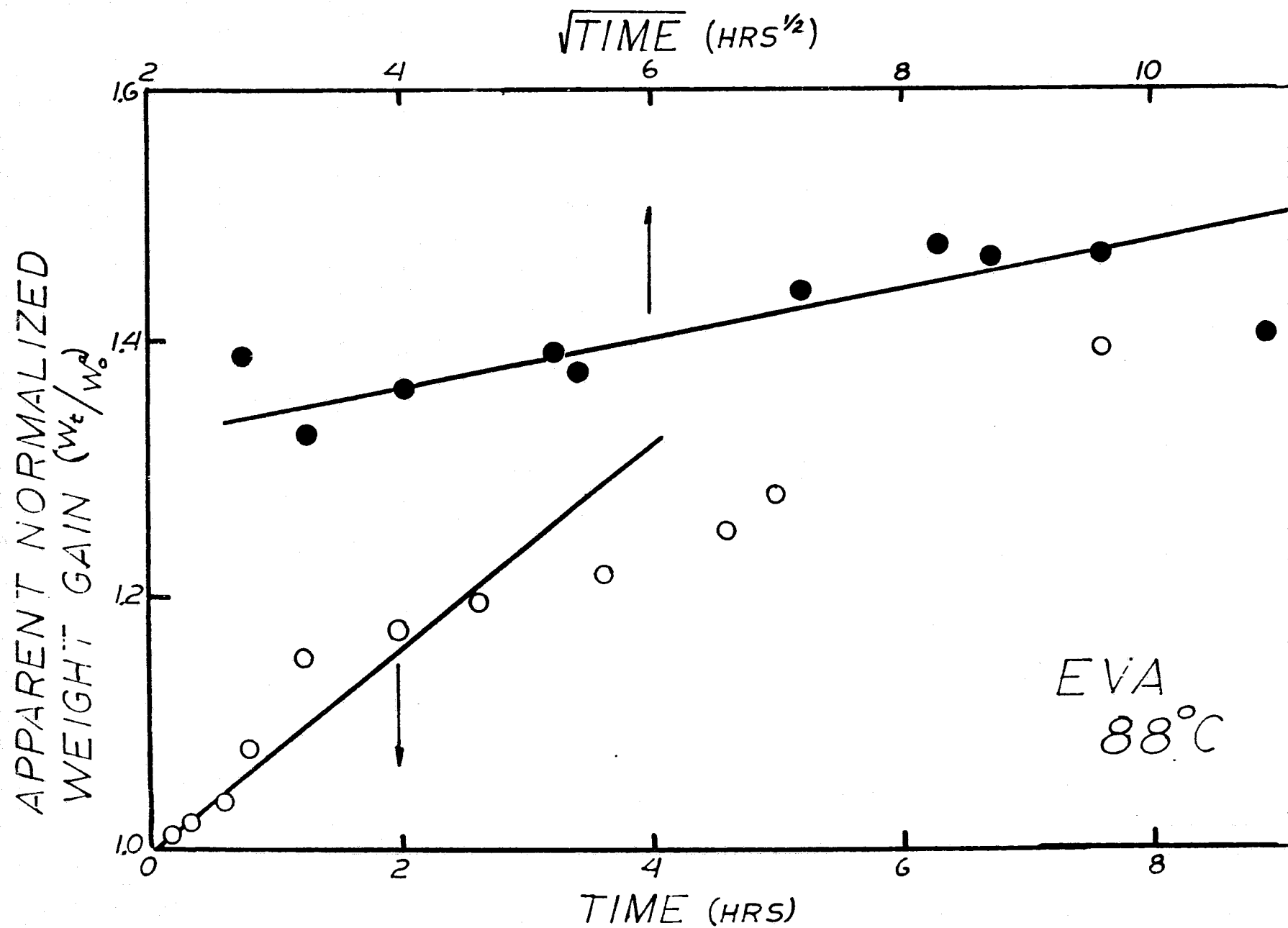


Fig. 3.7-Time and square root of time dependencies of normalized weight gain in EVA due to water absorption at 88°C.

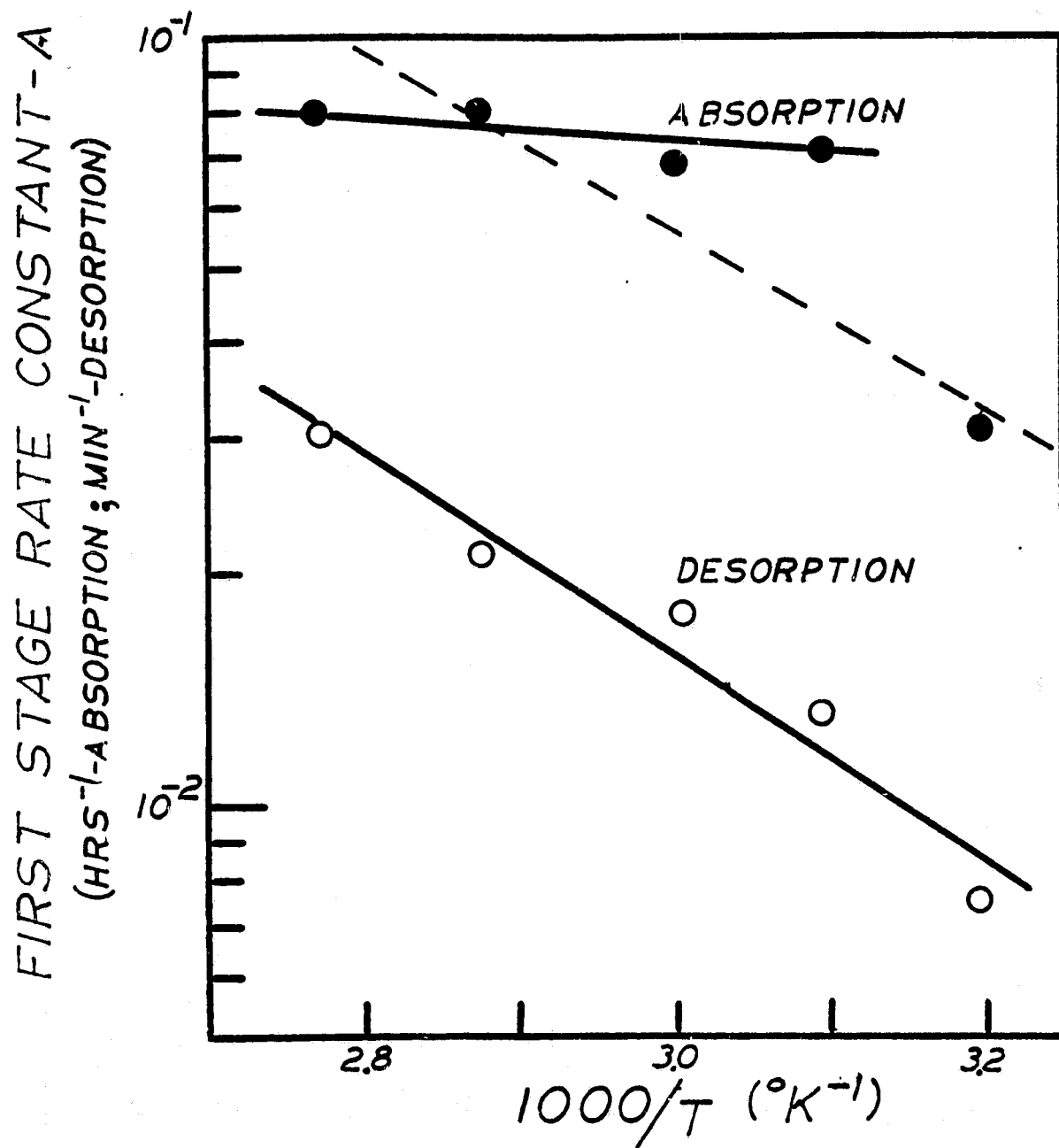


Fig. 3.8-Temperature dependence of the rate constant for first stage water absorption and water desorption in EVA.

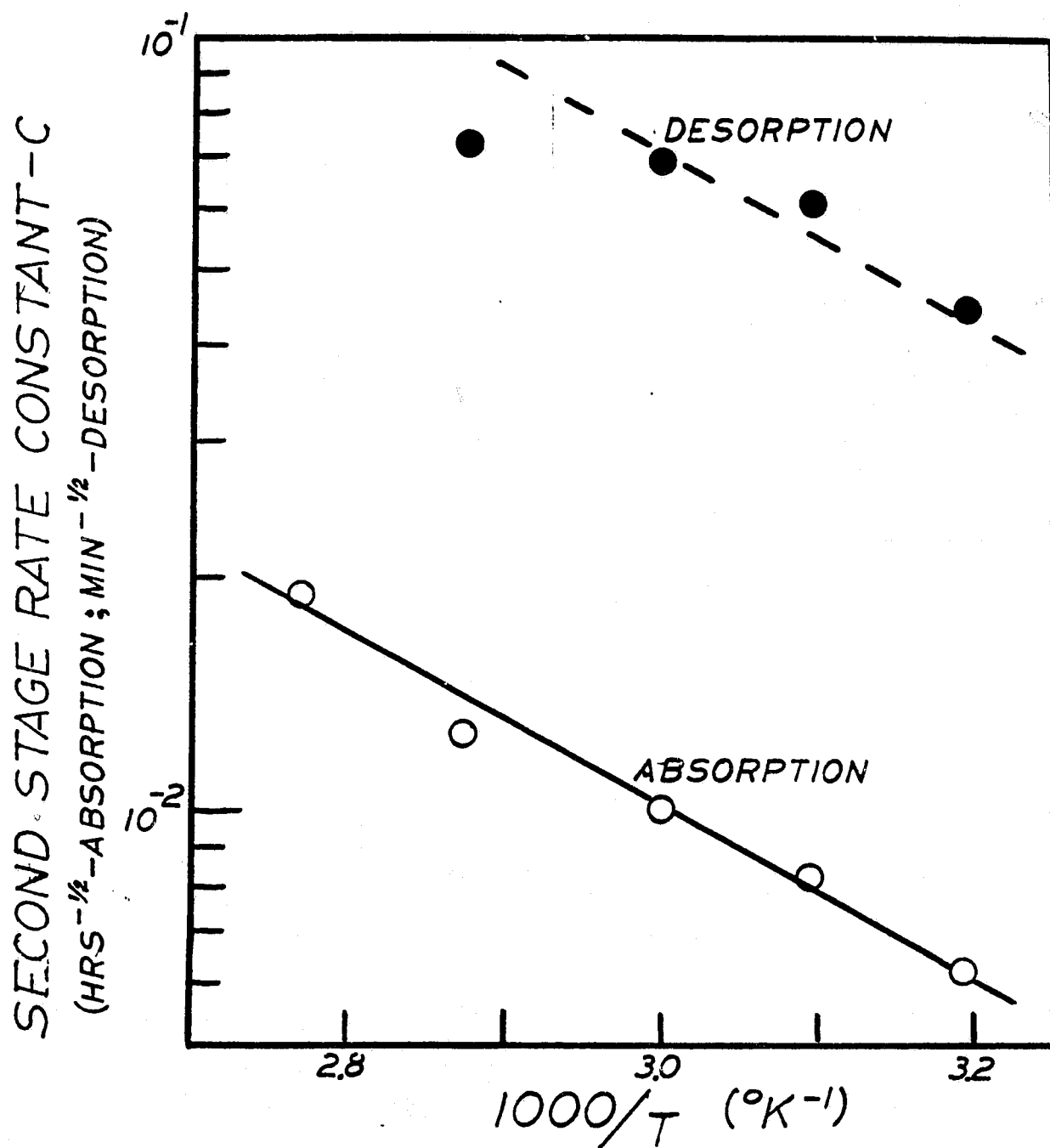


Fig. 3.9-Temperature dependence of the rate constant for second stage water absorption and water desorption in EVA.

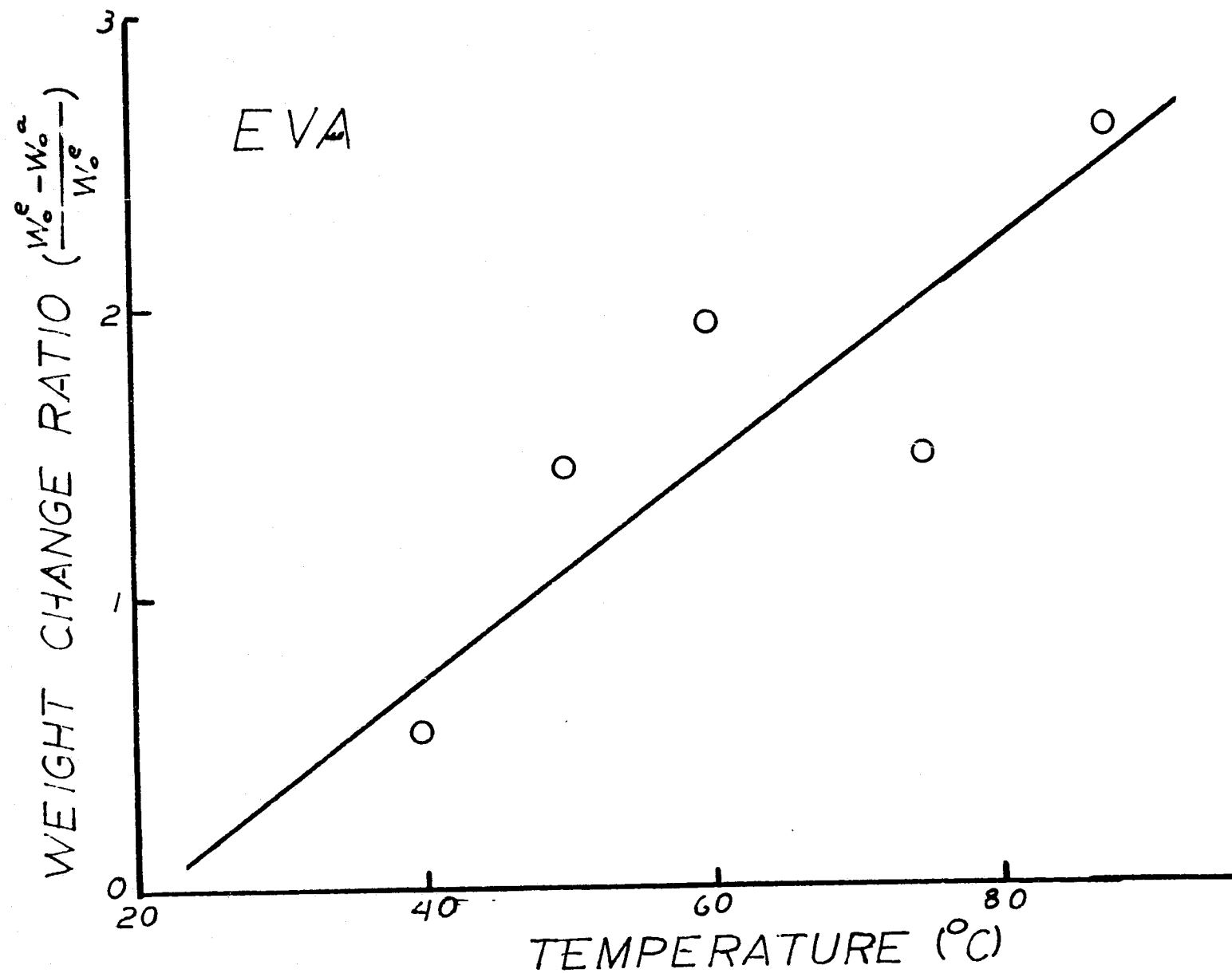


Fig. 3.10-Temperature dependence of the weight change ratio for the initially lost surface layer of water during water desorption in EVA.

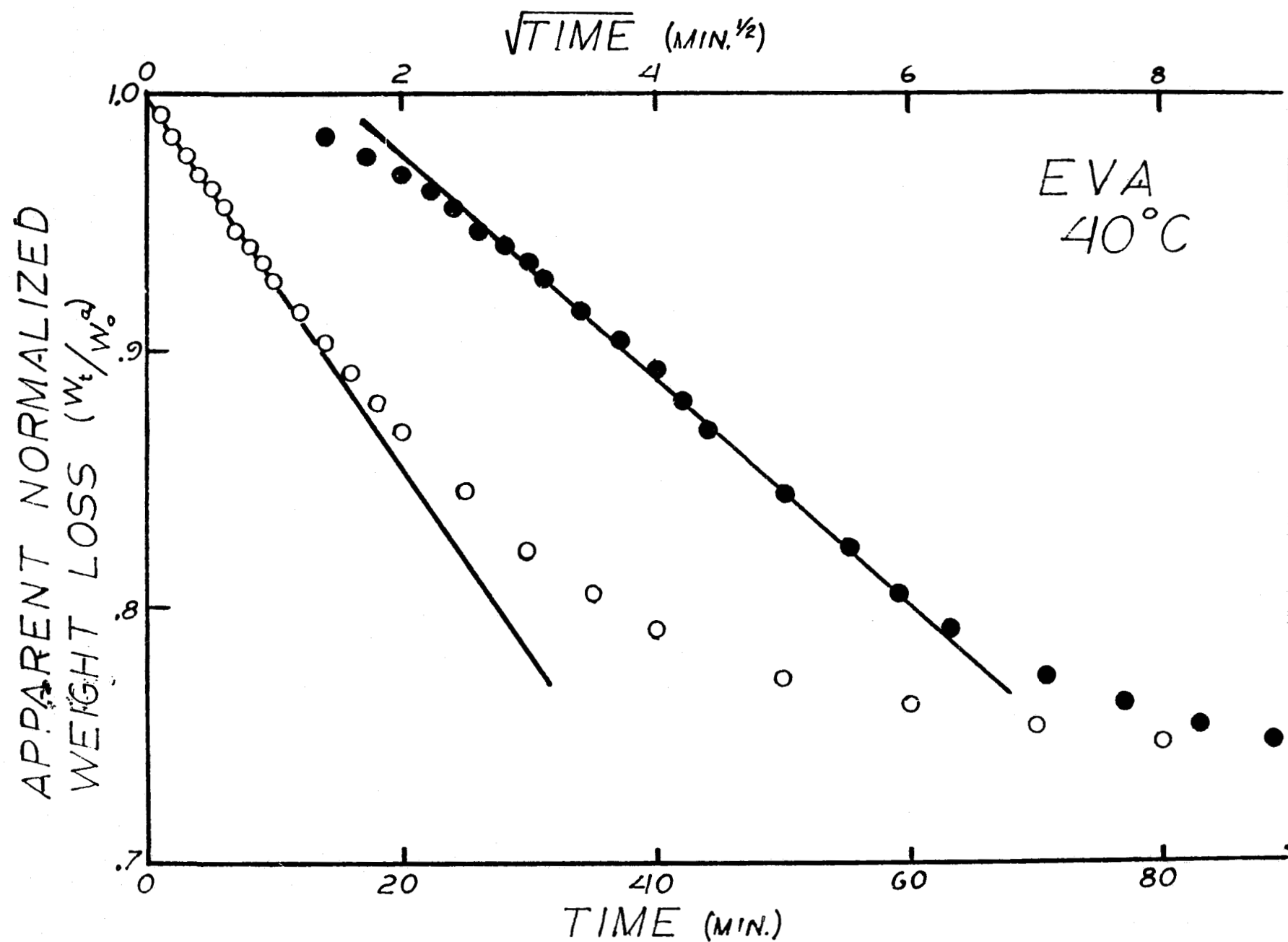


Fig. 3.11 - Time and square root of time dependencies of the normalized weight loss in EVA due to the water desorption at 40°C.

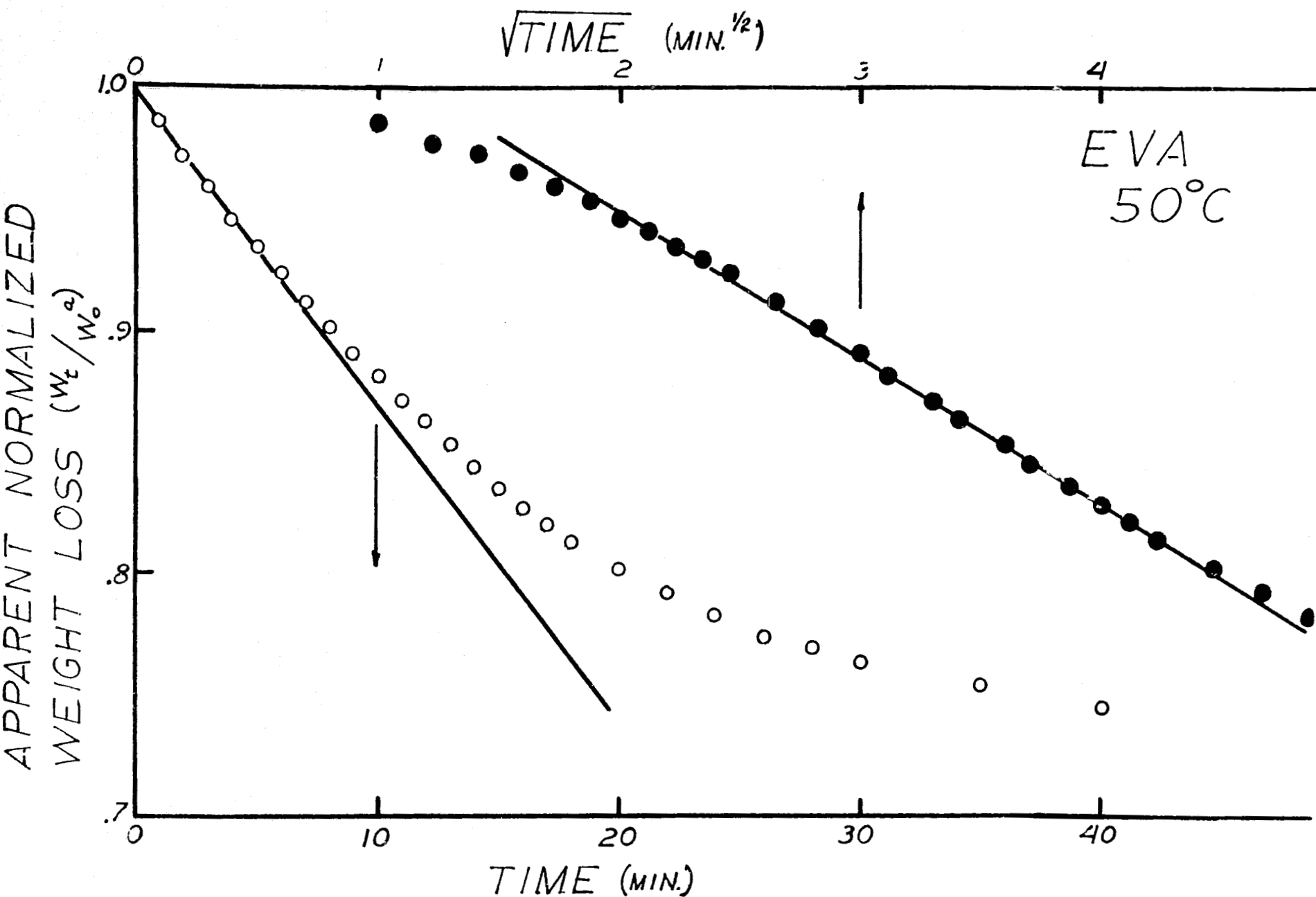


Fig. 3.12-Time and square root of time dependencies of normalized weight loss in EVA due to water desorption at 50°C.

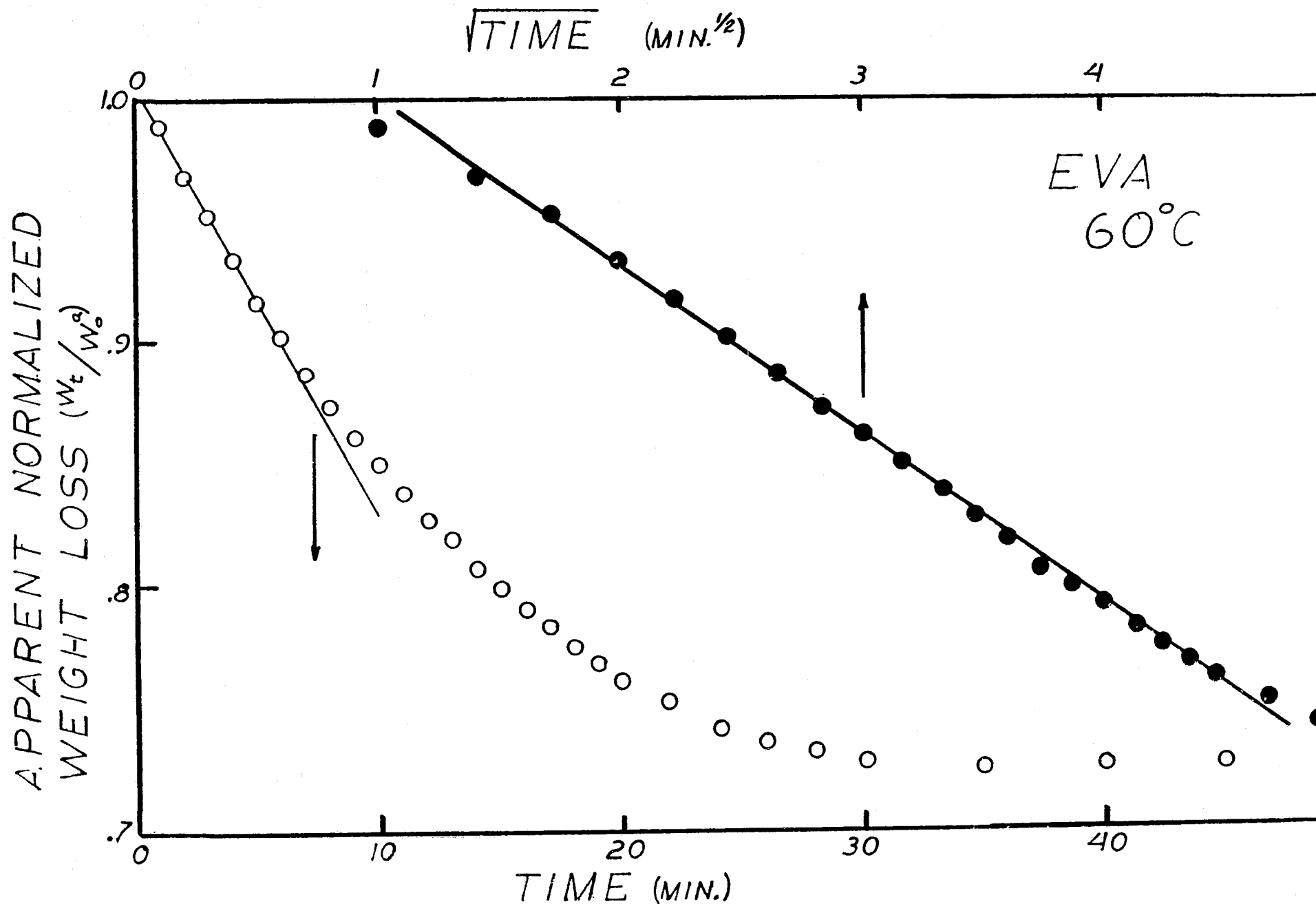


Fig. 3.13-Time and square root of time dependencies of normalized weight loss in EVA due to water desorption at 60°C.

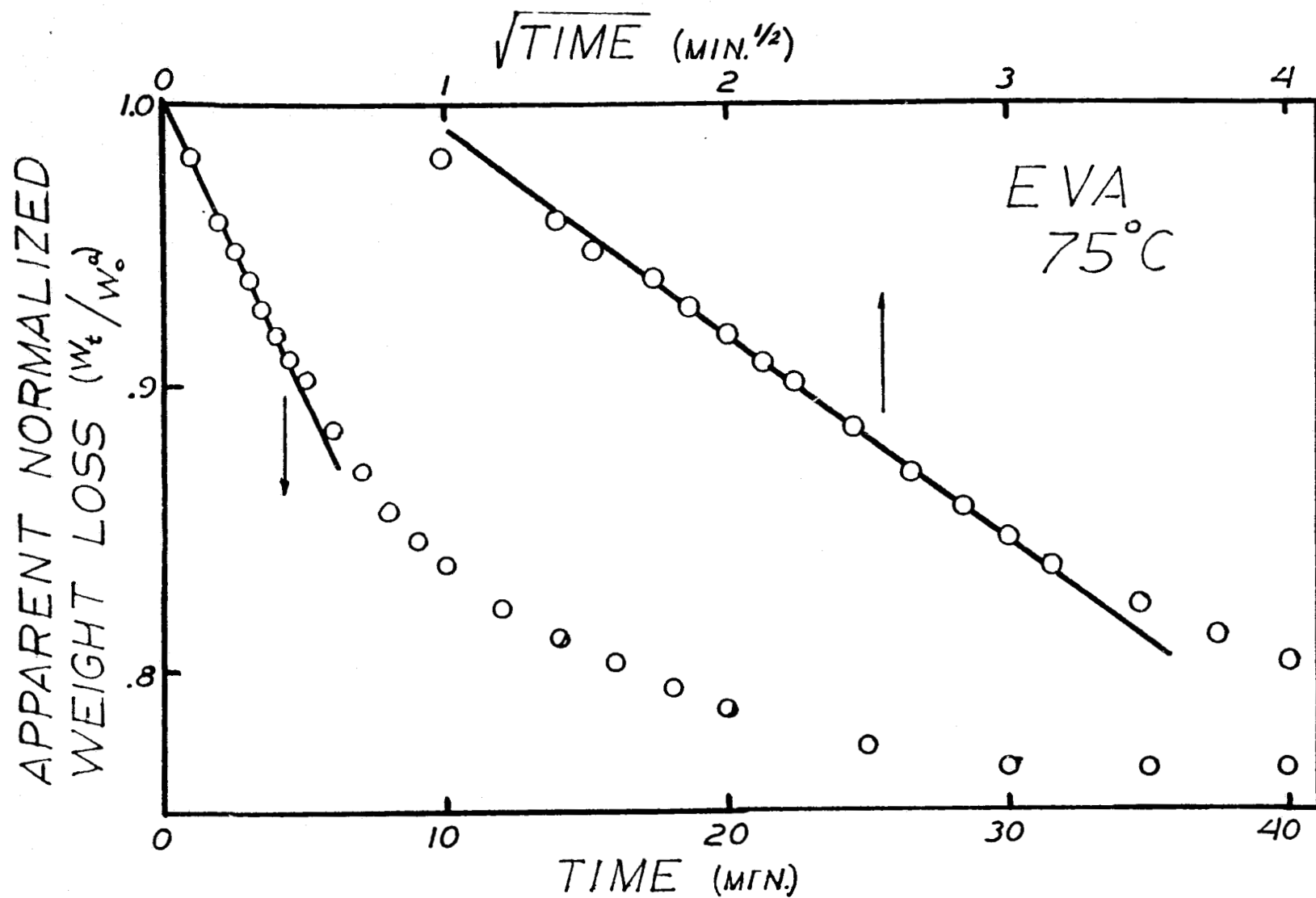


Fig. 3.14-Time and square root of time dependencies of normalized weight loss in EVA due to water desorption at 75°C.

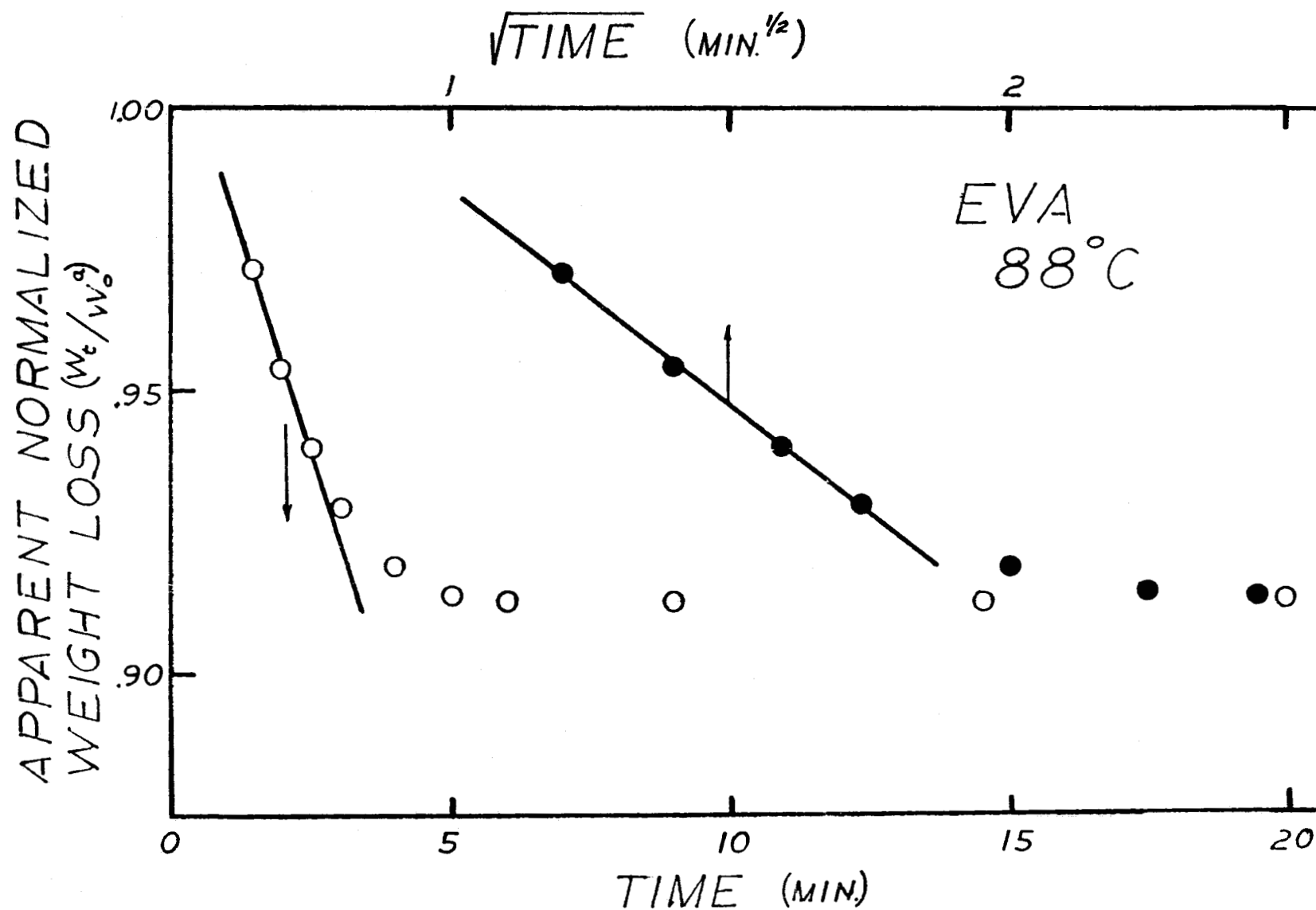


Fig. 3.15—Time and square root of time dependencies of normalized weight loss in EVA due to water desorption at 88°C.

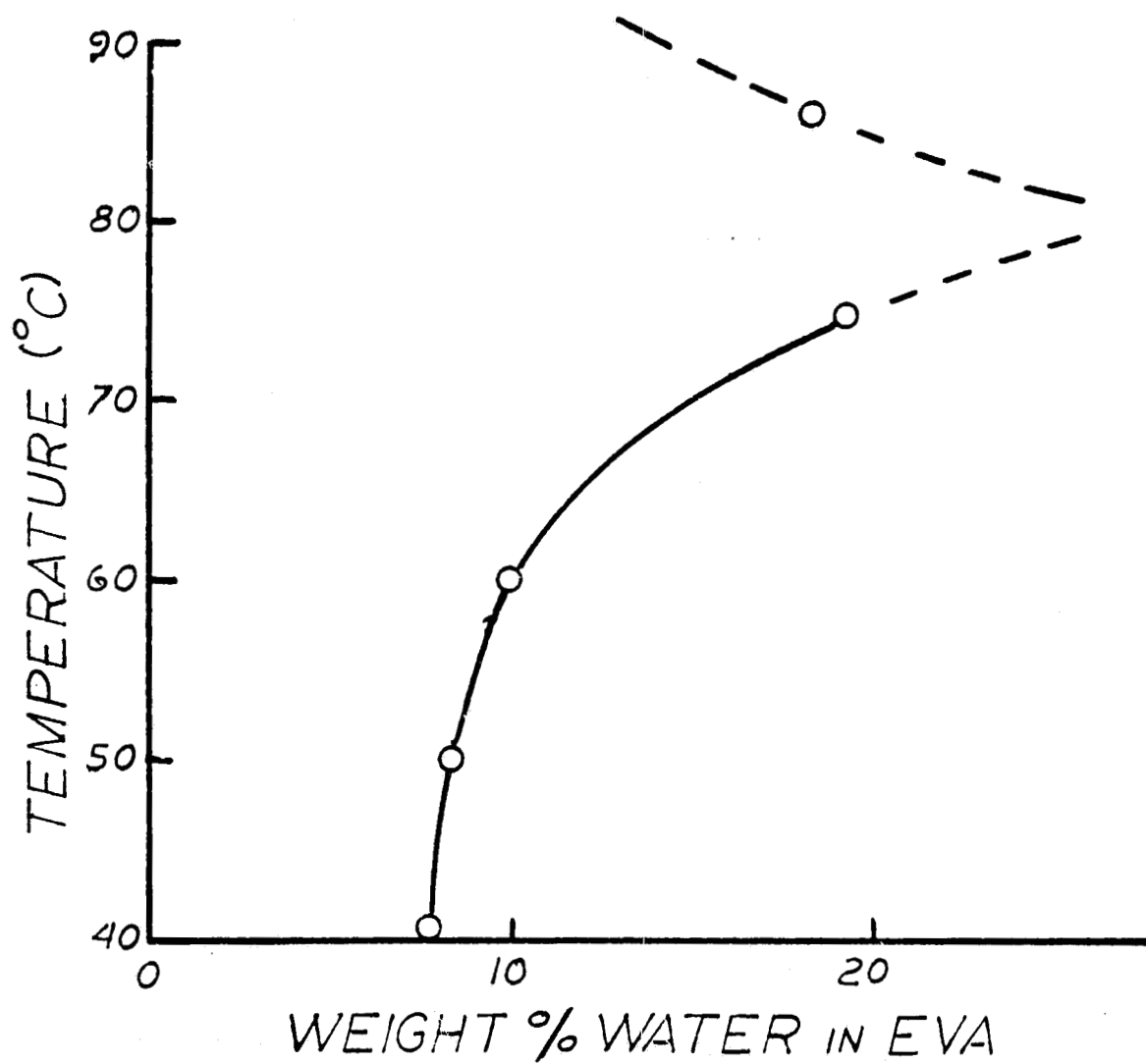


Fig. 3.16-Partial phase diagram for the binary H₂O EVA system where the solubility limit of H₂O in EVA as a function of temperature is shown.

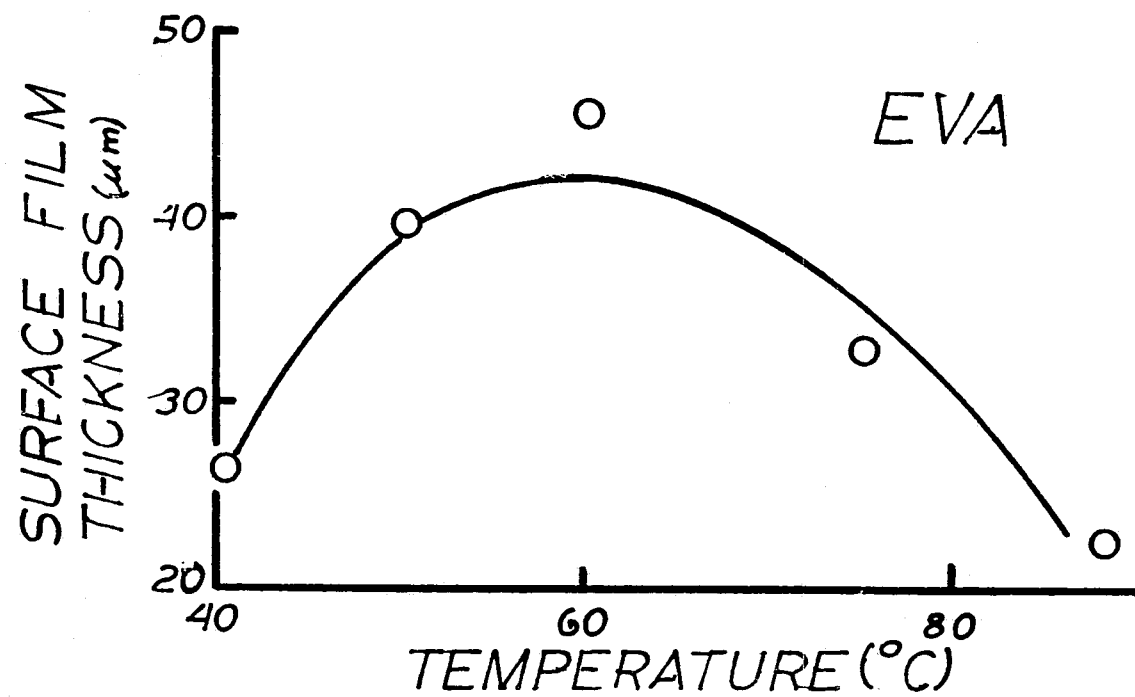


Fig 3.17—Temperature dependence for the thickness of the absorbed water layer on EVA.

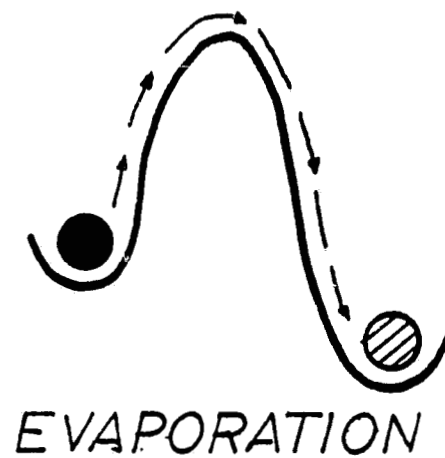
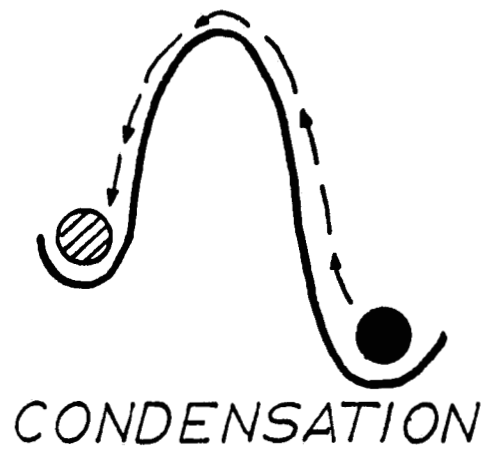


Fig. 3.18-Schematic illustration of the energy barrier for the condensation and evaporation processes in EVA.

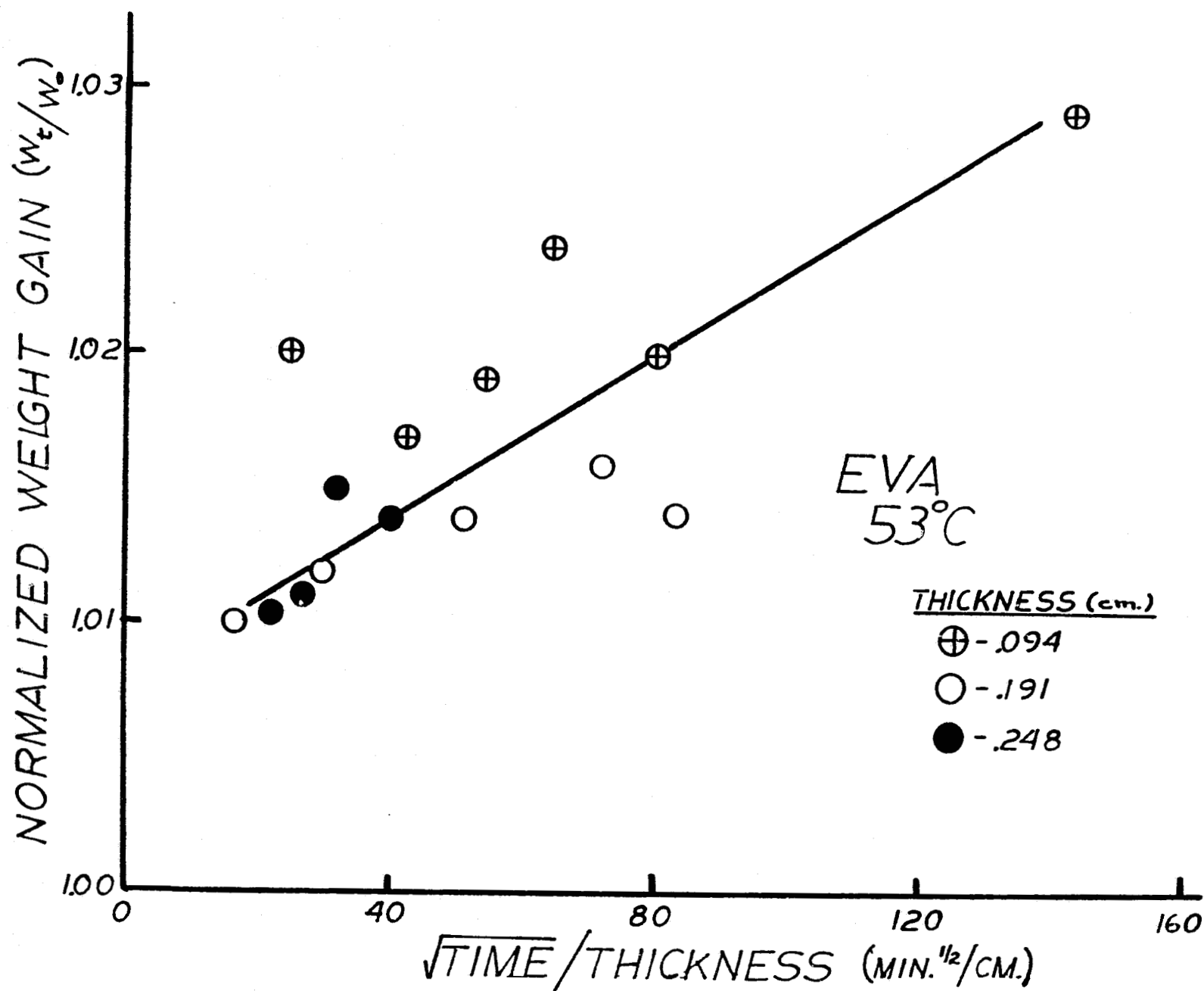


Fig. 3.19—Water absorption kinetics (thickness dependence) in EVA.

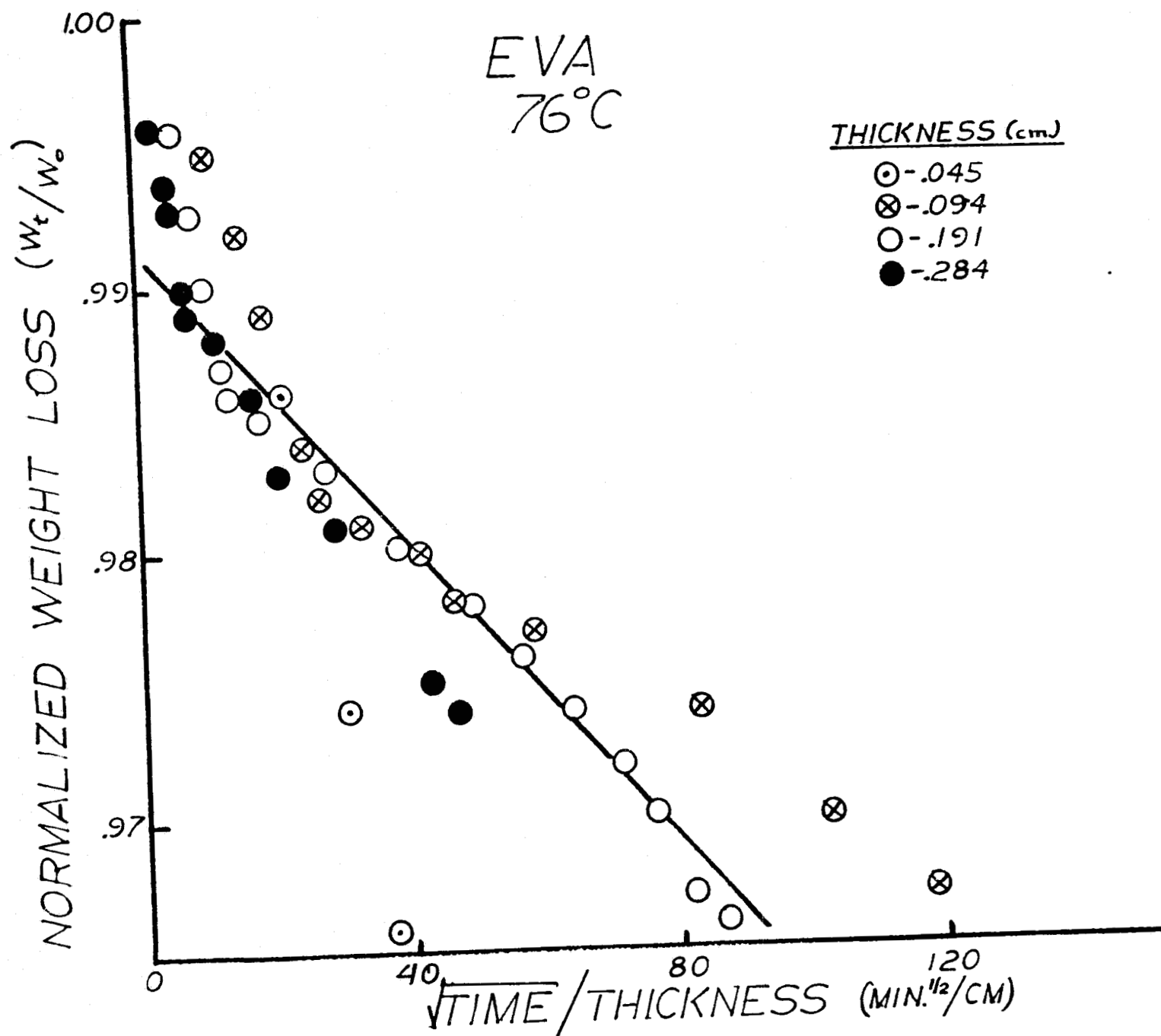


Fig. 3.20-Thickness dependence of water desorption kinetics in EVA.

IV. Electrical Properties of PVB

Experimental Procedure

Selected a.c. and d.c. electrical properties of PVB were evaluated as a function of temperature and humidity. The properties being investigated are the:

- (i) absorption current (d.c.)
- (ii) ionic resistance (d.c.)
- (iii) capacitance (a.c.)
- (iv) dissipation factor (a.c.)

The experimental procedure consists of encapsulating 200 mesh phosphorous bronze screening as parallel electrodes in the PVB samples. The samples were immersed in water for several weeks to obtain saturation equilibrium. Previous results showed that water saturation can be achieved in several weeks when the samples are immersed in water. After saturation with water, the samples were transferred to the temperature/humidity chamber at a selected temperature and at 100% humidity. After equilibrating for an additional twenty-four hours, the electrical properties were measured and then the humidity was lowered. Since the desorption kinetics are rapid (Section II), twenty-four hours were allowed to achieve equilibrium at the lower humidity level before the electrical properties were measured again. This experimental procedure was repeated at progressively lower humidity levels, and the electrical properties were determined as a function of the relative humidity for temperatures of 80⁰, 68⁰, 53⁰, 42⁰, and 25⁰ C. The d.c. electrical properties: absorption current and ionic resistivity, and the a.c. electrical properties: capacitance and dissipation factor, were measured.

The capacitance and dissipation factor of the samples were measured on a General Radio Capacitance Bridge. The absorption current was evaluated by applying a 390 d.c. voltage driving step to the samples and monitoring the time dependence of the d.c. current response function. When the current response became relatively time independent, the current-voltage characteristics were measured to determine the ionic resistivity.

Experimental Results

d.c. Properties

The time dependence of the current response to a step 390 volts d.c. forcing function for a PVB sample at 80⁰, 68⁰, 53⁰, 42⁰, and 26⁰ C are presented as a function of the relative humidity in Figures 4.1 to 4.6. An examination of these figures shows that the current response at elevated temperature/humidity conditions (80/100 and 68/100) obeys (Figs. 4.1 and 4.2) a single power law time dependency:

$$I = K t^{-\alpha}$$

4.1

over the entire time frame of the experiment until the current response becomes relatively time independent. At these higher temperatures, (80⁰, 68⁰ and 53⁰) and at the intermediate humidity levels (50% to 85%), the current response exhibits a two-stage power law dependency (Figs 4.1 to 4.3) where an initial transient was apparent (Figs. 4.2. and 4.3) in the data at 68⁰ and 53⁰ C. This initial transient was found (Figs. 4.7 and 4.8) to be exponentially related to the time:

$$I = I_0 \exp(-t/\tau)$$

4.2

As the combination of temperature and humidity decreases to lower values, both the two-stage power law and initial transient becomes less evident: at 80/30, 68/28, 53/48, 53/41, and 53/30 the initial transient is still apparent (Figs. 4.1 to 4.4) and is still exponentially time dependent

(Figs. 4.7, 4.9 and 4.10) while the two-stage power law response disappeared and became a single power law time dependence. At the lowest temperatures of 42⁰, and 26⁰C, no evidence of either a transient or a two-stage power law exists and the current response obeys a single power law time dependence (Figs. 4.5 and 4.6) for all humidity values.

If the transient is assumed to exist at 80⁰C, but is masked by the first stage power law then, as a general empirical rule, it appears that the transient exists at temperature (°C) and humidity levels whose products exceeds about 150:

$$[T(^{\circ}C)][H(\%)] > 150 \quad \text{transient behavior}$$

$$[T(^{\circ}C)][H(\%)] < 150 \quad \text{no transient}$$

a.c. Properties

The capacitance and loss factor at various temperatures as a function of frequency for different humidity levels is presented in Figure 4.11. This data is used to determine:

- (i) the humidity and temperature dependence of the capacitance at selected frequencies (Fig. 4.12 and 4.13)
- (ii) the humidity and temperature dependence of the loss factor at 1 KHz (Fig. 4.14).

These figures show that the capacitance is frequency sensitive only when the humidity is high (Fig. 4-11). The capacitance appears to be temperature insensitive (Fig. 4.12 and 4.13), and appears to be linearly related (Fig. 4.12 and 4.13) to the humidity by the expression:

$$C \approx 170 H + 200$$

4.3

The loss factor is a function of frequency (Fig. 4.11), temperature (Fig. 4.14), and humidity (Fig. 4.14) and approaches zero with decreasing temperature and humidity (Fig. 4.14). The specific form for the

temperature and humidity dependence of $\tan \delta$ can be obtained from Figure 4.14 where it is seen that

$$\tan \delta = m H + b \quad 4.4$$

where the slope and intercept values are presented in Table 4.1 and plotted in Figures 4.15 and 4.16 respectively. Fig. 4.15 shows that the slope obeys an Arrhenius temperature dependence of:

$$m = .32 \exp(-1500/T) \quad 4.5$$

corresponding to an activation energy of

$$Q_s = 3 \text{ Kcal/mole} \quad 4.6$$

Figure 4.16 shows that the intercept is approximately linearly related to the temperature:

$$b = -.56 T + 356 \quad 4.7$$

The temperature and humidity dependence of the loss factor then becomes

$$\tan \delta = .32 H [\exp(-1500/T)] - .56 T + 356 \quad 4.8$$

Table 4.2 summarizes these experimentally determined a.c. electrical features of PVB as a function of temperature and humidity.

Discussion of Results

d.c. Properties

A model that could account for the observed features of the experimental d.c. current data shown in Figures 4.1 to 4.10 suggests that the d.c. current (I) response is the sum of four major contributing current components: I_c , I_p , I_w , and I_i , as shown in Figure 4.17 where

$$I = I_c + I_p + I_w + I_i \quad 4.9$$

The individual mechanisms responsible for these component currents are:

(i) I_c capacitance charging current-- The samples are simple capacitors and, if they can be represented by a lumped series capacitor--resistor circuit, the d.c. current response I_c to a step d.c. voltage forcing function will be exponentially time dependent

$$I_c = I_{c_0} \exp(-t/\tau) = [390/R_0] [\exp(-t/\tau)] \quad 4.10$$

through an $R_0 C$ time constant ($\tau = R_0 C$) where R_0 is the initial resistance at time equals zero of the polymer sample to a 390 v forcing function.

$$R_0 = 390 / I_0 \quad 4.11$$

(ii) I_w (water dipole relaxation charging current)--Orientational polarization of absorbed water molecule dipoles in the polymer when subjected to an applied d.c. field is expected to be time sensitive where this sensitivity should yield an exponential time dependent charging current response (I_w):

$$I_w \sim \exp(-t/\tau_w) \quad 4.12$$

where τ_w is the dielectric relaxation time. Experimentally, the response current is frequency observed to obey a power law time dependency:

$$I_w = I_{w_0} t^{-\alpha_w} \quad 4.13$$

where the α_w coefficient is believed to be related to the orientational mobility of the water molecule dipole in the presence of an electric field. Since absorbed water molecules are not incorporated into the polymer structure by strong primary bonds, the orientation mobility of the water molecular dipole is expected to be large and this large mobility for the dipoles should result in a relatively large value for the α_w coefficient of a power law charging current is the characterizing response. Since dipole

orientation mobility is expected to be sensitive to temperature but not to the number of water molecules (n_w) absorbed in the polymer, the coefficient will be temperature (T) dependent but not humidity (H) dependent:

$$\alpha_w = fct(T)$$

4.14

$$\alpha_w \neq fct(H)$$

4.15

The value of the I_{w0} factor in the power law expression is dependent on the number of absorbed water molecules and should then be a function of humidity and temperature:

$$I_{w_0} = \text{fct. } (T, H)$$

4.16

Equations 4.14 to 4.16 show that I_w (Eq. 4.8) should be a function of temperature and humidity;

$$I_w = \text{fct } (T, H)$$

(iii) I_p (polymer dipole relaxation charging current) -- Polar polymer molecules will also experience a time dependent orientational polarization when subjected to an applied electric field and this time dependence can result in a power law time dependence response current (I_p):

$$I_p = I_{p0} t^{-\alpha_p}$$

4.17

where both α_p and I_{p0} are expected to be temperature dependent but not humidity dependent:

$$\alpha_p = \text{fct } (T)$$

4.18

$$\alpha_p \neq \text{fct } (H)$$

4.19

$$I_{p0} = \text{fct } (T)$$

4.20

$$I_{p0} \neq \text{fct } (H)$$

4.21

As a result I_p is expected to be a function of temperature only.

Since polymer molecules are locked into an amorphous crystal structure by strong primary bonds, the orientational mobility of the polymer dipoles is less than that of absorbed water dipoles. The α_p

coefficient should then be relatively small compared to α_w

$$\alpha_p < \alpha_w$$

4.22

(iv) I_i (intrinsic current) -- The intrinsic current contribution can result from two types of carriers: (a) mobile ions and (b) intrinsic electrons.

(a) Mobile Ions

Ions from impurities (absorbed water, plasticizer, compounding agents), from the corroding anode, or from disassociated polymer can contribute to a current response if the ions are mobile in the polymer. The response will be time dependent if the ions are not regenerative, and will be time independent if the ions are regenerative by equilibrium constant considerations or by anode corrosion considerations. The effects of temperature and humidity on the intrinsic current are difficult to predict if the ion carriers are nonregenerative, but are easy to predict from the Butler-Volmer equation if the ions are regenerative. For a corrosion current governed by a Butler-Volmer activation overpotential, the current is related to the applied voltage by:

$$I_i = 2 I_{i_0} \sinh (FV/2RT)$$

4.23

where F is the Faraday equivalent. This dependency for the intrinsic current on voltage is usually most evident at very large applied voltages. For the typical low voltages used in this experiment, the Butler-Volmer equation becomes:

$$I_i \approx I_{i_0} FV/RT$$

4.24

$$I_i \approx \sigma_i V$$

4.25

suggesting that an ohmic I-V response is expected where σ_i is the intrinsic conductance whose magnitude $I_{i_0} F/RT$ can also be expressed as

$$\sigma_i = q [n_H \mu_H + n_{OH} \mu_{OH} + n_p \mu_p + n_e \mu_e]$$

4.26

where n_{H^+} , n_{OH^-} , n_p and n_a are the number of ions from ionized water molecules, disassociated polymer molecules, and corroded electrode respectively, and where μ_{H^+} , μ_{OH^-} , μ_p , and μ_a are the respective mobilities of these ions. The intrinsic current component then becomes:

$$I_i \approx q [n_{H^+} \mu_{H^+} + n_{OH^-} \mu_{OH^-} + n_p \mu_p + n_a \mu_a] V \quad 4.27$$

Assuming that the mobilities of all ionic species are approximately equal

$$\mu_{H^+} = \mu_{OH^-} = \mu_p = \mu_a \equiv \mu \quad 4.28$$

the current becomes

$$I_i \approx q \mu [2K_1 n_w + n_p + n_a] V \quad 4.29$$

where K_1 is the ionization constant of water and n_w is the equilibrium number of impurity water molecules absorbed in the polymer at a given value of relative humidity and temperature.

The intrinsic resistance (R_i) would then be given by:

$$R_i = V / I_i = \{q \mu [2K_1 n_w + n_p + n_a]\}^{-1} \quad 4.30$$

Thermodynamic considerations require that the equilibrium number of impurity water molecules absorbed in the polymer will be determined by the partial pressure of water vapor in the surrounding ambient so n_w will be proportioned to relative humidity and temperature:

$$n_w = fct(H, T) \quad 4.31$$

Both the intrinsic resistance (Eq. 4.30) and the intrinsic current (Eq. 4.29) are then expected to be functionally dependent on both temperature and humidity:

$$R_i = f_{ct}(H, T) ; R_i \sim H^{-1} \quad 4.32$$

$$I_i = f_{ct}(H, T) ; I_i \sim H \quad 4.33$$

and to be time insensitive if the ions contributing to the intrinsic current are regenerative.

(b) Intrinsic Electrons

The equilibrium number of electrons (and holes) also contributes to the intrinsic current of the polymer. The intrinsic current due to electrons and holes will not be a function of time:

$$I_i \neq f_{ct}(\text{time})$$

but will be a function of temperature and humidity if the polymer can be assumed to behave like a band gap semiconductor and if the absorbed water and compounding impurities are assumed to behave like n-type or p-type dopants. With these assumptions, the intrinsic current is expected to be directly proportional to the humidity and exponentially proportioned to the temperature.

$$I_i \sim H \exp(-K/T) \quad 4.34$$

The intrinsic resistance becomes:

$$R_i \sim H^{-1} [\exp(K/T)] \quad 4.35$$

When these component currents (Eqs. 4.10, 4.13, and 4.17) are substituted into Equation 4.9., the time dependent current response to a step d.c. applied voltage becomes:

$$I = [390/R_0] \exp(-t/\tau) + I_{w_0} t^{-\alpha_w} + I_{p_0} t^{-\alpha_p} + I; \quad 4.36$$

where, at a sufficiently long time, the intrinsic current alone can be evaluated provided that it is time insensitive. This equation as illustrated in Figure 4.17 is the basis upon which the experimental results were analyzed.

Some of the contributing current components in this equation may be small enough to be neglected depending upon the temperature and humidity conditions. When the humidity is high, the equilibrium impurity water content in the absorbing polymer may be large enough so that

$$I_{w_0} > I_{p_0} \quad 4.37$$

since I_{w_0} is expected to be humidity dependent (Eq. 4.16) while I_{p_0} is believed to be insensitive to the humidity (Eq. 4.21). Almost all of the dipole relaxation current is then expected to result from the orientational polarization of water molecules

$$I_{w_0} t^{-\alpha_w} > I_{p_0} t^{-\alpha_p} \quad 4.38$$

and with this assumption, Equation 4.36 becomes:

$$I = [390/R_0] \exp(-t/\tau) + I_{w_0} t^{-\alpha_w} + I; \quad 4.39$$

If the resistance of the polymer is low at high humidity levels, the $R_0 C$ time constant τ will be small. When τ is small enough, the exponential decay term will be too fast to be recorded by the experimental arrangement and the capacitive charging component current will not be apparent. Equation 4.39, the apparent d.c. current response to a step

voltage forcing function will then contain only the power law current component characterized by α_w and the time independent intrinsic current contribution (I_i)

$$I = I_w t^{-\alpha_w} + I_i \quad 4.40$$

This predicted single stage power law response is consistent with the experimental data observed at high humidity (90%) levels at both 80°C and at 68°C (Figs. 4.1 and 4.2) where the slope for each single stage power law response was evaluated numerically and taken to be the α_w coefficient whose values are presented in Figures 4.1 and 4.2.

The intrinsic current (I_i) can also be evaluated from this experimental data. The approach to a time independent intrinsic current in Figures 4.1 and 4.2 appears to occur after a run time of 100 minutes. Because of the long time involvement, the intrinsic current was not recorded in great detail. In general, the intrinsic current was taken to be the current value after 120 minutes of run time. Intrinsic current values extracted from the experimental data by this procedure, are recorded in Tables 4.3 and 4.4 where a complete summary of the current component values and their characterizing parameters for the d.c. response at 80°C and 68°C are presented.

At intermediate humidity levels (50 to 85%) where the amount of absorbed water may be sufficiently small, the orientational polarization of both water molecules and polymer molecules may contribute equally to the dipole relaxation components. This suggests that at intermediate humidity levels:

$$I_w \approx I_p \quad 4.41$$

The dipole relaxation would then be the sum of the two power law time dependencies:

$$I_w t^{-\alpha_w} + I_p t^{-\alpha_p} \quad 4.42$$

and neither contributing factor may be neglected. At these intermediate humidity levels, the initial resistance (R_0) of the polymer sample may be sufficiently large that the $R_0 C$ time constant is long enough to permit a measurement of the current component due to capacitive charging provided the pre-exponential term ($380/R_0$) is not too small. The total current response to a d.c. step forcing voltage function would then contain all the proposed current components and be given by Equation 4.36 in its full form:

$$I = [380/R_0] \exp(-t/\tau) + I_{w_0} t^{-\alpha_w} + I_{p_0} t^{-\alpha_p} + I_i$$

The experimental data should display an exponentially decaying transient followed by a two-stage power time law dependency which eventually approaches a time independent intrinsic current. These predicted features are evident in the intermediate humidity (50 to 80%) data at 68°C and 53°C as shown in Figures 4.2, 4.3, 4.7, and 4.8. Except for the inability to record the initial transient, the two stage power law feature is also apparent in the 77% and 64% intermediate humidity data at 80°C for PVB (Figure 4.1).

Equation 4.22 requires that the first stage power law behavior with its large slope be associated with the orientation polarization of water molecules while the second stage power law behavior results from the orientation polarization of polar polymer molecules. The slope of each first stage power law response is taken to be the α_w coefficient while the slope of each second stage power law response is assigned to the α_p coefficient as shown in Figures 4.1, 4.2, and 4.3 and as tabulated in Tables 4.3 to 4.5.

The intrinsic current (I_i) values at these intermediate humidity levels at 80°C, 68°C, and 53°C, is again taken to be the current value after 120 minutes of run time and these I_i values are presented in Tables 4.3 to 4.5.

The initial transient current components were also evaluated from the data (Figs. 4.7 and 4.8) at the intermediate humidity levels and the

results for the characterizing τ and R_0 values are also presented in Tables 4.4 to 4.5.

At low humidity levels, (less than 50%) and possibly at low temperatures (less than 40°C) where the number of water molecules n_w absorbed in the polymer is probably small, the initial resistance of the polymer sample and the associated R_0C time constant of the sample are both expected to be very large. The large time constant permits a measurement of the capacitance changing current component provided the $390/R_0$ pre-exponential term is not unsignificantly small. Also at low humidities, the dipole relaxation current is expected to be dominated by the relaxation of the polymer molecules.

$$I_p t^{-\alpha_p} > I_w t^{-\alpha_w} \quad 4.43$$

Equation 4.36 then simplifies to an expression for the current response that contains only one power law time dependence, the intrinsic current component and possibly the capacitive charging current component:

$$I = [390/R_0] \exp(-t/\tau) + I_p t^{-\alpha_p} + I_c \quad 4.44$$

where this power law is characterized by the α_p coefficient. The experimental data at humidities less than 50% appear to be in reasonable agreement with these predicted features. A single power law time dependence current component with its assigned α_p slope is evident at all temperatures where the humidity is low: 80/30 (Fig. 4.1), 68/46 and 68/28 (Fig. 4.2), 53/48 to 53/16 (Fig. 4.4) and 26/51 and 26/45 (Fig. 4.6). The initial transient, capacitive charging current component is also evident (Figs. 4.7 to 4.10) when the temperature exceeds 50°C except at very low humidities (53/25 and 53/16--Fig. 4.4) but is not evident in the

data when the temperature is less than 53°C (Fig. 4.5 and 4.6) even when the humidity is high, probably because the initial resistance (R_0) is so large that the capacitive charging current is insignificantly small. A complete summary of the current components and their characterizing parameters (R_0 , R_i , I_{w0} , I_{p0} , α_w and α_p) are presented in Tables 4.3 to 4.7 for various temperature/humidity conditions. From this summary, the temperature and humidity dependence of the characterizing parameters can be evaluated.

The humidity dependence of the initial resistance (R_0) at various temperatures is shown in Figure 4.18. The initial resistance at all temperatures and for humidity values in excess of 40% appeared to be exponentially dependent on the humidity: (Fig. 4.18)

$$R_0 = A \exp(-\beta H)$$

4.45

where the coefficients A and β from the experimental data are presented in Table 4.8. The coefficient β appears to be relatively temperature insensitive with an average value of about .115(%)

$$\beta = .115(\%^{-1})$$

4.46

while the coefficient A is a strong function of temperature as indicated in Figure 4.19 where A is seen to obey an Arrhenius temperature dependency:

$$A = A_0 \exp(Q_0/RT)$$

4.47

characterized by an activation energy of

$$Q_0 = 24 \text{ Kcal/mole}$$

4.48

and a pre-exponential factor of

$$A_0 = 1.2(10^{-6}) \Omega$$

4.49

The coefficient A becomes

$$A = 1.2(10^{-6}) \exp(12000/T)$$

4.50

and the combined temperature and humidity dependence of initial resistance becomes:

$$R_0 = 1.2(10^{-6}) \exp(-.115H + 12000/T)$$

4.51

Figure 4.20 presents the intrinsic resistance as a function of humidity for various temperatures. The intrinsic resistance also appeared to be exponentially related to the humidity

$$R_i = B \exp(-\gamma H)$$

4.52

where the values for γ and B are given in Table 4.8. The γ coefficient appears to be temperature insensitive and to have an average value of about $.090 (\%)^{-1}$:

$$\gamma = .09 \text{ \%}^{-1} \quad 4.53$$

while the B coefficient is consistent with an Arrhenius relationship (Fig. 4.21)

$$B = B_0 \exp(Q_i/RT) \quad 4.54$$

where the activation energy and the pre-exponential factors are:

$$Q_i = 14 \text{ Kcal/mole} \quad 4.55$$

$$B_0 = 8.6 \quad 4.56$$

giving:

$$B = 8.6 \exp(7000/T) \quad 4.57$$

The temperature and humidity dependence of the intrinsic resistance becomes:

$$R_i = 8.6 \exp(-.09H + 7000/T) \quad 4.58$$

and this result is in modest agreement with the predicted relationship (Eq. 4.35).

The data in Tables 4.3 to 4.7 shows that the I_w contribution to the d.c. absorption current response, from reorienting water molecule impurities, exists only when the temperature exceeds 50°C and when the humidity is high. The pre-exponential factor I_{w0} as a function of humidity at temperatures above 50°C is shown in Figure 4.22 where I_{w0} is found to be very humidity sensitive:

$$I_{w0} = 10^{-8} \exp(0.127 H) \quad 4.59$$

but not at all temperature sensitive

$$I_{w_0} \neq f(t(T)) \quad 4.60$$

The characterizing power law coefficient α_w from Tables 4.3 to 4.5 is seen to be (Fig. 4.23) both temperature and humidity dependent and these dependencies from the limited data, can be very crudely approximated as:

$$\alpha_w = - .017H - .022T + 9.3 \quad 4.61$$

Substituting Equations 4.59 and 4.61 into Equation 4.13 shows that the I_w current component due to reorienting water molecules is given by:

$$I_w = 10^{-8} [\exp(0.127H)] t^{-.017H - .022T + 9.3} \quad 4.62$$

and is a function of both temperature and humidity as expected. The unexpected features are that the pre-exponential term I_{w0} is a function only of humidity (Eq. 4.59) and not temperature as predicted by Equation 4.16 and that α_w is found to be a function of both temperature and humidity (Eq. 4.61) while was expected to be a function only of temperature (Eq. 4.14).

The parameters I_{p0} and α_p for characterizing the current component I_p due to reorienting polar polymer molecules are also presented in Tables 4.3 to 4.7. The I_p absorption current contribution was found to exist at all temperatures and humidity levels. The humidity dependence of the pre-power law factor I_{p0} at various temperatures is shown in Figure 4.24 where I_{p0} is exponentially related to the humidity:

$$I_{p_0} = D \exp(\bar{z}H) \quad 4.63$$

where both D and \bar{z} are very temperature sensitive as is apparent in

Figure 4.24. The unusual and thought provoking feature illustrated in Figure 4.24 is that the humidity dependencies at the various temperatures extrapolate to a common value for I_{p0} of $2.4 (10^{-5})$ amps at a humidity of 100%. The humidity dependence of I_{p0} could then be more conveniently expressed as:

$$I_{p0} = 2.5(10^{-3}) \exp(\eta [100 - H]) \quad 4.64$$

where η (Table 4.8) is temperature dependent and this dependence (Fig. 4.5) for humidity values of 68% or less can be expressed as:

$$\eta = -5.4(10^{-8}) \exp(Q_{\eta}/RT) = -5.4(10^{-8}) \exp(4560/T) \quad 4.65$$

where Q_{η} equals 9.1 Kcal/mole. The temperature and humidity dependence of I_{p0} is then:

$$\ln I_{p0} = -6 - 5.4(10^{-8}) [100 - H] \exp(4560/T) \quad 4.66$$

Equation 4.66 and Figure 4.24 both illustrate that I_{p0} is very temperature sensitive at low humidities and becomes less temperature sensitive as the humidity approaches 100% where it becomes temperature independent. These experimental observations are at variance with the expectations (Egs. 4.20 and 4.21) where I_{p0} was predicted to be temperature dependent and humidity insensitive.

The α_p power law coefficient as a function of humidity at various temperatures is shown in Figure 4.26 where it is apparent that no systematic pattern exists except for the general observation that α_p is relatively humidity insensitive at low temperatures and temperature insensitive at high humidities. The α_p coefficient was expected to be independent of the humidity (Eg. 4.19) and to be dependent on temperature (Eg. 4.18)

Since both I_{p0} and α_p are functions of temperature and humidity, the I_p absorption current will also be a function of temperature and humidity:

$$I_p = 2.5(10^{-3}) \exp([100 - H][- 54(10^{-8}) \exp(4560/T)]) t^{-\alpha_p} \quad 4.67$$

The remaining component contributing to the d.c. current response is the capacitive charging current, and its characterizing parameter is the time constant τ whose values at 68° and 53°C are presented in Tables 4.4 and 4.5. These values are plotted in Fig. 4.27, and τ appears to be temperature sensitive but not necessary humidity dependent. Since τ is expected to be the product of R_0 and C:

$$\tau = R_0 C$$

and since R_0 was found to decrease with humidity (Eq. 4.51) while C was found to increase with humidity (Eq. 4.3); the time constant can be relatively humidity independent as is evident at 68°C (Fig. 4.27) but not evident at 53°C. Equations 4.3 and 4.51 show that R_0 increases with temperature while C is not a function of temperature so the time constant is expected to increase with temperature. This expected behavior is not confirmed in Figure 4.27. These inconsistencies between the measured time constants and the expected time constants determined from the $R_0 C$ product is illustrated quantitatively in Table 4.9 where the measured time constants are orders of magnitude larger than the calculated time constants. One possible reason for this discrepancy between measured and calculated values is that the equivalent electrical circuit for the PVB specimens is not simple resistance--capacitance series circuit but a more complex lumped circuit as illustrated in Figure 4.28, and as discussed in the following section on a.c. properties.

a.c. Properties

Experimentally, the capacitance was found to be sensitive to humidity. This result is expected since the amount of water absorbed in the sample is related to the humidity and water has a large dielectric constant (K_w) where:

$$k_w \cong 85$$

4.68

Since the dielectric constant (K_p) of PVB is about 4 ,

$$k_p \cong 4$$

the dielectric constant (K_{w-p}) of the PVB-water two phase composite system should increase with increasing amount of water in the PVB, assuming that the two phase system behaves like two capacitors in parallel. Since K_{w-p} increases with water content, the capacitance should increase with humidity as is observed experimentally.

Experimentally, the $\tan \delta$ loss factor was found to be strongly dependent on both temperature and humidity. This result is consistent with the observed and expected result that the electrical resistance is a strong function of temperature and humidity. Table 4.2 summarizes the temperature and humidity dependence of both the d.c. and a.c. properties that were investigated in this research activity.

The d.c. and a.c. data can be used to represent the PVB dielectric by a lumped equivalent circuit involving capacitive and resistive elements. The presence of the exponential transient in the d.c. current response characteristics suggests that the equivalent circuit is composed of a capacitor (C_{eq}) and resistor (R_{eq}) in series (Fig. 4.28 a) while the humidity dependence of the capacitance suggests that the equivalent circuit

capacitor is a parallel combination (Fig. 4.28b) of a capacitance (C_w) associated with the water impurity and a capacitance (C_p) associated with the PVB. The lumped equivalent circuit should then be the parallel capacitor combination in series with the resistance as shown in Figure 4.28 c. The frequency dependence of the capacitance at high humidity values (Fig. 4.11) is consistent with this circuit representation. The frequency dependence of both the capacitance at low humidity levels and the $\tan \delta$ loss factor (Fig. 4.11) is not consistent with this representation but is consistent with a parallel arrangement of capacitors and resistors (Fig. 4.28 d). These results demonstrate that a simple combination of resistors and capacitors in series or in parallel cannot be adequately used as an equivalent circuit representation of the PVB dielectric. A more complex arrangement of capacitors and resistors might be an appropriate lumped equivalent circuit where different arrangements may be appropriate at different values of temperature and humidity. Unfortunately, the experimental data is not extensive enough to allow for a determination of these possible equivalent circuits.

TABLE 4.1

Slope (m) and intercept (b) values of the humidity dependence of $\tan \delta$ where $\tan \delta = mH + b$ (Eq 4.4)

Temp (°C)	m -1 (%)	b
68	.0034	0
53	.0027	20
25	.0017	30

TABLE 4.2

PVB: Temperature and humidity dependencies of a.c. and d.c. electrical properties

$$C = 170 H + 200$$

$$C \neq f_{ct}(T)$$

$$\tan \delta = .32 H \exp(-1500/T) - .56 T + 356$$

$$R_o = 1.2(10^{-6}) [\exp(12000/T - .115 H)]$$

$$R_i = 8.6 [\exp(7000/T - .09 H)]$$

$$I_{\omega_o} = 10^{-8} [\exp(.127 H)]$$

$$I_{\omega_o} \neq f_{ct}(T)$$

$$\alpha_{\omega} = -.011 H - .022 T$$

$$I_{\omega} = 10^{-8} [\exp(0.127 H)] t^{-.011 H - .022 T + 9.3}$$

$$I_{p_o} = 25(10^{-3}) \exp([-.54(10^{-8})][100-H][\exp(4560/T)])$$

$$\alpha_p = f_{ct}(T)^* \quad \text{only at low humidities}$$

$$\alpha_p = f_{ct}(H)^* \quad \text{only at high temperatures}$$

$$\gamma \neq f_{ct}(H) \quad \text{at } 68^\circ\text{C}$$

$$\gamma = f_{ct}(T)^*$$

* - unable to evaluate functional form

TABLE 4.3

D.C. Current response characteristics of PVB at 80°C					
Relative Humidity (%)	Current Component (amps)	α	τ (min)	R_o (Ω)	R_i (Ω)
92	$I_{w0} = 1.2 (10^{-3})$ $I_i = 1.7 (10^{-4})$	$\alpha_w = .43$		$3(10^5)$	$2(10^6)$
77	$I_{w0} = 1.5 (10^{-4})$ $I_{p0} = 4.1 (10^{-5})$ $I_i = 2.5 (10^{-5})$	$\alpha_w = .78$ $\alpha_p = .23$		$2(10^6)$	$1.5(10^7)$
64	$I_{w0} = 4 (10^{-5})$ $I_{p0} = 4.6 (10^{-5})$ $I_i = 4 (10^{-6})$	$\alpha_w = .85$ $\alpha_p = .52$		$4(10^6)$	$1(10^8)$
30	$I_{c0} = 3.2 (10^{-5})$ $I_{p0} = 5 (10^{-5})$ $I_i = 7 (10^{-6})$	$\alpha_p = .52$	41	$7(10^7)$	$6(10^7)$

TABLE 4.4

D.C. response characteristics of PVB at 68°C

Relative Humidity (%)	Current Components (amps)	α	τ (min)	R_o (Ω)	R_i (Ω)
95	$I_{w0} = 2(10^{-3})$ $I_i = 2(10^{-4})$	$\alpha_w = .56$		$2(10^5)$	$1.9(10^6)$
79	$I_{c0} = 1.1(10^{-4})$ $I_{w0} = 1(10^{-4})$ $I_{p0} = 2(10^{-5})$ $I_i = 1.5(10^{-5})$	$\alpha_w = 1.0$ $\alpha_p = .17$	2.9	$2.8(10^6)$	$2.6(10^7)$
67	$I_{c0} = 4.2(10^{-5})$ $I_{w0} = 3(10^{-5})$ $I_{p0} = 5(10^{-6})$ $I_i = 3(10^{-6})$	$\alpha_w = 1.1$ $\alpha_p = .19$	2.4	$9(10^6)$	$1.3(10^8)$
46	$I_{c0} = 1.4(10^{-5})$ $I_{wp} = 5(10^{-6})$ $I_{p0} = 4(10^{-6})$ $I_i = 8(10^{-7})$	$\alpha_w = .72$ $\alpha_p = .36$	1.9	$2.8(10^7)$	$4.9(10^8)$
28	$I_{c0} = 4.2(10^{-6})$ $I_{p0} = 2(10^{-6})$ $I_i = 4(10^{-7})$	$\alpha_p = .45$	1.2	$9.2(10^7)$	$9.8(10^8)$

TABLE 4.5

D.C. current response characteristics of PVB at 53°C

Relative Humidity (%)	Current Components (amps)	α_p	τ (min)	R_o (Ω)	R_i (Ω)
84	$I_{co} = 5(10^{-5})$ $I_{wo} = 8(10^{-5})$ $I_{po} = 1(10^{-5})$ $I_i = 1(10^{-5})$	 $.5 (= \alpha_w)$ $.18$	15	$8(10^6)$	$4(10^7)$
48	$I_{co} = 7(10^{-7})$ $I_{po} = 7(10^{-7})$ $I_i = 4(10^{-7})$	$.20$	46	$5(10^8)$	$1(10^9)$
41	$I_{co} = 4(10^{-7})$ $I_{po} = 3(10^{-7})$ $I_i = 2(10^{-7})$	$.18$	30	$1(10^9)$	$2(10^9)$
30	$I_{co} = 2(10^{-7})$ $I_{po} = 9(10^{-8})$ $I_i = 1.3(10^{-7})$	$.13$	46	$2(10^9)$	$3(10^9)$
25	$I_{po} = 6(10^{-8})$ $I_i = 1(10^{-7})$	$.10$		$2(10^9)$	$4(10^9)$
16	$I_{po} = 4(10^{-8})$ $I_i = 7(10^{-8})$	$.08$		$3(10^9)$	$6(10^9)$

TABLE 4.6

D.C. current response characteristics of PVB at 42°C

Relative Humidity (%)	Current Components (amps)	α_p	R_o (Ω)	R_i (Ω)
82	$I_{p0} = 8(10^{-5})$ $I_i = 6(10^{-5})$.07	$5(10^6)$	$6.5(10^6)$
67	$I_{p0} = 8(10^{-6})$ $I_i = 6(10^{-6})$.05	$5(10^7)$	$6.5(10^7)$

TABLE 4.7

D.C. current response characteristics of PVB at 26°C

Relative Humidity (%)	Current Components (amps)	α_p	R_o (Ω)	R_i (Ω)
100	$I_{p0} = 7(10^{-6})$ $I_j = 6(10^{-6})$.05	$6(10^8)$	$7(10^8)$
64	$I_{p0} = 2(10^{-7})$ $I_j = 2(10^{-7})$.02	$2(10^9)$	$2(10^9)$
51	$I_{p0} = 5(10^{-8})$ $I_j = 5(10^{-8})$.01	$8(10^9)$	$8(10^9)$
45	$I_{p0} = 3(10^{-8})$ $I_j = 3(10^{-8})$.01	$1(10^{10})$	$1(10^{10})$

TABLE 4.8

Characteristics parameter for the humidity dependence of the initial resistance (R_0), the final resistance (R_i) and the polymer absorption current I_{p0} , at various temperatures.

<u>Temp. (°C)</u>	<u>$R_0 = A e^{-\beta H}$</u>		<u>$R_i = B e^{-\gamma H}$</u>		<u>$I_{p0} \sim e^{\eta[100-H]}$</u>
	<u>β (%)</u>	<u>$A(\Omega)$</u>	<u>γ (%)</u>	<u>$B(\Omega)$</u>	<u>η (°⁻¹)</u>
80	.115	1(10 ⁹)	.135	-----	+0.020
68	.104	3.5(10 ⁹)	.092	1.5(10 ¹⁰)	-0.032
53	.115	3(10 ¹⁰)	.088	3(10 ¹⁰)	-0.075
25	.144	3(10 ¹¹)	.092	3(10 ¹¹)	-0.230

TABLE 4.9

Comparison of measured and calculated ($\tau = R_o C$) time constants

Temperature/Humidity <u>(°C/%)</u>	τ Measured <u>(min.)</u>	τ Calculated <u>(min.)</u>
53/100	16	$6.5(10^{-6})$
53/84	15	$5.4(10^{-5})$
53/48	46	$2.7(10^{-3})$
53/41	30	$4.3(10^{-3})$
53/30	46	$8.3(10^{-3})$
68/79	2.9	$2.0(10^{-5})$
68/67	2.4	$1.1(10^{-4})$
68/46	1.9	$2.5(10^{-4})$
68/28	1.1	$8.6(10^{-4})$

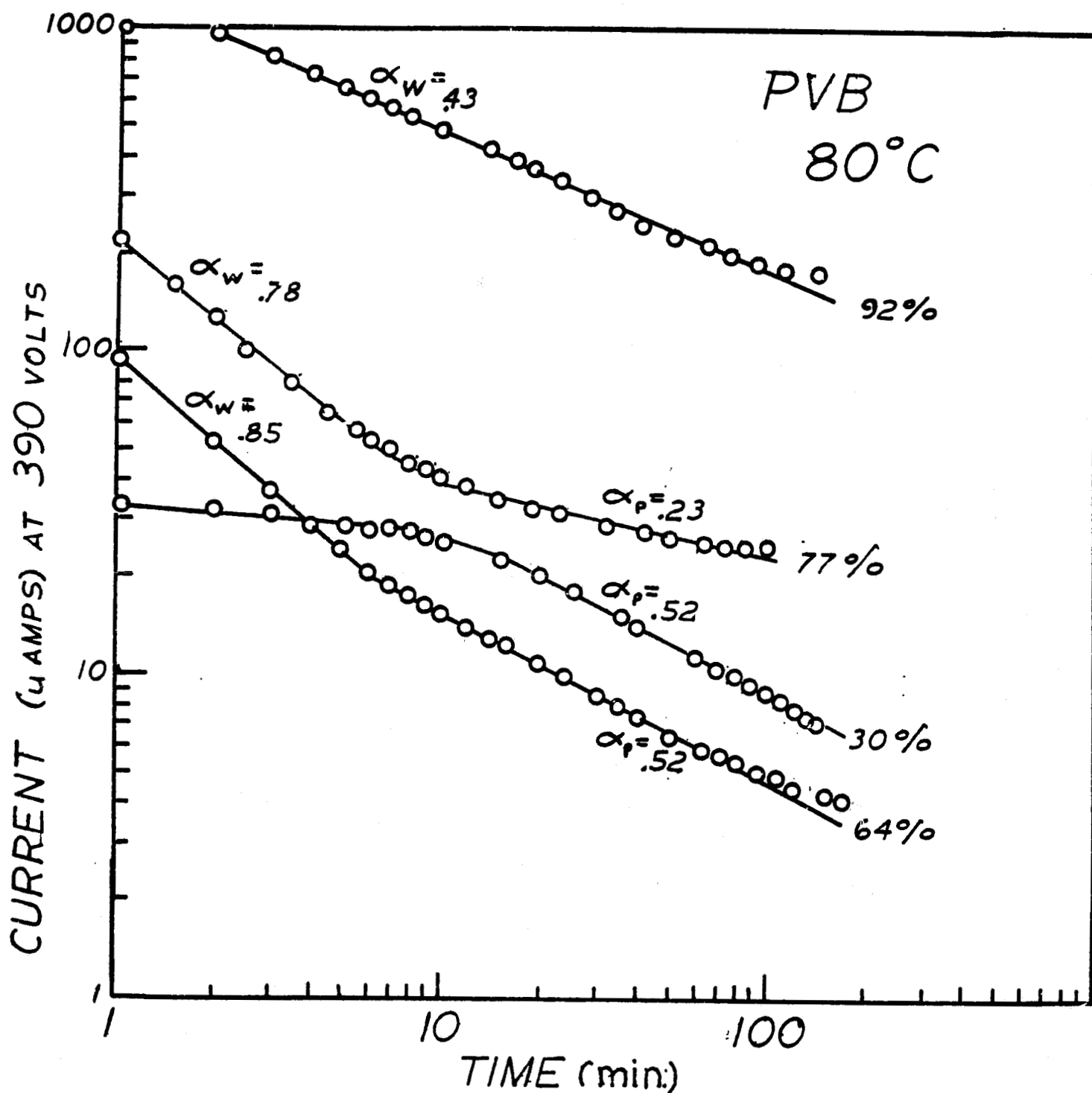


Fig. 4.1-Time dependence of the d.c. response current resulting from a 390 volt step forcing function applied to PVB at 80°C and various relative humidity levels.

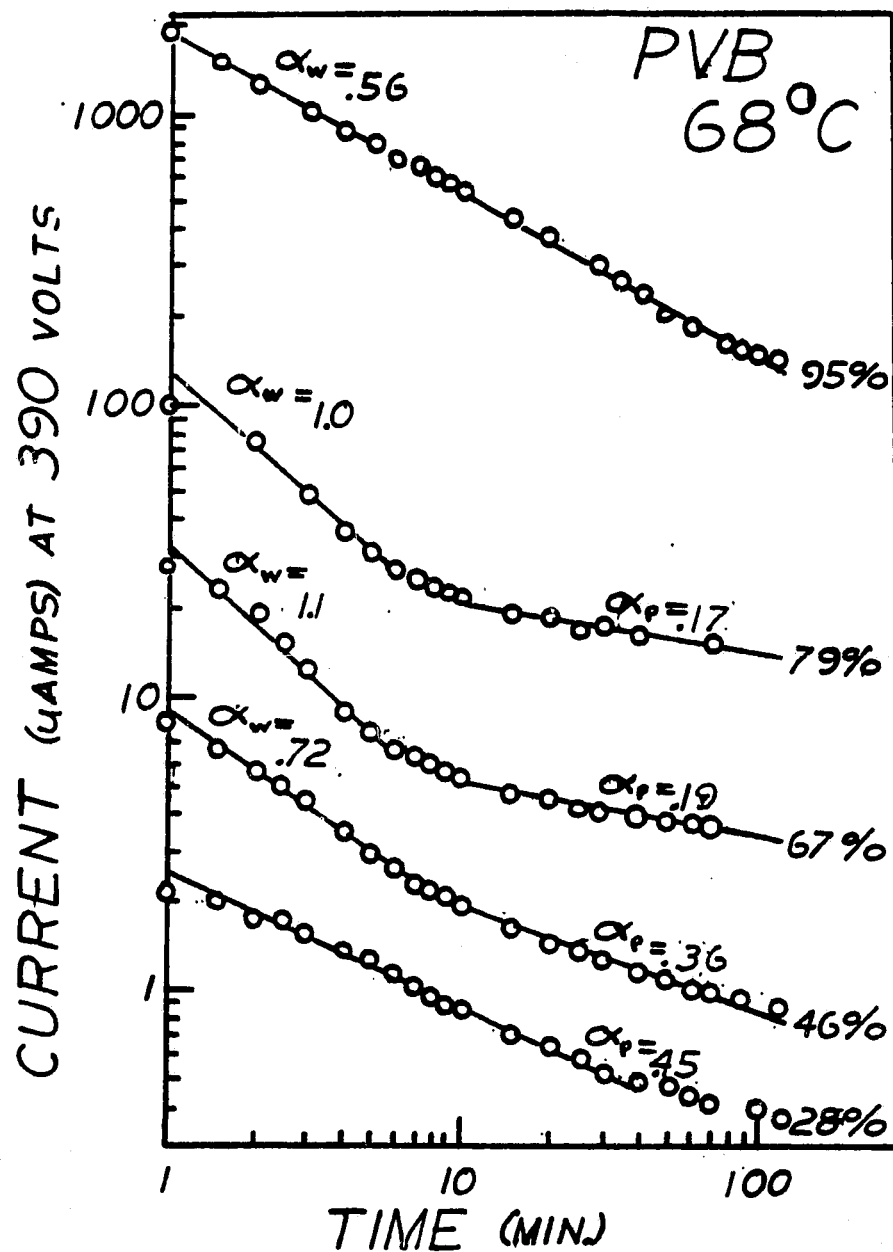


Fig. 4.2-Time dependence of the d.c. response current resulting from a 390 volt step forcing function applied to PVB at 68°C and various relative humidity levels.

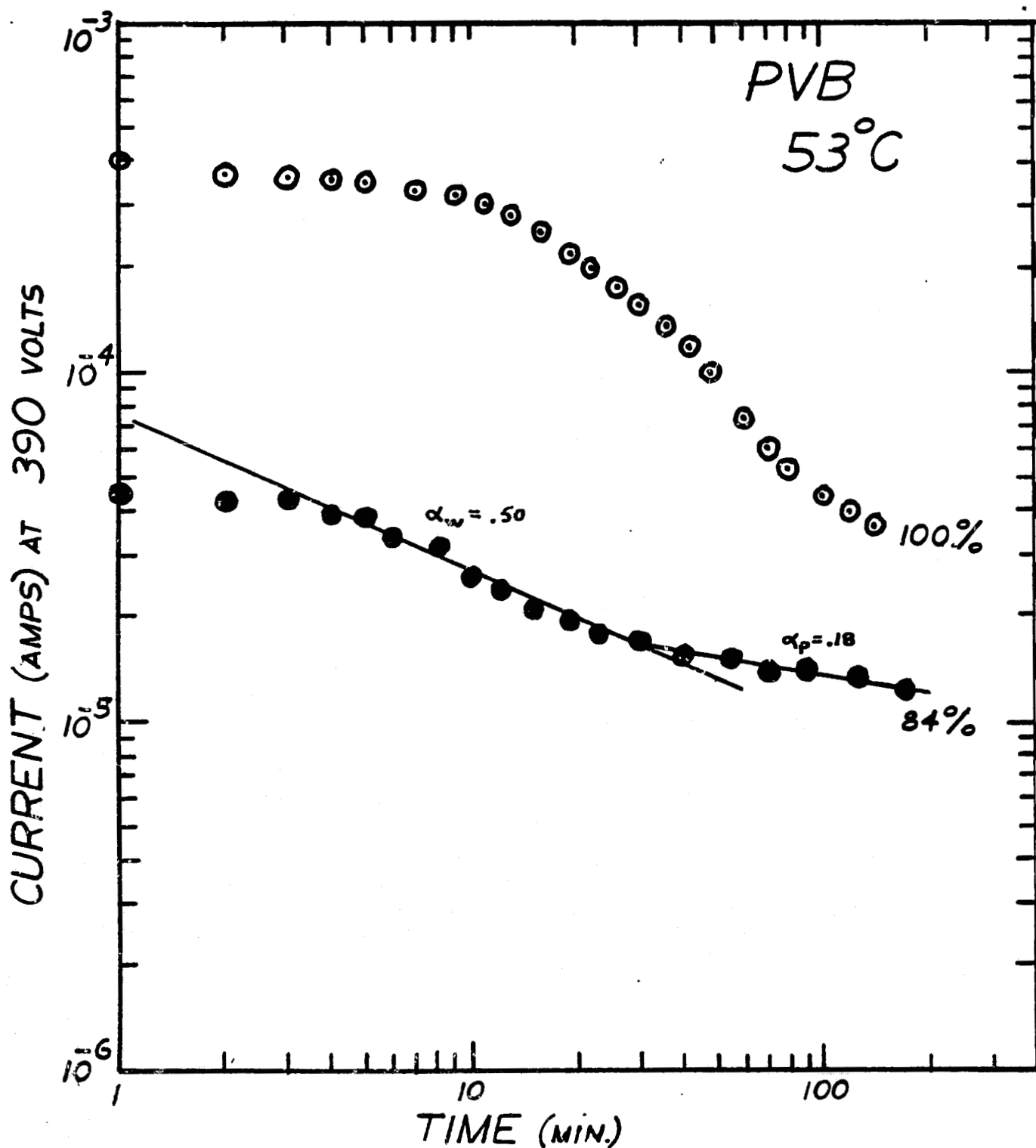


Fig 4.3-Time dependence of the d.c. response current resulting from a 390 volt stop forcing function applied to PVB at 53°C and various relative humidity levels.

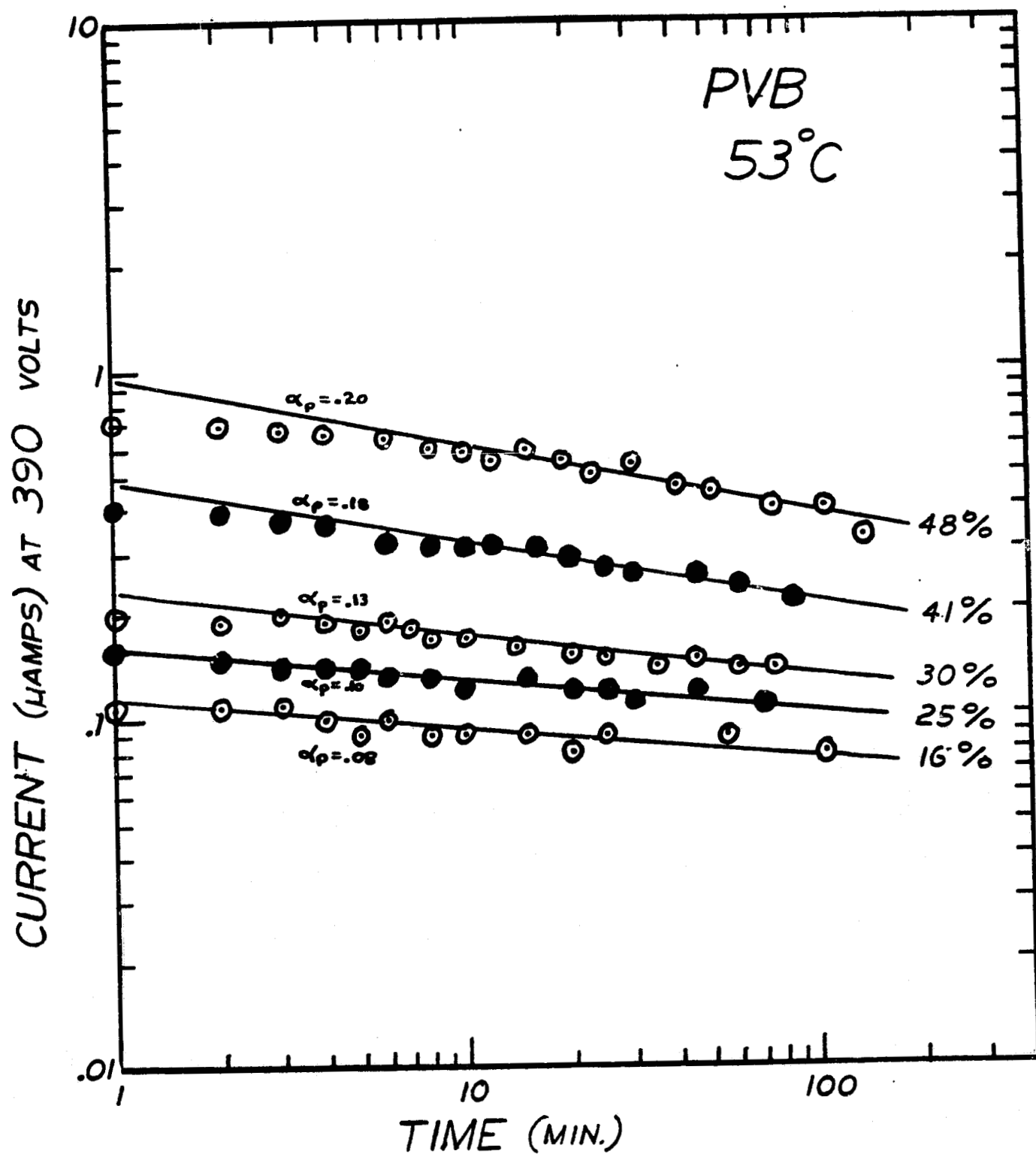


Fig 4.4 - Time dependence of the d.c. response current resulting from a 390 volt step forcing function applied to PVB at 53°C and various relative humidity levels.

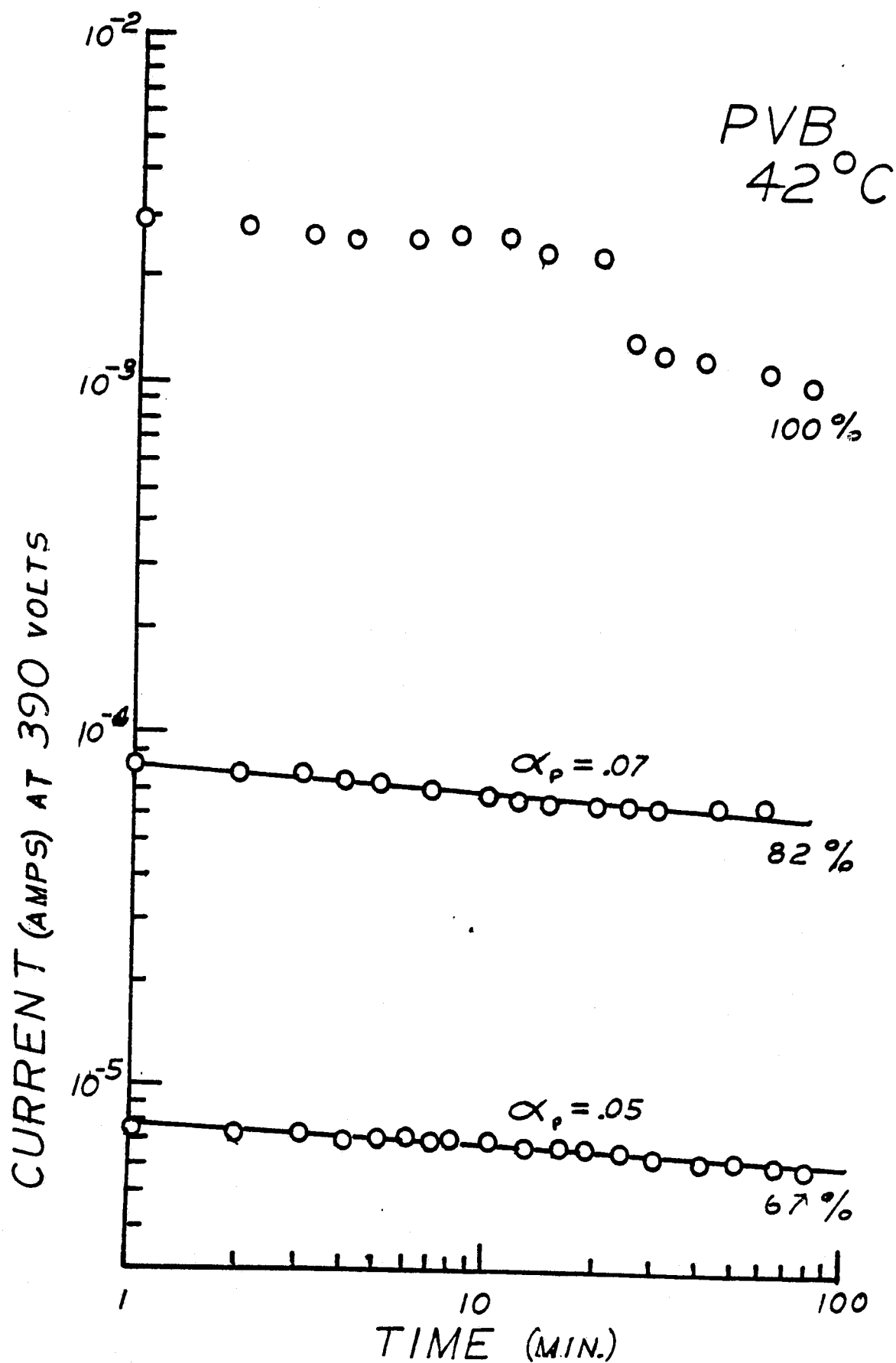


Fig. 4.5--Time dependence of the d.c. current response resulting from a 390 volt step function applied to PVB at 42°C and various relative humidity levels.

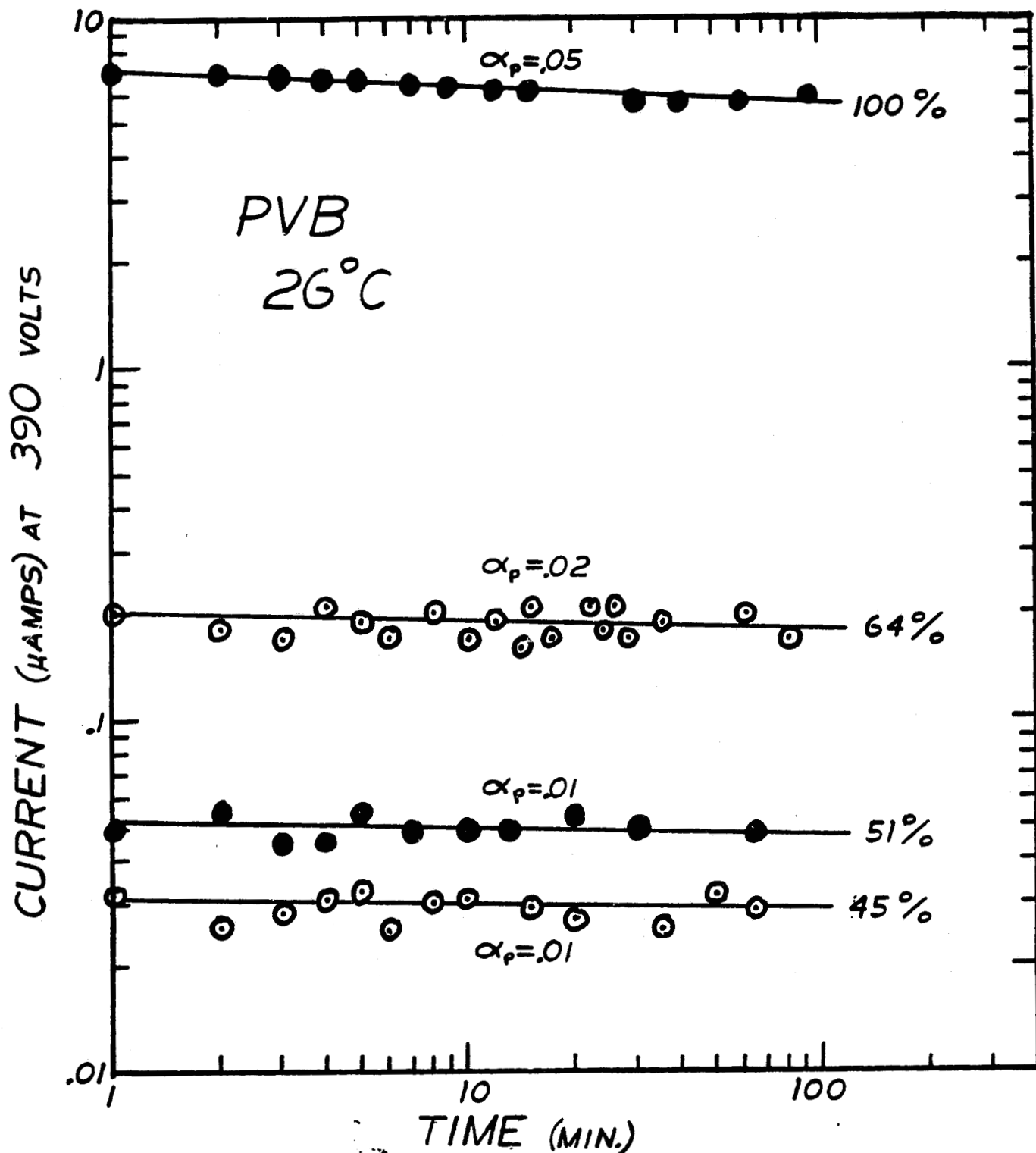


Fig. 4.6-Time dependence of the d.c. response current resulting from a 390 volt step forcing function applied to PVB at 26°C and various relative humidity levels.

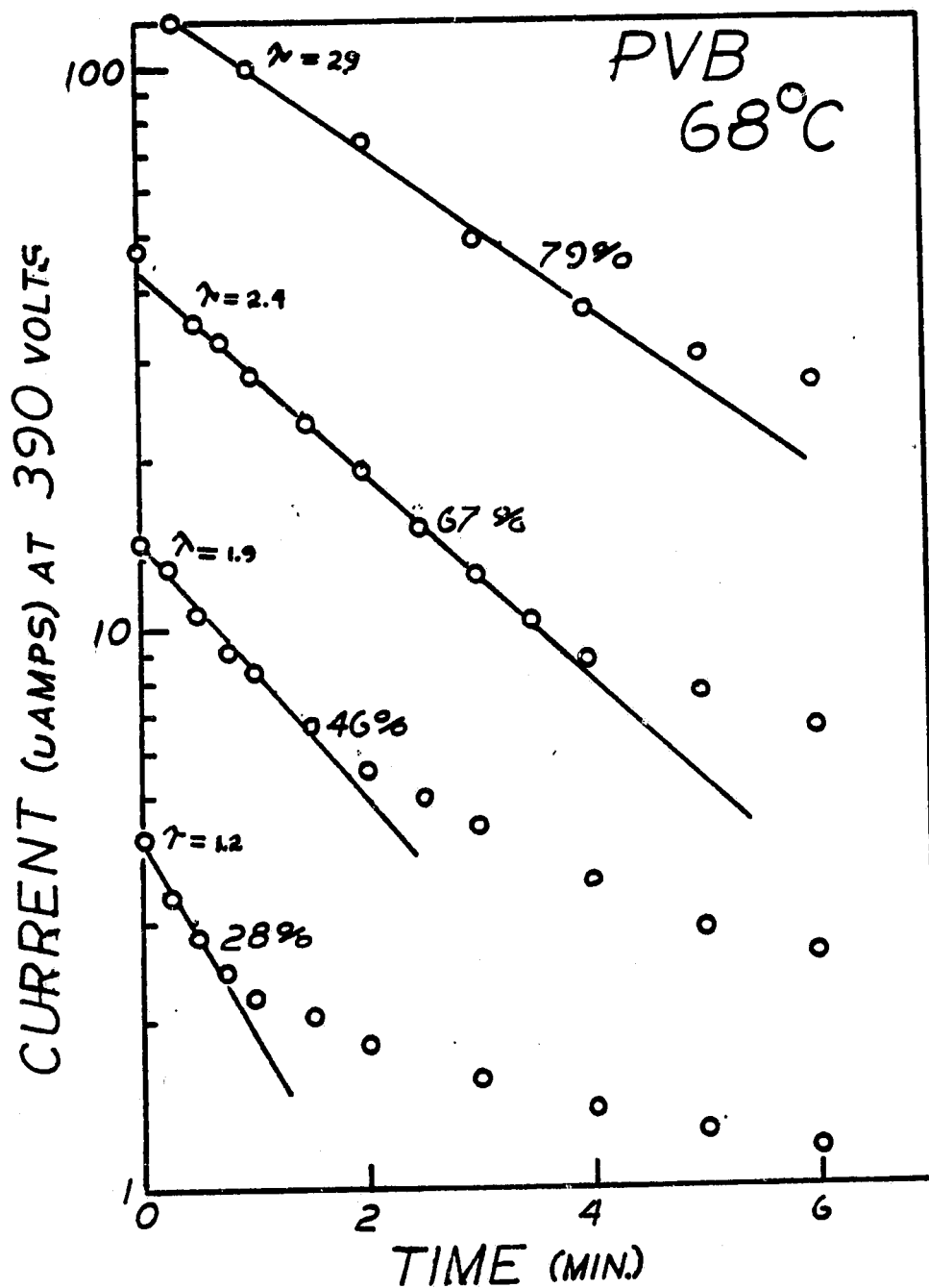


Fig. 4.7-Initial transient behavior for the d.c. current response data shown in Figure 4.2

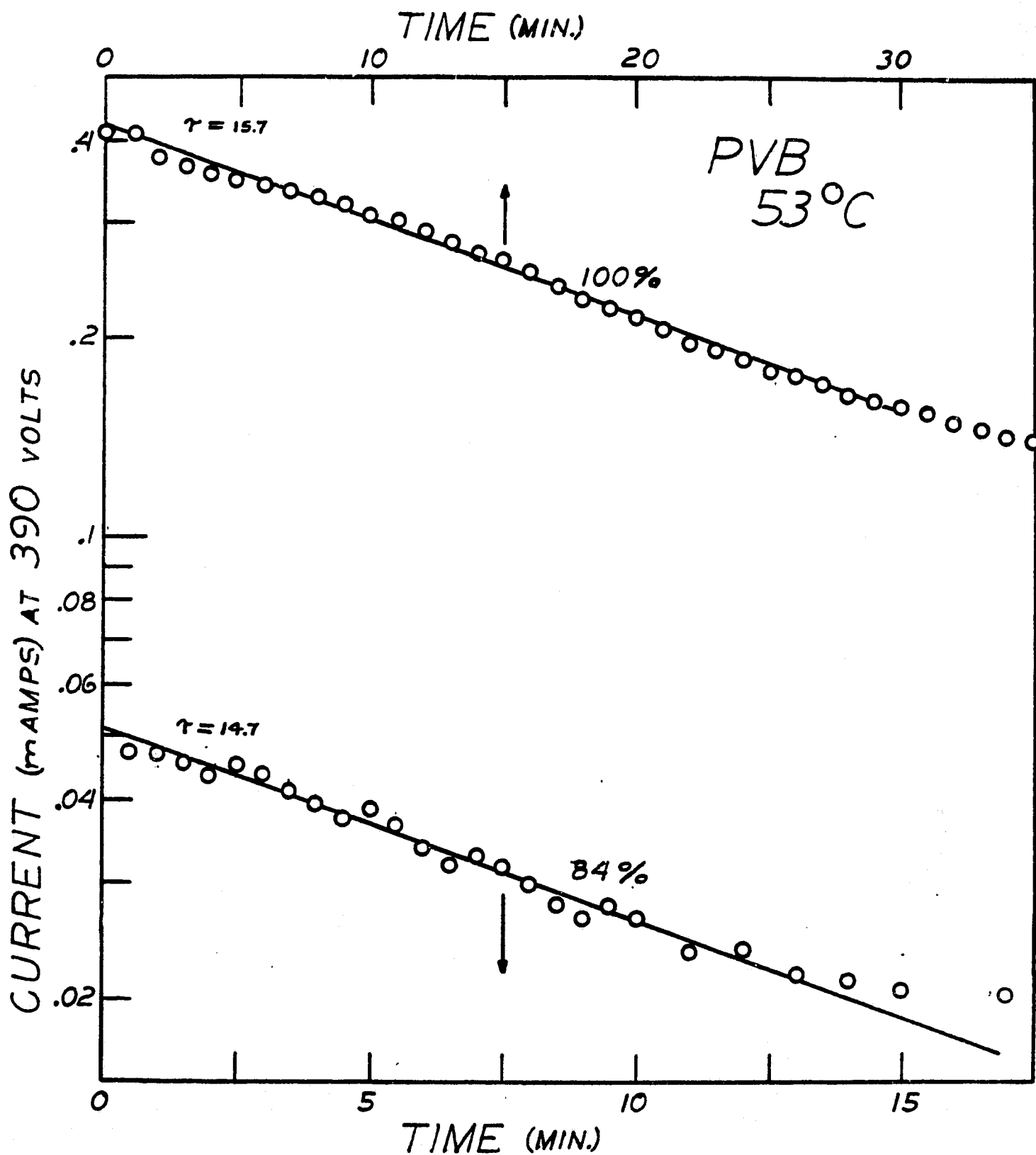


Fig 4.8-Initial transient behavior for the d.c. current response data shown in Figure 4.3.

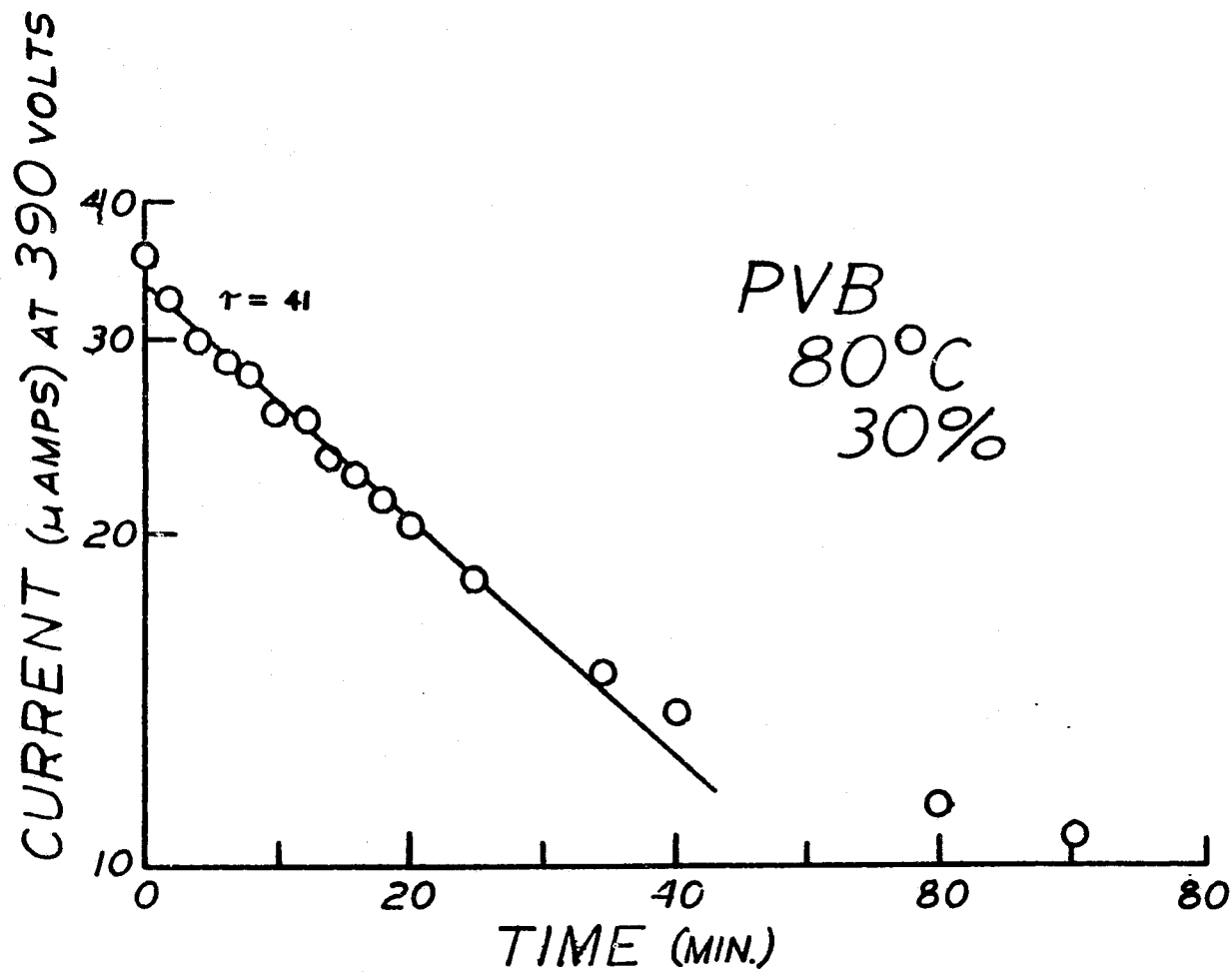


Fig 4.9-Initial transient behavior for the d.c. current response data at 30% relative humidity shown in Figure 4.1.

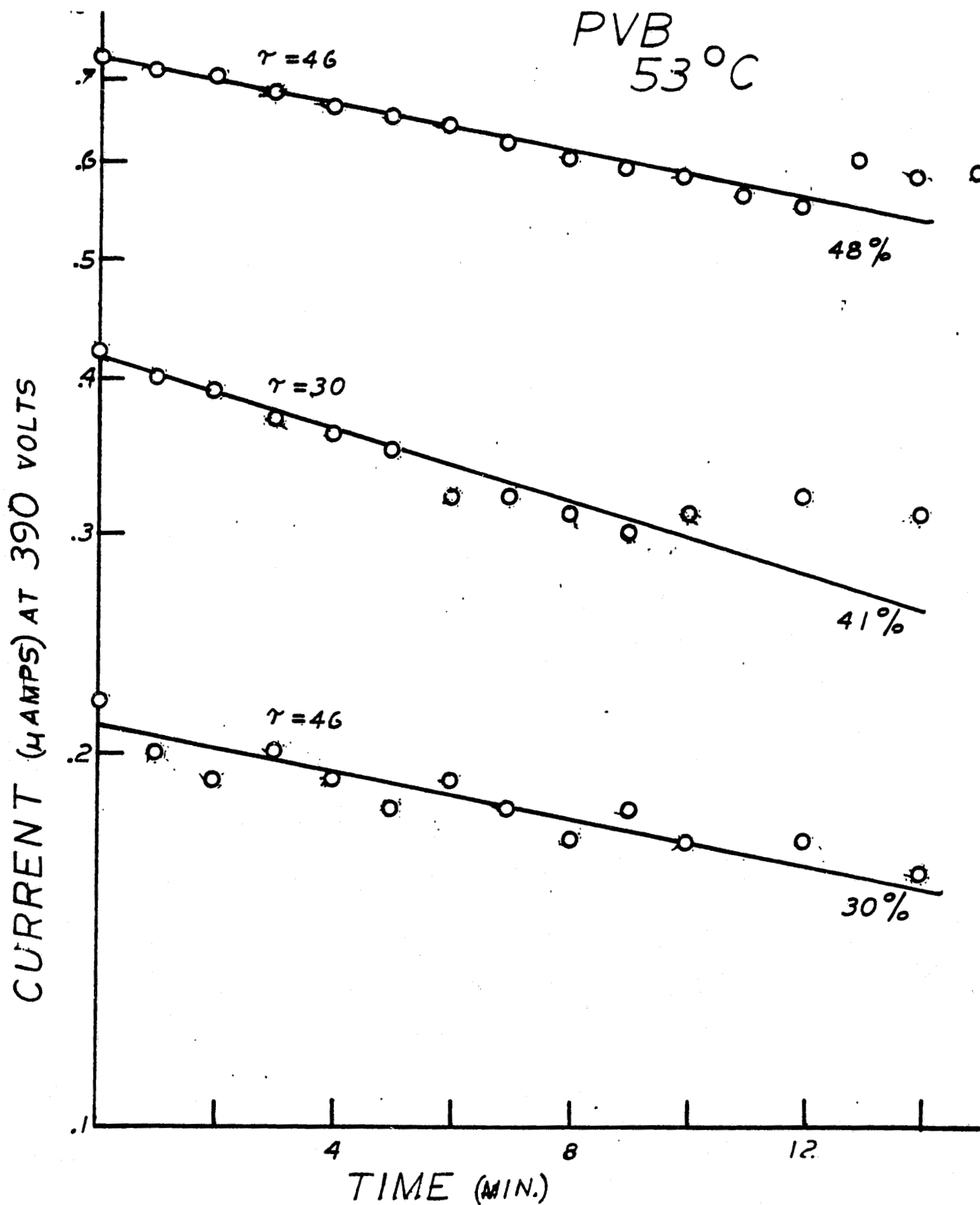


Fig 4.10-Initial transient behavior of the d.c. current response data shown in figure 4.4.

PVB

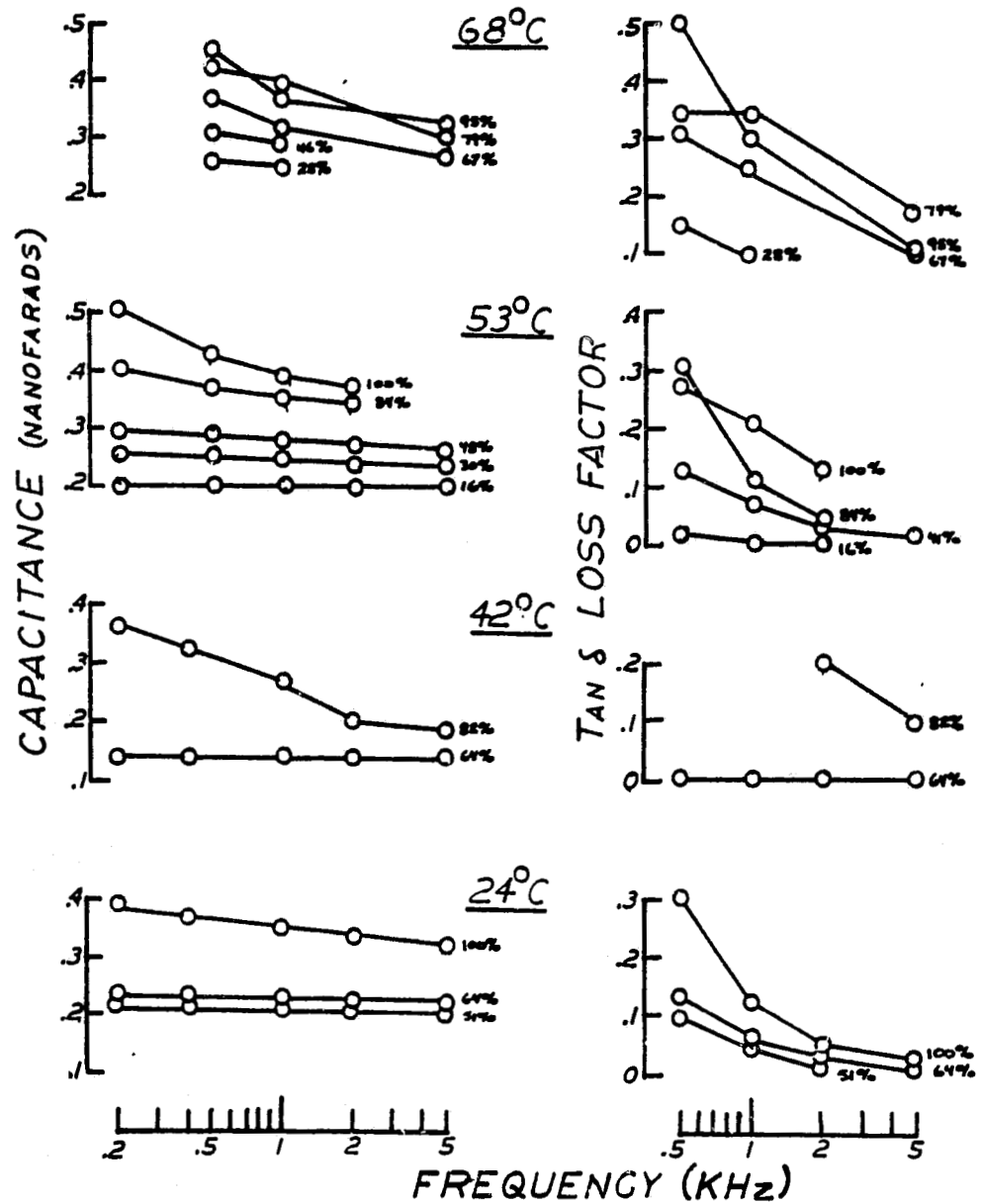


Fig. 4.11-Capacitance and $\tan \delta$ dissipation factor as a function of frequency for PVB at 68°C for various values of the relative humidity.

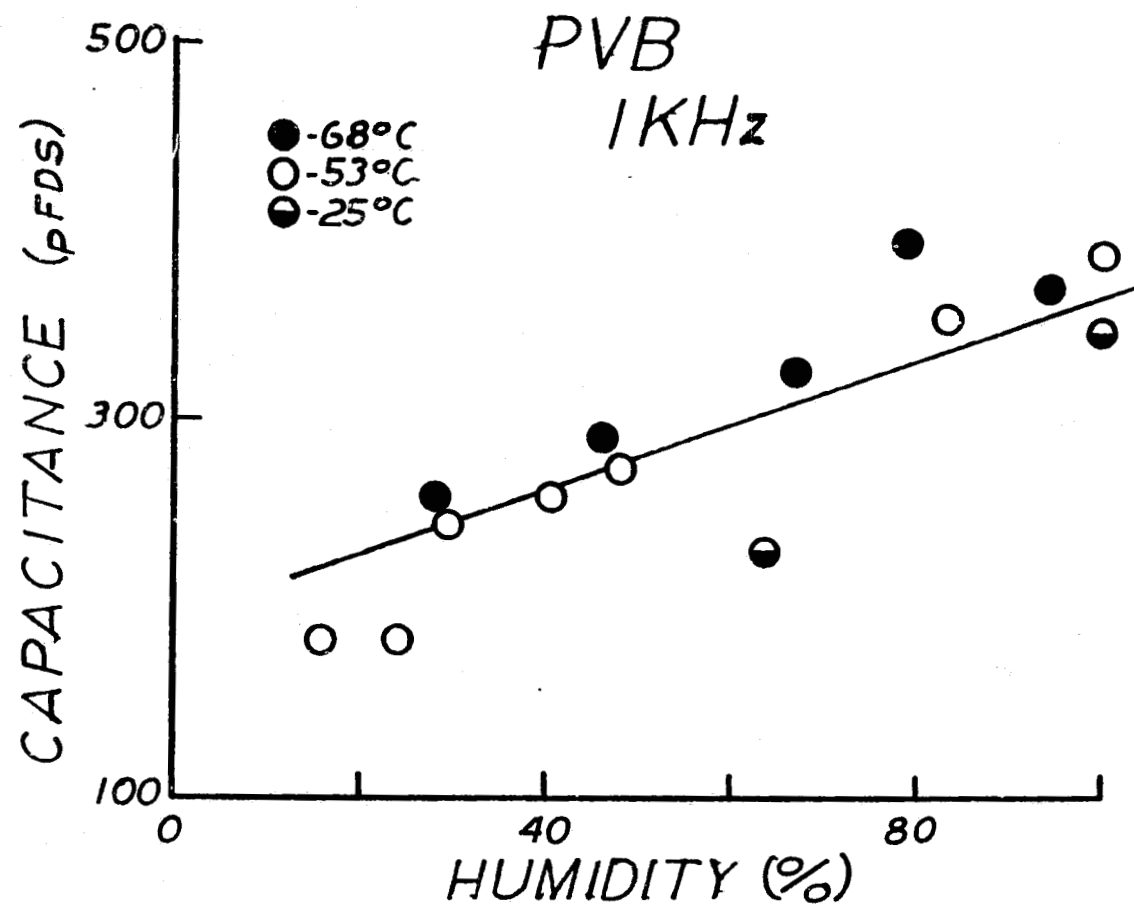


Fig. 4.12-The a.c. (1KHz) capacitance of PVB as a function of humidity at various temperatures.

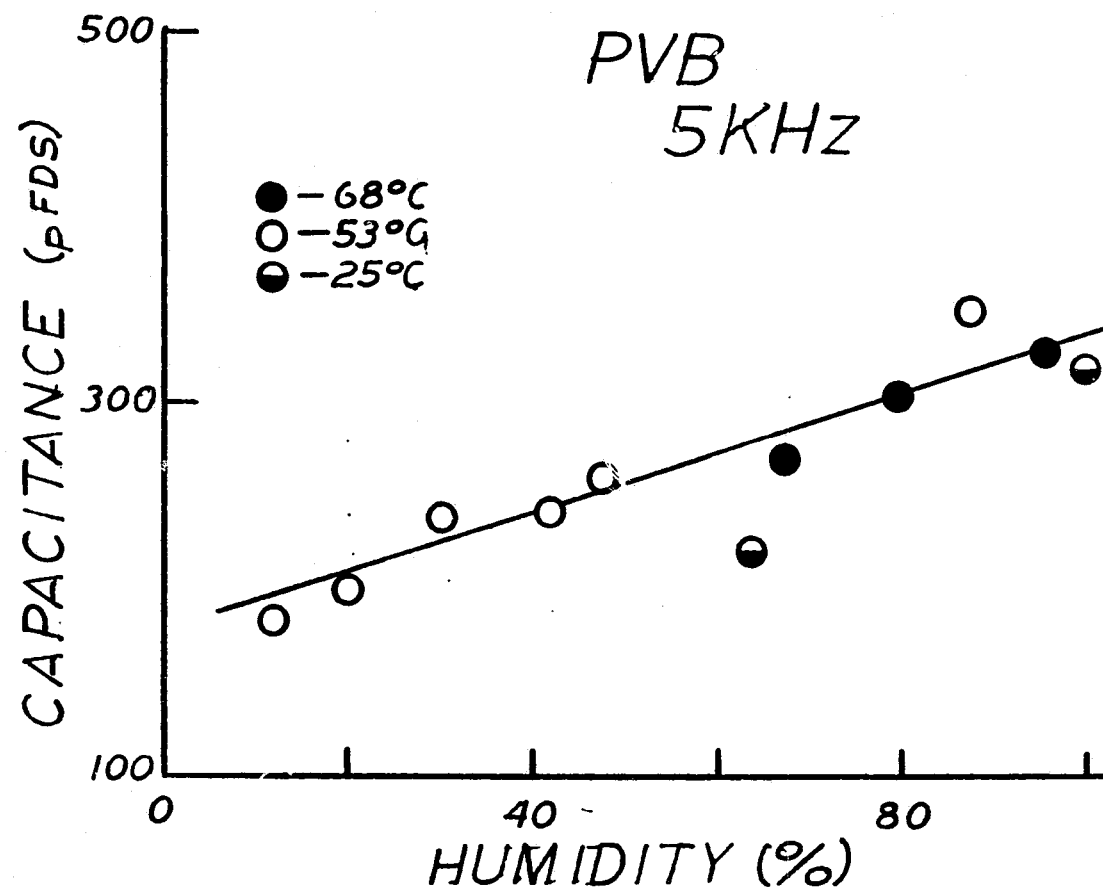


Fig 4.13-The a.c. (5KHz) capacitance of PVB as a function of humidity at various temperatures.

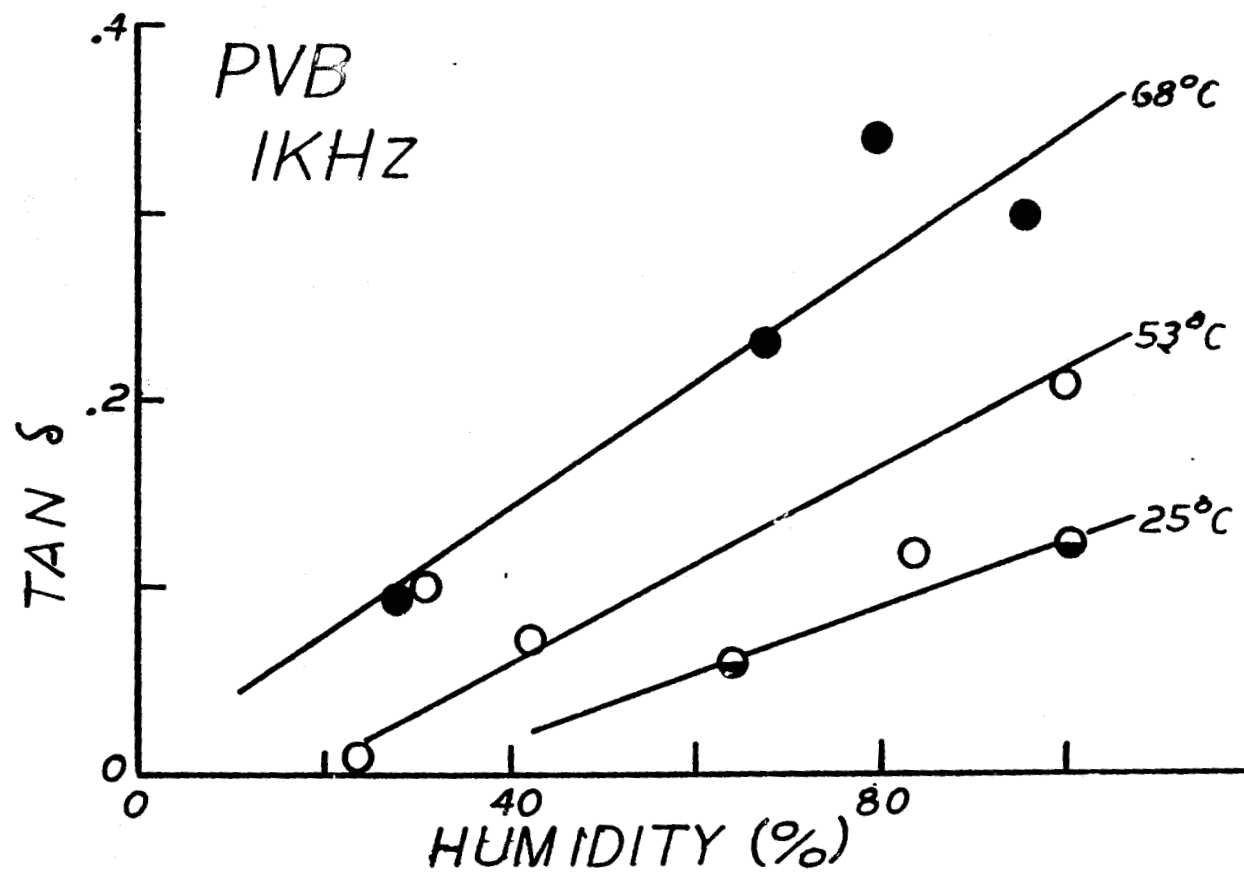


Fig. 4.14-The humidity dependence of the loss factor in PVB at various temperatures.

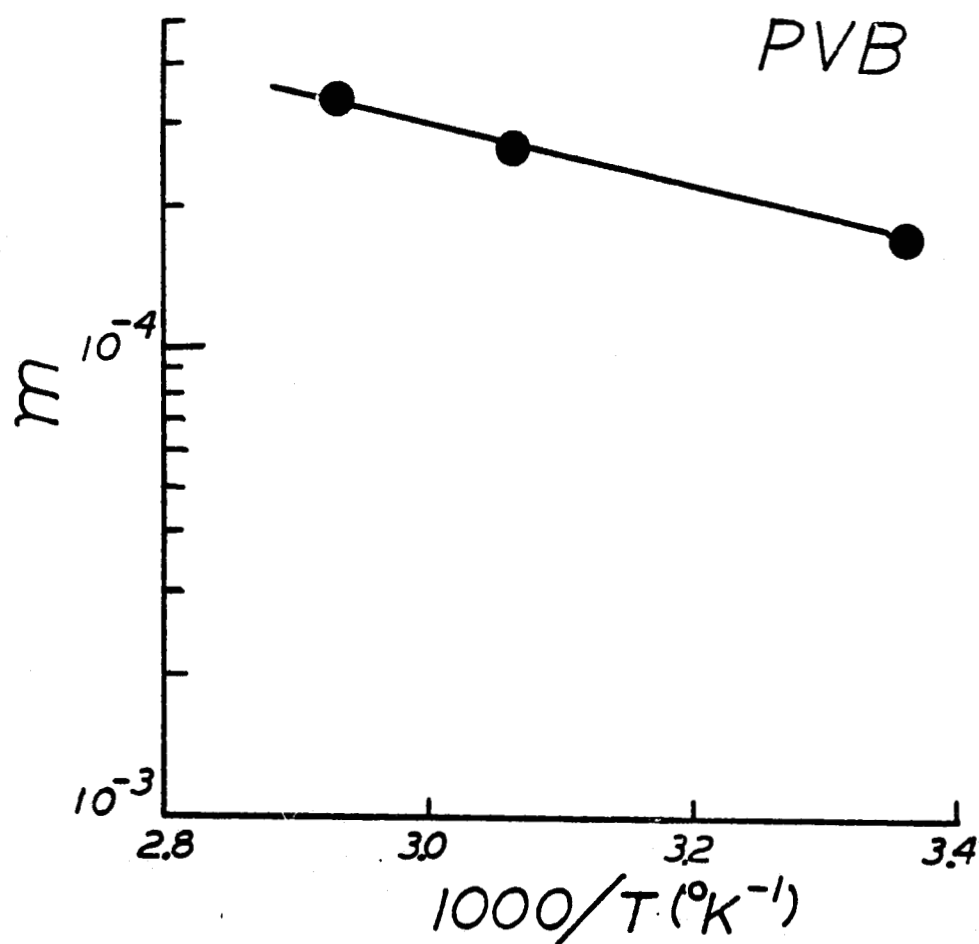


Fig. 4.15-Temperature dependence of the coefficient in Equation 4.4 for the loss factor.

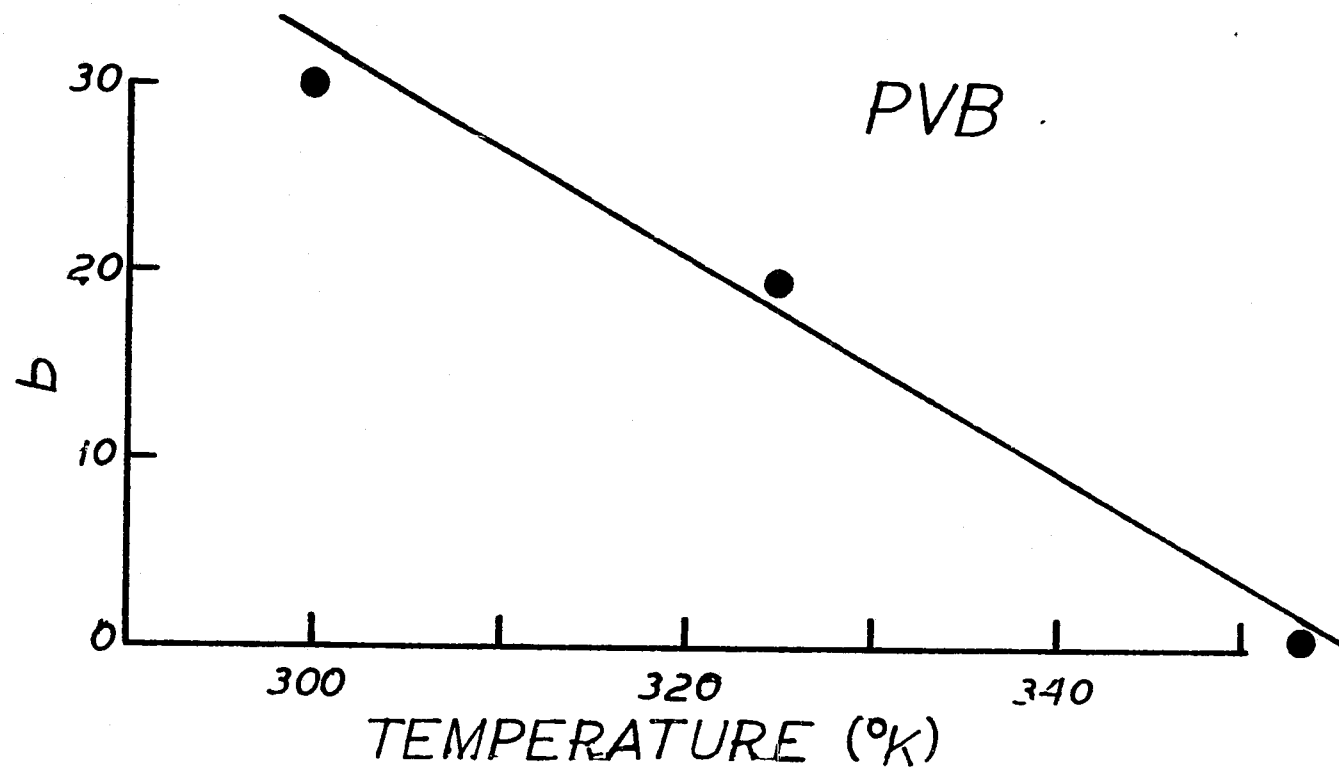


Fig. 4.16-Temperature dependence of the b constant in Equation 4.4 for the loss factor in PVB.

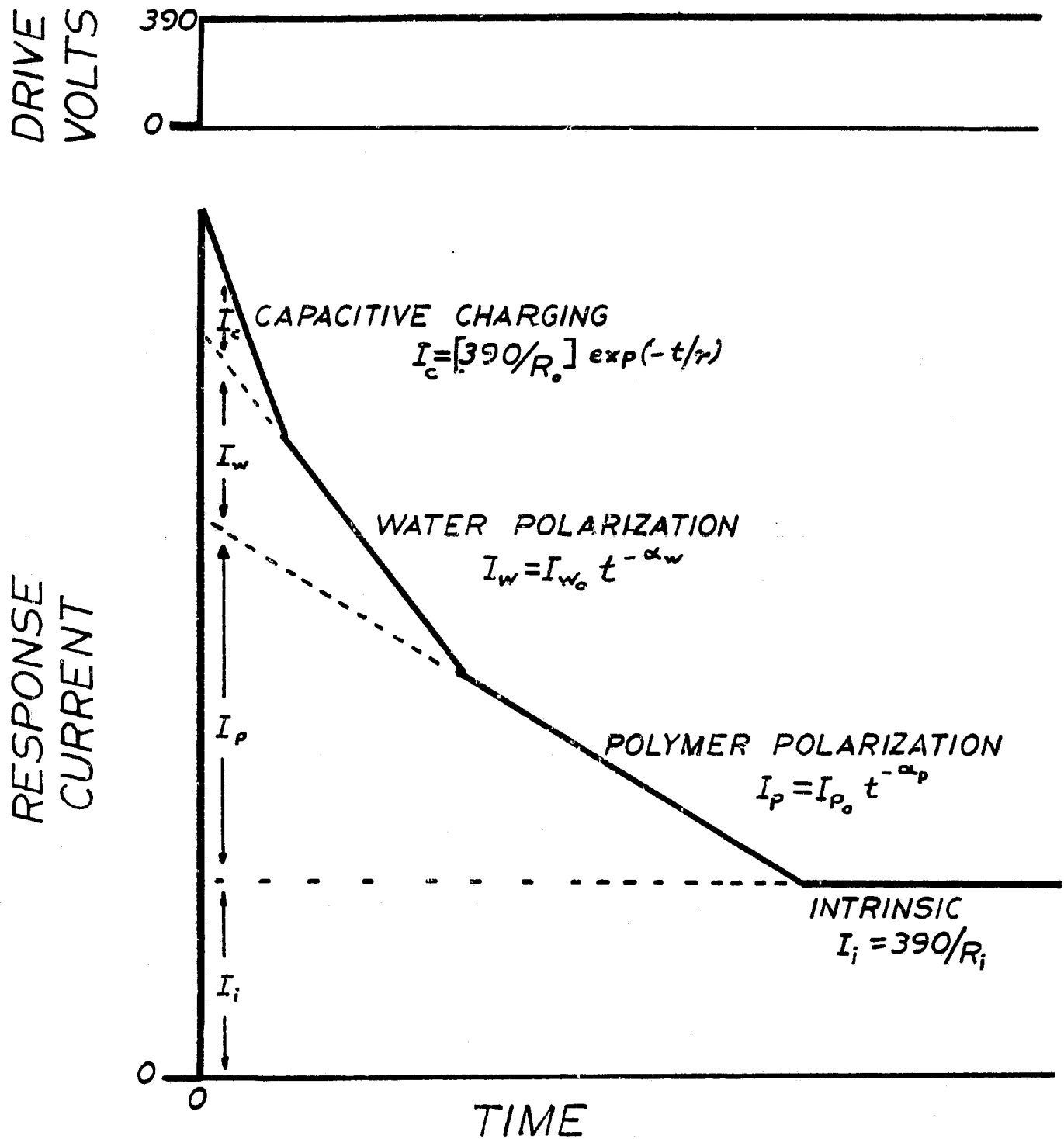


Fig. 4.17-Proposed current response mechanisms and associated time dependencies in a water absorbing polymer when subjected to a 390 d.c. voltage step forcing function.

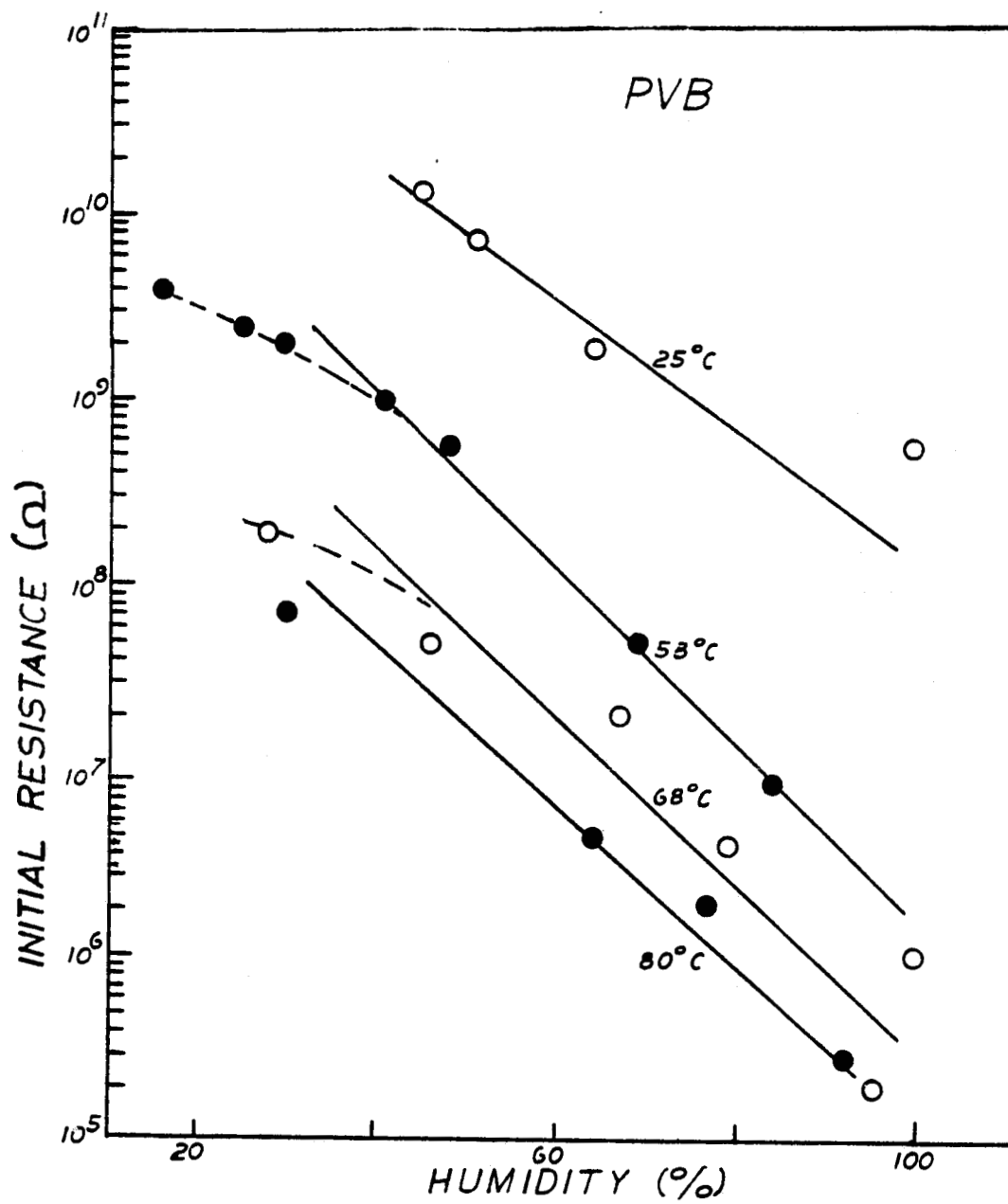


Fig. 4.18 - Initial resistance as a function of humidity for PVB at selected temperatures.

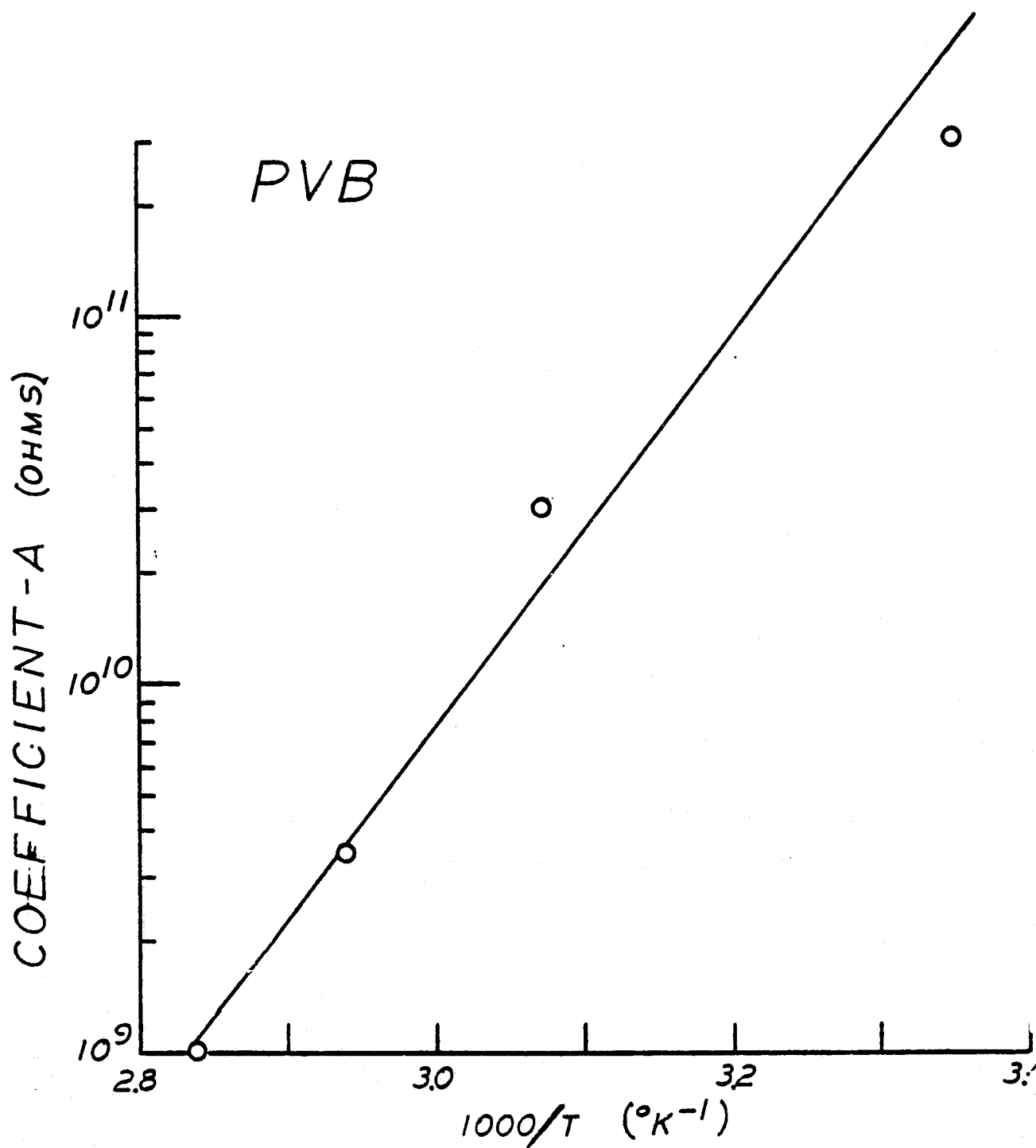


Fig. 4.19-Temperature dependence of the coefficient A in Equation 4.45 for characterizing the initial resistance of PVB.

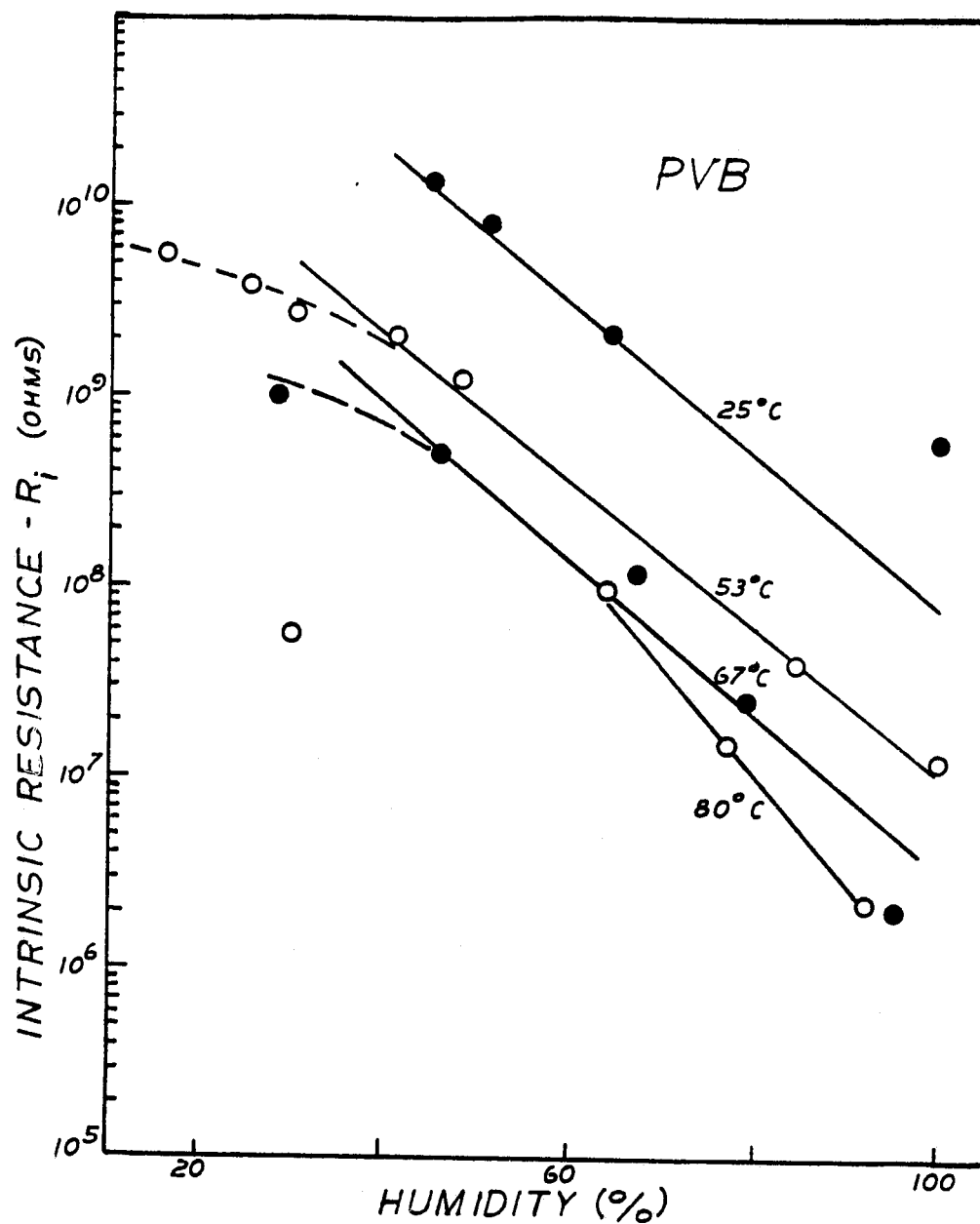


Fig. 4.20 - Intrinsic resistance as a function of humidity for PVB at selected temperatures.

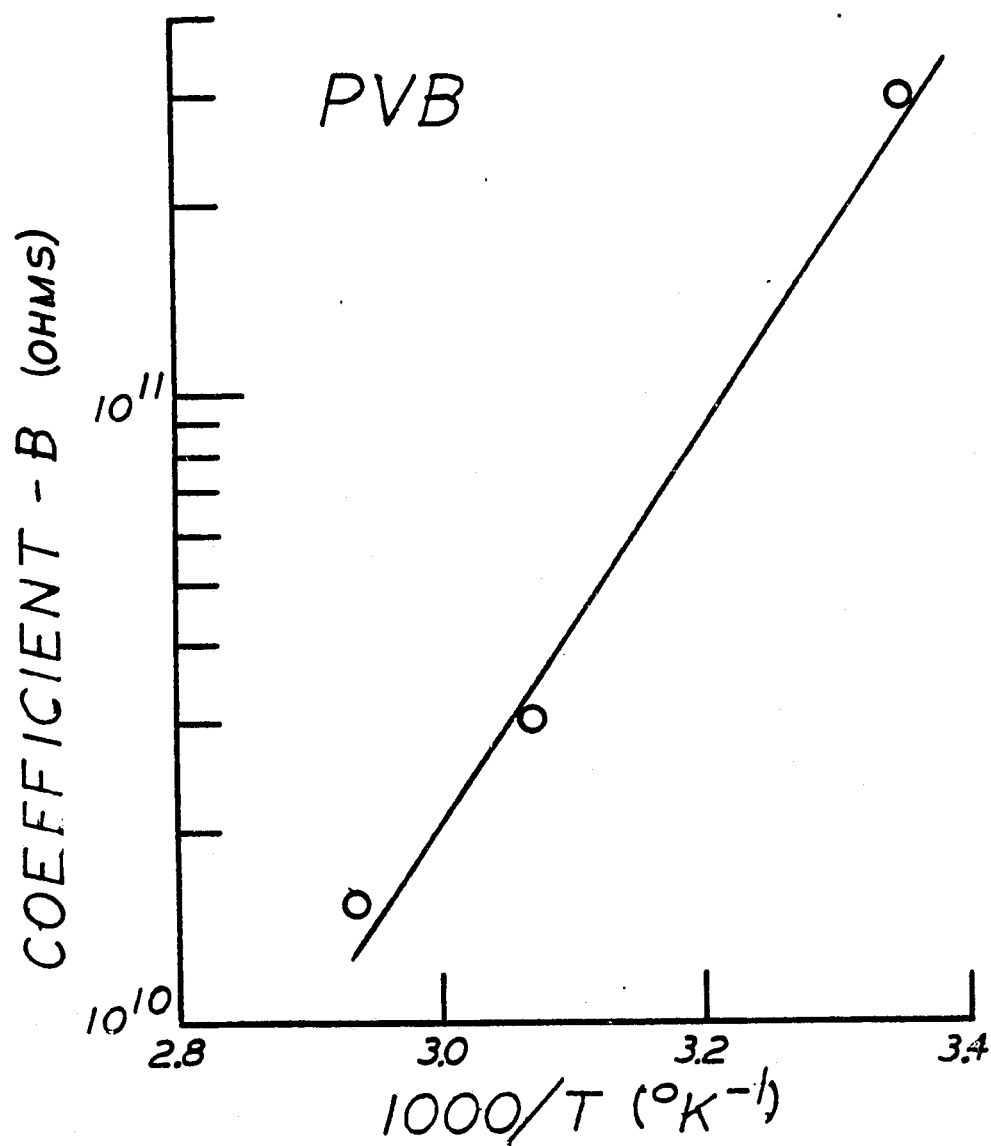


Fig. 4.21-Temperature dependence of the coefficient B in Equation 4.52 for characterizing the intrinsic resistance of PVB.

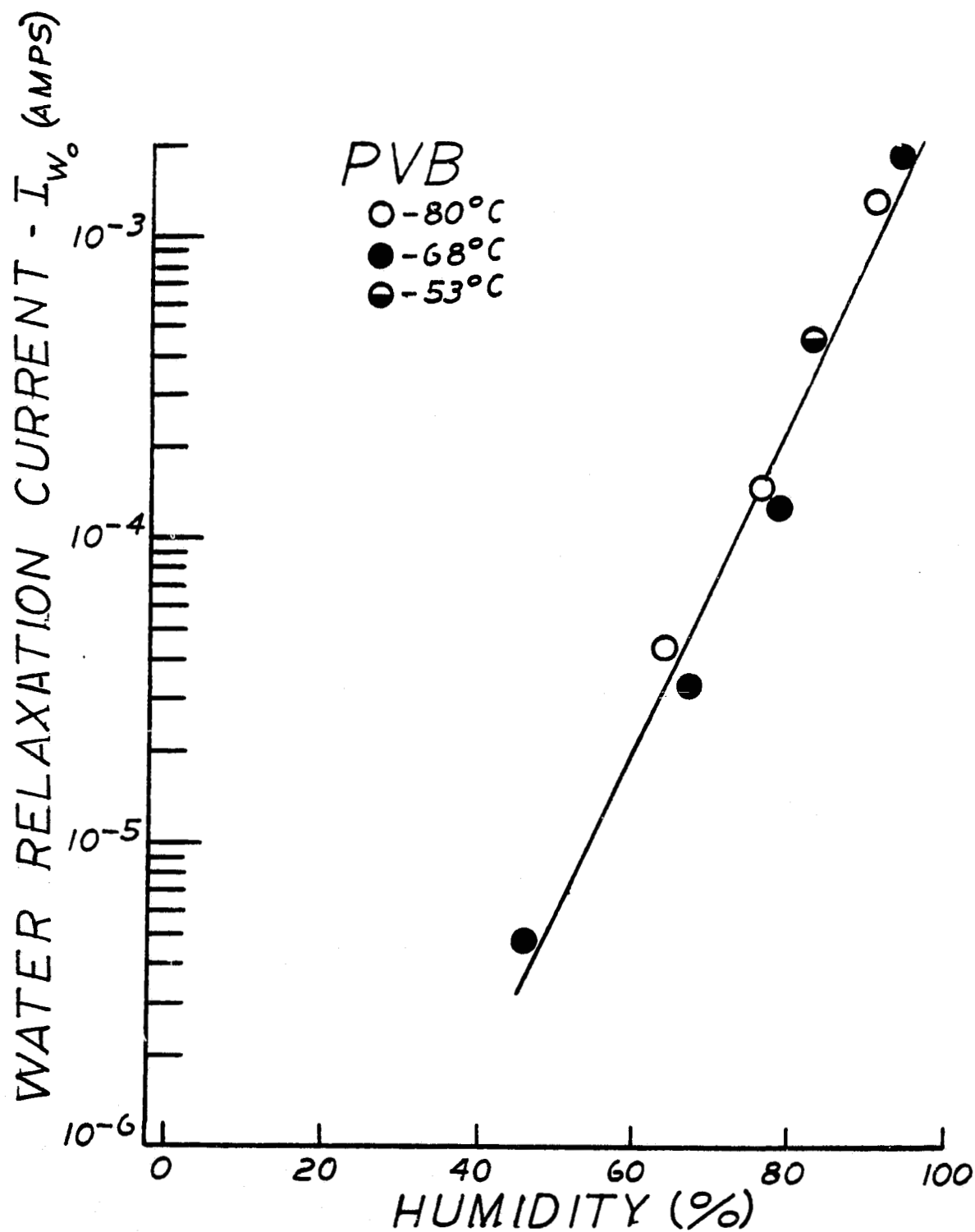


Fig. 4.22-Water relaxation current component as a function of humidity at selected temperatures.

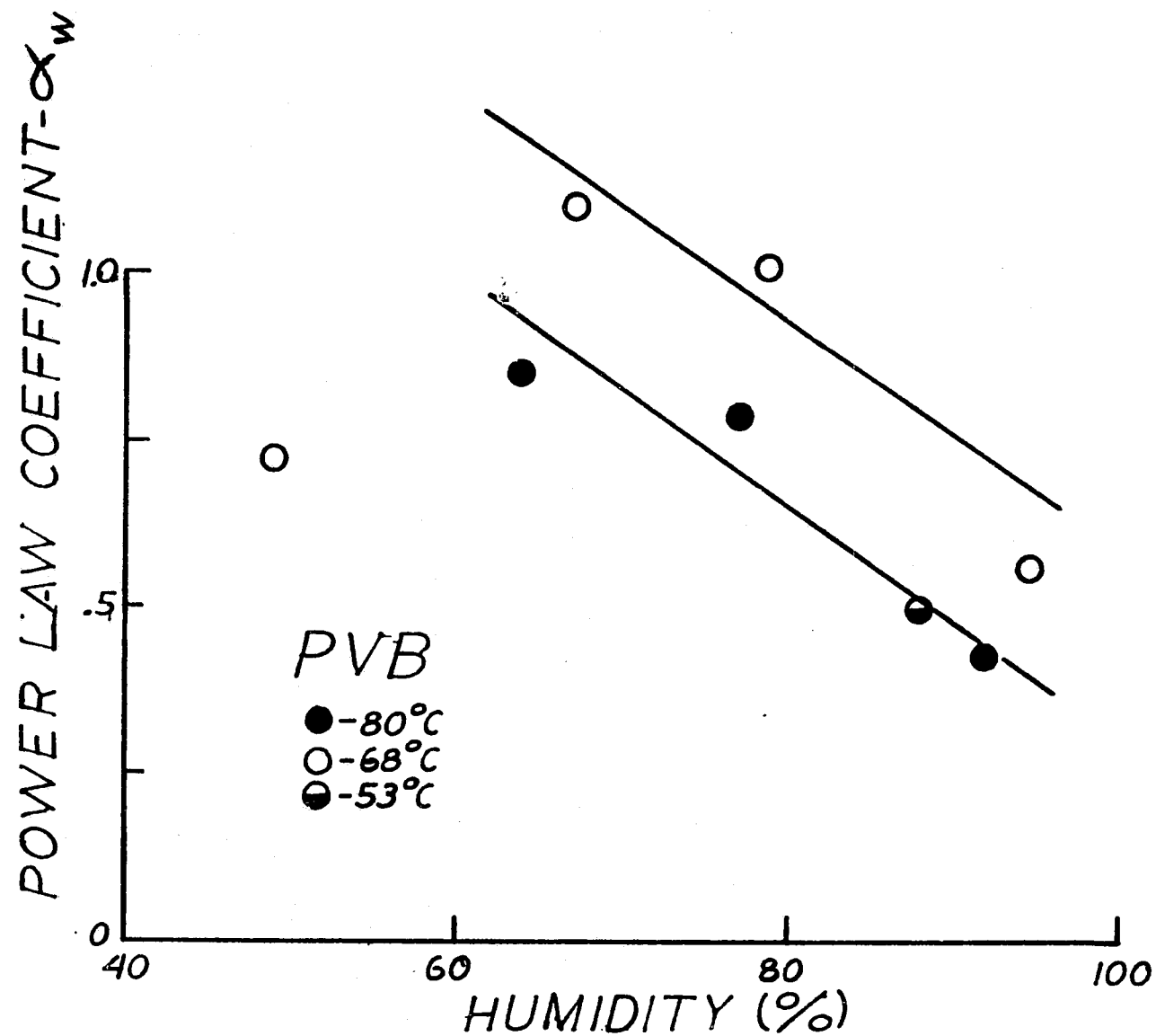


Fig. 4.23-Water relaxation power law coefficient as a function of humidity at various temperatures.

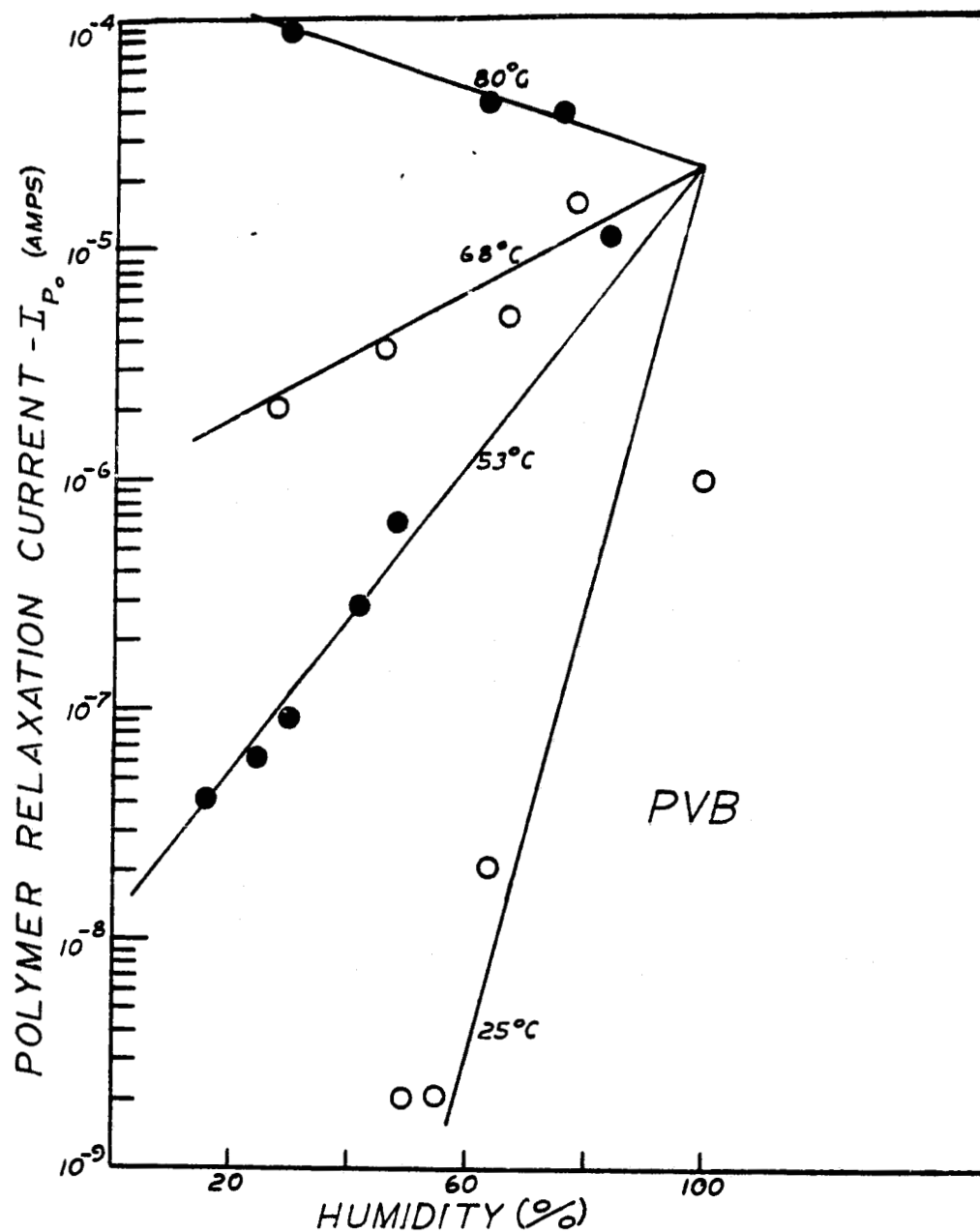


Fig. 4.24 - Polymer relaxation current component as a function of humidity at selected temperatures.

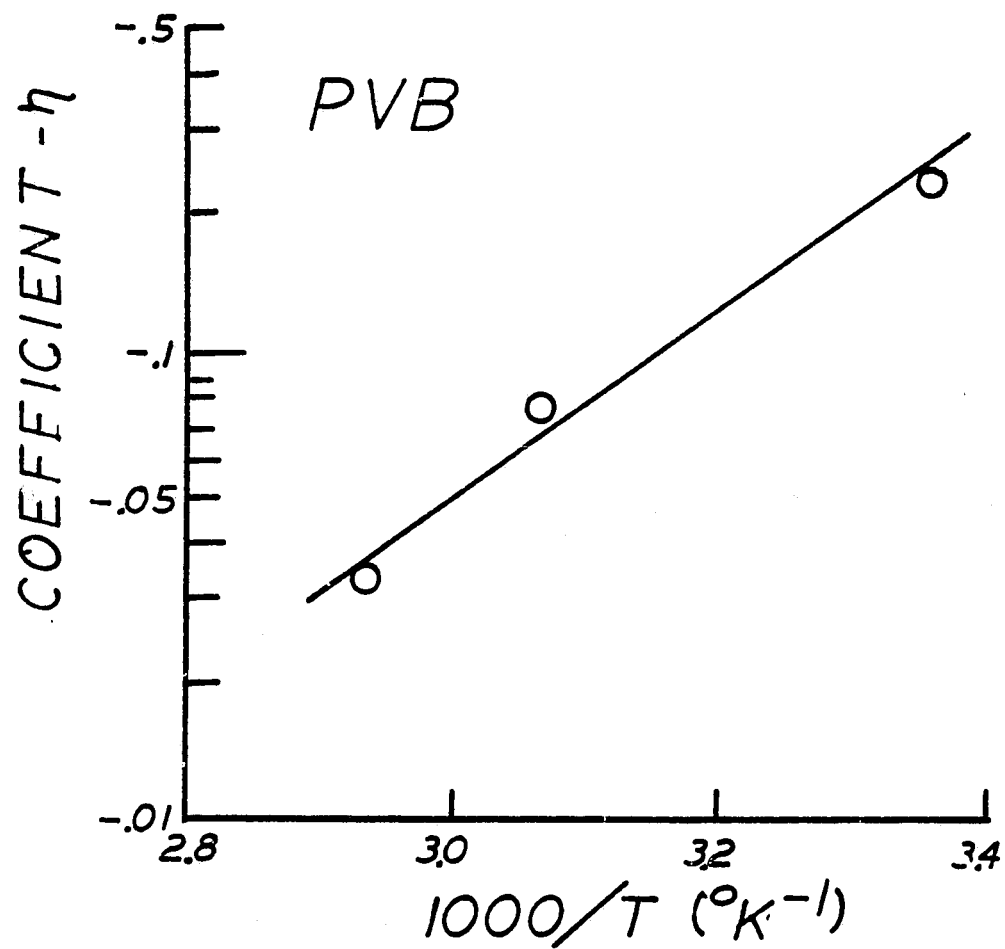


Fig. 4.25-Temperature dependence of the coefficient η for characterizing the polymer relaxation current in PVB.

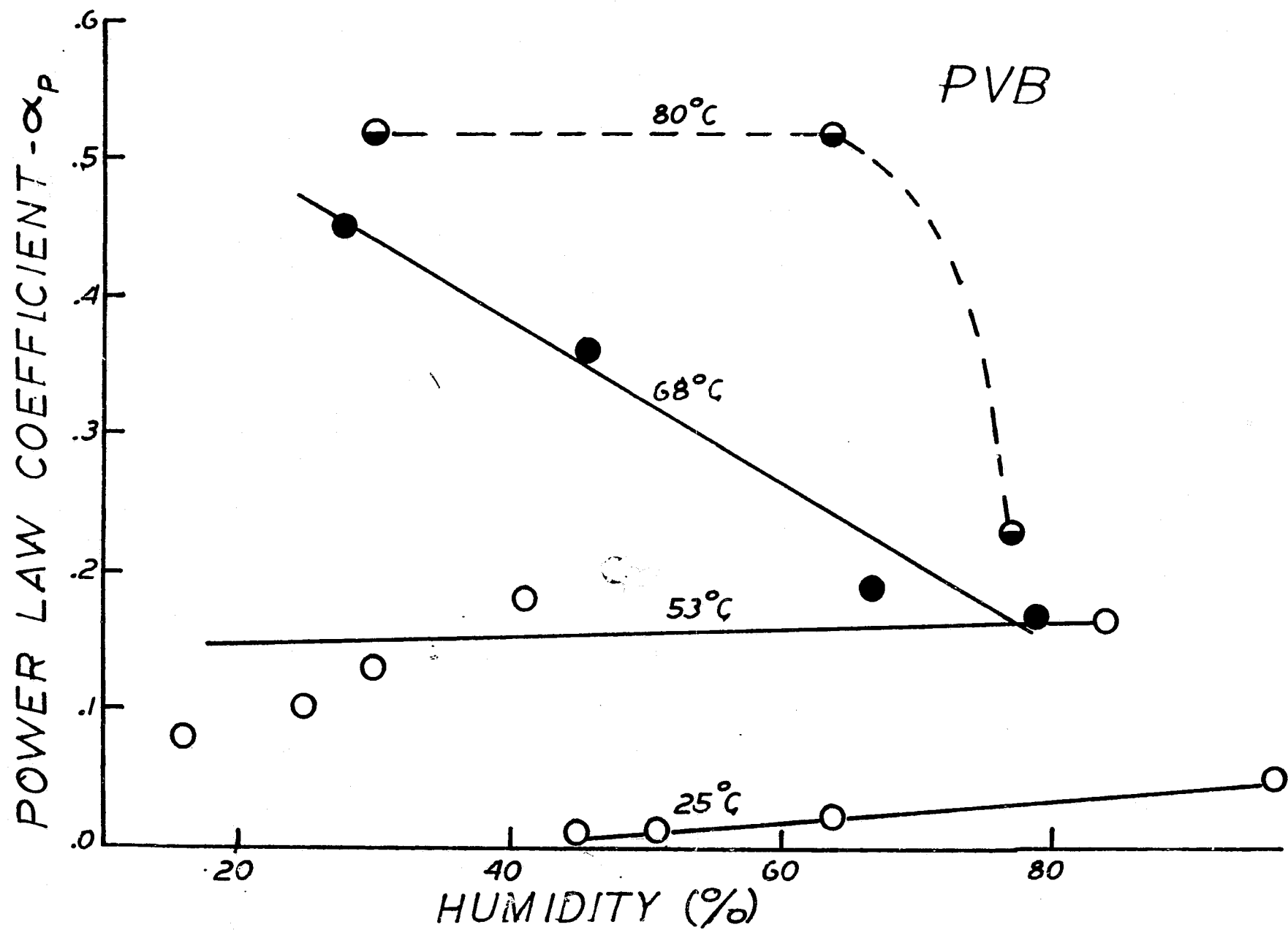


Fig. 4.26-Power law coefficient for the polymer relaxation current component as a function of humidity at various temperatures.

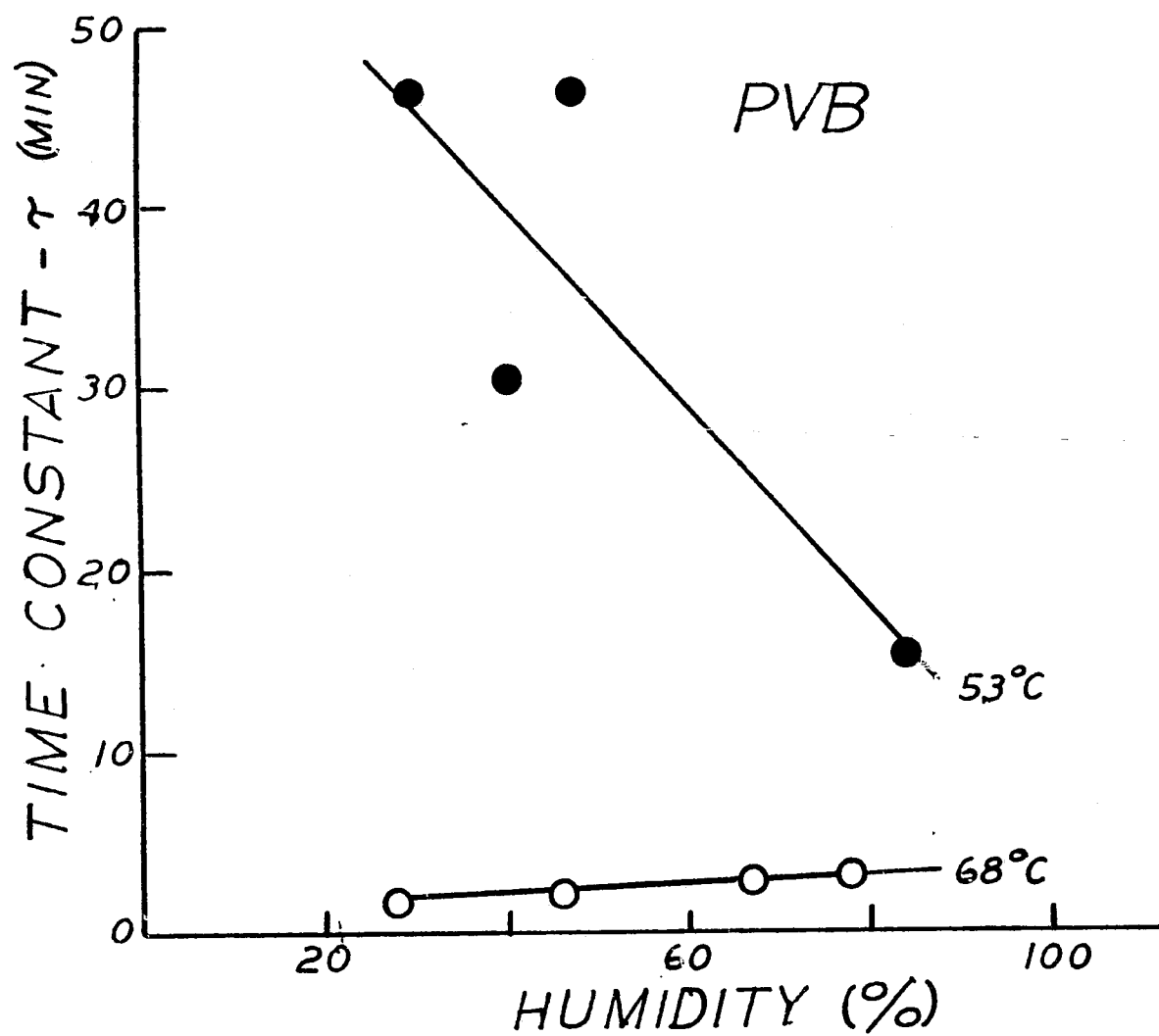


Fig 4.27-Humidity dependence of the time constant for the initial transient d.c. current response in PVB at 68° and 53°C.

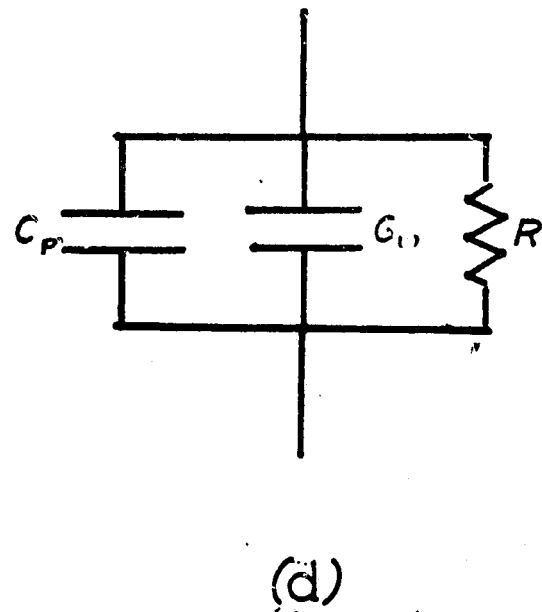
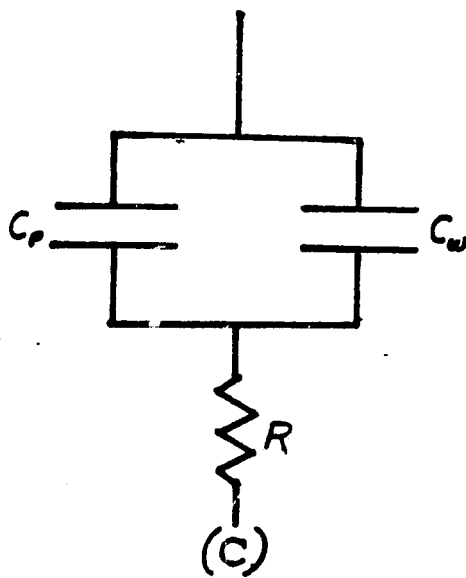
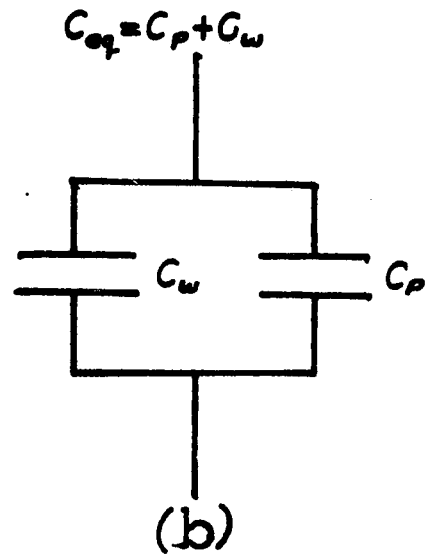
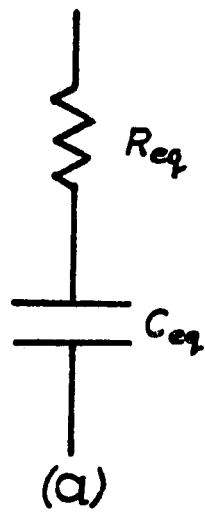


Fig 4.28 - Possible lumped equivalent circuit representations of a PVB dielectric.

V. Electrical Properties of EVA

Experimental Procedure

The absorption current, ionic resistance, capacitance, and dissipation factor of EVA were measured as a function of temperature and humidity. The experimental procedure for making these measurements is described in Section IV for the PVB study.

Experimental Results

The time dependence of the d.c. current response to a 390 volt step forcing function at 68⁰, 53⁰, and 42⁰C for various humidity values are presented in Figures 5.1 to 5.4. These results show that the current response obeys a single stage power law time dependence

$$I = K t^{-\alpha} \quad 5.1$$

At 68⁰C for all humidity levels and at 53⁰C for the high humidity levels, this power law behavior is preceded by a transient (Figs. 5.1 to 5.3) where this transient appears to be exponentially time dependent (Figs. 5.5 to 5.6).

$$I = I_0 \exp(-t/\tau) \quad 5.2$$

This transient was not evident in the experimental data at 42⁰ or at 53⁰C when the humidity was less than 30% (Fig. 5.3). These results suggest that the transient exists at progressively lower humidity levels as the temperature increases. As an empirical relationship, the transient exists when the product of temperature in degrees centigrade of about 150 and humidity in percent exceeds a value of about 150:

$$[T(^{\circ}C)][H(\%)] > 150 \quad \text{transient behavior} \quad 5.3$$

$$[T(^{\circ}C)][H(\%)] < 150 \quad \text{no transient} \quad 5.4$$

This same empirical relationship was also apparent in the PVB data.

The capacitance of EVA as a function of frequency for various humidity values at 68⁰, 53⁰ and 42⁰C is shown in Figure 5.7. The capacitance is seen to be relatively independent of the frequency in the range 0.5, to 5 KHz. The capacitance at 1 KHz as a function of humidity at 68⁰, 53⁰, and 42⁰C is illustrated in Figure 5.8 where it is apparent that the capacitance is not a function of humidity, and appears to be a function of temperature. This apparent temperature dependence as shown in Figures 5.8 and 5.9 where the capacitance appears to increase and then decrease with increasing temperature, may not be a correct indication of the true behavior of the capacitance as a function of temperature. A different sample was used at each temperature of measurement, and each sample may have had a different spacing between the inbedded screens electrodes as a result of the lamination process in fabricating the samples. Changes in the spacing (d) between the electrodes from sample to sample would directly influence the capacitance since:

$$C = K \epsilon_0 A / d$$

5.5

It is suspected that the capacitance of EVA like that of PVB is relatively temperature insensitive over the limited range of temperatures used in this investigation. The apparent behavior of the capacitance as a function of temperature as shown in Figure 5.9 is not a result of temperature, but is a consequence of the suspicion that the spacing between the electrodes of the samples is not the same.

The tan δ loss factor for EVA was found to be very small, and this smallness prevented an accurate evaluation of the dependence of tan δ on temperature, humidity, and frequency. In general, the tan δ values were usually .01 or less at all the investigated temperatures, humidities, and frequencies. A typical result for tan δ as a function of frequency for several different humidities at 68⁰C is shown in Figure 5.10.

Discussion

The same model used to analyze the d.c. current response of PVB to a forcing applied step voltage is also used to evaluate the EVA current response data. The model proposes that the current response is the sum of four component currents: I_c , I_w , I_p , and I_i . Since the response current in EVA never exhibits a two stage power law dependency and since EVA is known to absorb only small amounts of water compared to PVB, the I_w water dipole absorption current component was assumed to be insignificant in EVA. The single stage power law time dependencies observed in the experimental data was then assumed to result from polymer effects.

The associated slopes were assigned as the α_p coefficient values as shown in Figures 5.1 to 5.4 and the intercepts were taken to be the I_{p0} values. When an exponential transient existed in the current data, the time constants were determined along with the I_{c0} ($=390/R_0$) intercept values. The intrinsic current was again taken as the current after 100 minutes of elapsed time. A summary of the current components and their associated characteristic parameters at 68⁰, 53⁰ and 42⁰C is presented in Table 5.1 to 5.3.

From this summary, the temperature and humidity dependence of initial resistance (R_0) the intrinsic resistance (R_i), the polymer relaxation current (I_{p0}), the α_p power law coefficient, and the time constant (τ) can be evaluated.

The initial resistance (R_0) as a function of humidity at the various run temperatures is shown in Figure 5.11. At 53⁰, the initial resistance is exponentially related to the humidity:

$$R_o = 6.5(10^{12}) \exp(-.116 H)$$

5.6

which is consistent with the observed dependence in PVB. An exponential humidity dependence at 42°C but not at 68°C appears to be indicated by the limited data in Fig. 5.11. Because of the limited data, the temperature dependence of R_o could not be evaluated.

Figure 5.12 shows the intrinsic (R_i) resistance as a function of humidity at the various run temperatures. At 53°C, the intrinsic resistance is exponentially related to the humidity:

$$R_i = 1.8(10^{13}) \exp(-.123 H)$$

5.7

An exponential relationship appears (Fig. 5.12) to be valid at 42°C but not at 68°C. The data is not sufficient for an evaluation of the temperature dependence of R_i .

The polymer absorption current (I_{p0}) as a function of humidity at the various 53°C and 68°C is presented in Figure 5.13 where it is apparent that I_{p0} at 53°C is exponentially related to the humidity

$$I_{p0} = 2.3(10^{-10}) \exp(+.096 H)$$

5.8

The α_p power law coefficient characterizing the polymer absorption current is plotted against humidity for the various run temperatures in Fig. 5.14. Aside from the general observation that α_p seems to decrease with decreasing temperature as it did in PVB, no systematic pattern is evident for the dependence of α_p on humidity and temperature.

Finally, the time constant associated with the capacitive charging current component is presented as a function of the humidity at 68°C and 53°C (Fig. 5.15). The time constant appears to be independent of both humidity and temperature.

A summary of the temperature and humidity dependence of these various a.c. and d.c. electrical properties and their characterizing

parameters for EVA is presented in Table 5.4. With the exception of the data at 53°C, none of the EVA parameters appear to be highly dependent on the humidity which provides a remarkable contrast with the PVB data where (Table 4.2) the parameters are highly dependent on the humidity. This observation is consistent with the fact that PVB is known to absorb enormous quantities of water in a humid environment while water absorption in EVA is relatively meager.

The temperature and humidity dependencies for the a.c. and d.c. properties were difficult to obtain in EVA simply because the d.c. current response, capacitance, and $\tan \delta$ loss factor measurements were pushing the limits of experimental detection with the available equipment. The problem was particularly prevalent at the low temperatures and humidity values. Even with this problem, the data indicates that the d.c. resistive properties of EVA are considerably larger than that of PVB at similar temperature and humidity levels. The a.c. capacitance and loss factor of EVA apparently are also considerably smaller than that of PVB. The question to be resolved is: Are the apparent differences in properties between PVB and EVA an inherent characteristic of those two polymers or a result of the fact that PVB absorbs much more water from a humid environment. This question can be resolved by comparing several selected properties of EVA and PVB as a function of humidity at the same temperature. Figures 5.16 to 5.18 shows these comparisons for the original resistance, the capacitance and the loss factor respectively. The differences between these particular properties of PVB and EVA diminish considerably as humidity decreases, and by extrapolating to zero humidity, the inherent value of these properties for PVB and EVA can be estimated. The extrapolated values are presented in Table 5.5. At zero humidity, these properties in PVB are not that much different than in EVA: R_0

differs by a factor of 10, C differs by a factor of 2, and $\tan \delta$ is the same. This data suggests that the larger amounts of absorbed water in PVB than in EVA at any particular humidity level, is primarily responsible for the large differences in the properties of these two polymers.

TABLE 5.1

D.C. current response characteristics of EVA at 68°C

Relative Humidity (10%)	Current Components (amps)	α_p _____	τ (min.)	R_o (Ω)	R_i (Ω)
79	$I_{co} = 2.3(10^{-7})$ $I_{po} = 2.8(10^{-7})$ $I_i = 7.0(10^{-8})$.28	19	$1.6(10^9)$	$5.5(10^9)$
67	$I_{co} = 2.3(10^{-7})$ $I_i = 6.0(10^{-8})$ $I_j = 6.0(10^{-8})$.36	19	$1.6(10^9)$	$6.5(10^9)$
46	$I_{co} = 1.6(10^{-7})$ $I_{po} = 2.2(10^{-7})$ $I_i = 4.0(10^{-8})$.36	19	$2(10^9)$	$1(10^{10})$
28	$I_{co} = 9(10^{-8})$ $I_{po} = 1.5(10^{-7})$ $I_i = 2(10^{-8})$.38	23	$4(10^9)$	$2(10^{10})$

TABLE 5.2

D.C. current response characteristics of EVA at 53°

Relative Humidity (%)	Current Components (amps)	α_p	τ (min.)	R_o (Ω)	R_i (Ω)
100	$I_{po} = 6(10^{-6})$ $I_i = 3(10^{-6})$.12		$6.5(10^7)$	$1.3(10^8)$
84	$I_{po} = 1.4(10^{-6})$ $I_i = 1(10^{-6})$.11		$2.8(10^8)$	$4(10^8)$
48	$I_{co} = 1.7(10^{-8})$ $I_{po} = 2(10^{-8})$ $I_i = 7(10^{-9})$.26	20	$2.3(10^{10})$	$5.5(10^{10})$
41	$I_{co} = 9.6(10^{-9})$ $I_{po} = 1(10^{-8})$ $I_i = 3(10^{-9})$.30	17	$4(10^{10})$	$1.3(10^{11})$
30	$I_{po} = 5(10^{-9})$ $I_i = 1(10^{-9})$.38		$7.8(10^{10})$	$4(10^{11})$
16	$I_{po} = 5(10^{-9})$ $I_i = 3(10^{-9})$.10		$7.8(10^{10})$	$1.3(10^{11})$

TABLE 5.3

D.C. current response characteristics of EVA at 42°C

Relative Humidity <u>(%)</u>	Current Components <u>(amps)</u>	α_p <u> </u>	R_o <u>(Ω)</u>	R_i <u>(Ω)</u>
100	$I_{po} = 3(10^{-3})$ $I_i = 1(10^{-3})$.11	$1.3(10^5)$	$4(10^5)$
82	$I_i = 1(10^{-7})$		$4(10^9)$	$4(10^9)$
67	$I_{po} = 3(10^{-8})$ $I_i = 2(10^{-8})$.11	$1.3(10^{10})$	$2(10^{10})$

TABLE 5.4

EVA: Temperature and humidity dependencies of a.c. and d.c. electrical properties:

$$C \neq \text{fct} (T, H)$$

$$\tan \delta^+$$

$$R_0 = 6.5(10^{12}) \exp(-.116 H)^* \quad \text{at } 53^\circ\text{C}$$

$$R_0 \neq \text{fct} (H) \quad \text{at } 68^\circ\text{C}$$

$$R_i = 1.8(10^{13}) \exp(-.123H)^* \quad \text{at } 53^\circ\text{C}$$

$$R_i \neq \text{fct} (H) \quad \text{at } 68^\circ\text{C}$$

$$I_{po} = 2.3(10^{10}) \exp(.095 H)^* \quad \text{at } 53^\circ\text{C}$$

$$I_{po} \neq \text{fct} (H) \quad \text{at } 68^\circ\text{C}$$

$$\alpha_p \neq \text{fct} (H)$$

$$\alpha_p = \text{fct} (T)^\bullet$$

$$\tau \neq \text{fct} (T, H)$$

+ -- unable to evaluate T and H dependencies if any

* -- unable to evaluate T dependence if any

● -- unable to evaluate functional form

TABLE 5.5

Comparison of the original resistance (R_o) capacitance (C) and loss factor ($\tan \delta$) for PVB and EVA at zero humidity and 68°C:

	<u>PVB</u>	<u>EVA</u>
R_o (Ω)	$5(10^8)$	$5(10^9)$
C (pfs)	200	100
$\tan \delta$	0	0

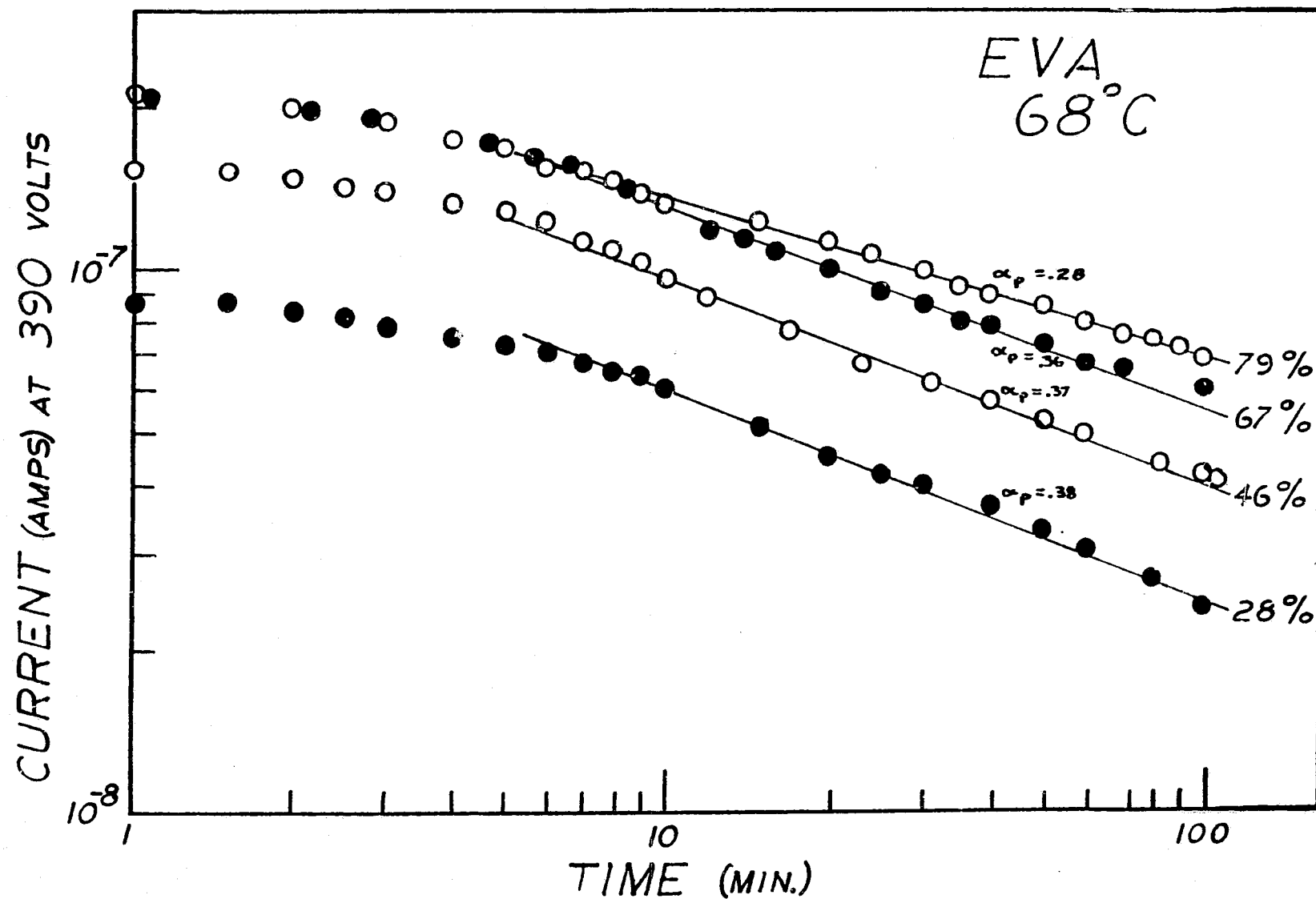


Fig. 5.1-Time dependence of the d.c. response current resulting from a 390 volt step forcing function applied to EVA at 68°C and various relative humidity levels.

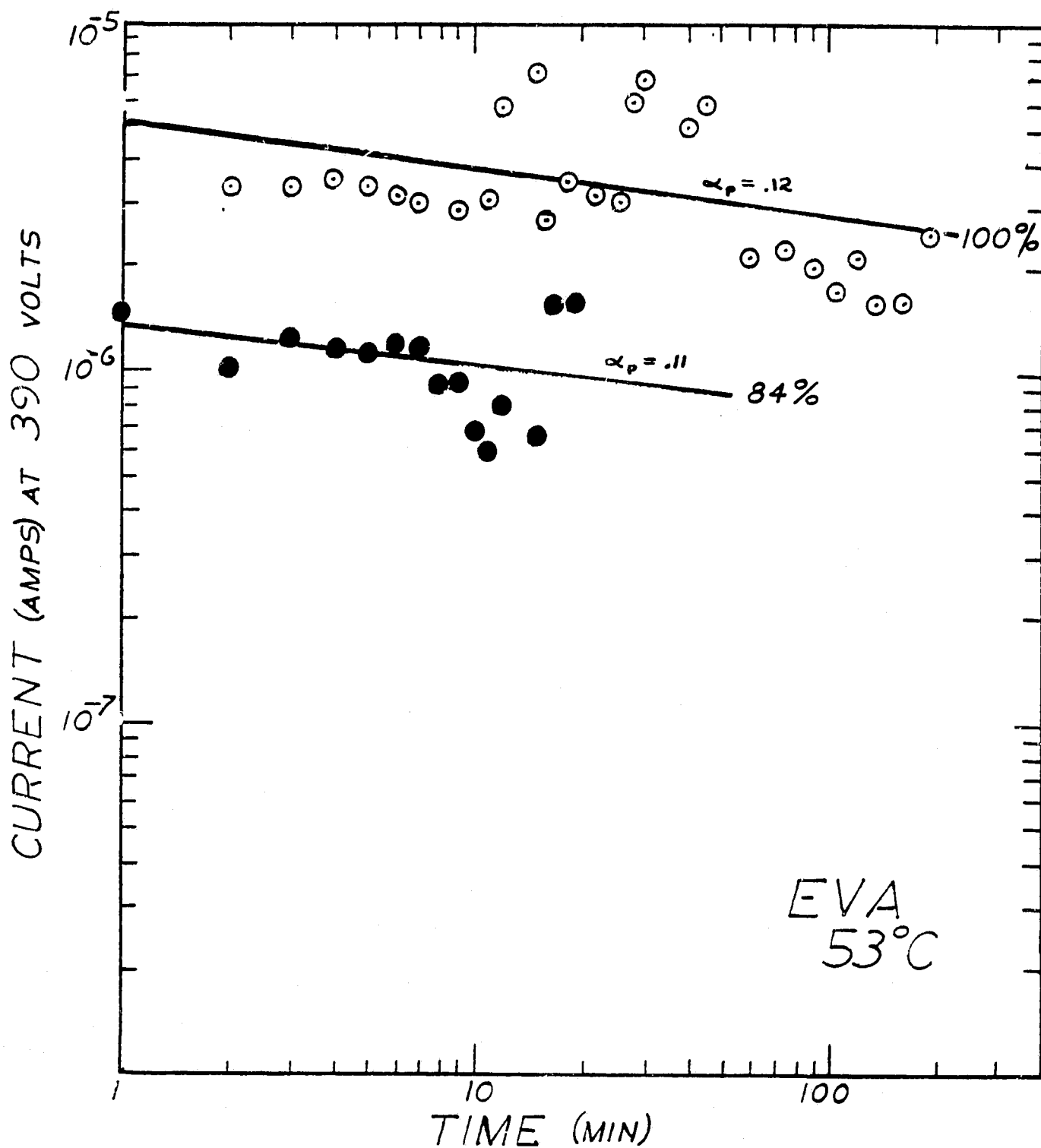


Fig. 5.2—Time dependence of the d.c. current response resulting from a 390 volt step function applied to EVA at 53°C and various relative humidity levels

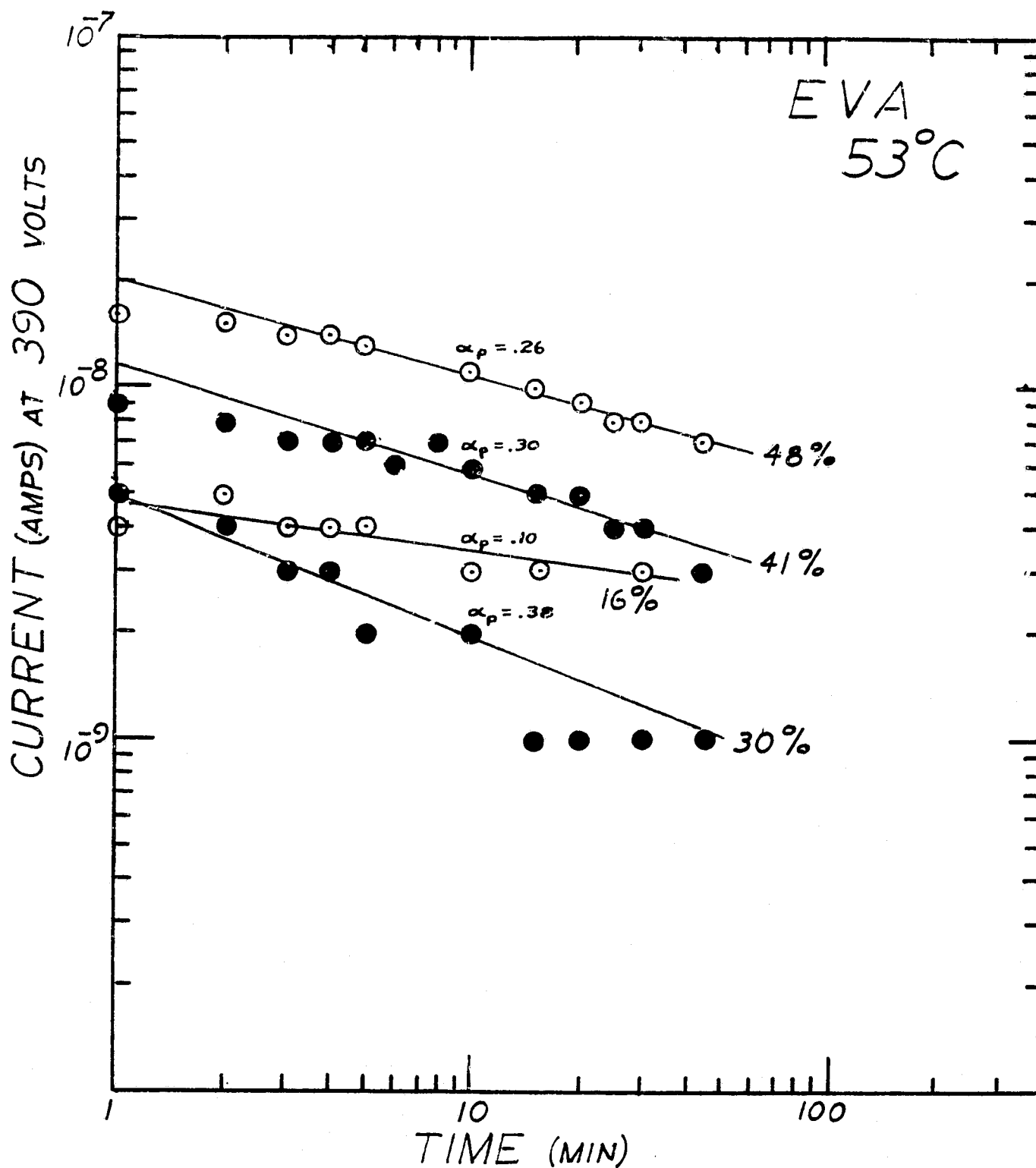


Fig. 5.3-Time dependence of the d.c. current response resulting from a 390 volt step function applied to EVA at 53°C and various relative humidity levels.

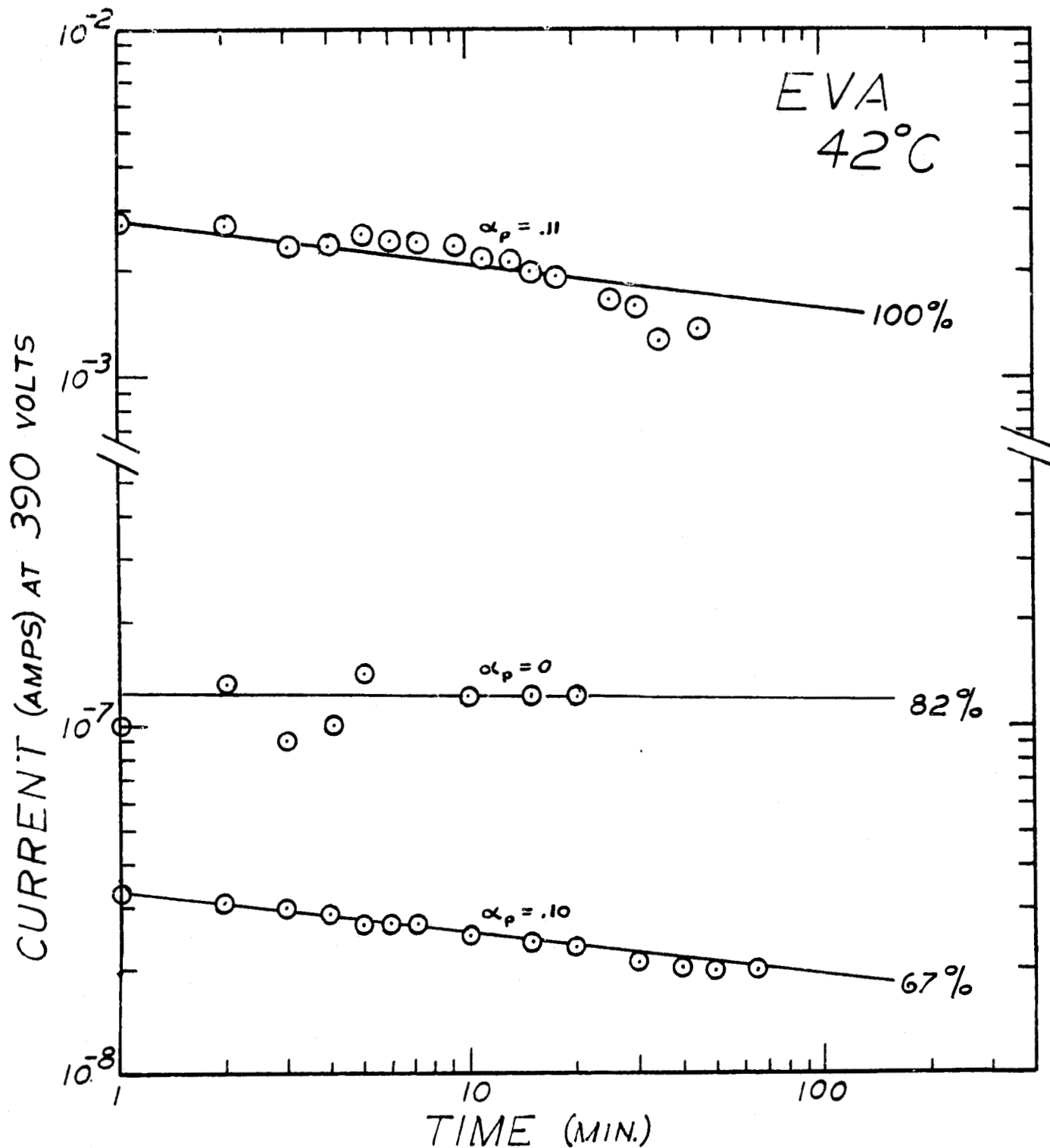


Fig. 5.4-Time dependence of the d.c. current response resulting from a 390 volt step function applied to EVA at 42°C and various relative humidity levels.

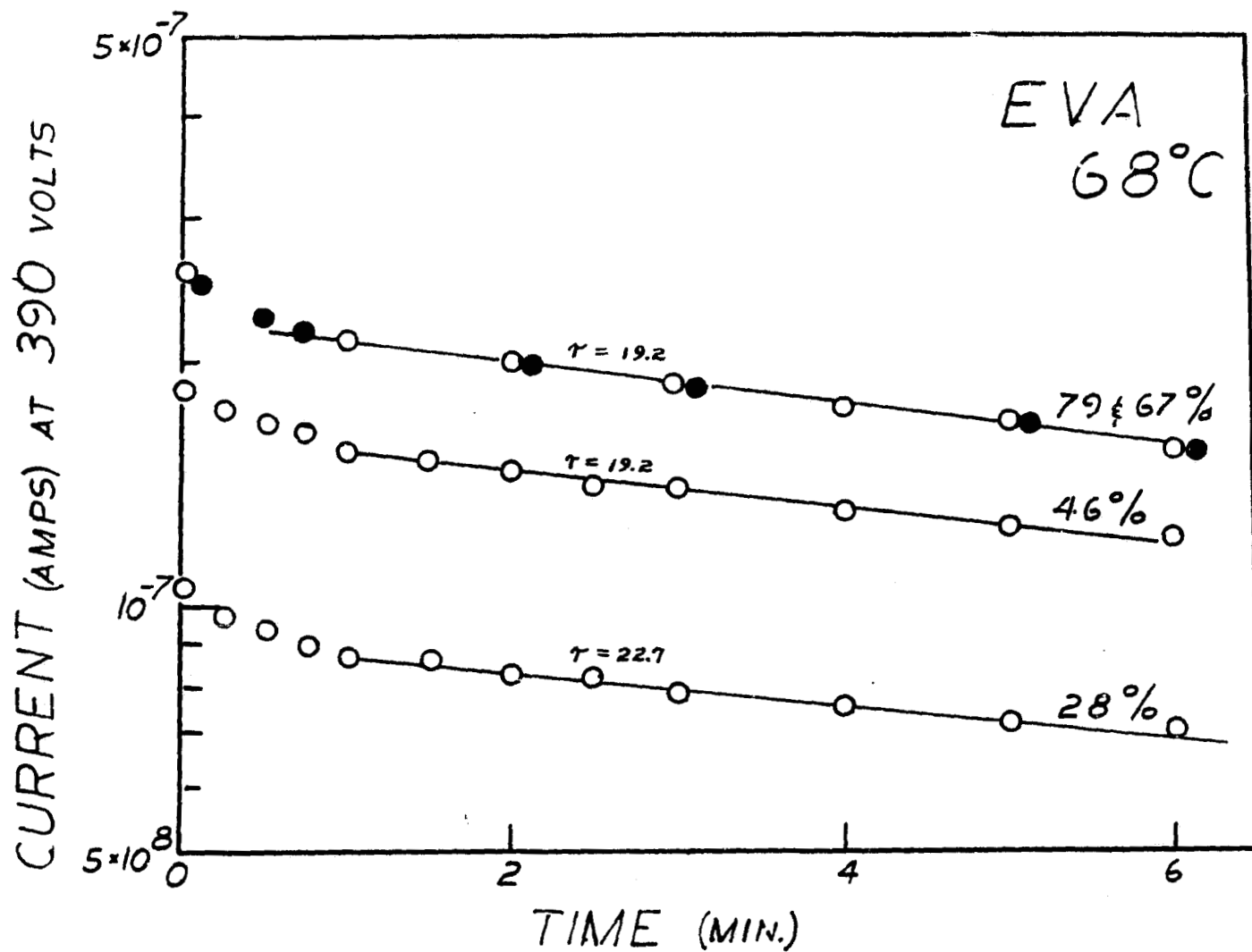


Fig. 5.5-Initial transient behavior for the d.c. response data shown in Figure 5.1.

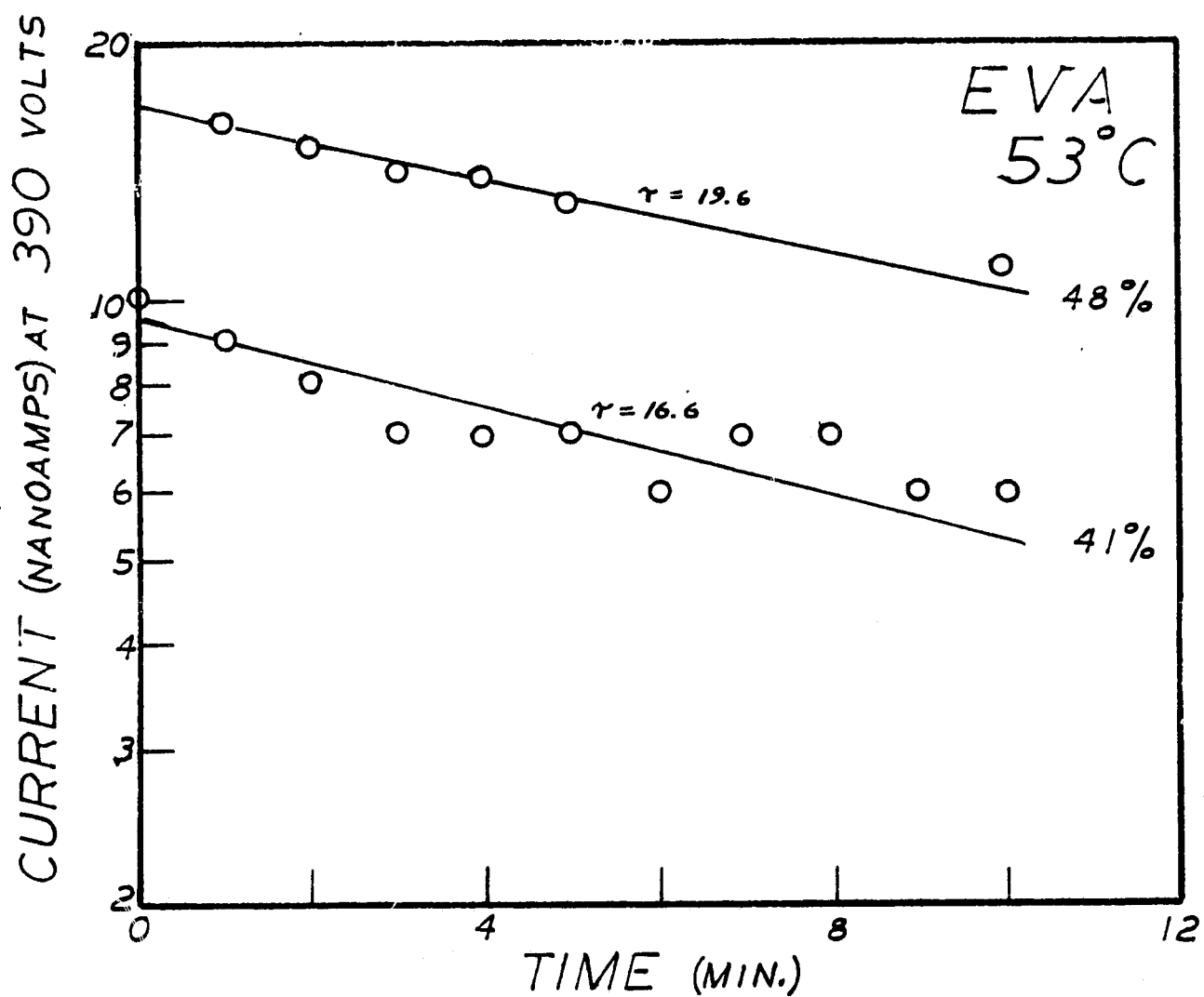


Fig. 5.6-Initial transient behavior for the d.c. current response data shown in Figure 5.3.

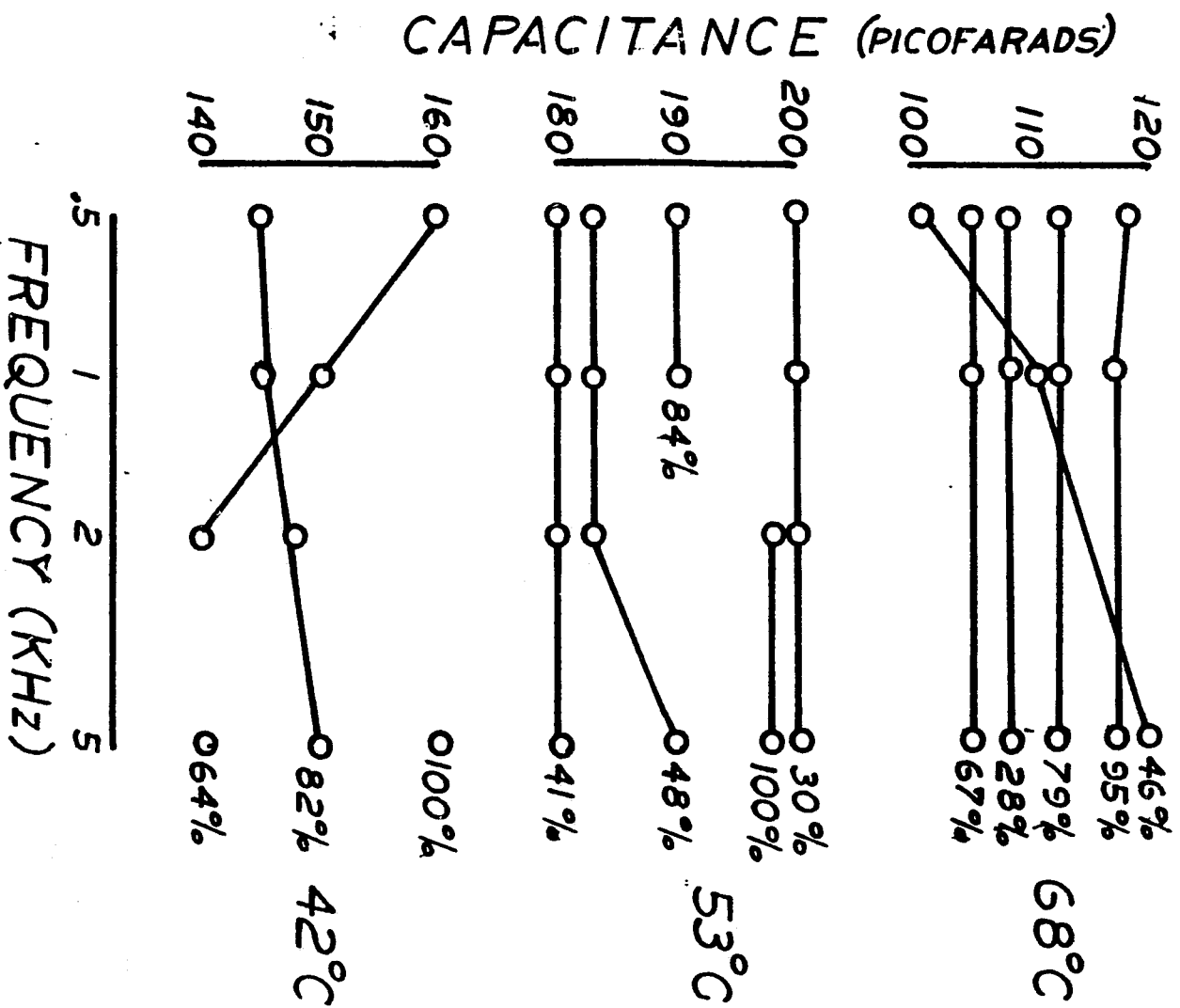


Fig. 5.7 - Frequency dependence of the capacitance of EVA at various temperatures and relative humidities.

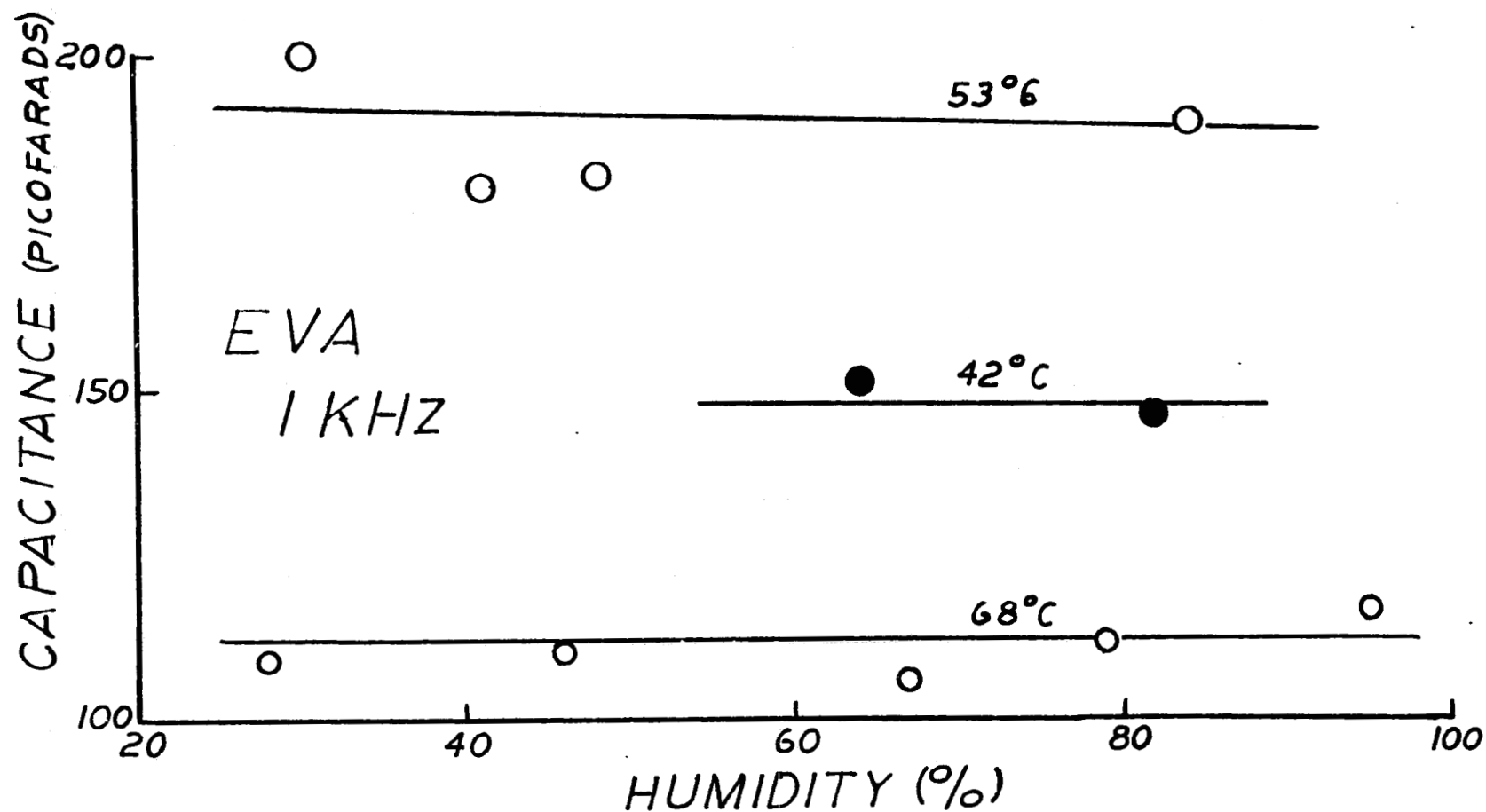


Fig. 5.8-Humidity dependence for the capacitance of EVA at 1KHz and various temperatures.

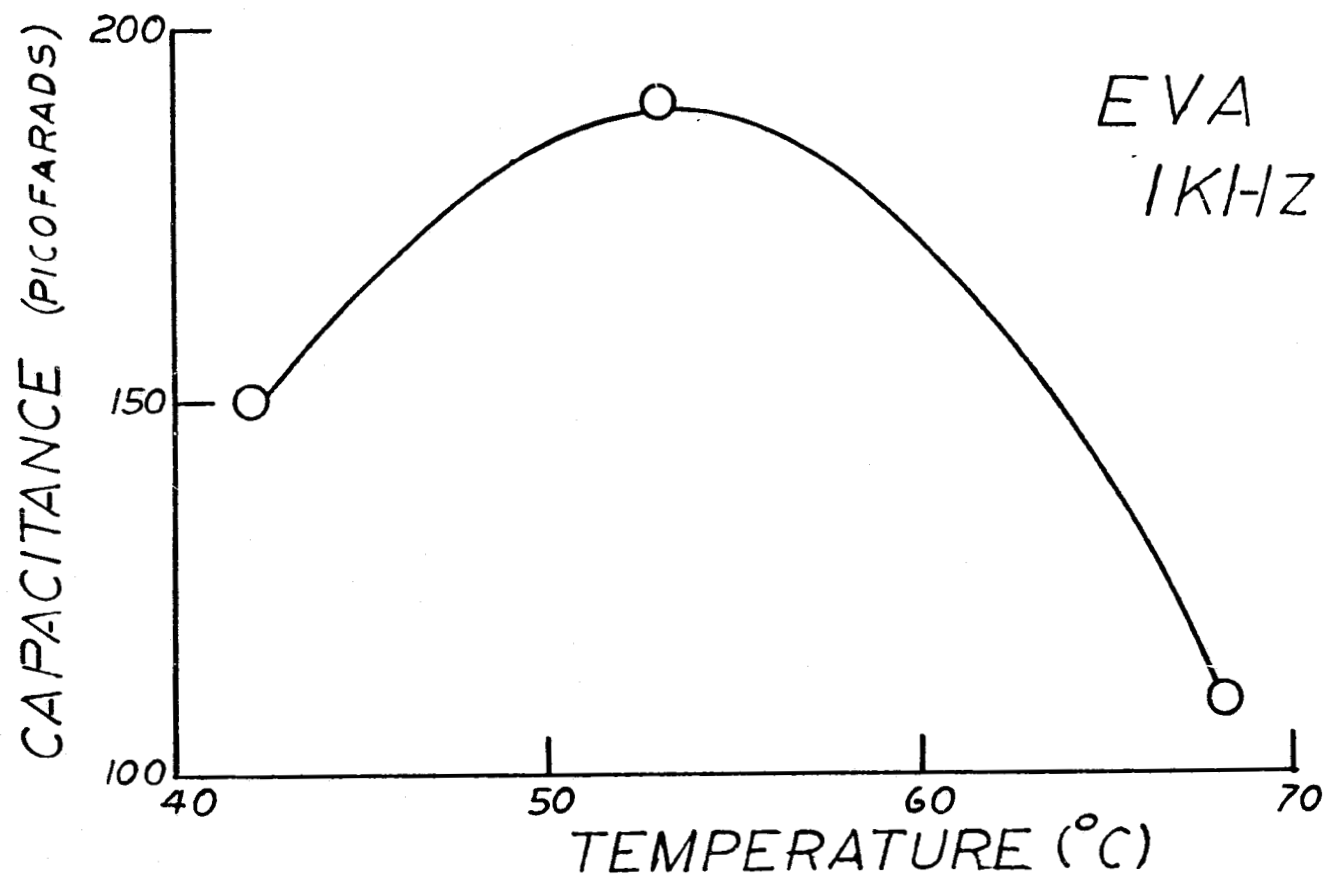


Fig 5.9--Temperature dependence for the capacitance at 1KHz of EVA at 100% humidity.

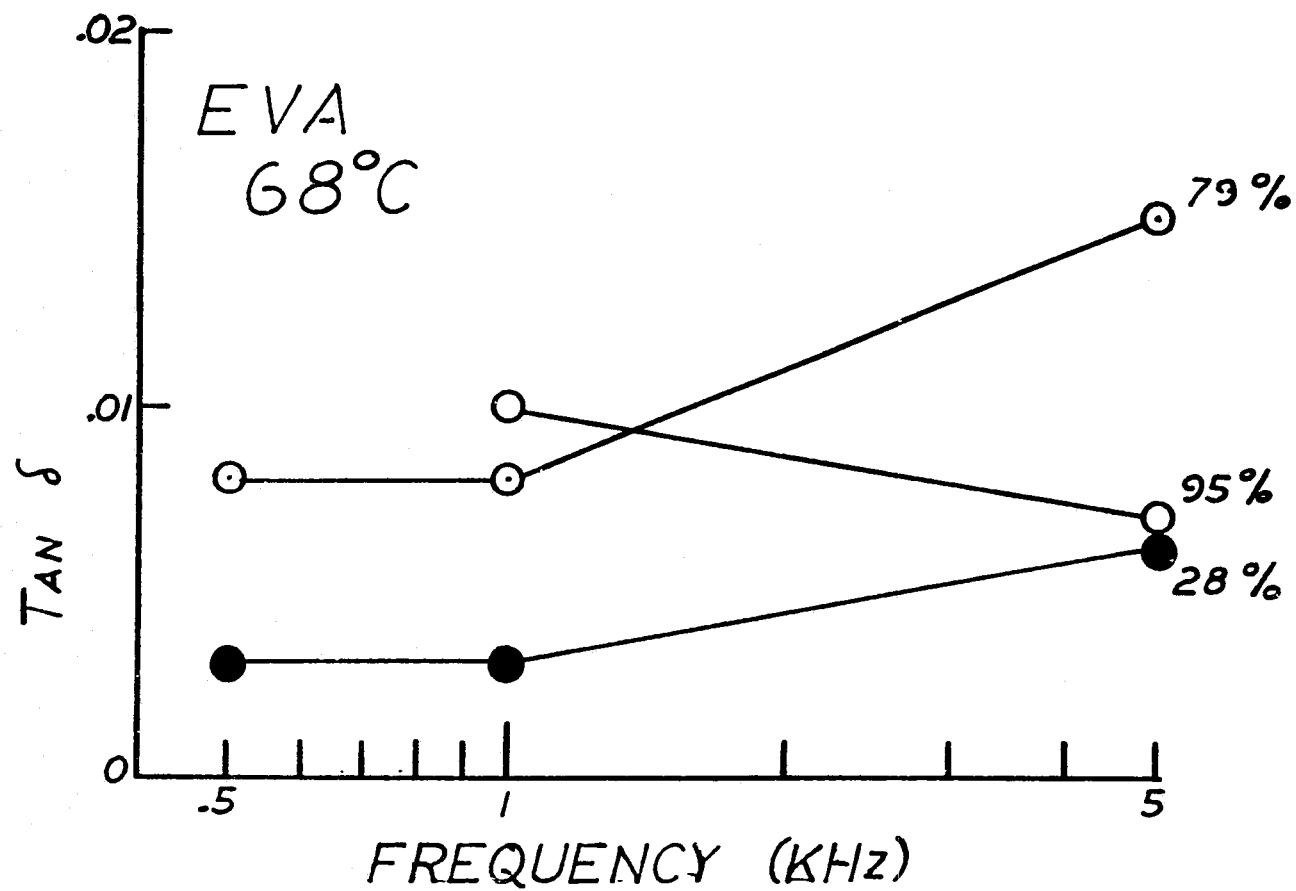


Fig. 5.10 - Frequency dependence of the loss factor in EVA at 68°C for various relative humidity levels.

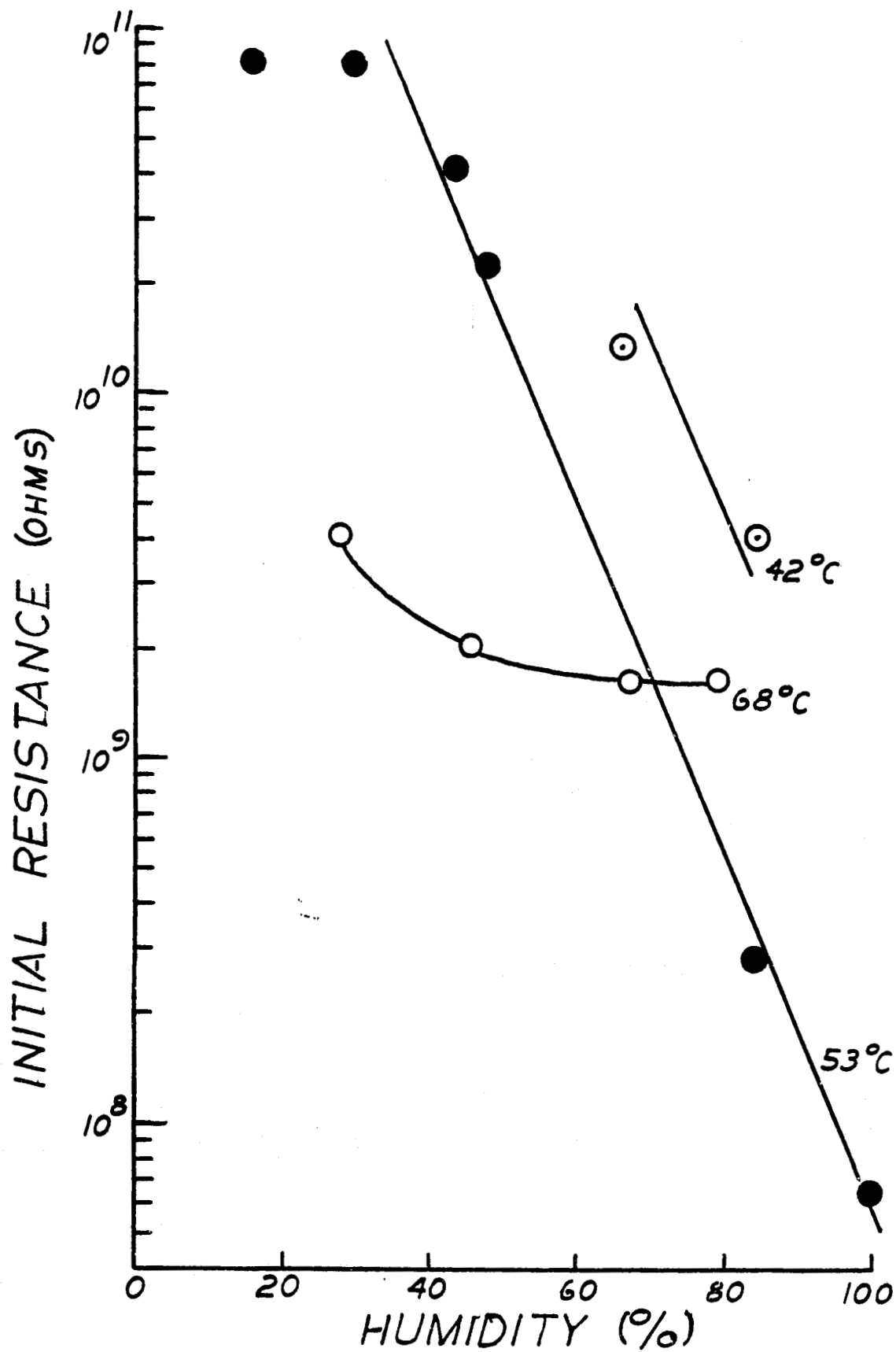


Fig. 5.11-Initial resistance of EVA as a function of humidity at various temperatures.

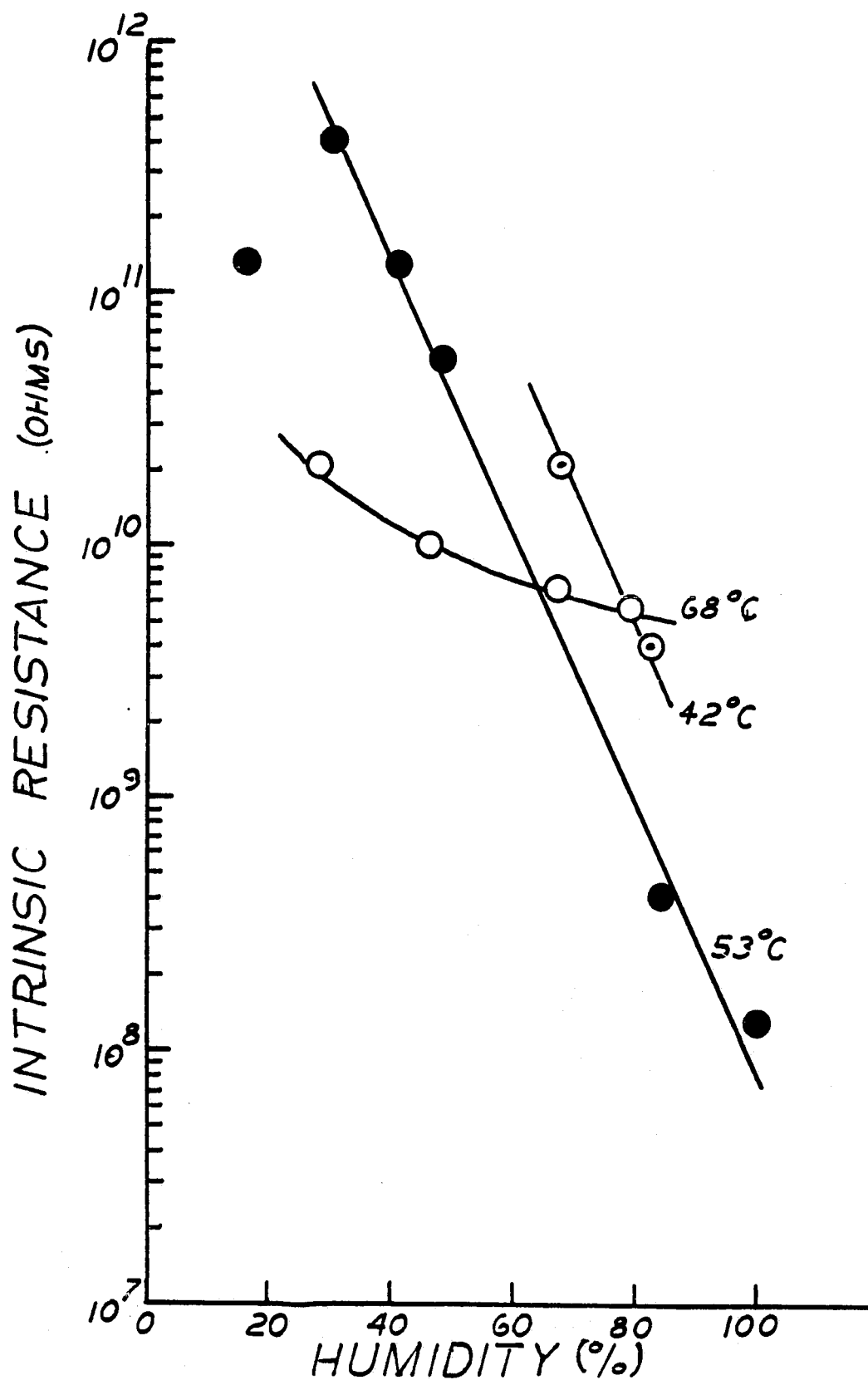


Fig. 5.12-Intrinsic resistance of EVA as a function of humidity at various temperatures.

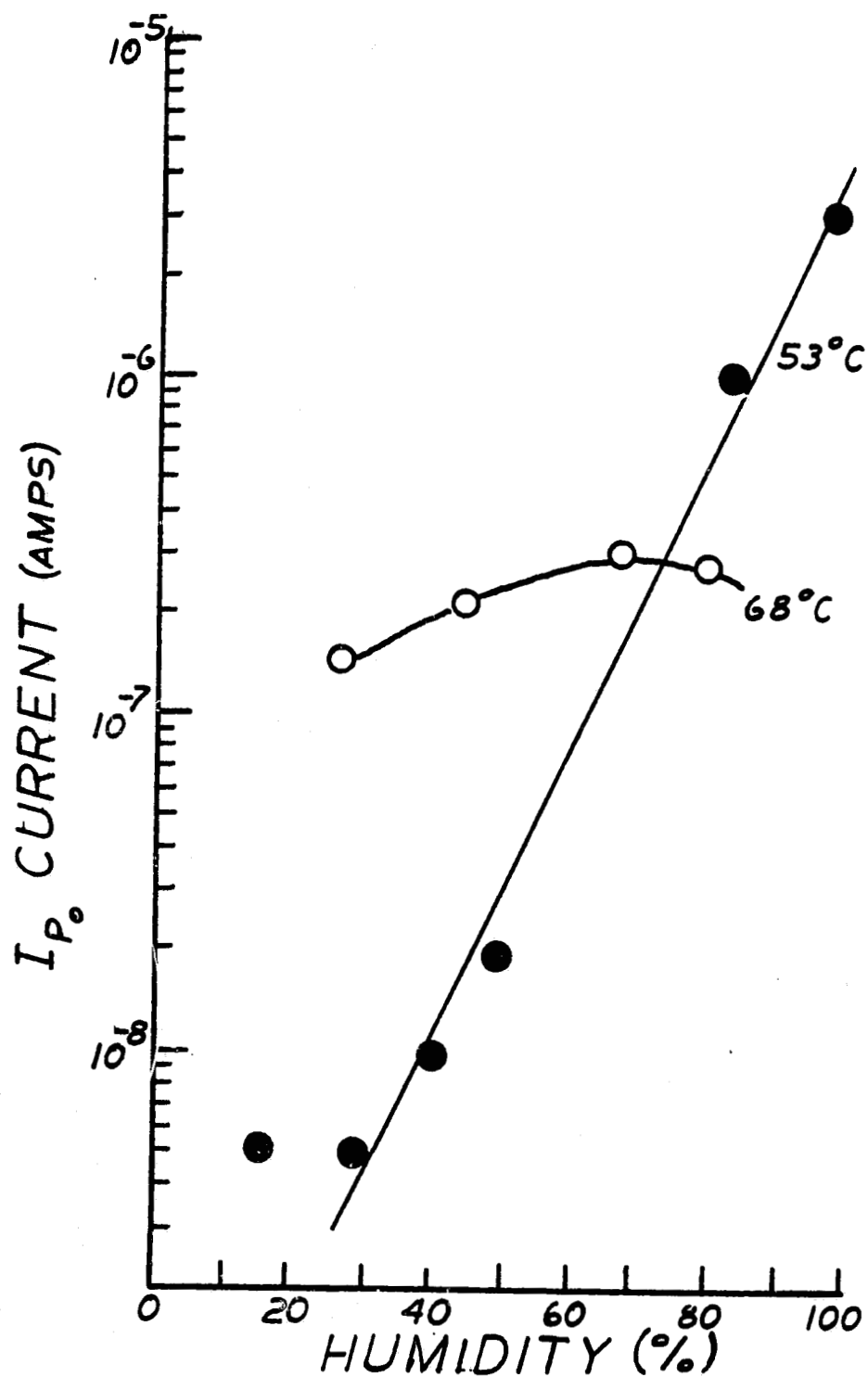


Fig. 5.13-Characteristic polymer polarization absorption current as a function of humidity at various temperatures.

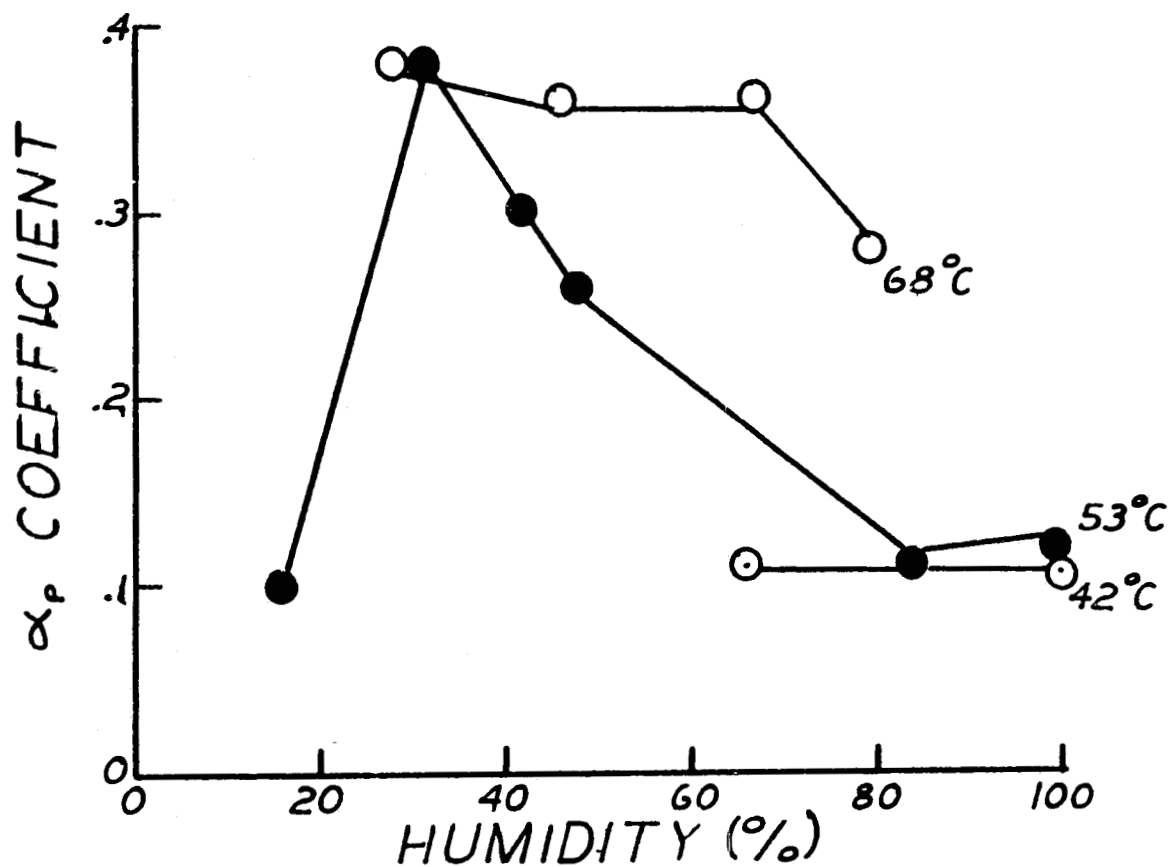


Fig. 5.14-Humidity dependence of the power law coefficient (α_p) for the polymer absorption current in EVA at various temperatures.

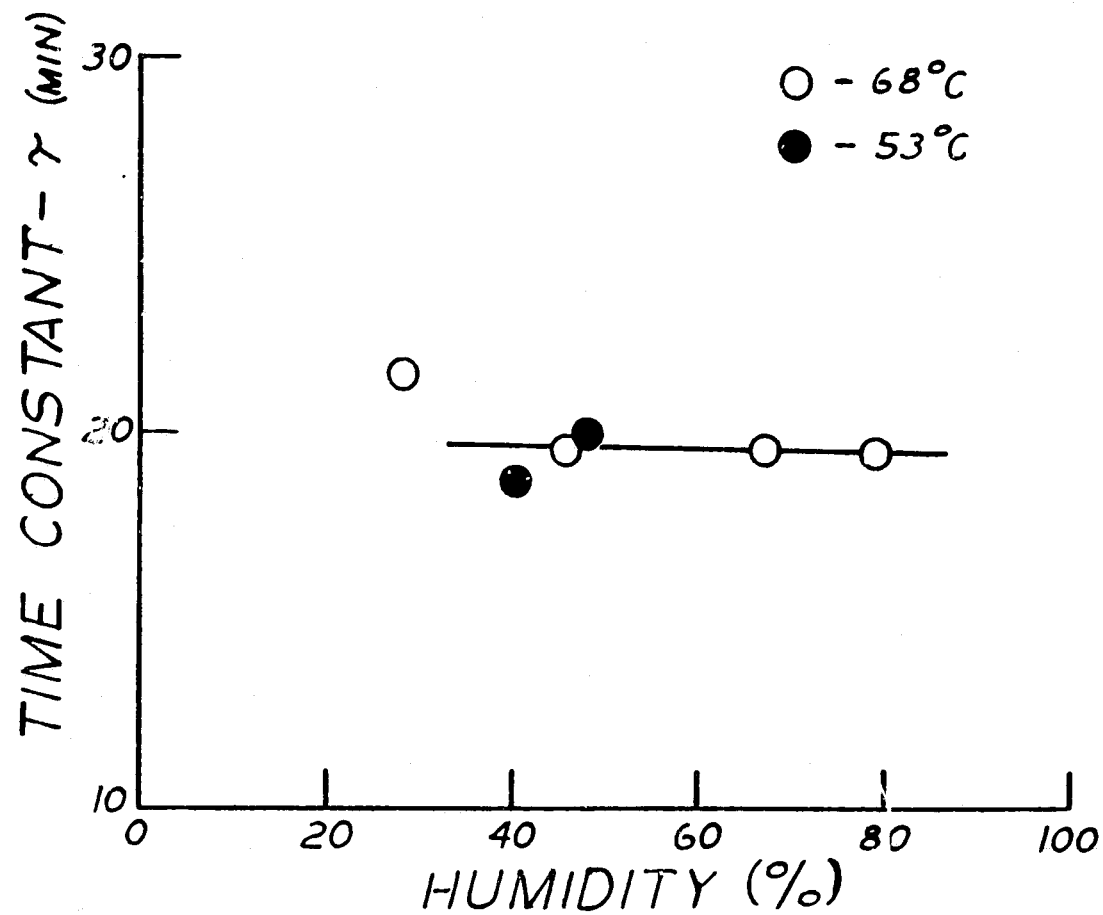


Fig 5.15-Humidity dependence of the time constants associated with the initial transient current response data shown in Figures 5.5 and 5.6 for EVA at 53° and 68°C.

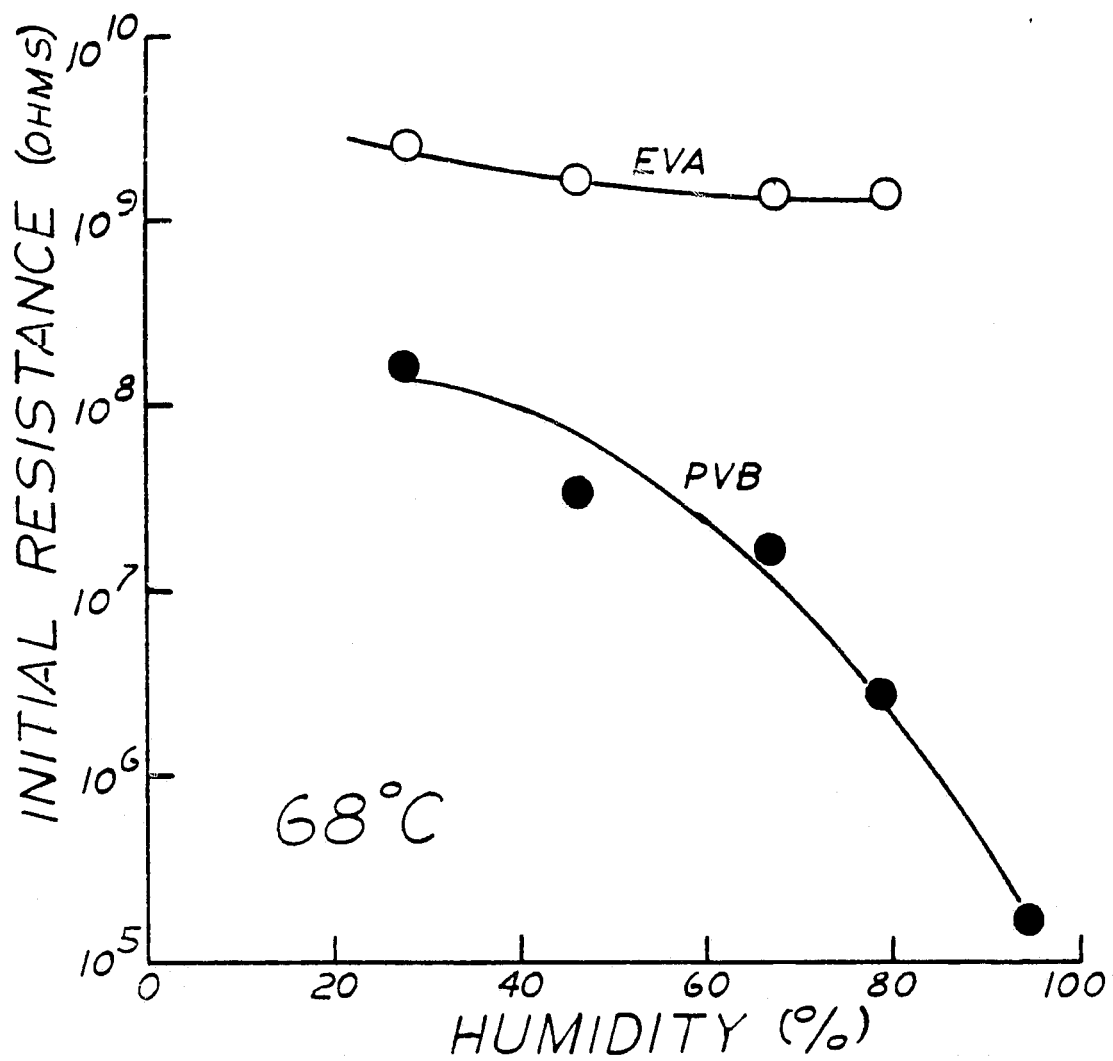


Fig 5.16-A comparison of the initial resistance as a function of humidity for EVA and PVB at 68°C .

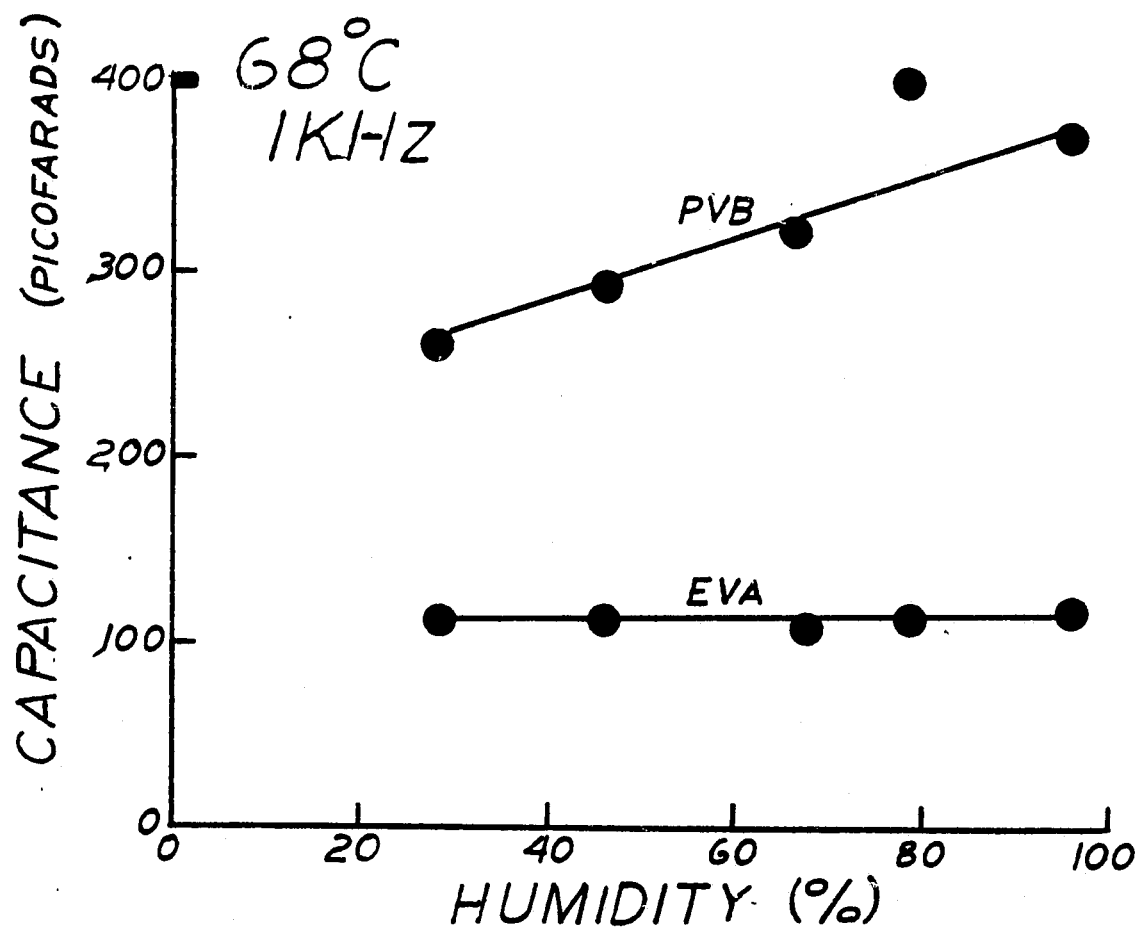


Fig. 5.17-Comparison of the capacitance at 1KHz of PVB and EVA at 68°C.

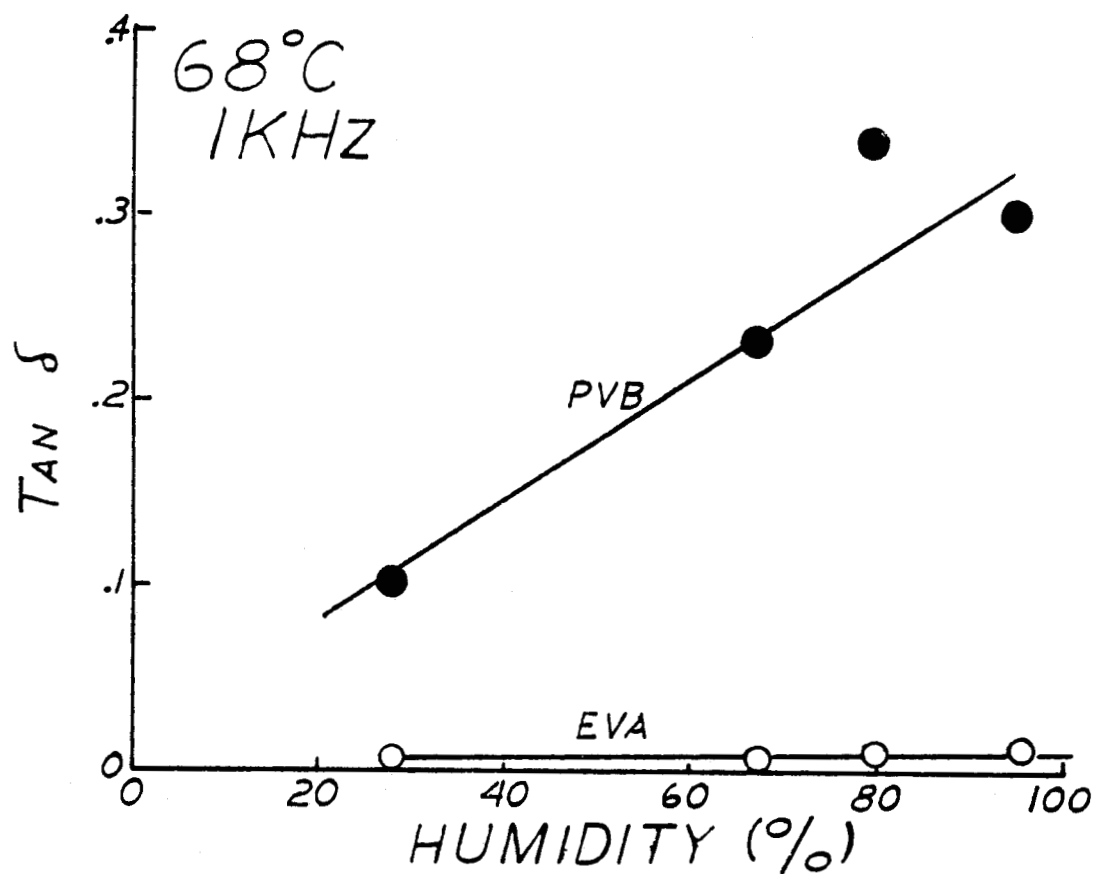


Fig. 5.18-A comparison of the dissipation factor at 1KHz as a function of humidity for EVA and PVB at 68°C.

VI. Solar Cell Corrosion Characteristics:

Corrosion in array mounted, polymer encapsulated solar cells in photovoltaic modules is expected to result from three major causes:

(i) intracell galvanic action corrosion -- The composite structure of dissimilar materials: (metallization layers, anti-reflection coating, silicon substrate) in ohmic contact on a single cell will result in corrosion effects on that cell provided the encapsulating polymer can serve as an electrolyte.

(ii) Inter-cell impressed voltage corrosion -- The potential differences that must exist between adjacent cells in an illuminated array, makes one solar cell anodic relative to its cathodic neighbor. In the presence of an electrolytic encapsulating polymer, the resulting oxidation reaction at the anodic solar cell is corrosive while the associated reduction at the cathodic solar cell can result in plating. Both reactions are expected to degrade the output characteristics of their respective solar cells.

(iii) Intracell IR potential drop corrosion -- The current that flows through the solar cells as a result of illumination can be corrosive on each individual cell as a result of the IR potential drop that must exist across each cell.

The ultimate questions to be resolved in a study of corrosion effects in solar cells are: What is the relative magnitude of each of these corrosion causing effects, how can these effects be minimized to obtain reliable-long lifetime cells, and how are these effects related to the solar cell output characteristics and to solar cell parameters such as the series and shunt resistances?

An evaluation of these corrosion effects involved two experiments:

(A) Corrosion effects in water immersed and in EVA encapsulated solar cells.

(B) Corrosion effects in PVB encapsulated solar cells.

(A) Corrosion in Water Immersed and in EVA Encapsulated Solar Cells

An attempt was made to evaluate the influence of the intercell and the intra cell corrosion effects on the I-V characteristic response curves of the illuminated cells and on the visual physical features of the cells. Figure 6.1 illustrates the experimental arrangements used to separate and evaluate each corrosion effect. Arrangement #4 represents a single solar cell. When this cell arrangement is immersed in an electrolyte, only the intracell galvanic corrosion effect is occurring and being evaluated. In arrangement #3, a single solar cell is forward biased to produce a diode current through the cell. When immersed in an electrolyte, both intracell galvanic action and intracell IR potential drop corrosion effects are activated. A comparison of the corrosion characteristics of the cells in arrangements #3 and #4 yields an evaluation of the IR drop corrosion effect. Arrangement #2 consists of two solar cells properly connected to a power supply so a potential difference exists between the cells but no current flows through the cells. When immersed in an electrolyte, only a corrosion current flows between the cells. A comparison of the corrosion characteristics of the cells in arrangements #2 and #4 give the intercell impressed voltage corrosion effect at an anodic and a cathodic cell. Arrangement #1 is used to simulate actual corrosion conditions in solar cell arrays where all three corrosion effects are present. The solar cells used in these studies were supplied by ASEC.

The corrosion testing consisted of immersing one set of these four cell arrangements in water as an electrolyte at 25°C. Another set was encapsulated in EVA and then immersed in water at 85°C. The cells were allowed to corrode for 120 hours. During the corrosion time, the solar cells were removed occasionally from the bath, and their I-V characteristic response curves were evaluated. The normalized short circuit response as a function of corrosion time is shown in Figures 6.2 and 6.3 for a water electrolyte and a EVA electrolyte respectively. A visual inspection of the cells after the 120 hour corrosion treatment revealed a number of effects caused by the corrosion treatment. These effects for the various corrosion conditions are presented in Table 6.1. A careful comparative examination of Table 6.1 and Figures 6.2 and 6.3 indicates that the intracell galvanic effect is not a major contributor to corrosion in solar cells. In general, the intracell IR drop corrosion effect does not appear to be the dominant effect causing corrosion degradation of the cells. Corrosion appears to result mostly from potential differences between adjacent cells. These conclusions are tentative since there was no real definitive trends apparent in the data, and since several cells were apparently of poor quality and went bad almost immediately during corrosion testing. One trend apparent when comparing Figure 6.2 with Figure 6.3 is that the cells in EVA degraded significantly faster than the cells tested in water. The only apparent reason for this behavior is that EVA with its absorbed water may be a more hostile electrolytic environment than water. A simple pH test appears to confirm this suggestion. A sample of EVA was placed in a beaker of water for three months. The pH of the water was originally 6.7 and after three months the pH was 6.2. A similar test using a PVB sample resulted in a final pH of 4.5 (Table 6.2). Apparently water absorbed in EVA or PVB can be acidic, and corrosive to solar cells.

(B) Corrosion in PVB Encapsulated Solar Cells

These experiments consisted of encapsulating ASEC solar cells in a PVB pottant. After encapsulation, the assemblies were immersed in water to saturate the PVB. The testing procedure for evaluating cell degradation due to corrosion consisted of measuring the I-V characteristics curves of each encapsulated cell as a function of immersion time in water for various testing arrangements designed to evaluate intercell and intracell corrosion activity. The first test arrangement (Cell #1) was an unbiased, nonilluminated, short circuited single cell where any degradation of the original I-V response curve as a function of immersion aging time would result from the intracell galvanic corrosion effect alone. The second test arrangement (Cell #2) was an illuminated, short circuited cell where any observed degradation of the original I-V response curve is expected to be a measure of the combined effects of both the intracell galvanic and intracell IR drop corrosion effects. The third test arrangement (cells #3 cathode and #4 anode) was a coupled anode--cathode configuration where the cells were both biased and illuminated. These encapsulated cells were coupled by short circuiting their front side metallurgies and by connecting a 5 volt biasing battery between their back side metallurgies. No junction current due to the biasing battery is expected since the #3 cathode cell was back biased in the coupling arrangement. Any observed degradation of the original I-V response curves of both the anode and cathode cells should then reflect the combined effects of intercell and intracell corrosion mechanisms. By simply comparing the relative changes in the I-V response curves of these four cells in these three testing arrangements as a function of immersion time, the magnitudes of the intercell, and intracell degradation effects can be separated and evaluated.

Results

A typical sequence of I-V response curves at various immersion times is shown in Figure 6.4 for the #3 cathode cell. From these curves for all four cells, the short circuit current (I_{SC}) and the series (R_S) and shunt (R_{sh}) resistances were determined as a function of immersion time.

The results for the short circuit are presented in Figure 6.5. For up to five days of testing, there appeared to be no significant difference between the degradation of I_{SC} in cell #1 (intracell-galvanic corrosion) and cell #2 (intracell-galvanic and IR drop corrosion).

On the basis of these observed features, it was concluded that the intracell IR drop corrosion effect has little or no influence on solar cell degradation. After five days of testing, the I_{SC} response of cell #4 (anode-intercell and intracell corrosion) was found to degrade much more (Figure 6.5) than cells, #1, #2 and #3 (cathode--intercell and intracell corrosion).

After twenty days of testing, the degradation of I_{SC} in both the cathode and anode cells is about equal and significantly larger than the I_{SC} degradation in cell #2 (Figure 6.5). The intercell and intracell effects can be separated by comparing the results for cell #2 with cells #3 and #4. For twenty hours of testing, this separation is shown on Figure 6.5 where it is apparent that the degradation of I_{SC} due to intercell corrosion appears to be about equal in magnitude to that due to intracell corrosion. Since the applied potential difference between the two cells in this study

is small compared with potential differences frequently occurring between adjacent cells in module mounted arrays, the intercell corrosion effect is expected to have a significantly larger influence on degrading solar cell activity than the intracell corrosion effect. The surprising feature of the data after twenty days, is that I_{sc} for the cathodic cell degraded as much as for the anodic cell.

The time dependence of R_s and R_{sh} can also be evaluated from the I-V curves for each cell in the various testing arrangements. A comparison of R_s as a function of time for the anodic and cathodic cells is presented in Figure 6.6. The series resistance for the anodic cell increased continuously with time while R_s for the cathodic cell remains relatively time independent for time values less than ten days. After ten days, R_s of the cathode cell increases rapidly.

The continuous increase of R_s with time for the anodic cell can be justified from simple considerations. As a first approximation, the series resistance would be given by

$$R_s = \rho_c l_c / A_c \quad 6.1$$

or

$$dR_s = -[\rho_c l_c / A_c^2] dA_c \quad 6.2$$

where ρ_c is the composite resistivity of the front side metallization, l_c is its effective length and A_c is its cross sectional area. Faraday's law suggests that electrochemical corrosion at the anode will decrease the cross sectional area at a constant rate (K):

$$dA_c / dt = -K \quad 6.3$$

so

$$dR_s = [\rho_c l_c / A_c^2] K dt$$

6.4

or

$$R_s \sim t$$

6.5

This predicted continuous increase in R_s with time is evident in the anode data shown in Figure 6.6.

The observed time dependence for the R_s data of the cathode can also be justified by simple considerations. Electrochemical plating occurs at the cathode. The series resistance could then be given approximately by

$$1/R_s = 1/R_c + 1/R_f = A_c / \rho_c l_c + A_f / \rho_f l_f$$

6.6

where ρ_f , l_f and A_f are the resistivity, effective length and cross sectional area of the plated film. The cross sectional area of the plated film is proportional to its thickness (x_f):

$$A_f \sim x_f$$

6.7

and x_f for a simple plating operation is directly proportional to the time:

$$x_f \sim t$$

6.8

The series resistance for the cathode cell from Equation 6.6 would then involve a composite resistance term (R_c).

$$R_c = \rho_c l_c / A_c = f_c t(t)$$

6.9

which is time independent and a plated film resistance term R_f

$$R_f = \rho_f l_f / A_f = f_f t(t)$$

6.10

which is time dependent. Initially when the plated thickness is thin, so

$$R_c < R_f$$

6.11

and the series resistance will simply be equal to the time independent composite resistance term

$$R_s = R_c$$

6.12

The experimental data support this conclusion in that R_s for the cathode cell is independent of time when time is less than 5 days (Fig. 6.6). At longer immersion time values when X_f is not thin

$$R_f < R_e$$

6.13

and the series resistance becomes linearly time dependent:

$$R_s \approx R_f = K, t$$

6.14

This predicted feature is also evident in the experimental data of the cathode cell (fig. 6.6) for time values in excess of five days.

The series resistance of cell #2 which monitors intracell corrosion effects as a function of time, is shown in Figure 6.7 and is seen to be much less time dependent than was evident in the anodic or cathodic cell results (Fig. 6.6). This comparative feature supports the previous suggestion that intercell corrosion is more influential than intracell corrosion in causing solar cell degradation.

The behavior of the shunt resistance as a function of time for these various cells is presented in Figures 6.8 and 6.9. The shunt resistance of the cathodic cell decreases continuously and rapidly with time (Fig. 6.8) while R_{sh} for the anodic cell remains time independent until about five days have elapsed, and then decreases rapidly with time (Fig. 6.8). The time dependence of R_{sh} for cell #2, is shown in Figure 6.9 and is almost identical to the functional response seen in Figure 6.8 for the anodic cell. This similarity suggests that only the intracell corrosion effect is governing the R_{sh} behavior of the anodic cell.

Simple intercell plating considerations can be used to explain the time dependence of R_{sh} in the cathodic cell. The continuous decrease in R_{sh} with time in the cathodic cell shown in Figure 6.8, will result when

plating occurs on a cell edge. This plated film effectively shorts the front side metallization to the back side metals with a film that gets progressively thicker (less resistive) with increasing time as suggested by Equation 6.8.

For the anode cell, simple intercell corrosion considerations would suggest that R_{sh} should remain constant--or perhaps even increase--and not decrease with time. This feature is evident in Figure 6.8 for the anode for time values less than five days. For time values greater than five days, the shunt resistance decreases rapidly. The reason for this decrease is not clear. Figure 6.5 suggests that intracell corrosion effects become evident after five days so the corresponding intracell plating or possible dendrite formation may be responsible for the decrease in R_{sh} .

These simplified plating concepts that were used to explain the behavior of R_{sh} and R_s as a function of time in the cathodic cell can also be used to show that I_{sc} should decrease with time in the cathodic cell. A thin plated film decreases the intensity of the light being transmitted through the film into the solar cell by an amount that is governed by the absorption law which for a plated film of thickness x_f is:

$$P_s \sim \exp(-\alpha x_f) \quad 6.15$$

where α is the absorption coefficient and P_s is the intensity of the light transmitted into the cell. Since I_{sc} is directly proportional to P_s

$$I_{sc} \sim P_s \quad 6.16$$

then the short circuit current becomes

$$I_{sc} \sim \exp(-\alpha x_f) \quad 6.17$$

or from Equation 6.8

$$I_{sc} \sim \exp(-k_2 t)$$

6.18

showing that the short circuit current decreases with time for the cathode cell as is evident in Figure 6.5 which shows a linear decrease even though Equation 6.18 predicts an exponential decrease.

Summary

Intracell corrosion effect in solar cells by either galvanic action or an IR potential drop is not primarily responsible for cell degradation with time.

Intercell corrosion at anodic cells and intercell plating at cathodic cells are instrumental in causing cell degradation.

The experimentally observed degradation of R_s , R_{sh} , and I_{sc} , as a function of time for the anodic and cathodic solar cells were in reasonable agreement with predictions based upon simple corrosion and plating concepts.

TABLE 6.1

Visual characterization of various corrosion effects in EVA encapsulated and water immersed solar cells.

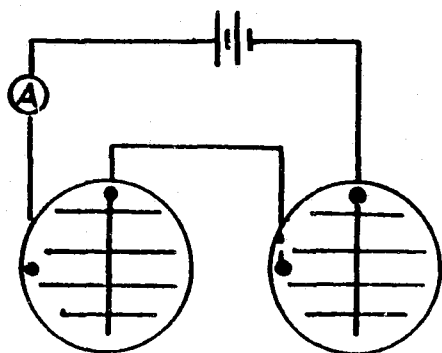
Corrosion Conditions	Corrodes (C) or Undermines (U) Grid Metalliz.	Attacks A/R Coating	Discolors Backside Metalliz.	Lifts Backside Metalliz.
EVA ENCAPSULATED				
Galvanic, diode & voltage (anode)				X
Galvanic, diode & voltage (cathode)		X		X
Galvanic & voltage (anode)		X		X
Galvanic & voltage (cathode)		X		X
Galvanic				
NOT ENCAPSULATED (IN WATER)				
Galvanic, diode & voltage (anode)				
Galvanic, diode & voltage (cathode)				
Galvanic & voltage (anode)	X (U)		X	X
Galvanic & voltage (cathode)				
Galvanic & diode	X (U)	X	X	
Galvanic				

TABLE 6.2

The influence of immersed EVA and PVB samples on the pH of water.

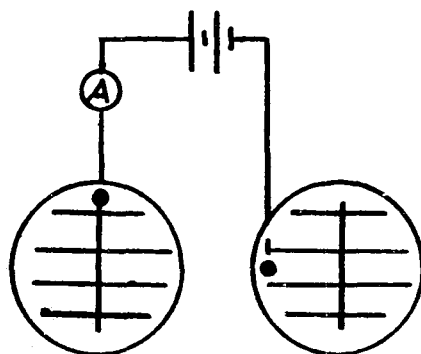
	pH
Original Water	6.7
Water after three months with immersed EVA sample	6.4
Water after three months with immersed PVB sample	4.5

#1
ARRANGEMENT



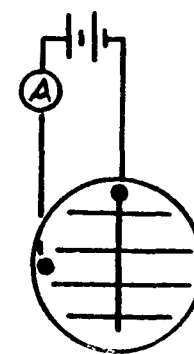
ANODE **CATHODE**
INTERCELL IMPRESSED VOLTAGE
CORROSION; INTRACELL DIODE
CURRENT CORROSION; AND
INTRACELL GALVANIC
CORROSION EFFECTS

#2
ARRANGEMENT



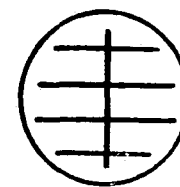
ANODE **CATHODE**
INTERCELL IMPRESSED
VOLTAGE CORROSION AND
INTRACELL GALVANIC
CORROSION EFFECTS

#3
ARRANGEMENT



INTRACELL DIODE
CURRENT CORROSION
AND INTRACELL
GALVANIC CORROSION
EFFECTS

#4
ARRANGEMENT



INTRACELL
GALVANIC
CORROSION
EFFECT

Fig. 6.1-Biasing conditions of various solar cell arrangements for evaluating various corrosion effects.

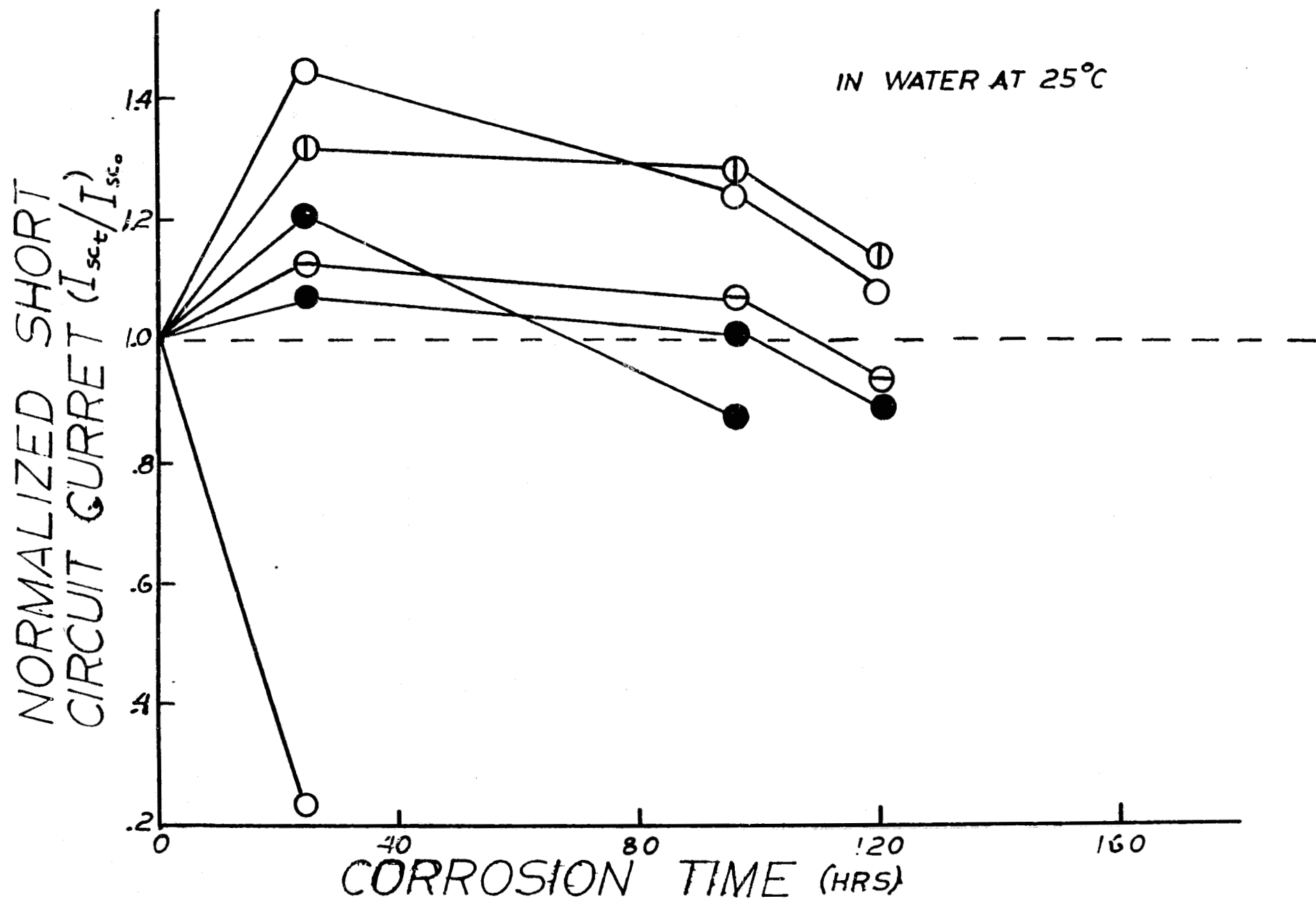


Fig. 6.2-Normalized short circuit current as a function of corrosion time for solar cells exposed to the #1 to #4 arrangements of Figure 6.1 when the cells are tested in water at 25°C.

EVA ENCAPSULATED CELLS AT 25°C

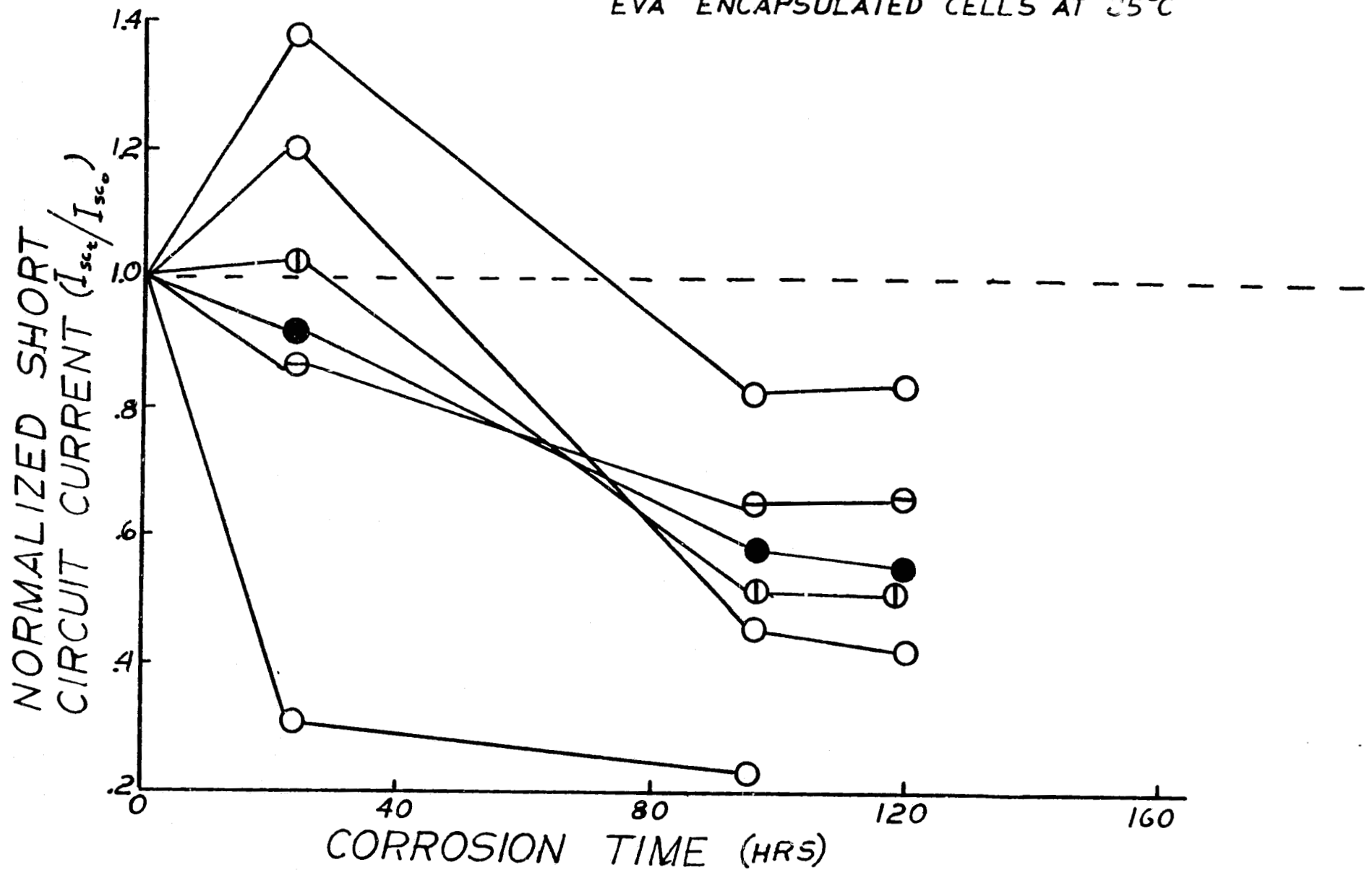


Fig. 6.3-Normalized short circuit current as a function of corrosion time for solar cells exposed to the #1 to #4 arrangements of Figure 6.1 when the cells are EVA encapsulated and tested in water at 85°C.

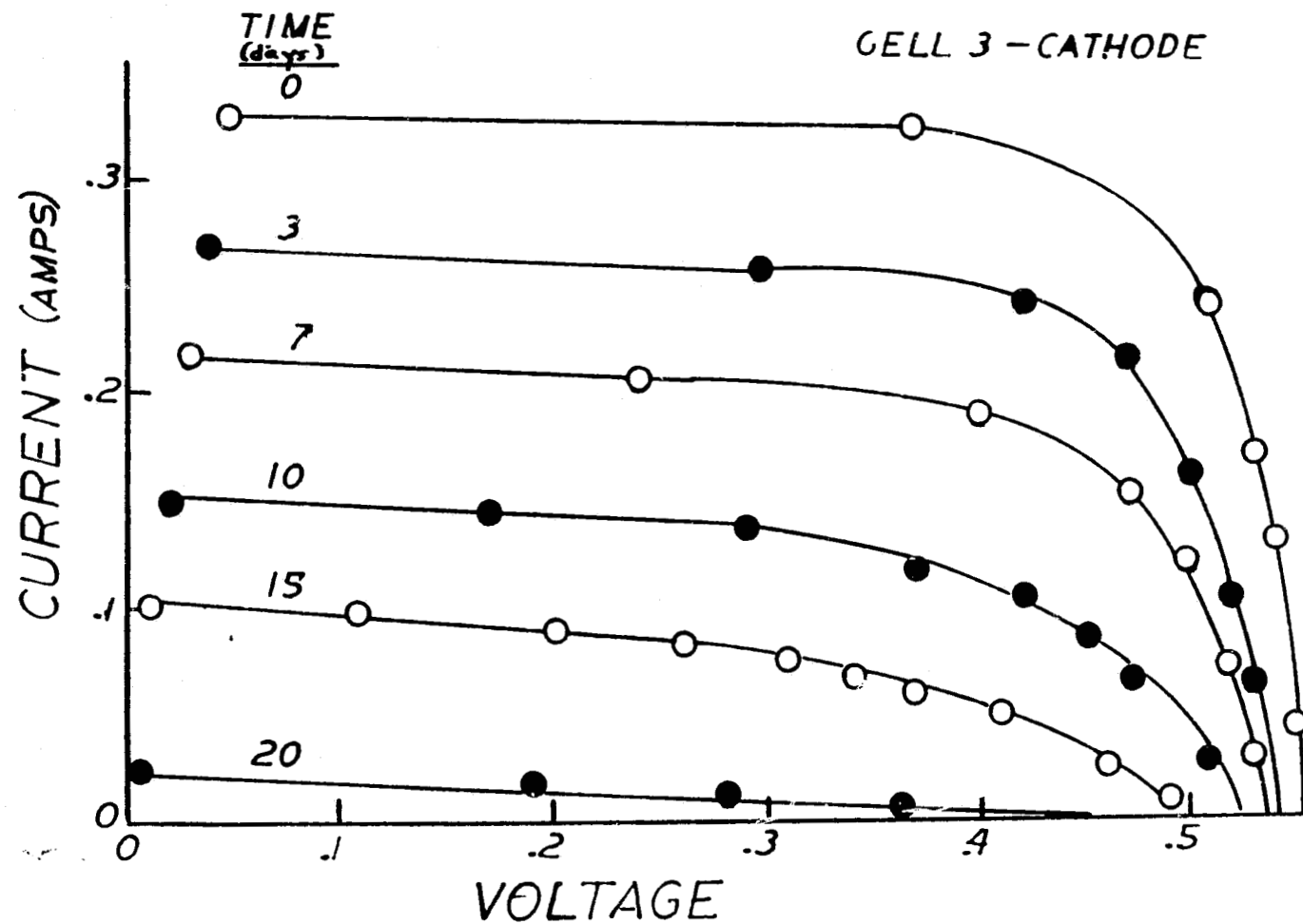


Fig. 6.4-Characteristic current voltage response curves of a cathodically polarized, PVB encapsulated solar cell for various aging times.

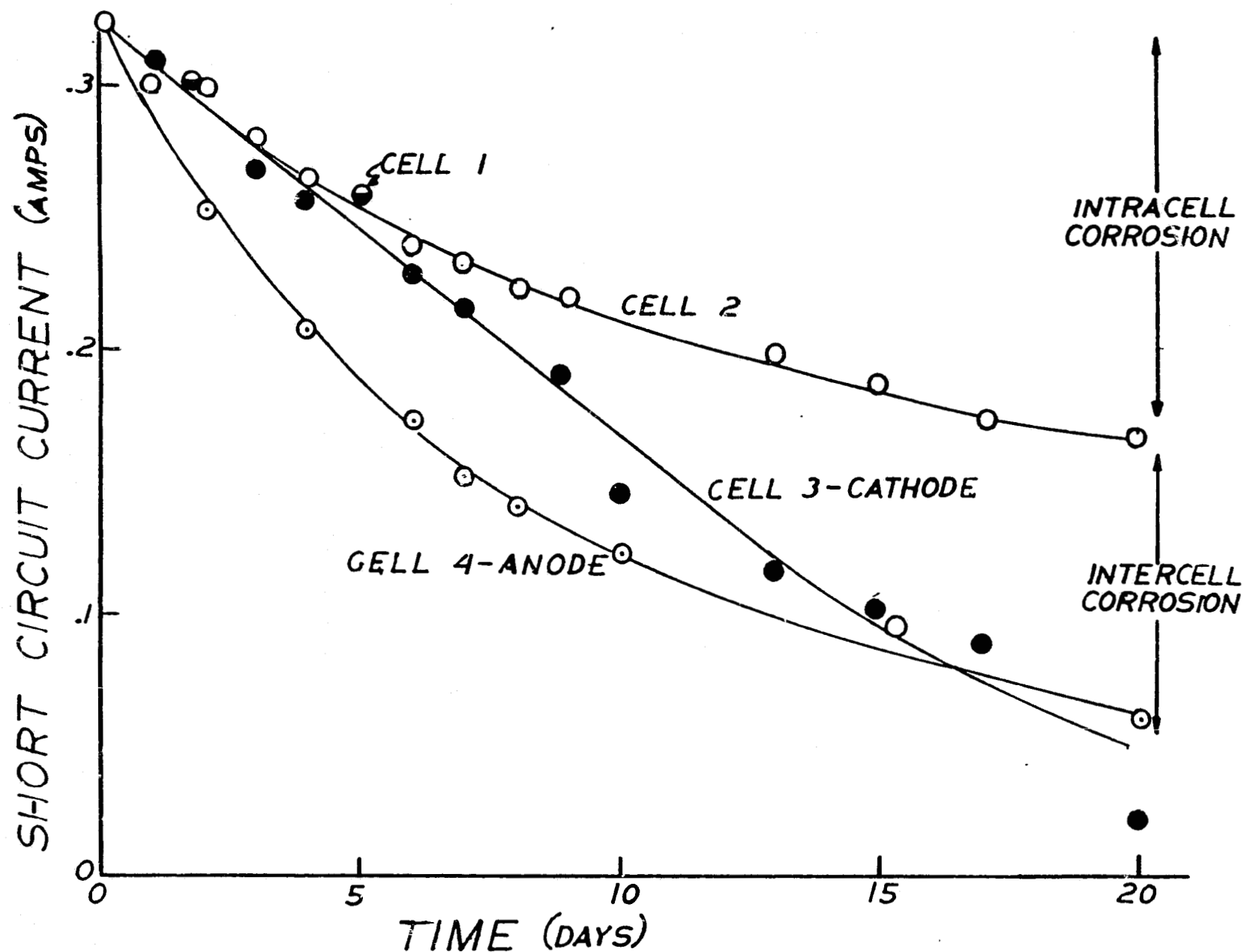


Fig. 6.5-Short circuit current as a function of aging time for PVB encapsulated solar cells representing: intracell galvanic corrosion (cell #1); intracell galvanic and IR drop corrosion (cell #2); and intracell galvanic, IR drop and intercell corrosion (cell #3 -cathodically polarized and cell #4 anodically polarized).

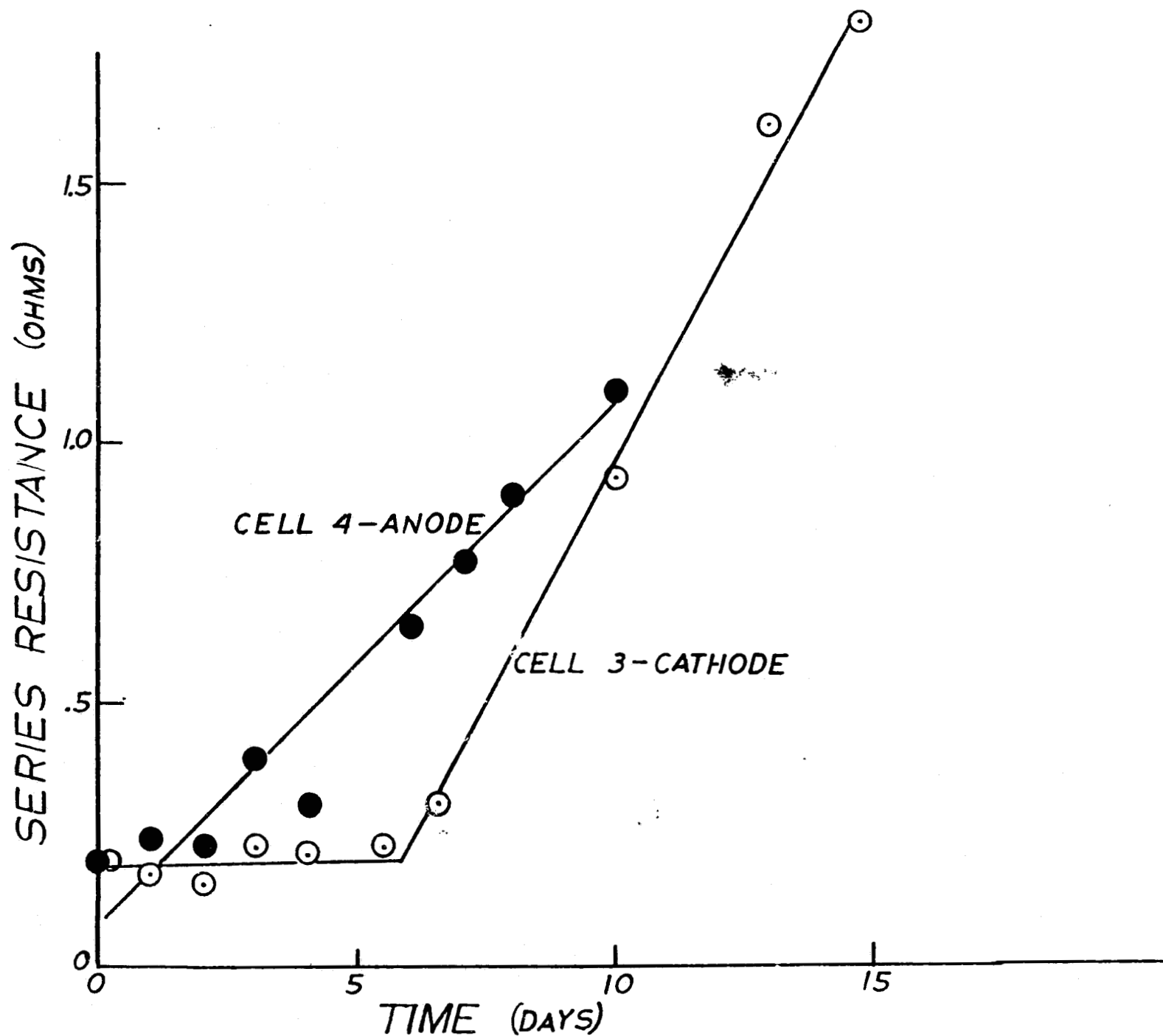


Fig 6.6-Series resistance as a function of aging time for PVB encapsulated solar cells experiencing intercell and intracell corrosion effects in cathodic polarization (cell #3) and in anodic polarization (cell #4).

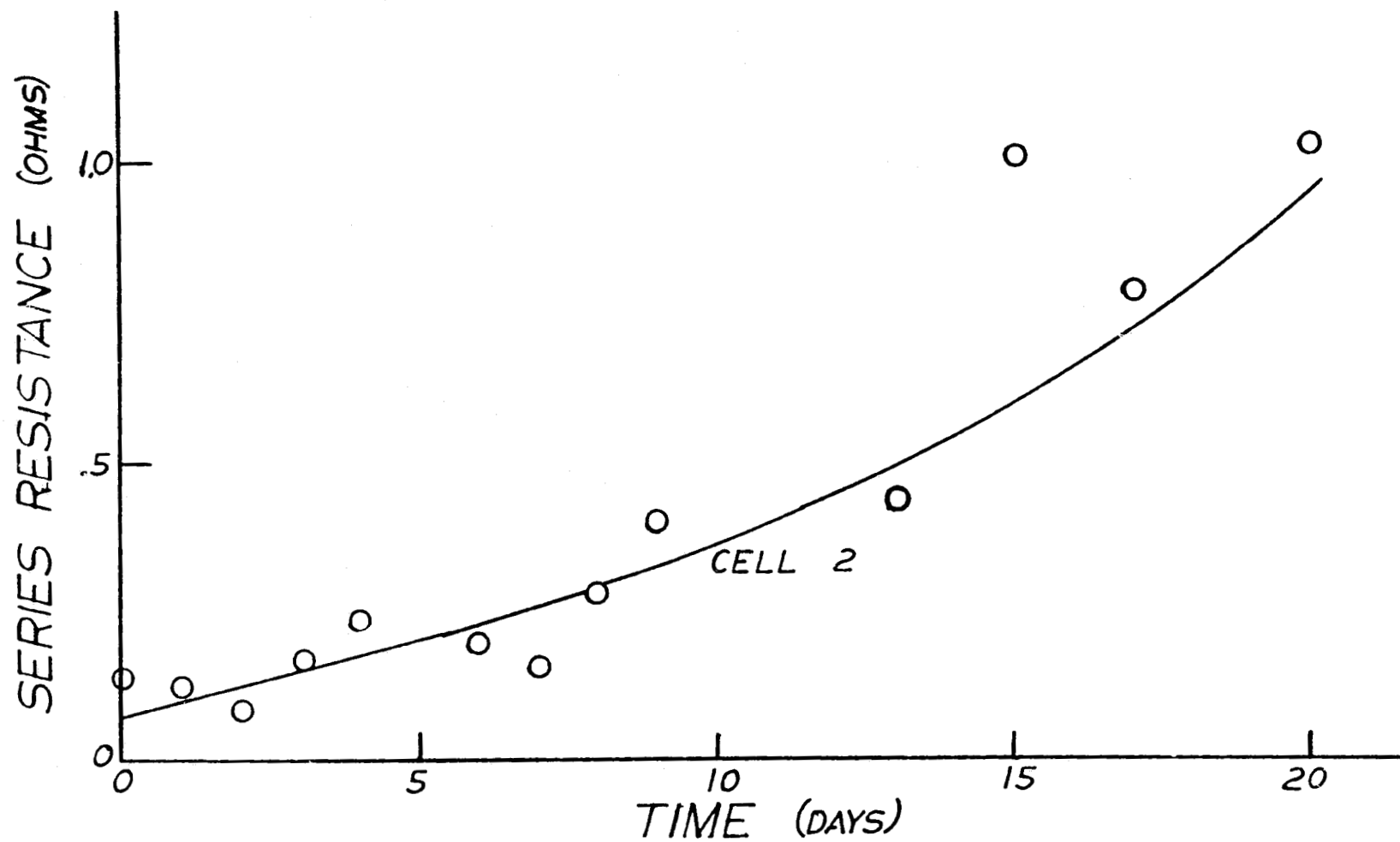


Fig. 6.7 - Series resistance as a function of aging time for a PVB encapsulated solar cell experiencing intracell corrosion effects.

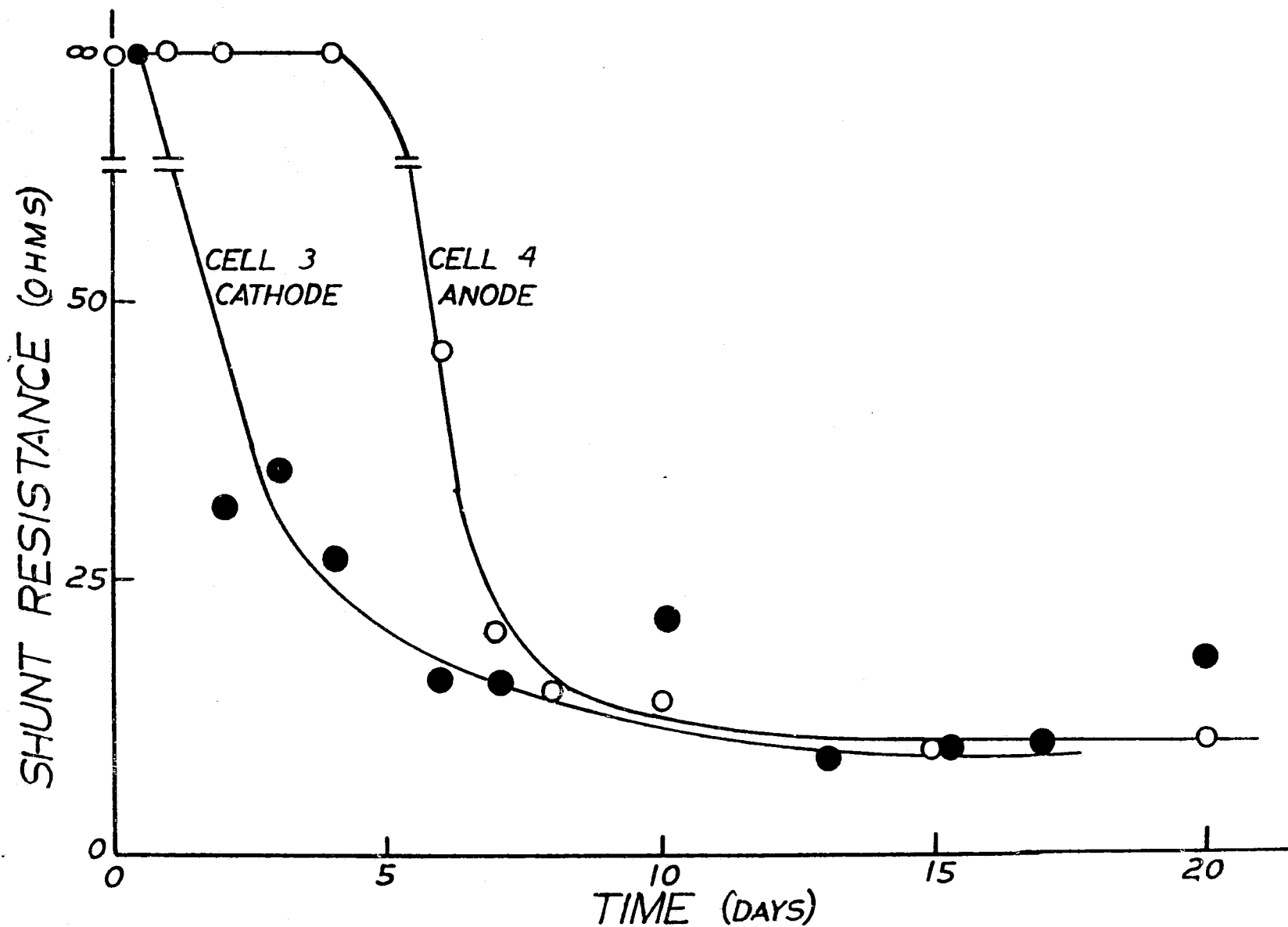


Figure 6.8-Shunt resistance as a function of aging time for PVB encapsulated solar cells experiencing intercell and intracell corrosion effects in cathodic polarization (cell #3) in anodic polarization (cell #4).

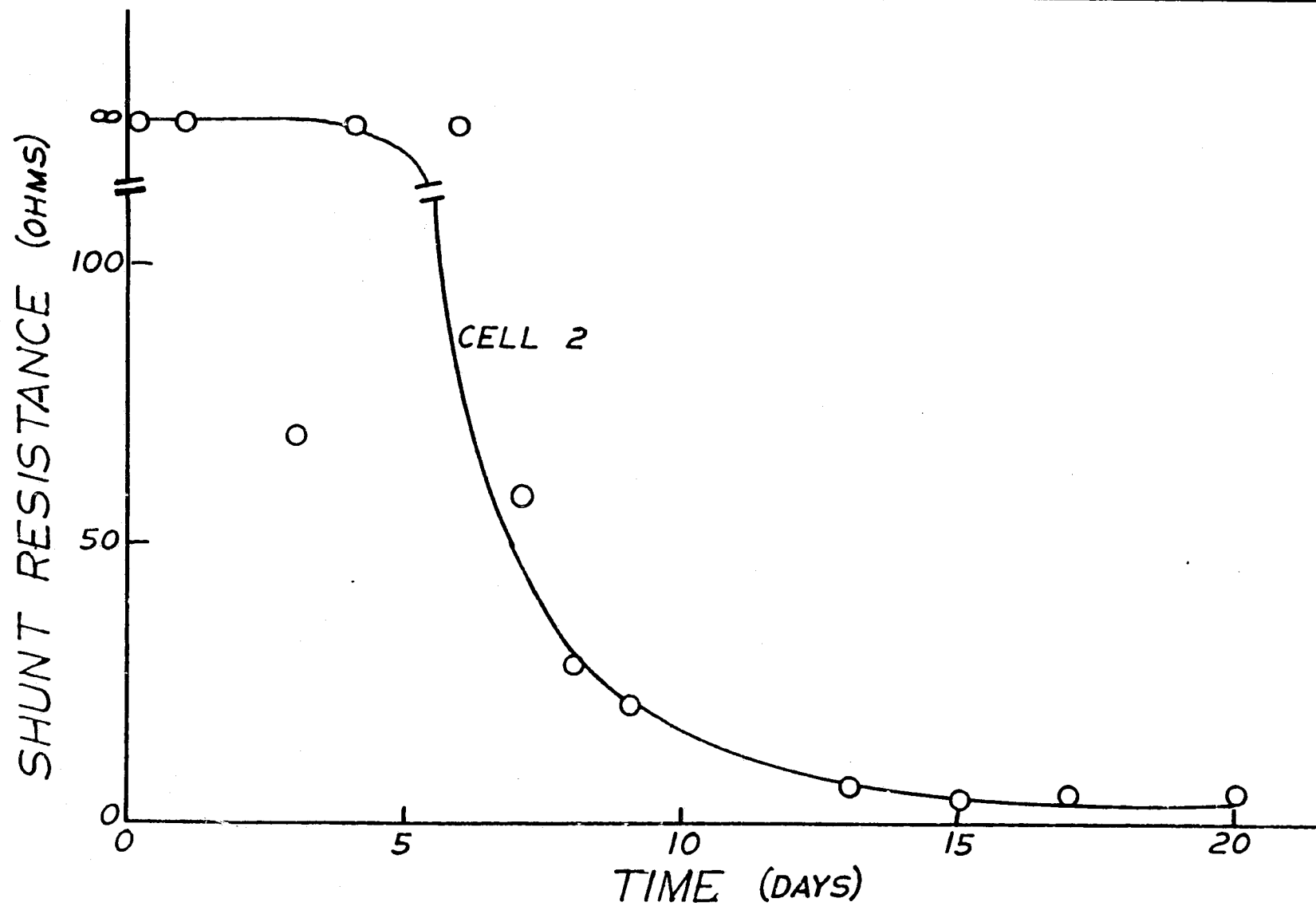


Fig. 6.9 - Shunt resistance as a function of aging time for a PVB encapsulated solar cell experiencing intracell corrosion effects.

VII Water Absorption Effects in PVB and EVA

PVB was found to absorb large amounts of water at 100% humidity. Since the amount of water absorbed should be proportional to the humidity, and since the electrical properties of PVB were found to be influenced profoundly by the humidity, it becomes instructive to examine water absorption effects in both PVB and EVA. Two specific effects were examined:

- (A) The influence of plasticizer on water absorption in PVB;
- (B) UV light effects on water absorption in PVB and EVA.

(A) Influence of Plasticizer on Water Absorption in PVB

The water absorption characteristics of unplasticized PVB and plasticized PVB were evaluated. Samples of both materials were immersed in water at 25°C and the weight gain characteristics were monitored periodically over a time span of 500 hours. The results are shown in Figure 7.1. The unplasticized PVB absorbs considerably more water than the plasticized PVB. This result suggests that the plasticizer occupies an excludable volume in the PVB, and when the plasticizer is removed, this excludable volume can be occupied by water. Experimentally observed numbers appear to support this suggestion. Commercial PVB is about 30 weight percent plasticizer and this plasticized PVB can absorb about 10 weight percent water. On an excludable volume basis, unplasticized PVB would be expected to accommodate up to 40 weight percent water which is in reasonable agreement with the observed 50 weight percent saturation value. The numbers appear to add up correctly but there is no fundamental reason why they should.

(B) UV Light Effects on Water Absorption in PVB and EVA

Gravimetric techniques were employed to monitor the influence of UV radiation on the water absorption kinetics of PVB and EVA. The normalized weight response of plasticized PVB samples in a 100% humid environment at 75⁰ and 50⁰C while being exposed to UV radiation is shown in Figure 7.2. For comparative purposes, the normalized weight response for non-irradiated PVB samples exposed to the same temperature/humidity environment is also shown in Figure 7.2. The experimental arrangement proved to be awkward, and a considerable amount of scatter in the data was evident. Even with this uncertainty, the data clearly showed that non-irradiated PVB samples gained much more weight than the UV-irradiated samples. The other feature evident in the data is that at longer exposure times, the UV-irradiated samples lost weight. The implications of this data are that an exposure to UV light will hinder the water absorption characteristics of PVB and will accelerate the kinetics of plasticizer loss in PVB. These tentative conclusions are partially supported by simple observations of the samples after terminating the experiments. The non-irradiated sample had an opaque cloudy appearance which is typical of PVB containing a large amount of water. The UV-irradiated samples remained transparent throughout the entire experimental run, indicating that very little water was absorbed. After the runs were terminated, another noticeable distinction was apparent between the irradiated and nonirradiated samples: the UV-irradiated samples collapsed around the wire support picture frame across which they had been attached, while non-irradiated samples remained intact, and stretched across the frame. Apparently, the PVB samples after UV light exposure at 100% humidity and temperatures in excess of 50⁰C, lost a considerable amount of strength as a probable

result of chain scission by the UV light. The collapsed UV-irradiated PVB samples were soft and flexible indicating that chain scission could have occurred or that the amount of plasticizer loss in these samples was minimal. A summary of the contrasting characteristics between the irradiated and non-irradiated PVB samples is presented in Table 7.1.

The water absorption characteristics of UV-irradiated and non-irradiated EVA at 75°C and 100% humidity are shown in Figure 7.3. The scatter in the data is again uncomfortably large, but the results clearly demonstrate that EVA absorbs a relatively small amount of water while it is being radiated with UV light, compared to the amount of water absorbed by the non-irradiated EVA sample. A visual comparison of the irradiated and non-irradiated EVA samples after terminating the experimental run did not reveal any distinguishable differences between the sample in their transparency or mechanical characteristics (Table 7.1).

TABLE 7.1

Characteristics of EVA and PVB samples after a 50 hour exposure to 100% humidity at temperatures above 50°C.

	UV- irradiated <u>PVB</u>	non- irradiated <u>PVB</u>	UV- irradiated <u>EVA</u>	non- irradiated <u>EVA</u>
color	transparent	cloudy	transparent	transparent
strength	weak	strong	strong	strong
water absorption	small	large	small	large

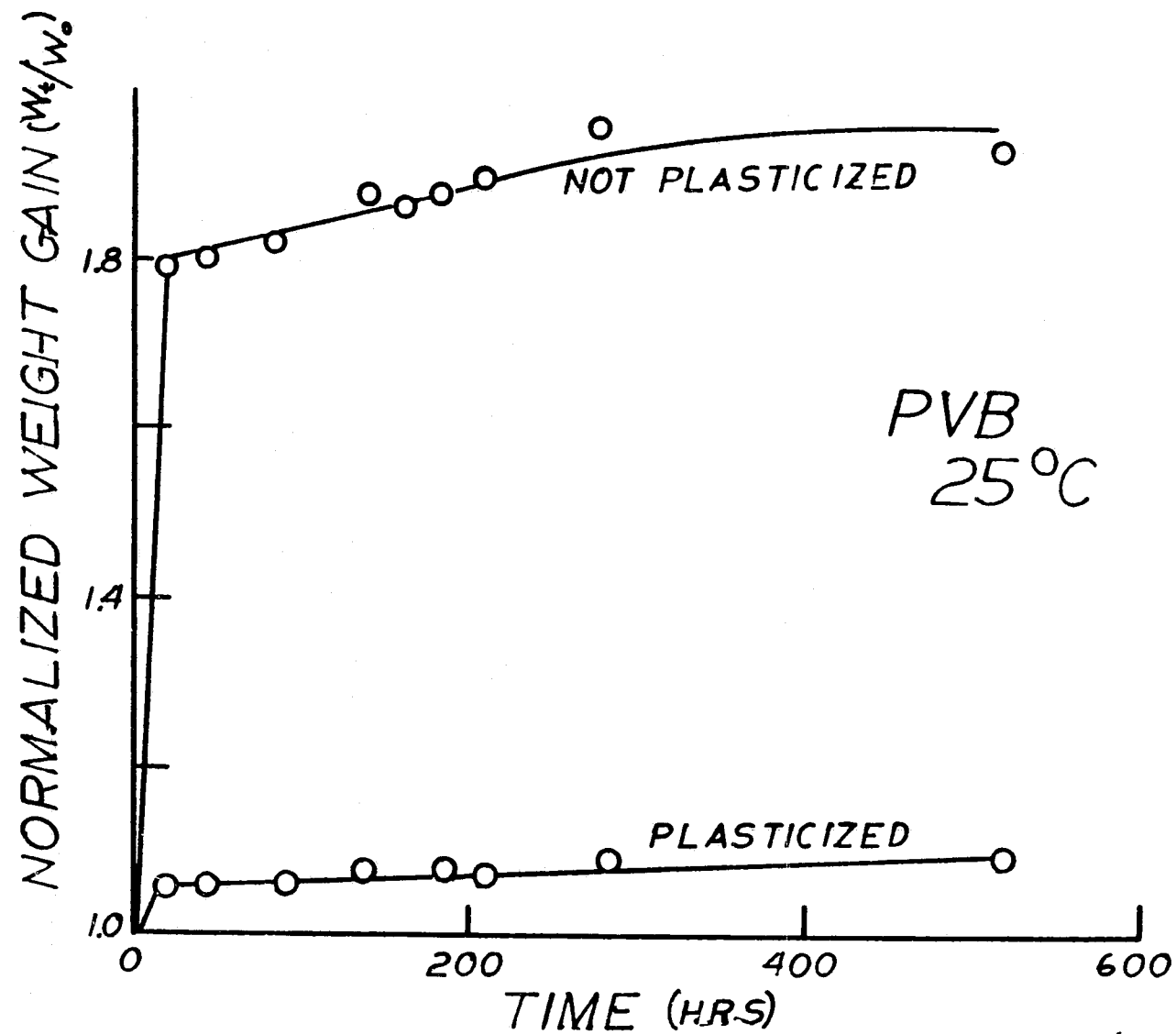


Fig. 7.1 - Time dependence of the normalized weight gain due to water absorption in plasticized and unplasticized PVB samples.

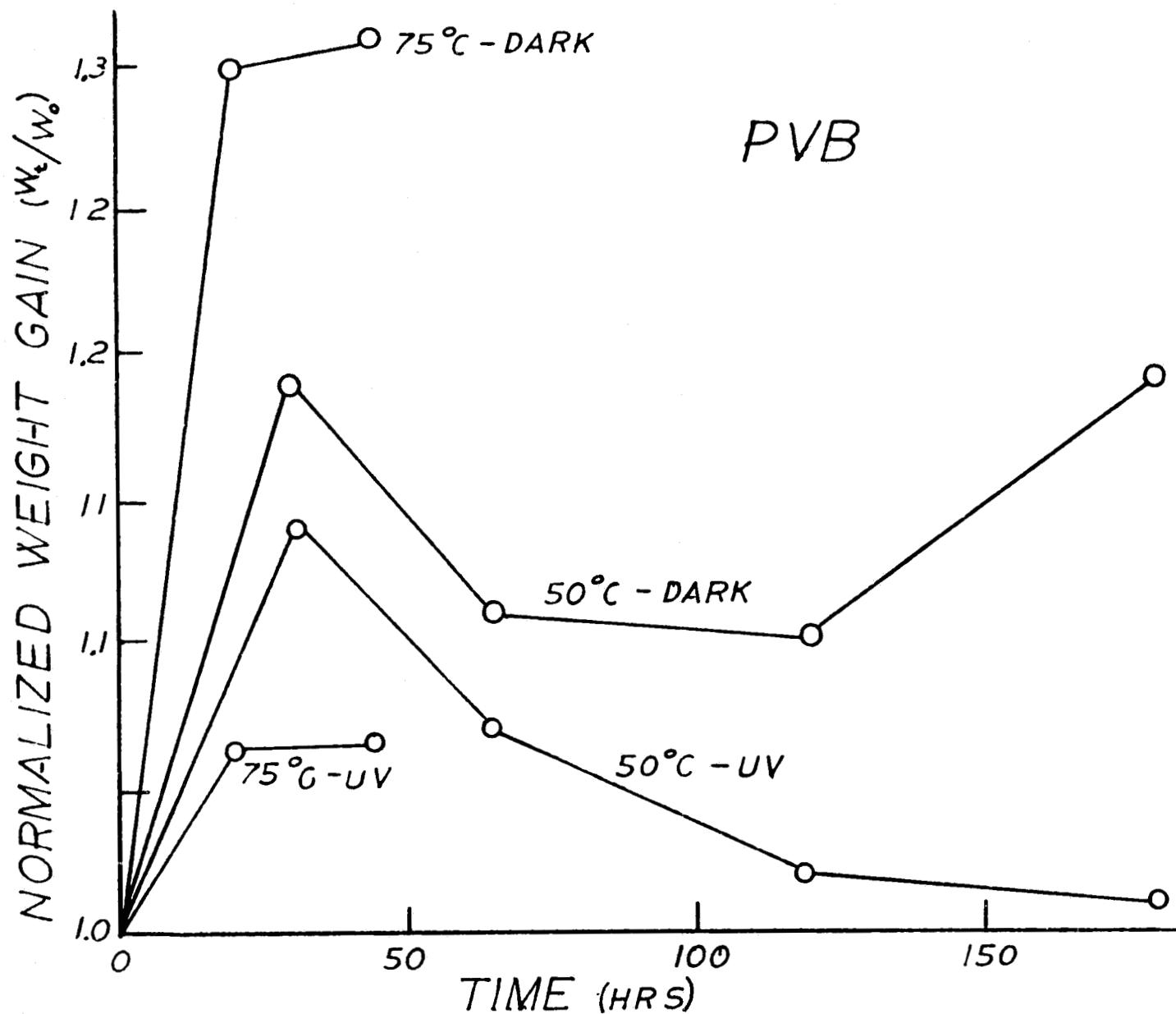


Fig. 7.2—Time dependence of normalized weight gain due to water absorption in PVB samples during UV light exposure and in unexposed PVB samples.

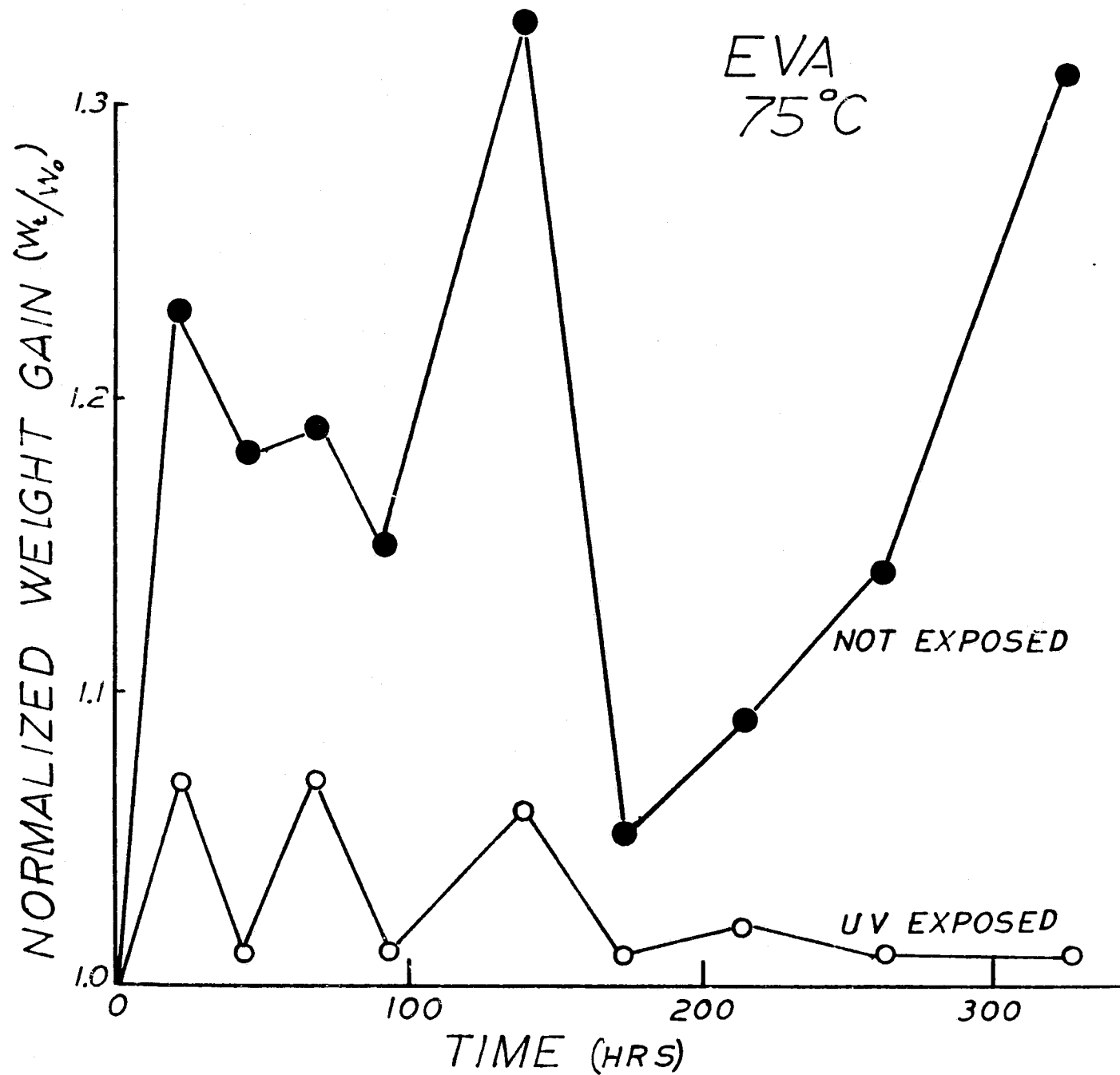


Fig. 7.3—Time dependence of normalized weight gain due to water absorption in an EVA sample during UV light exposure and in an unexposed EVA sample.

VIII. Ion Implantation and Radiation Effects in PVB and EVA

Introduction

Two important concerns in the terrestrial photovoltaic energy program are the lifetime degradation of the solar cells as a result of corrosion effects, and the stability of the polymer pottant material when exposed to ionizing radiation. Both these concerns were addressed experimentally by investigating the influence of proton bombardment on the properties of PVB and EVA samples.

For corrosive action, the necessary ingredients--dissimilar materials, electrically conductive connecting paths, potential differences, and an ionically conducting electrolyte--are all inherently present in the polymer encapsulated, solar cell array modules. Except for the electrolyte, these ingredients in the molecules are not easily receptive to modification for minimizing corrosion, and any effort in corrosion control to improve reliability and service lifetime must then focus primarily on the ions in the polymer pottant electrolyte. A simple study of ionic effects in PVB and EVA polymer pottants was made by a proton bombardment experiment where the effect of proton fluence on the electrical resistivity of PVB and EVA was evaluated.

The mechanical and chemical stability of PVB and EVA to proton bombardment was also evaluated. The elastic modulus was used to monitor mechanical stability of a PVB sample as a function of proton fluence. The chemical stability of both EVA and PVB sample was determined by the amount of sample dissolved per unit time in methanol as a function of proton fluence.

EXPERIMENTAL PROCEDURE

PVB and EVA samples were exposed to 100 KeV proton bombardment for fluence up to $1.6 (10^{15}) / \text{cm}^2$. The PVB samples employed in this study were obtained from Monsanto, and the EVA samples were supplied by Springborn Laboratories. The resistance of the samples before and after irradiation were measured by the ASTM specified two probe, grounded ring technique.

The elastic modulus was evaluated from simple tensile tests. The chemical inertness was determined by immersing preweighted irradiated and non-irradiated samples in methanol for forty-eight hours and then reweighing to determine the weight percent polymer dissolved in this solvent.

RESULTS

Proton bombardment had a significant influence on the resistivity. The resistivity of EVA as a function of fluence is shown in Figure 8.1. At low fluences, proton bombardment exposure increases the resistivity while continued bombardment then decreases the resistivity linearly with fluence (ϕ):

$$\rho (\Omega\text{-cm}) = -2.8(10^{-3}) \phi + 57(10^{12}) \quad 8.1$$

The resistivity of the PVB sample increased continuously and linearly with fluence (Fig. 8.2):

$$\rho (\Omega\text{-cm}) = 2.4(10^{-7}) \phi + 10^8 \quad 8.2$$

Proton bombardment had only a very small influence if any of the chemical reactivity of these polymers. PVB before and after bombardment, dissolved appreciably in methanol (Fig. 8.3) and the amount of dissolution appeared to be independent of the fluence. Pre-bombarded EVA was inert

in methanol. When exposed to a low fluence, the EVA appeared to behave as a swollen gel by gaining weight rather than dissolving. At large fluence, the EVA dissolved very slightly (Fig (8.3).

Proton bombardment had an enormous influence on the elastic modulus (Fig 8.4). Exposure to a low fluence increased the elastic modulus by a factor of two while continued exposure to a fluence of $2(10^{15})/\text{cm}^2$ decreased the modulus to its pre-bombarded value.

DISCUSSION

Electrical Resistivity

The movement of ions rather than the movement of electrons is generally accepted to be the dominant mechanism that governs the conductivity characteristics of insulating polymers. The conductivity (σ) and its reciprocal the resistivity (ρ) of a typical insulating polymer is then dependent on the sum of the movement of all positive and negative ionic species contained in the polymer. This dependency can be expressed by an equation that relates the reciprocal resistivity to the summed product of the number of each ion (n), the mobility (μ) of each ion, and the charge (q) of each ion:

$$1/\rho = \sum_i n_i \mu_i q_i + \sum_j n_j \mu_j q_j \quad 8.3$$

where the summation taken places over all i positive ions and j negative ions in the polymer. Numerous positively charged and negatively charged ionic species can exist in a typical polymer. The peroxide type initiators, the cross linking agents, the compounding agents for heat and light stability, plasticizing agents, absorbed water, ionized polymer or monomer molecules are all possible sources for supplying both the positive and negative ions whose number and mobility determine the resistivity of the polymer.

When the polymer is bombardment with protons, the implanted protons can change the resistivity characteristics of the polymer for several possible reasons. If the implanted protons remain in the polymer as unreacted ions, the resistivity of the polymer will be given by:

$$1/\rho = \mu_p n_p q_p + \sum_i n_i \mu_i q_i + \sum_j n_j \mu_j q_j \quad 8.4$$

where n_p is the concentration, μ_p the mobility and q_p the charge of the implanted unreacted protons. A comparison of Equations 8.3 and 8.4 shows that the resistivity of a bombarded polymer whose implanted protons remain unreacted, is expected to be less than that of the pre-bombarded polymers, and is expected to be inversely related to the fluence since the number of unreacted protons is equal to the number of implanted protons (n_x) which is directly related to the fluence:

$$1/\rho \sim n_p = n_x = K\phi \quad 8.5$$

where K is a constant.

If the implanted protons react with some of the negatively charged ions in the polymer to form charged molecules, proton bombardment will then either increase or decrease the resistivity depending on the numbers of implanted protons and negatively charged ions that react and lose their ionic character for transporting current. In the limiting case where all the implanted protons react with all the available negative ions, then

$$n_p = 0 = n_j$$

and the reciprocal resistivity would be given by

$$1/\rho = \sum_i n_i \mu_i q_i \quad 8.6$$

showing that the resistivity of the bombardment polymer would be larger than the pre-bombarded value given by Equation 8.3.

Equations 8.3 to 8.6 form the basis upon which the resistivity response (Figs. 8.1 and 8.2) of PVB and EVA to proton bombardment can be analyzed.

For EVA at low fluence levels, the resistivity is larger than its pre-bombardment value indicating that the implanted protons are reacting with the negative ions, contained in the EVA to reduce the number of intrinsic n_i negatively charged ions. The process is suspected to continue with increasing fluence until enough protons have been implanted to react with all the negatively charged ions. The resistivity of EVA would reach its maximum value (given by Equation 8.6) as shown in Figure 8.1. Since all the negatively charged ions have been reactively removed at this fluences, subsequent bombardment would then implant protons that remain in their unreacted ionic state. A decreasing resistivity with continued fluence is then expected for EVA as shown in Figure 8.1.

While this model is quite adequate to describe qualitatively the fluence dependence for the resistivity of EVA, the agreement between the quantitative predictions of the model and the observed experimental results is not as adequate. At a large fluence where all the negative ions have been reacted, and proton carriers are now being implanted, the model predicts that the reciprocal resistivity should be given by:

$$\frac{1}{\rho} = [n_i - n_j] \mu_p q_p + \sum_i n_i \mu_i q_i + \sum_j n_j \mu_j q_j \quad 8.7$$

Since the number of implanted proton carriers is given directly by the fluence (Eq. 8.5), Equation 8.7 becomes:

$$\frac{1}{\rho} \approx K \Phi \mu_p q_p + \sum_i n_i \mu_i q_i \quad 8.8$$

showing that the resistivity should decrease with increasing fluence according to the inverse law:

$$\rho \sim \Phi^{-1} \quad 8.9$$

This particular expected decreasing resistivity behavior with increasing fluence for EVA is not consistent with the experimental observations where the resistivity decreases with increasing fluence according to the linear relationship (Eq. 8.1):

$$\rho = -2.8(10^{-3})\phi + 5.7(10^{12})$$

for fluence values greater than $10^{14}/\text{cm}^2$.

The resistivity response of PVB increases continuously with fluence (Fig. 8.2) and does not display the peaked behavior evident in the EVA data. The implications of this continuously increasing resistance response is that PVB, in comparison to EVA, contains a relatively large number of negatively charged ions and, that even at a fluence of 10^{15} cm^2 , there are not enough implanted protons to react with all the negative ions. This comparison has some merit because PVB typically contains about 40 W/o compounding agents--usually a plasticizer--while EVA contains only about 10 W/o compounding agents as a potential source of negative ions.

While the model is in good qualitative accord with the experimental results, the quantitative aspects of the model can be evaluated in more detail by examining the expected dependence of resistivity on the fluence and comparing the results with the experimentally observed dependence.

The expected influence of fluence on the resistivity of PVB where implanted protons are reacting with negative ions, can be obtained from Equation 8.3 where n_j is now fluence dependent according to the relationship

$$n_j = n_{j_0} - n_i = n_{j_0} - k\phi$$

8.10

where n_{j_0} is the number of negative ions present in the pre-bombarded sample and where n_i , the number of implanted protons, is also the number of the negative ions that have reacted with implanted protons to form

molecules assuming that each of the implanted protons react with a negative ion. Using this result, the reciprocal resistivity becomes

$$1/\rho = \sum_i n_i \mu_i q_i + \sum_j [n_{i_0} - \kappa \Phi] \mu_j q_j \quad 8.11$$

which shows that the resistivity should increase with fluence according to a generalized law in the form of:

$$\rho \sim [A - B\Phi]^{-1} \quad 8.12$$

This predicted dependency is not consistent with the experimentally observed dependency in PVB where the resistivity increases linearly with fluence (Eg. 8.2):

$$\rho = 2.4(10^{-7}) \Phi + 10^8 \quad 8.13$$

Clearly, the models for the resistivity response with fluence in both EVA and PVB need some refinement to resolve these discrepancies between experimental observation and theoretical predictions.

The preceding analysis for the behavior of the resistivity as a function of the fluence was based upon ionic carriers and their interaction with implanted protons. The bombarding protons also introduce structural damage in the form of chain scission or cross linking into the molecular network of the polymer. The influence of this radiation induced damage on the resistivity of a amorphously structured polymer insulating material is difficult to quantify but is suspected to be extremely small if observable at all. Chain scission and cross linking as a result of proton bombardment should have a measurable influence on the elastic modulus and the chemical inertness.

Chemical Inertness and Elastic Modulus

Chain scission should create a more readily dissolvable polymer where the amount of dissolution should increase with increasing fluence and scission should also decrease the elastic modulus for a polymer in

proportion to the fluence. Cross linking is expected to increase the elastic modulus and decrease the dissolution rate of the polymer in a suitable solvent.

Experimentally, proton bombardment is found to have only a very slight influence on the dissolution characteristics of EVA in methanol (Fig 8.3). This slight influence appears to indicate that proton bombardment causes the EVA molecules to cross link at low fluence and then to experience chain scission at large fluence values.

Proton bombardment appears to have no systematically recognizable influence on the dissolution characteristics of PVB, and does not apparently have a sizable impact on the elastic modulus. The elastic modulus data suggests that PVB molecules are cross linked at low fluence and then suffer chain scission at large fluence.

No systematic correlation is evident between the proposed structural damage and the experimental resistivity values as a function fluence in these EVA or PVB samples. Structural damage then appears to have little or no effect on the resistivity of these two amorphously structural polymers.

CONCLUSIONS

(1) A conductivity model based on intrinsic ionic current carriers and their interaction with implanted protons was found to provide a reasonable qualitative explanation of the fluence dependence for the resistivity of the proton bombarded PVB and EVA samples where the resistivity of the PVB samples was found to increase with fluence while the resistivity of EVA first increased and then decreased with fluence.

(2) The exact form of these dependencies was not consistent with the predictions of the proposed models.

(3) Structural damage does not appear to influence the dissolution characteristics of PVB in any systematic way, but had an enormous effect on the elastic modulus. The dissolution data for EVA and the modulus data for PVB suggests that structural damage caused by 100KeV bombarding protons appears to be cross linking at low fluence and chain scission at large fluence.

(4) Structural damage introduced into PVB and EVA by proton bombardment appears to have little influence on the electrical resistivity; suggesting that the observed changes in resistivity with fluence results from the implanted protons.

(5) PVB can be made a more attractive pottant material for module use by proton bombardment since the implanted protons apparently react with anions to form neutral molecules. The proton bombarded PVB then becomes a better electrical insulator and less electrolytic for supporting corrosion effect.

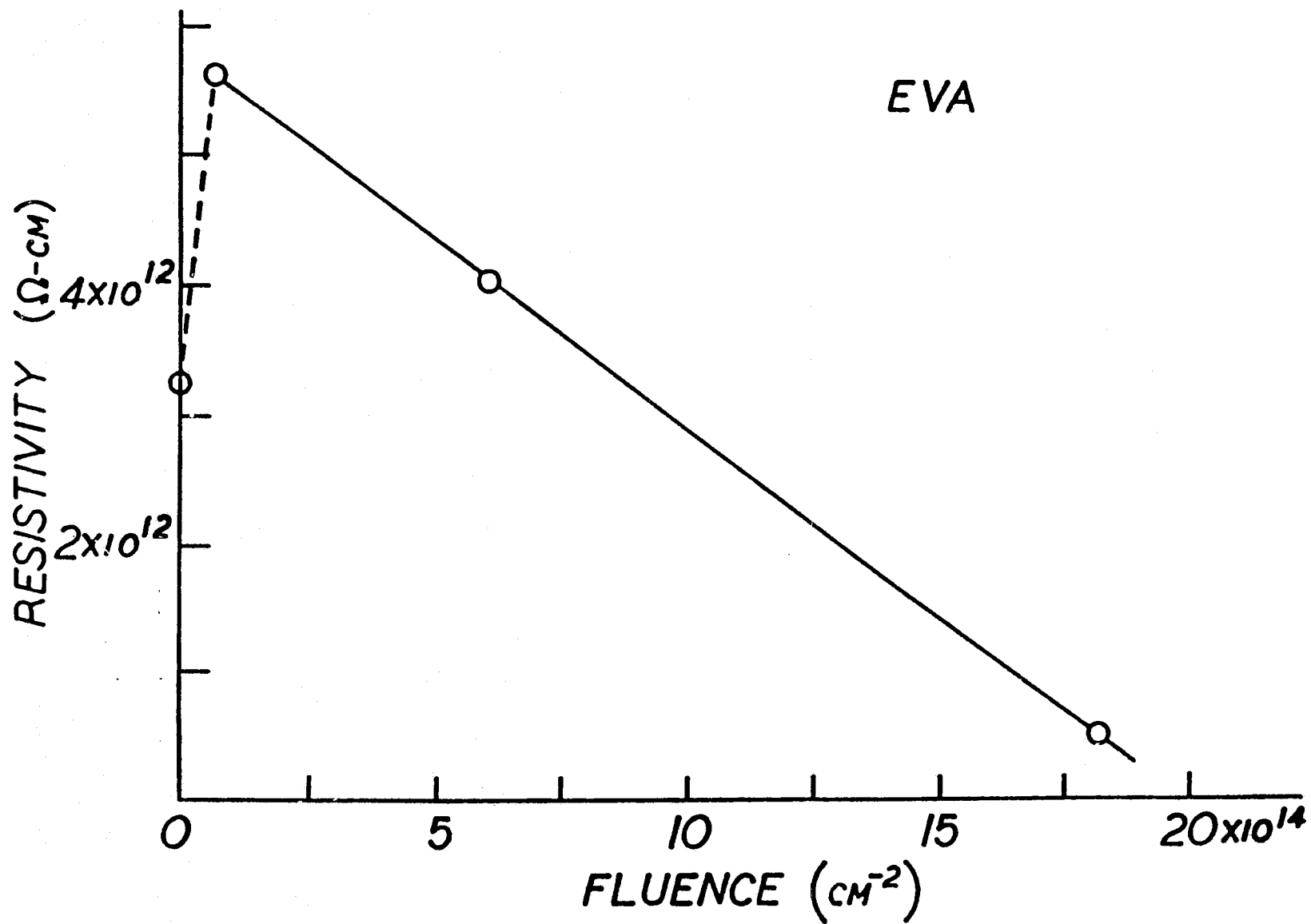


Figure 81 - Resistivity of EVA as a function of proton fluence

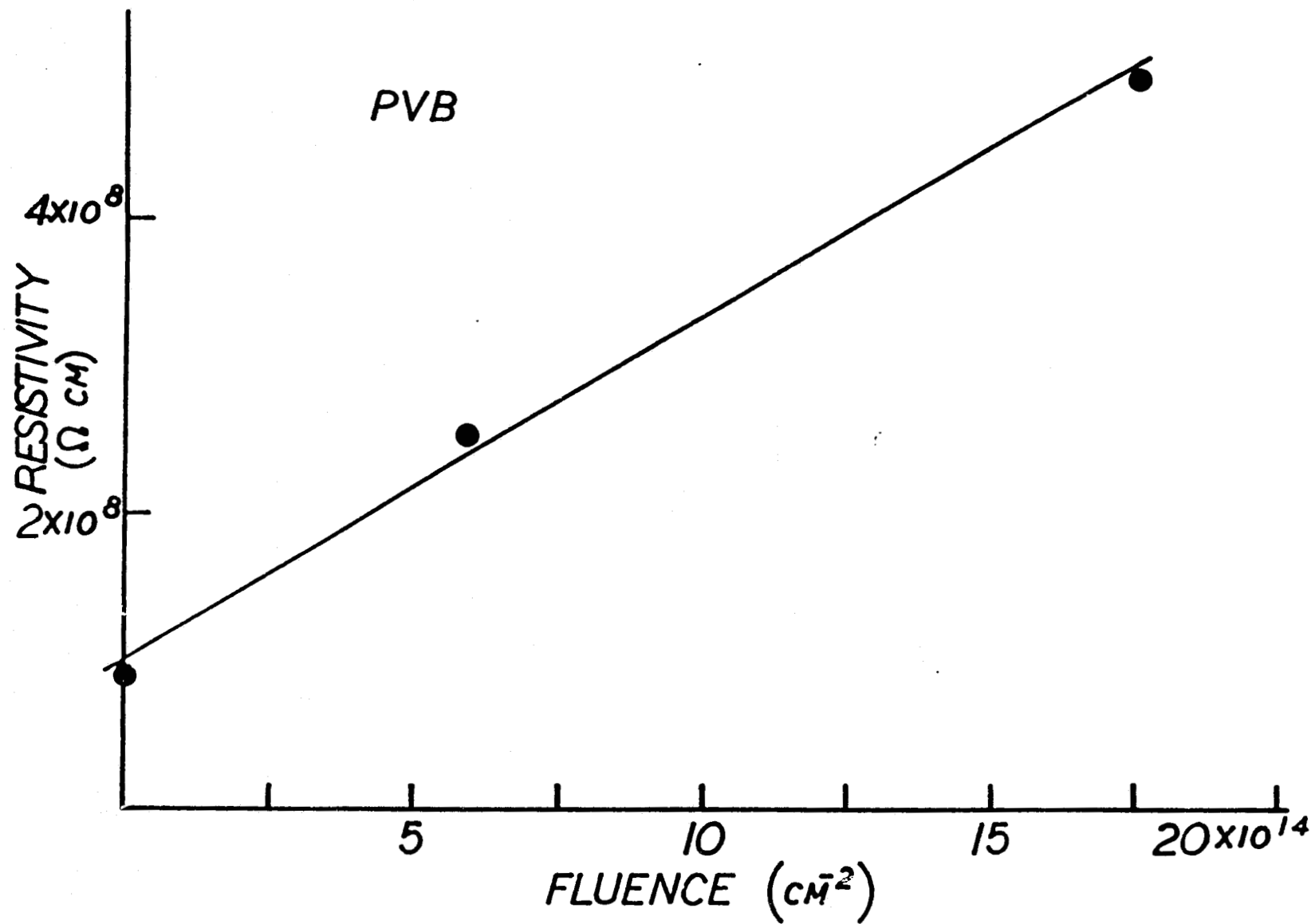


Figure 82 - Resistivity of PVB as a function of proton fluence

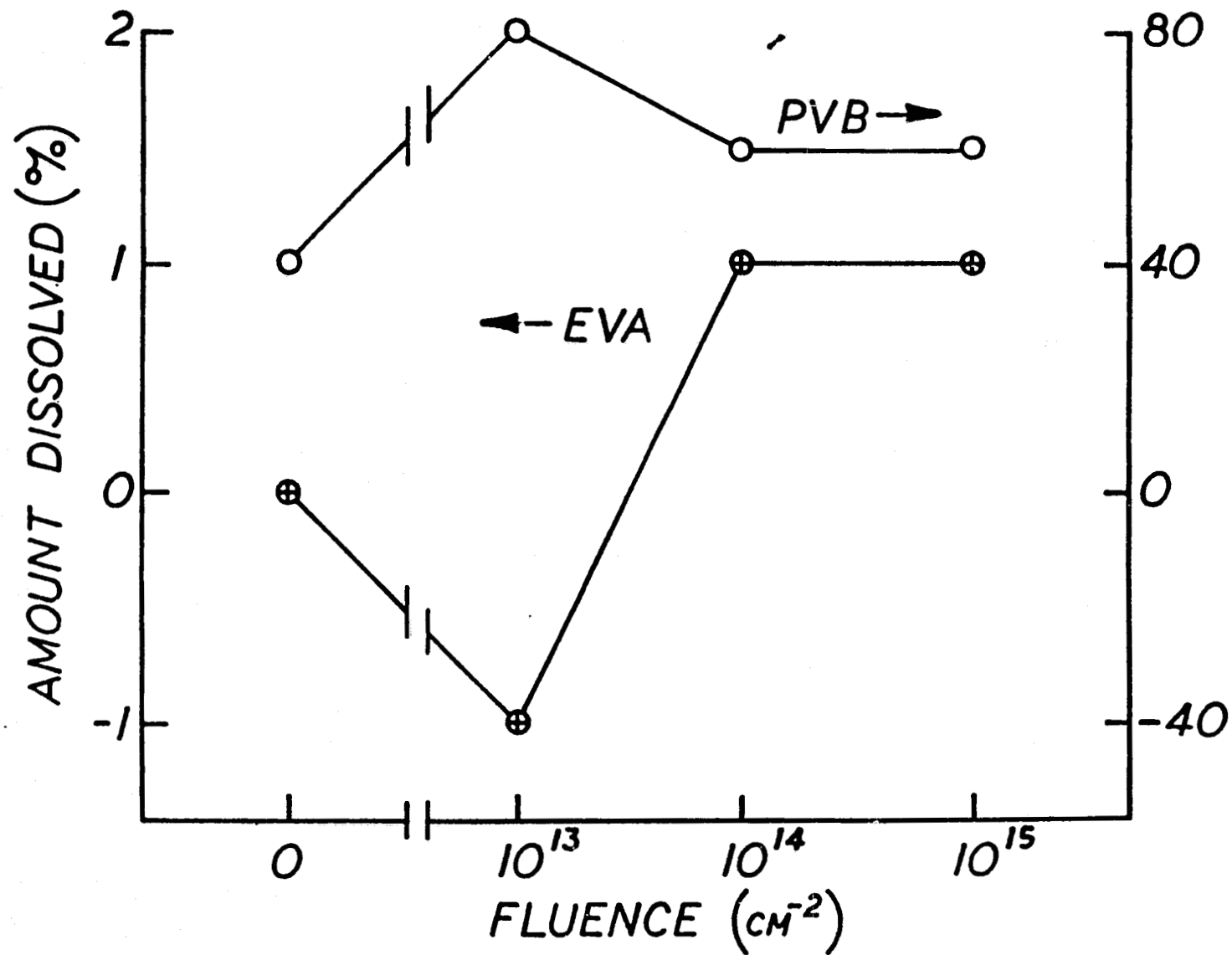


Figure 83- Effect of fluence on weight percent PVB and EVA dissolved in methanol

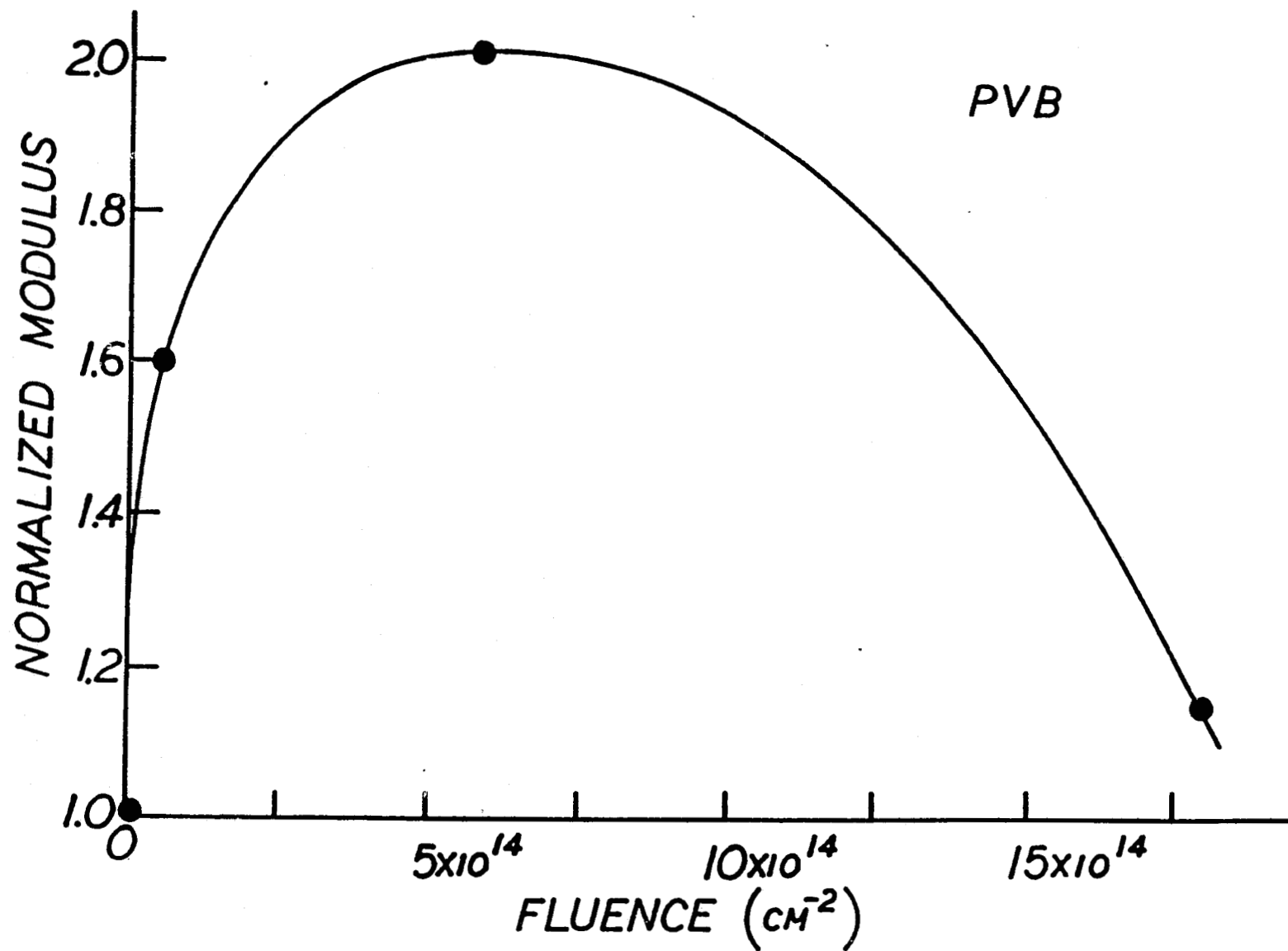


Figure 84- Normalized elastic modulus as a function of proton fluence